Dissertation in Astronomy
submitted to the
Combined Faculties of the Natural Sciences and Mathematics
of the Ruperto-Carola-University of Heidelberg, Germany,
for the degree of
Doctor of Natural Sciences

Put forward by
Dipl.-Phys. *Ronald Läsker*
born in Lutherstadt Wittenberg

Oral examination: 08.02.13

Supermassive Black Holes and their Host Galaxies

Fundamental Scaling Relations

Ronald Läsker

Max-Planck-Institut für Astronomie

Zusammenfassung

Die in dieser Doktorarbeit präsentierte Forschung hat zum Ziel, die Charakterisierung der Skalenrelationen zwischen den Massen von zentralen (Supermassiven) Schwarzen Löchern einerseits, und den Bulge- sowie Gesamtleuchtkräften ihrer Heimatgalaxien andererseits, zu präzisieren und zu erweitern. Diese Skalenrelationen sind für unser Verständnis der Galaxienentwicklung und der Herkunft Supermassiver Schwarzer Löcher bedeutsam. Im Rahmen der durchgeführten Untersuchung wurden 35 Galaxien, in welchen die Masse des zentralen Schwarzen Loches jeweils bekannt ist, im nahinfraroten Wellenlängenbereich beobachtet. Die erhaltenen Bilddaten wurden einer sorgfältigen Analyse unterzogen, wodurch Bulge- und Gesamtleuchtkräfte zuverlässig bestimmt werden konnten. Im Ergebnis konnte gezeigt werden, dass der lineare Anstieg der Korrelation zwischen Massen von Schwarzen Löchern und Bulgeleuchtkräften bisher überschätzt wurde. Weiterhin wurde ermittelt, dass die Korrelation mit den Gesamtleuchtkräften ebenso signifikant ist wie jene mit Bulgeleuchtkräften. Eine lineare Regressionsmethode wurde entwickelt, welche es erlaubt, detaillierte Kenntnisse über die kosmische Streuung der Skalenrelationen zu erhalten. Im letzten Teil der Arbeit wurde die Masse eines Schwarzen Loches mittels dynamischer Modellierung bestimmt. Die ermittelte Masse übertrifft die Voraussagen der Skalenrelationen bei weitem, wodurch deren universelle Gültigkeit in Frage gestellt wird, sich andererseits aber auch prinzipiell neue Möglichkeiten ergeben, zu einem physikalischen Verständnis der Entstehung von Galaxien und Schwarzen Löchern zu gelangen.

Abstract

The research presented in this thesis aims at improving the characterization of the scaling relations of the masses of central Supermassive Black Holes with bulge and total luminosities of their host galaxies. These scaling relations are significant for our understanding of the evolution of galaxies and the origins of Supermassive Black Holes. As part of this investigation, 35 galaxies with known central Black Hole mass were observed at near-infrared wavelengths. The obtained images were subjected to a thorough photometric analysis, which led to reliable bulge and total luminosities. As a result, it could be shown that the slope of the correlation between central Black Hole masses and bulge luminosities was previously overestimated. Further, it was found that the correlation with total luminosity is equally tight as the correlation with bulge luminosity. A linear regression method was devolped that enables extraction of more detailed information about the cosmic scatter in the scaling relations. In the last part of this thesis, a Black Hole mass was determined by means of dynamical modeling. The measured mass far exceeds the prediction from current scaling relations, thereby putting the universality of the scaling relations in question and principally opening up opportunities to better understand the physics of galaxy and Black Hole formation.

Für meine Schwester Katharina,
eine Blume, ein Flusspferd,
und eine sanfte Seekuh.

CONTENTS

INTRODUCTION

Black Holes are amongst the most interesting and fascinating objects in the Universe. They are also subject of ongoing theoretical and experimental (observational) research, as their properties and related physical phenomena are still, almost a century after being predicted by Albert Einstein's *Allgememeine Relativitätstheorie*, not fully understood. Despite being simple, at least from a macrosopic perspective, they challenge our imagination and intuition, as well as our understanding of fundamental physics. "Black Hole" (BH for short) is a popular name[1] for any object featuring a so-called *event horizon*, a surface enclosing a region of space which can be crossed only in one direction. Anything can enter its interior, but *nothing* can escape from it - therefore the denomination "Hole". This unidirectionality even holds for light; hence the Hole is "Black". The event horizon is usually not only taken as the defining property of a BH, but also as a natural definintion of the BH boundary. As no information of any kind can ever leave the BH interior[2], it is causally disconnected from the rest of the universe - therefore the "horizon" shields interior "events" from being detected by an outside observer. Nevertheless, BHs can be observed, since they have mass, angular momentum, and (probably very little) electrical charge. It is chiefly through their mass, which is necessary and directly responsible for formation of the event horizon, that they interact with the rest of the universe, occasionally causing spectacular high-energy phenomena. This way, BHs may play a prominent role in the evolution of galaxies. The most massive BHs are thought to be responsible for the observed correlations of their masses with host galaxiy properties. These correlations are the subject of the PhD thesis presented here.

---

[1]coined by John Archibald Wheeler

[2]this statement *may* have to be adapted if quantum field fluctuations are taken into account (see below)

BLACK HOLES AND GENERAL RELATIVITY

Before turning to the connection that Black Holes have with their environment, and the evolution of galaxies in particular, I would like to briefly describe several other aspects of BHs that make them significant for our physical understanding of the universe. BHs are amongst the phenomena described by General Relativity (Allgemeine Relativitätstheorie, Einstein 1915), a theory of gravitation that can be considered tantamount to "ideal" for the following reasons. First, the theory is grounded, ultimately, on only two statements: (1) the observation that the speed of light is independent of and equal for every observer, and (2) the postulate of the Einstein Equivalence Principle, which extends the classical Galileian ("weak") equivalence principle to all forces. That is, the theory is based on very few assumptions. Second, it describes and predicts a host of phenomena, the majority of which additionally were far outside most of contemporary research and empirical accessibility, as well as beyond the original motivation - which was, to reconcile the framework of *Special Relativity* (Einstein, 1905) with accelerated motion under the influence of gravity. Third, these predictions, as well as the two initial assumptions, have eluded falsification in spite of a century of fast-growing technological progress and a dramatic increase in experimental opportunities and precision. The list of such phenomena includes, but is not limited to, bending of light curves, perihelion precession, gravitational reshift, gravitational time delay, frame dragging, gravitational waves and event horizons - BHs.

General Relativity, together with Special Relativity, makes us realize that space and time are inseparable, forming a 4-dimensional contimuum[3] called "spacetime", and that gravitation is not a force, but a consequence of otherwise force-free objects following geodesics (which humans on Earth continue to resist on a daily basis) in a space-time that is *curved* by mass or, equivalently, energy. Moreover, it has radically changed *cosmology*, to the point of calling it into life as "proper", that is experimental and quantitative, field of research. General Relativity is therefore central to our understanding of the universe, its origin and future, as well as our place within. It renders the descriptive framework for phenomana such as cosmological redshift, gravitational lensing and cosmic expansion, and is thus indispensible for the interpretation of modern astronomical observations that probe ever deeper into the realms of the distant cosmos.

BHs emerge theoretically as solutions to the Einstein field equations, and are in the simplest case (non-rotating, uncharged BHs) described in form of the (exterior) *Schwarzschild metric*, which implies a point-mass as the source of gravitation. As such, BHs represent the simplest conceivable spacetime, apart from empty and homogenously-filled spacetimes, and play the same elementary role in General Relativity as point charges do in electromagnetism. The simplicity comes at a price: the singularity at the centre, where not only matter density is infinite, but also spacetime curvature. Even if the matter-energy distribution enclosed in the event horizon

---

[3]more precisely, a pseudo-Riemannian manifold

initially occupied a finite volume, complete collapse and formation of a singularity is unavoidable. Yet, the singularity is unphysical for all we know. It conflicts with quantum machanics (the Heisenberg uncertainty principle) in particular, and an infinitely curved spacetime has no meaning. Therefore, BHs have the remarkable quality of implying the break-down of the very theory that predicts them. From a theoretical perspective, they are the ideal conceptual testbed for a theory of *quantum gravity* and, by extension, a theory-of-everyting.

Another, related, challenge for fundamental physics may arise from the "no-hair theorem", according to which there are only 5 (!) quantities that characterize a BH for an outside observer, at least if quantum effects are discounted: mass, angular momentum and electric charge. Therefore, BHs "swallow" most of the information of the matter-energy that enters them. If they indeed emit *Hawking radiation* due to vacuum quantum fluctuations, they may "evaporate" eventually, but the information that was stored inside the event horizon would be lost if the radiation is thermal, as predicted[4]. Evaporation of BHs may indeed already be observed in form of short-lived gamma-ray bursts, or become observable in experiments like the Large Hadron Collider.

One important aspect has not been discussed yet: BH formation. The question of whether and how BHs can come into existence is no trivial one. Existing analytic BH solutions of the field equations are stationary, and hence do not describe emergence or evolution. The desired solutions would also have to include other (complicated) particle physics that describes the pre-BH state. The problem may be illustrated by remarking that in order to transform the Earth into a BH of the same mass, it needs to be compressed to a sphere of 9 mm radius, approximately 10^{-27} times Earth's current volume. Nonwithstanding, we know of a BH formation channel with relative certainty: gravitational collapse of a dense stellar core after cessation of energy production (nuclear fusion) at the end of a star's "life", accompanied by a cataclysmic event known as *supernova*. In this scenario, which is strongly supported by both theory and observation, gravity becomes strong enough to overcome the quantum-mechanical degeneration pressure of electrons and neutrons (cf. white dwarf and neutron star), which leaves no force left to prevent further collapse and, eventually, formation of an event horizon. The resulting BH has a mass on the same order-of-magnitude as the Sun's ("stellar mass BH").

Yet, some BHs are observed to be up to 10 orders of magnitude more massive than conceivable stellar remnants, highlighting the existence of other formation channels (for example *primordial BHs*) or efficient mechanisms to grow stellar-mass BHs to presently observed masses. The latter is inevitably connected to the galaxies that these very massive BHs reside in. Further, while the net electrical charge of astrophysical BHs should be negligible, their angular momentum (described by the Kerr-metric) may well be considerable, up to the maximum allowed value for a given BH mass (e.g. McClintock et al. 2006). This could make both the frame-dragging and

---

[4]cf. "BH information paradox"

the related *Penrose process* observable, and is predicted to affect matter accretion, jet production, and hence potentially also leaves an imprint on evolution of the *host galaxy* that a BH is part of.

BLACK HOLES AND OBSERVATIONS

Black Holes necessarily have mass, and thus wield influence on objects around them due to gravity (spacetime curvature). This influence may not be large though, depending on the BH mass. It also differs in no way from that of any other object of the same mass at distances equal or greater to the object's boundary. For example, the orbits of the planets in the solar system would be the same if the Sun was replaced by a BH having exactly one solar mass (and the Sun's angular momentum). Apart from the matter, radiation and fields present in the Sun, a gravitational difference would only arise in a region inside the solar radius: while the gravitational field eventually declines as one approaches the Sun's centre, it would continue to increase ad infinitum if the mass was hidden behind an event horizon. In short, the exterior metric for stars and BHs is exactly the same (the exterior Schwarzschild metric).

Yet, and fortunately for astronomers, dramatic phenomena can occur in the vicinity of an event horizon. Due to these, a BH may become indirectly detectable, even if the region of significant gravitational effects (the so-called *sphere-of-influence*) is smaller than the telescope's resolution limit. As is often the case, also here nature fulfills our expectations and even exceeds them. Already half a century ago, quasi-stellar objects (QSOs, or "quasars") betrayed the existence of BHs, although this realization took years to develop. As their name suggests, such objects were first seen as point sources. Yet, their spectra are different from stars and indicated (via their *redshift*) that they were the most distant objects seen by mankind, billions of light years away. They emit electromagnetic radiation in a broad continuum, from radio to X-ray wavelenghts. At estimated power outputs of up to a trillion solar luminosities, they were also the most luminous known objects, a status that they retain until today (apart from gamma-ray bursts, which are extremely short-lived in comparison). Quasars exhibit brightness variability on timescales that imply that the energy is produced in a small region, no larger than typical planetary orbits. Therefore, their power densisty is extremely high, and given their quasi-permanent nature, the only conceivable responsible energy production mechanism is conversion of gravitational binding energy.

It is now consensus that the quasar radiation source is matter in the process of accretion onto a central massive object so compact that is very likely a BH. In order to generate the observed effects, its mass must be millions to billions of solar masses. The radiating matter consists of gas that is subject to compression and internal friction due to differential kinematics, turbulence, viscosity and, probably, magnetic fields. The resulting high temperatures cause ample emission,

which in turn facilitates energy loss that lets the gas settle into an *accretion disk*. In order for matter to eventually decrease its orbit and vanish behind the event horizon, angular momentum needs to be transported outwards, a process which is still difficult to model. Through mechanisms that are even less well understood than those in the accretion disk, frequently also disk winds and *jets* form. Their synchrotron emission (at radio wavelengths) indicates the presence of magnetic fields that are implied in aiding jet formation. Many such jets are observed to travel at speeds close to light speed (e.g. in case of M87), and extend tens or even hundreds of kiloparsecs away from the source (e.g., Cyg A). When interactinging with the interstellar/intergalactic medium, they can cause shock-heating and "lobes" that are also visible at optical and X-ray wavelengths (e.g., Cen A). Every quasar is located at the centre of a galaxy, which was only initially unobserved due to limited resolution and the relative brightness of the quasar. Radiation and jets may inject energy and momentum into the galaxy's interstellar medium and thereby modify galactic gas inflow, dynamics and cooling, as well as star formation. It may manage to unbind all or part of a galaxy's gas reservoir ("feedback"), and even act on galaxy cluster scales in case of the brightest quasars.

We know now that quasars are a bright representative of a more general polpulation of similar objects, known as *Active Galactic Nuclei* (AGN). All AGN are thought to produce their energy in the above-described way, only the accretion rate or energy conversion efficiency within the accreted gas is lower. Still, a BH with mass greater than $\approx 10^6$ and up to $\approx 10^{10}$ solar masses resides at the disk's centre, as indicated by the gas dynamical information contained in the AGN spectrum. Spectral features and time variability have lead to several AGN sub-classifications. Yet, as supported by observations, in all AGN the accretion disk is surrounded by dust as well as gas of spatially varying composition, pressure, velocity, turbulence and ionization state. These properties of the accretion disk environment, together with the viewing angle we have on it, are held responsible for emergence the different spectral types. Today, accretion disks and the associated emission is observed even in systems in which the attractor is not heavier than an ordinary star (cf. X-ray binaries, microquasar). In these systems, tidal forces extract gas from a companion star, which then "flows over" and becomes ingested in the accretion disk which surrounds the BH. It should be noted that in these cases, the accretor is not always a BH, but could be a white dwarf or neutron star.

Not all BHs are "active" (accrete), or at least not enough to be detectable by the resulting radiation. But now, with increased telescope resolution and sensitivity, BHs (at least the most massive ones) are routinely observed by their influence on the kinematics of gas and stars on larger scales, through various techniques of dynamical modelling. Thereby, the central mass, as well as maximum size of the region enclosing it, can be inferred, without need to resort to the (still poorly known) structure and physics of the gas in the circumnuclear region. The most prominent example is the BH in the centre of our own galaxy, at the location of Sagittarius A*. Here, stars that

orbit the BH can be observed (their positions and velocities measured) individually, and their orbits come so close to the central mass that it represents the best case that scientists have for excluding any object other that a BH. Another special (and lucky) case are BHs surrounded by a *megamaser* disk, such as in galaxy NGC4258 (M106). Here, observations can be carried out using the technique of very-long basline interferometry with radio telescopes, making it possible to observe the kinematics of the disk at extremely high spatial resolution, to exclude any other object but a BH with high confidence, and to measure its mass with high precision.

In most cases, especially in distant galaxies, BH masses are determined by observing the kinematics of a *circumnuclear disk* (larger than and distinct from an accretion disk), or integrated stellar kinematics. The former requires assumptions about the geometry and orientation of the disk, which may be constrained by two-dimensional kinematic data or other observations (for example the presence of a jet). Unfortunately, internal dynamics (e.g. turbulence) and non-gravitational forces (e.g. from magnetic fields) are poorly known, and the kinematics are usually asymmetric to some degree, all of which principally compromise reliability of the results. BH mass measurments from stellar kinematics have to deal with the problem that individual stars are not resolved, and hence the kinematic information in the spectra is a superposition of many orbits. Also, the contribution of the stars to the gravitational potential is uncertain, as is the projection onto the plane of the sky. Therefore, BH masses (and simultaneously the stellar mass distribution, orbital structure and viewing angle) is estimated by forward modeling.

All the above methods require high signal-to-noise and spectral resolution to obtain enough information about both the BH mass and its kinematic tracers. The uncertainty in the BH mass measurement also increases sharply when spatial resolution falls short of the sphere-of-influence of the BH. This has so far limited BH mass measurements to "nearby" galaxies, that is, distances usually below $\approx 100\,\mathrm{Mpc}$, as well as BHs more massive than $\approx 10^6\,M_\odot$, so-called *Supermassive BHs*. The latter are subject of this thesis, and we will refer to those whenever the term "Black Hole" (or BH) is used in all else that follows. The data is also usually not enough to "prove" that the central massive object is indeed a BH. Nevertheless, in most of these, other scenarios, for example dense clusters of dark stars (such as neutron stars) or an extremely high stellar mass-to-light-ratio, seem contrived and unlikely for several reasons. It is therefore now believed that BHs lurk at the centres of almost all massive (above $\approx 10^{11}\,M_\odot$) galaxies. The number of such directly determined *reliable* BH masses has reached ≈ 70 as of this writing, supplemented by ≈ 100 upper limits.

BLACK HOLES AND THEIR HOST GALAXIES

The masses of BHs correlate with several properties of the *host galaxies* that they reside in. This was first realized in 1995 by Kormendy & Richstone, who found a correlation ("*scaling relation*") between the Black Hole (BH) mass, $M_\bullet$, and the (optical, *B*-band) luminosity of the host galaxy's bulge. Several other correlations have been discovered since, most notably the $M_\bullet - \sigma_\star$-relation between BH mass and stellar velocity dispersion (Ferrarese & Merritt 2000). The scaling relations can be used to estimate BH masses in a large number of galaxies or for those where direct $M_\bullet$ measurements would be unfeasible or impossible. Large numbers of thus indirectly inferred BH masses are used for *BH demography*, that is the study of the space density of BHs as a function of their mass (and possibly other factors). The scaling relations are also used as calibrators of secondary or tertiary $M_\bullet$ estimation methods, namely the method of Reverberation Mapping and the related "single-epoch" method. These are used, for example, to infer the cosmic evolution of the scaling relations, at distances where direct determination of BH masses is impossible with current observational means.

The scaling relations are also frequently implied as conveyors of information about the evolution of BHs (i.e. their growth mechanisms) and their host galaxies. As described above, BH feedback may be an important factor in galaxy evolution, and conversely, BH growth is expected to depend on the way its host can supply "food" for BH growth. Moreover, galaxies are known (observationally and by concordance cosmology) to frequently undergo *mergers*, and simultaneous mergers of their central BHs probably play a role in the emergence of the scaling relations. Astrophysical models of galaxy-BH co-evoluion attempt to describe these processes, and the scaling relations serve as (part of the) boundary conditions that these models must fulfill. In this context, also formation of the first BHs, the *BH seeds*, is relevant and the scaling relations mayf urther our understanding of the physics of BH formation.

The important observational benefits and astrophysical insights offered by the BH-galaxy scaling relations depends, naturally, on their reliable characterization, which has not been achieved yet. To advance this characterization is the main focus of the present thesis.

OUTLINE OF THE THESIS

The main part of this thesis investigates the correlations of BH masses ($M_\bullet$) with near-infrared (NIR, *K*-band) bulge and total luminosity of the host galaxy (L_{bul} and L_{tot}). In Chapter 2, I present a dedicated imaging survey which was designed to significantly improve the image quality previously available for BH host galaxies, and a specialized data reduction procedure for the notoriously difficult NIR-background subtraction. Chapter 3 gives a detailed account of the

photometric properties and decomposition process for each of the sample galaxies individually. The resulting accurate bulge and total luminosities are related to BH masses from the literature in Chapter 4, whereas the impact of different photometric methods on the scaling relations is quantified. The intrinsic scatter of the $M_\bullet - L_{\mathrm{bul}}$ and $M_\bullet - L_{\mathrm{tot}}$ relations is compared, providing information about their relative observational and theoretical significance. In Chapter 5, an advanced method of fitting the BH scaling relations is developed and used to extract additional information about the relations' intrinsic scatter. Chapter 6 presents dynamical modeling of a galaxy with an unusually massive BH that questions the universality of the BH scaling relations. I summarize this thesis and discuss prospects for related future work in Chapter 7.

2

BULGE LUMINOSITIES FROM DEDICATED NEAR-INFRARED DATA[*]

ABSTRACT

In an effort to secure, refine and supplement the existing relations between central supermassive black hole masses, $M_\bullet$, and the bulge luminosities of their host galaxies, L_{bul}, we obtained deep, high spatial resolution K-band images of 35 nearby galaxies with securely measured $M_\bullet$, using the wide-field WIRCam imager at the Canada-France-Hawaii-Telescope (CFHT). A dedicated data reduction and sky subtraction strategy was adopted to estimate the brightness and structure of the sky, a critical step when tracing the light distribution of extended objects in the near-infrared. From the final image product, bulge and total magnitudes were extracted via two-dimensional profile fitting. As a first order approximation, all galaxies were modeled using a Sérsic-bulge + exponential-disk decomposition. However, we found that such models did not adequately describe the structure that we observed in the majority of our sample galaxies, including cores, bars, nuclei, inner disks, spiral arms, rings and envelopes. In such cases, more complex models that allow for additional components, and sometimes required profile modifications, were also explored. Perhaps not surprisingly, bulge magnitudes were very sensitive to the details and number of components used in the models, while total magnitudes remain almost unaffected. Usually, the luminosities and sizes of the bulges are overestimated when a simple bulge+disk decomposition is adopted in lieu of a more realistic model, but underestimates also may occur. Notably, we found that some spheroids are not well fit by a single fixed-ellipticity Sérsic model, the adoption of which can lead to substantial biases in the derived parameters. This chapter presents the details of the image processing and analysis, while in Chapter 4 we discuss how model-induced biases and systematics in bulge magnitudes impact the $M_\bullet - L_{bul}$ relation.

---

[*]This chapter is adapted from the paper Läsker, Ferrarese & van de Ven (2013, in prep.)

2.1   INTRODUCTION

The correlation between supermassive black hole (BH) masses, $M_\bullet$, and the luminosity of their host galaxies' bulges, $L_{\rm bul}$, is noteworthy for at least two reasons. First, it is believed to hold important clues regarding the origin of BHsand the evolution of galaxies (e.g., Silk & Rees 1998; Granato et al. 2004; Hopkins et al. 2006; Croton et al. 2006; Volonteri et al. 2011; Jahnke & Macciò 2011). Second, it allows to infer BH masses – which are notoriously difficult to measure as for the required high spatial resolution of the kinematics – from a more readily available estimate of the bulge luminosity. This, in turn, enables detailed studies of BH demographics, both in the local and high redshift Universe (e.g., McLure & Dunlop 2004; Marconi et al. 2004; Shankar et al. 2004; Tundo et al. 2007). There are, therefore, very good reasons to pursue the calibration of the $M_\bullet - L_{\rm bul}$ relation in a precise and unbiased manner. Of particular interest is the relation at near-infrared (NIR) wavelenghts, not only because dust obscuration is a lesser concern, compared to optical bands, but also because the NIR luminositiy is a better tracer of the underlying stellar mass, due to the fact that the stellar mass-to-light ratio is a weaker function of stellar population (age, metallicity) in the NIR than in the optical (Bell & de Jong 2001; Cole et al. 2001). If the $M_\bullet - L_{\rm bul}$ relation is reflecting a more fundamental relation with bulge mass, its scatter is therefore expected to decrease when moving from optical to NIR bands (Marconi & Hunt 2003; Häring & Rix 2004).

The $M_\bullet - L_{bul,NIR}$ relation was first investigated using 2MASS J, H and K data by Marconi & Hunt (2003) [hereafter MH03]. Although the details of the photometric analysis were not included in MH03, analysis of the 2MASS data by one of us (CYP), using the *same* 2D-decomposition method (GALFIT) as in MH03, led to bulge magnitudes that are significantly different from the values published in MH03. This suggested to us that the limited depth and resolution of the 2MASS data, as well as uncertainties in the sky subtraction, might preclude a reliable bulge/disk decomposition and lead to largely degenerate bulge/disk parameters.

These limitations were addressed by Vika et al. (2012) [V12 hereafter], who used data from the UKIDSS survey for a sample of 29 galaxies with reliable $M_\bullet$ measurement (a subsample of 19 for their adopted result). Thanks to the improved depth and spatial resolution of the UKIDSS data (≈ 2 mag deeper and with $\approx 3\times$ better resolution than 2MASS data), Vika et al. were able to include nuclei, bars and cores in the decompositions, although proper modeling of the sky background remained a concern in their analysis.

Our work represents the next step forward. Exploiting the superior image quality at Mauna Kea, we used the $20' \times 20'$ WIRCam imager at the Canada-France-Hawaii Telescope (CFHT) to obtain deep, wide-field K-band images for 35 galaxies with secure $M_\bullet$ detections. Our data are approximatively 2 mag deeper than the UKIDSS data, and 4 mag deeper than 2MASS data, and

represent an improvement of a factor 2-4 in spatial resolution. In addition, they benefit from a dedicated observational strategy and data reduction pipeline designed to produce a reliable map of the spatial and temporal variation of the NIR background. We exploit the superior quality of the data, as well as the flexibility offered by the latest GALFIT profile fitting code (Peng et al. 2010), to perform 2D-decompositions that extend well beyond "standard" bulge+disk models. We find additional components and profile modifications to be justified and necessary *in almost all galaxies harbouring disks*, and demonstrate the large impact on the resulting bulge magnitudes. Model-based total luminosities are supplemented by parameter-free estimates. Additionally, we use the same data to derive the, hitherto unpublished, correlation between $M_\bullet$ and *total K*-band luminosity of the host, $L_{\rm tot}$.

This chapter is organized as follows: In §2.2 we present the BH host galaxy sample, and describe in detail the data characteristics, sky-subtraction strategy, and data reduction pipeline. The photometric analysis is described in §2.3, including the decomposition technique, the shortcomings of bulge+disk models, and the improved decompositions. The resulting parameters are given in §4.3, where we also present a comparison between several derived magnitudes and literature values. We summarize our findings in §4.5. The BH scaling relations derived from this data are presented and discussed in chapter 4.

2.2   NIR Imaging Data

Our sample of BH host galaxies comprises 35 galaxies with securely measured[1] $M_\bullet$ as listed in Table 2.1. Based on these criteria, we removed some galaxies from the full MH03 sample, and added galaxies of which a reliable $M_\bullet$ measurement became available before our proposal submission. V12 include a number of galaxies for which $M_\bullet$ was measured since then, while the survey data used therein does not cover about half of our galaxies. For details on the sample selection criteria and applied distances, please see §4.2.1 in chapter 4.

2.2.1   Data Acquisition

As mentioned in the introduction, existing (bulge) luminosities and the ensuing scaling relations in the NIR have so far been based on 2MASS (MH03) or UKIDSS (V12) data. The shallow depth and limited spatial resolution of the 2MASS data, as well as difficulties in background subtraction, especially for large galaxies, pose a challenge for reliable decomposition. Identification and fitting of small components (other than bulge and disk) benefits from higher *resolution*. De-

---

[1] only direct (dynamical) measurements based on resolved stellar or gas dynamics

tection of faint components is improved, and degeneracy between the components reduced, by increased *depth (signal-to-noise ratio)*. Oversubtracted or spatially varying *background* likewise is degenerate with the fitted galaxy components and may lead to photometric error (random and systematic), especially in the extended "wings" of giant elliptical galaxies. These shortcomings were partially addressed in V12, but uncertainty about the reliability of the background subtraction, as well as the number of required components, remained.

Our homogeneous imaging data set has sub-arcsecond resolution (median $0''.8$ in the final image stack, compared to 2 to $3''$ of the 2MASS data), and reaches a signal-to-noise ratio of S/N=1 at $24 \, \mathrm{mag/arcsec^2}$, a factor of 40 (4 mag) deeper than 2MASS and 2 mag deeper than the UKIDSS data used in V12. Moreover, we developed and applied an optimized dithering strategy and data-reduction pipeline that reduces both random and systematic uncertainty in the modeling and removal of the sky background.

All observations were carried out using WIRCam (Puget et al. 2004) at the CFHT, in order to benefit from the exquisite seeing on Mauna Kea, reduced NIR sky emissions at this high altitude, and a large ($20' \times 20'$) FOV. The latter allows imaging of the largest of our targets and, for the smaller galaxies, dispensation with time-consuming nodding otherwise necessary to monitor the sky background. WIRCam's FOV is composed of an array of 4 detectors, of which each contains 2048^2 pixels, resulting in a pixel scale of $0''.3$ that comfortably samples the point spread function (PSF). The $45''$-gaps between the detectors, as well as several bad pixel areas located mainly in the detector corners, need to be recovered by multiple and dithered exposures. WIRCam's read noise ($30 \, \mathrm{e^-}$) is small compared to the background flux noise (at average sky brightness, $\approx 180 \, \mathrm{e^-}$ on a 20s-exposure), and dark current ($\approx 0.05 \, \mathrm{e^-/s}$) is negligible compared to the background flux ($\approx 400 \, \mathrm{e^-/s}$). Typical total exposure times range from $\approx 500 \, \mathrm{s}$ to $1000 \, \mathrm{s}$, divided into ≈ 24 to 48 single exposures of $\approx 20 \, \mathrm{s}$ duration to avoid saturation (the background flux fills half the electron well after $\approx 25 \, \mathrm{s}$).

For all galaxies, the observing strategy consisted of a sequence of a large followed by a small dithering pattern. Each sequence started with the galaxy centered on one of the four detectors; after one $\approx 20 \, \mathrm{s}$ exposure, the telescope was slewed by $\approx 10'$ (1/2 of WIRCam's FOV), thus centering the target on an adjacent detector. Once a series of four exposures (each with the galaxy centered on one of the 4 detectors) was completed, the pointing was changed according to a small ($1''.5$) dithering pattern, and the large dithering pattern was repeated. The entire large/small dithering sequence was repeated between 4 and 28 times, depending on the galaxy, until the final total exposure time was reached (see Table 1).

The small dithering pattern was designed to permit correction for detector artifacts and removal of small sources when building the sky frame. Due to the large-scale dithering, about half of our target galaxies are entirely imaged within a single detector, allowing the remaining 3 detectors to

be used for background *structure* determination (see §2.2.2). For the remaining galaxies, which are indicated in column (6) of Table 2.1), separate sky exposures were acquired before and after each series of 4 large-dithered exposures by slewing the camera ($\approx 1.5°$), and we ascertain the background structure on these. Still, the background *level* of a given exposure may be measured from uncontaminated parts of the field. Only in the case of the largest galaxies, namely NGC221 (M32), NGC4258 (M106), NGC4347 (M84) and NGC4486 (M87), which were expected to fill most of WIRCam's FOV, we obtained sky exposures after every science frame in order to estimate the background.

Finally, for every galaxy, shorter exposures (2.5s) were obtained to recover the centres of galaxies that saturate in the long exposures.

2.2.2   DATA REDUCTION PIPELINE AND BACKGROUND SUBTRACTION

Data reduction is performed using IRAF routines unless otherwise stated. We start by inspecting all detrended frames (as provided by CFHT) and reject a few exposures that show abnormally high background levels, have erroneous pointing, or miss information in the headers (WCS, ZP). All remaining exposures are bias-subtracted and rescaled to a common zero point, using the standard-star zero points given in the image headers. Note that final photometric calibration is performed on the *co-added* frames at the end of the reduction pipeline, due to their vastly superior signal-to-noise and background quality that enables much better stellar flux estimates that the single frames.

Before the images can be co-added, the background needs to be subtracted. Although it is possible in the 2D modeling analysis described in §3 to treat and model the sky as a separate component (tilted plane), doing so can lead to significant degeneracies, especially for galaxies with extended low-surface-brightness wings. Sky subtraction on NIR exposures is a challenging task, since the typical sky surface brightness in the K-band is $\mu_b \sim 13.5$ to $14.5 \, \mathrm{mag/arcsec}^2$, ~ 10 magnitudes brighter than the galaxy surface brighness limit we wish to reach. Additionally, the background is modulated by a spatial pattern (structure) as well as temporal variability which, if not properly modeled, can lead to severe biases and systematics in the final galaxy photometry.

In what follows, we first describe the NIR background characteristics as we observe them in our data. Afterwards, we present our background subtraction strategy.

In WIRCam images, the background can be properly characterized as the sum of two separate components. The first component arises from the sky background. It is highly time variable, but exhibits relatively little spatial structure and may therefore be described almost entirely by its *level*, μ_b. This component varies by $\sim 1\% \times \mu_b$ ($\sim 19 \, \mathrm{mag/arcsec}^2$) on a 30-second

Galaxy	Hubble type	$m - M$	ref.	A_K	exposure time	sky	σ_b	FWHM ["]	β
(1)	(2)	(3)	(4)	(5)	(6)	(7)	(8)	(9)	(10)
CygA	E	36.88 ± 0.24	2	0.140	112×18s = 2016s	no	26.0	0.90	7.8
IC1459	E3	32.27 ± 0.28	1	0.006	20×24s = 480s	yes	25.0	0.57	2.1
IC4296	E	33.53 ± 0.16	7	0.023	24×18s = 432s	yes	25.0	0.82	4.3
NGC0221	cE2	24.49 ± 0.08	1	0.023	16×24s = 384s	yes	24.0	0.68	4.3
NGC0821	E6	31.85 ± 0.17	1	0.040	24×24s = 576s	yes	25.4	0.66	2.1
NGC1023	S0	30.23 ± 0.16	1	0.022	24×24s = 576s	yes	25.4	0.96	4.6
NGC1300	SBbc	31.39 ± 0.24	2	0.011	48×24s = 1152s	yes	25.9	0.49	2.0
NGC1399	E1pec	31.63 ± 0.06	8	0.005	24×24s = 576s	yes	24.7	1.05	3.8
NGC2748	SAbc	31.90 ± 0.24	2	0.010	40×20s = 800s	no	25.5	0.72	4.1
NGC2778	S0	31.74 ± 0.30	1	0.008	52×24s = 1248s	no	25.8	1.26	2.5
NGC2787	SB(r)0	29.31 ± 0.26	1	0.048	20×20s = 400s	no	25.2	0.70	4.9
NGC3115	S0	29.87 ± 0.09	1	0.017	24×24s = 576s	yes	24.8	1.08	2.1
NGC3227	SAB(s)pec	31.13 ± 0.24	2	0.008	54×24s = 1296s	yes	25.6	1.39	2.4
NGC3245	SB(s)b	31.54 ± 0.20	1	0.009	48×24s = 1152s	no	25.7	0.90	2.0
NGC3377	E5	30.19 ± 0.09	1	0.013	24×24s = 576s	yes	25.0	0.87	2.7
NGC3379	E1	30.06 ± 0.11	1	0.009	24×24s = 576s	yes	25.0	0.99	2.6
NGC3384	SB(s)0-	30.26 ± 0.14	1	0.010	24×24s = 576s	yes	25.0	0.94	2.3
NGC3608	E2	31.74 ± 0.14	1	0.008	48×18s = 864s	no	25.5	0.67	2.2
NGC3998	SA(r)0	30.71 ± 0.19	1	0.006	24×18s = 432s	yes	24.9	0.75	2.9
NGC4258	SAB(s)bc	29.29 ± 0.09	4	0.006	24×18s = 432s	yes	24.5	0.83	3.5
NGC4261	E2	32.44 ± 0.19	1	0.007	24×18s = 432s	yes	24.8	0.93	3.7
NGC4291	E3	32.03 ± 0.32	1	0.013	48×18s = 864s	no	25.6	0.84	3.8
NGC4342	S0	30.62 ± 0.25	2	0.008	48×18s = 864s	no	25.7	0.62	2.0
NGC4374	E1	31.34 ± 0.07	5	0.015	24×18s = 432s	yes	24.7	0.65	4.0
NGC4473	E5	30.92 ± 0.07	5	0.010	24×18s = 432s	yes	24.8	0.80	4.2
NGC4486	E0pec	31.11 ± 0.08	5	0.008	24×18s = 432s	yes	24.8	0.87	2.5
NGC4564	S0	31.01 ± 0.07	5	0.013	24×18s = 432s	yes	25.2	0.71	2.4
NGC4649	E2	31.08 ± 0.08	5	0.010	24×18s = 432s	yes	24.8	0.76	5.7
NGC4697	E6	30.49 ± 0.06	1	0.011	26×18s = 468s	yes	24.8	0.76	1.7
NGC5252	S0	34.94 ± 0.24	2	0.012	48×18s = 864s	no	25.4	0.76	2.1
NGC5845	E*	32.01 ± 0.21	1	0.020	48×18s = 864s	no	25.7	0.80	2.0
NGC6251	E	35.15 ± 0.24	2	0.032	48×18s = 864s	no	25.5	0.90	3.3
NGC7052	E	34.15 ± 0.24	2	0.044	53×18s = 954s	no	25.6	0.60	2.3
NGC7457	SA(rs)0-	30.55 ± 0.21	1	0.019	40×20s = 800s	no	25.5	1.07	3.5
PGC49940	E	35.93 ± 0.24	2	0.024	96×18s = 1728s	no	26.1	0.78	3.2

Table 2.1: Targets and image quality of our survey. Columns (1,2) give the name and Hubble type of each target. Distance moduli and their references are given in columns (3,4). The code in column (4) is 1: Tonry et al. (2001), 2: redshift distances, 4: Herrnstein et al. (1999), 5: Mei et al. (2007), 7: Jensen et al. (2003), and 8: Blakeslee et al. (2009). Distance moduli are based on surface brightness fluctuations (SBF) when available, but 0.06 mag have been subtracted from the Tonry et al. results to include the updated cepheid distances (Freedman et al. 2001), consistent with Mei et al.. Redshift distances are derived using $H_0 = (72 \pm 8)$ km/s/Mpc (Freedman et al., consistent with the SBF distance calibration) and velocities from NED, corrected for Virgocentric infall following Mould et al. (2000). Column (5) : K-band galactic foreground extinctions (NED). Columns (6,7) give the number of on-target exposures and exposure times, and whether off-target ("sky") exposures were taken to monitor the background (see §6.2.2 for details on the observing strategy). Short exposures that recover saturated galaxy centres are not listed. Column (8) gives the average background uncertainty σ_b on the final image stack in magnitudes, as measured across an area of 1arcsec^2. Columns (9,10) give the full width at half-maximum and asymptotic log-slope (β) of the PSF as modeled by a Moffat profile, $I = I_0(1 + (R/R_d)^2)^{-\beta}$, where FWHM = $2R_d \sqrt{2^{1/\beta} - 1}$.

timescale (the length of an individual exposure plus readout/dithering overhead), and $\sim 2.5\% \times \mu_b$ (~ 18 mag/arcsec^2) on a 80-second timescale (the typical time between subsequence exposures when slewing to the sky). The sky structure, by contrast, is virtually time-independent: the r.m.s. of the difference between subsequent images, after correction for the time-independent detector signature (as described below) is ~ 23 mag/arcsec^2, i.e. 40 to 100 times fainter than the temporal variation in the sky level.

The second component is characteristic to each detector and is due to emission from the instrument and its housing, illumination effects, deviant pixels and flatfield residuals. This component is virtually time-independent. Its spatial structure is however much more pronounced, with an amplitude of $\sim 5\% \times \mu_b$ (corresponding to an r.m.s. deviation of $\sim 2\% \times \mu_b$). It is dominated by a smooth large-scale ($\approx 10'$, i.e. the variation length is comparable to the detector size) pattern, but also includes bright streaks, smooth doughnut-like rings and sharp-edged patches, all approximately a few arcminutes in size, as well as some regions compromised by dark arcsecond-scale patches. Dark rows on the boundaries between blocks assigned to different amplifiers are also visible.

The background levels of the four detectors differ by a near-constant factor (up to $\sim 10\% \times \mu_b \simeq 17$ mag/arcsec^2 *after* scaling to a common zero-point as mentioned above), and therefore needs to be measured and subtracted separately from each detector. Additionally, the background needs to be accurately removed *before* co-adding individual science frames: due to detector gaps and dithering, pedestals would otherwise remain between different areas of the mosaiced co-added frame.

Background determination and subtraction is performed using two separate iterations of the same procedure. All objects (the target galaxy as well as foreground stars and other contaminants) are identified and masked in each exposure. We create a mask using an automated algorithm SEXTRACTOR (Bertin & Arnouts 1996), with which small objects are releliably identified. Yet, extended objects and low-surface brightness features can elude detection; each image is therefore inspected by eye and objects missed by SEXTRACTOR are masked by hand. To account for small-scale variations in the background, in the first iteration SEXTRACTOR is run using a small (32 pixel) background grid. The mask thus obtained is combined with the bad pixel mask provided by the standard CFHT pipeline. Once all objects and bad pixels are masked, we measure the median sky level (a single number for each detector) on all detectors that are sufficiently unaffected by flux from extended sources, adopting a maximum allowed mask fraction of 10%, and normalize them. This criterion automatically excludes the detector that contains the target galaxy. The normalized detector frames (including those obtained on off-target exposures) are then median-combined to obtain a map of the time-independent component of the background (large-scale pattern, rings, streaks, etc, as described above); in the process unidentified hot/dead pixels are detected and added to the bad pixel mask. The detector-specific background map thus obtained is

subtracted from each individual frame (before normalization), producing images that are largely corrected for the time-independent background component. This way, the images become much more suitable for reliable source detection (masking) and measurement of the time-variable sky level.

The procedure is then repeated: a new mask is created, this time by running SEXTRACTOR while masking the objects detected in the first pass, and with a wider (128 pixels) background grid, thereby improving the detection of extended sources (e.g., in the "wings" of stellar profiles). The median is measured again, detector-by-detector, in combination with the improved masks. This time, the time-variable sky level is estimated also on detectors containing the target galaxy, by extrapolating the median background levels measured on adjacent detectors. The background levels thus determined are subtracted from each frame.

At this stage, the frames are ready to be co-added. Although an astrometric solution is given in the headers of the detrended images provided by CFHT, we found it to be too imprecise for our purposes. A new astrometric solution is therefore computed and all frames are corrected for field distortion using SCAMP (Bertin 2006) with a 4th-order polynomial. This ensures minimal degradation of the point-spread function (PSF). The resulting frames are then co-added using SWARP (Bertin et al. 2002). This step is performed separately for the main (long) exposures, the off-target ("sky") exposures and the short exposures. Short and long exposures are *not* co-added together.

The procedure described above already produces good results. Yet, we make use of the fact that the co-added frame has a *much* higher signal-to-noise ratio than the input indivudal frames, on which objects were hitherto identified. We hence create a mask from the deep co-added frame, again by automatic (here SEXTRACTOR was used with a 128 pixel, median-filtered background grid) as well as visual source identification. This increases the fraction of masked object flux, primarily as originiating in low-surface brightness features (including but not limited to the target galaxy), which are most problematic for background characterization. The entire procedure as described above (from creation of the detector-specific map of the time-invariant background, to the final co-addition) is repeated once more, using the (reprojected) "deep" mask throughout this second iteration.

We note that although for some galaxies, in anticipation of them possibly covering the entire FOV, separate sky exposures were obtained after *every* on-target exposure (see §6.2.2), we find that in the additional time it takes to perform a large slew to the sky (60s, compared to 10s for a regular dithering), its level evolves quickly enough to introduce significant uncertainties when interpolating between bracketing sky exposures. For these galaxies, after extensive experimentation, we found it better to apply the same subtraction method as for all other galaxies, after generous masking. Only M32 requires additional manipulations, due to the overlap with the

M31 disk.

Finally, the images are photometrically calibrated by cross-correlating point sources detected in the co-added images with the 2MASS catalog. The centers of galaxies that saturate in the long exposures are replaced with data from the short exposure stacks, scaled by the average flux ratio measured on an annulus surrounding the saturated galaxy centre.

2.3   IMAGE ANALYSIS

Our measurements of apparent magnitudes are based on two-dimensional (2D) image decomposition performed by GALFIT (Peng et al. 2010). Before describing the procedure in detail, we provide a general overview of our approach to the modelling.

We require each galaxy model to contain a "bulge" component, with radial surface brightness profile of a Sérsic form (Sérsic 1963):

$$\Sigma(R) = \Sigma_e \exp \left\{ b_n \left[1 - (R/R_e)^{1/n} \right] \right\} , \tag{2.1}$$

where b_n is defined such that half of the total flux is enclosed within R_e, the effective radius. Σ_e, R_e and the Sérsic index n characterize the profile aned are allowed as free parameters. Wherever it can be identified (see §3.1), a "disk" component with exponential radial profile (equivalent to a Sérsic profile with $n \equiv 1$) is added. All parameters, including position of the center (x_0, y_0), axis ratio q and position angle (PA) of the bulge and disk component are unconstrained and, when fitting a bulge and a disk, allowed to be independent. Such Sérsic bulge (+ exponential disk) models have been applied in most previous studies that aim at bulge extraction, and we refer to them as "standard models".

The apparent bulge magnitude, $m_{b,std}$, is one of the GALFIT output parameters, and can be easily converted into absolute bulge magnitude $M_{b,std}$ and K-band luminosity $L_{b,std}$ using the distance moduli and extinction corrections listed in Table 1, as well as the absolute K-band magnitude of the Sun[2]. For standard models, the disk component magnitude, m_d, is added to yield the galaxy's total magnitude ($m_{t,std}$).

After fitting all images with standard models, and measuring the corresponding bulge and total magnitudes, most (30 out of 35) galaxies showed characteristic residuals in the model-subtracted images. While large residuals are expected for spiral galaxies, bulge(+disk) profile mismatches are observed in *all* galaxies with a disk component, and even in some of the ellipticals. This leads us to perform more detailed and complex fits to account for additional components (usually bars,

---

[2]$M_{K,\odot} = 3.28$ as taken from: http://www.ucolick.org/ cnaw/sun.html

central point sources and spiral arms), necessary profile modifications, such as disky/boxiness and truncations, and masking of giant ellipticals' cores (see §3.3). We refer to those extended and modified models as "improved" throughout the remainder of this work. We will retain the standard models' results in order to allow for comparison with previous studies of $M_\bullet - L_{\rm bul}$ scaling relations, and present them along with magnitudes derived from improved models.

In the following subsections, we detail the steps leading to our bulge magnitude measurements, and elaborate on the most common challenges in obtaining them in an accurate, yet consistent and systematic manner. The GALFIT results (i.e., the best-fit parameters) are presented in Table 2.2.

2.3.1 RADIAL PROFILES

We extract one-dimensional semi-major axis (SMA) profiles for every galaxy before commencing the two-dimensional fits via GALFIT. This is done using the IRAF task *ellipse*. Extraction of 1D-profiles, as well as GALFIT modelling, requires object masks; in both cases we use the final masks derived as part of the background estimation procedure (§2.2.2) after un-masking the target galaxy. *Ellipse* produces SMA profiles for surface brightness Σ, ellipticity ε, position angle *PA*, and the higher-order harmonic amplitude B_4 that measures isophotal deviations from perfect ellipsoids (disky and boxy).

The purpose of the 1D profiles is to help choosing the GALFIT component configuration and suitable initial parameter values. For instance, while visual inspection of the images is usually enough to reveal the presence of a disk, the profiles confirm (or refute) the visual impression in a quantitative way. Maxima in ellipticity, especially when met in conjunction with maxima in B_4 (diskiness), are also a good indicator of (embedded) disks. Throughout the 2D-fitting process, the 1D information is also a tool to judge the quality of a particular fit and to assess subsequent fitting strategy. When fitting the improved models, the 1D-profiles aid in finding configurations that include additional components; for example, bars may be indicated and confirmed by means of extrema in position angle, and a nucleus by a (negative) inflection in the otherwise smoothly-curved brightness profile of the bulge.

2.3.2 INPUT METADATA TO GALFIT

Apart from the science image, for every galaxy we provide GALFIT with a images of masked pixels / regions (the same as discussed in §2.2.2), the point-spread function (PSF), and the noise map. All are indispensable for realistic modeling and may have a significant impact on the fit result.

Therefore, care should be taken in order to construct them reliably.

The PSF image is crucial since GALFIT needs to convolve each model prior to computing χ^2 and its derivatives. We extract the PSF individually for each stacked image by co-adding several (typically 5-15) cutout images of stars with high signal but without signs of interlopers or saturation. We emphasize that a PSF image derived this way is superior to an analytic function, since the PSF is clearly neither Gaussian nor elliptical in shape. To indicate image quality, we measure the full-width at half-maximum (FWHM) by fitting a Moffat function (see Table 2.1), which we found, in all cases, to match the PSF radial profile well.

The image of the local expected pixel noise ("sigma image") directly enters the GALFIT χ^2 computation and optimization. We calculate the sigma image by measuring the background noise after applying complete source masking, modulate it by the local weight (image provided by SWARP, see §2.2.2), and add it in quadrature to the local signal noise (ADU × local gain, see the GALFIT user's manual[3]).

Aside from these metadata images, GALFIT requires the fitted image region to be defined. As we demonstrate and discuss in Appendix 2.A, inclusion of (correctly background subtracted) image regions far outside the optical radius of the target galaxy is essential for accurate modeling and determination of parameters, including the magnitude. Therefore, the fitted image region ought to be as large as possible, at least ≈ 10 effective radii, especially for elliptical galaxies. This contrasts with claim in Sani et al. (2011), who limited fitting to a central region with high χ^2 per pixel.

2.3.3   BEYOND BULGE+DISK MODELS

Improved models are necessary to model the majority of our target galaxies, for which a considerable structural diversity is evidenced by the characteristic residuals seen when using standard (bulge or bulge+disk) models. The latest version of GALFIT (Version 3.0) allows for considerable complexity, although we try to converge on the simplest models that produce adequate fits to the data. To decide whether to include a disk or additional components as well as profile modifications in our analysis, we take a multi-prong approach, based on the 1D profiles discussed in §2.3.1, the χ^2 of the standard model fit, and a visual analysis of the residual image produced by subtracting the best model from the original image. Additionally, we judge the quality of a standard model by how "robustly exponential" the disk is: we replace the exponential by a Sérsic profile, and observe how far the best-fit Sérsic index deviates from $n = 1$. Models should also be non-degenerate, converging to a best-fit (minimum-χ^2) solution quickly and robustly, i.e. not

---

[3]currently available at http://users.obs.carnegiescience.edu/peng/work/galfit/galfit.html

depending on the initial fit parameters within a wide range.

We found that our target galaxies broadly constitute several classes in terms of the characteristic deviations remaining after obtaining the best-fit Sérsic or Bulge+Disk model, and that the latter are sometimes accompanied by difficulties in determining a robust solution.

Elliptical galaxies are not always fit well by a (2D-)Sérsic profile. Several of them (IC1459, IC4296, NGC1399, NGC3379, NGC4261, NGC4291, NGC4374, NGC4486, NGC4649) exhibit a *core*, a central light deficit with respect to a Sérsic model. Cores in the optical have been found to typically be $R \lesssim 1''$ in size (e.g., Ferrarese et al. 2006), but we find all of them to extend out to at least $2''$, and up to $8''.4$ (for M87), corresponding to $\approx 0.3 \ldots 0.7 \, \text{kpc}$. Finding such large core, and them being larger in the NIR than in the optical, is an interesting finding that deserves further investigation, which is outside the scope of this thesis. In the improved models, we correct for this mismatch and the incurred bias (underestimated magnitude, effective radius and Sérsic index) by masking the core. Even more common in ellipticals, including cored ellipticals, are residuals from *isophotal deviations*. This includes *ellipticity gradients* (e.g. NGC7052), deviations from ellipses (B_4 and gradients thereof, e.g. NGC4261), and isophotal twists (e.g. IC1459). We do not account for these structures in our improved models both because they are generally mild and should therefore not strongly affect the derived magnitudes, and also because GALFIT cannot reproduce radial variations in ε and B_4 using a single-component model[4]. In some ellipticals we detect weak small-scale *substructure* that often resembles embedded highly-flattened disks (NGC4473, NGC5845). We still fit those galaxies with a single Sérsicprofile unless a corresponding robust (i.e., unique and non-degenerate) multi-component model including an *exponential* disk can be established.

There is a group of early-type galaxies (NGC821, NGC3115, NGC3377, NGC4342, NGC4697) harbouring an embedded disk that *can* be robustly fit with an exponential, but *only* if a separate Sérsic component (in addition to the bulge) is included. Because of the very low axis ratio of the disk, these galaxies are probably seen nearly edge-on. The ellipticity typically rises from a low value in the centre and, after peaking at intermediate radii, levels out to an intermediate value at large radii. Sometimes we even encounter a second ellipticity peak, as well as one or more maxima in diskiness. If the extra Sérsic component is omitted (i.e if a bulge+exponential disk model is fitted), residuals barely improve over a single-Sérsic model, and the fitted disk component is too flattened ($q \lesssim 0.1$). Moreover, the bulge Sérsic indices in the standard model ($n = 5.3$ to 8.7) are higher than generally seen in early-type galaxies at the respective magnitude (e.g. Ferrarese et al. 2006), likely because they are biased by component(s) that are not properly accounted for. The residuals strongly improve if the Sérsic index of the disk is allowed to stray from $n = 1$, in which case the best fit solution for the "disk" has $n > 2$. Forcing $n = 1$ for

---

[4]two components with coupled parameters, differing only in, e.g., ellipticity, may be joined by mirror-symmetric truncation, but we found that such models converge very slowly and usually still yield unsatisfactory residuals

the disk therefore requires an additional component. Unfortunately, interpretation of the extra component is not unambiguous: it may represent part of a bulge that is insufficiently modeled by a single Sérsic profile in two dimensions due to the ellipticity gradients, or it could be a genuine component distinct from the bulge, such as a thick ("hot") disk. This ambiguity is reflected in the "minimal" and" maximal" bulge magnitudes (see §2.4.1). We henceforth refer to the Sérsic component with higher central surface brightness as "bulge", and the second Sérsic as "envelope". The latter may have higher or lower axis ratio than the bulge, but is always less flattened than the disk.

The most common deviations from the bulge+disk morpholgy in lenticular and spiral galaxies are *bars* and *nuclei*. We identify and fit the former in NGC1023, NGC1300, NGC2778, NGC2787, NGC3227, NGC3245, NGC3384, NGC3998, NGC4258 and NGC7457, usually confirming their Hubble classification as given in deVaucouleurs' RC3 catalogue. Bars are represented by a Sérsic profile with allowed boxiness (GALFIT input file parameter $C_0 > 0$) and are required to have $n < 1$. Nuclei are represented by a point source (point-spread function after convolution) and we include them in the models of NGC1300, NGC2787, NGC3998, NGC4697 and NGC7457. Other galaxies show signs of a nucleus (NGC821, NGC1023, NGC3245, NGC3377, NGC4486, ...) but we do not include them in the model since they are generally to faint to allow for accurate modeling (the non-thermal nucleus in M87 is masked).

Another obvious additional component are spiral arms, observed in NGC1300, NGC2748, NGC3227 and NGC4258. They are modeled by a Sérsic profile (not an exponential), modified by a *rotation function*, as described in Peng et al. (2010). An exception is NGC2748, where the spiral arms are, in part due to the high inclination, too tightly wound for the fit of the rotational parameters to converge robustly.

In the case of NGC1300, the spiral arms component is further modified by an inner *trunction* via multiplication with a tanh-function (see Peng et al. 2010). We also found it necessary to introduce such a truncation for the disk component of NGC2787 and NGC3998 in order to account the for the ring, and for NGC2787's bar which does not connect through the galaxy centre. We generally do not truncate bulge components in order to maintain consistency with equation (2.1) throughout.

2.3.4 MODEL-INDEPENDENT MAGNITUDES

Considering the intricacies and potential biases involved in 2D-image modeling, we also derive alternative magnitudes, m_{24}, calculated from a non-paramtetric curve of growth analysis as $m_{24} = m_{ZP} - 2.5 \log F_{24}$, where $F_{24} = F(< R_{24})$ is the flux inside the radius at which the surface brightness drops below 24 mag/arcsec^2. We do not extrapolate the flux, in order to maintain

independence of image-specific residual background fluctuations and (uncertain) assumptions about the galaxy profile in the outer parts. The surface-brightness limit was chosen to be as low as possible, but well above the background fluctuations we observe in our images.

Curve-of-growth magnitudes are derived on circular apertures, but use the ellipse analysis (§2.3.1) by replacing masked or saturated pixels with values from the IRAF.*ellipse* model image. Curve-of-growth magnitudes can be compared to those of GALFIT-based models and reveal shortcomings of a model. For galaxies with improved models, the curve of growth profile is shown in the panels of individual galaxy decompositions (Chapter 3).

2.4   RESULTS

Table 2.2 lists the most relevant parameters resulting from the GALFIT 2D-image analysis: the bulge magnitude, effective radius and Sérsic index in columns (2-4) and, when fitted, disk magnitude and scale radius in colummns (5) and (6). Each of columns (2-6) can have up to two entries: the first corresponds to the parameters derived for the "standard" model (either a single Sérsic bulge or a Sérsic bulge plus exponential disk, see §2.3), while the second corresponds to the bulge and disk parameters derived when additional components are included ("improved" model, see §2.3.3). In the case of IC1459, IC4296, NGC1399, NGC3379, NGC4261, NGC4291, NGC4374, NGC4486 and NGC4649 the second entries in columns (3-5) correspond to parameters derived when masking the core. For improved models with multiple components, the magnitudes of the additional components are listed in columns (7)-(10), along with the type of the component (in brackets). The extra component types are "psf" for point source (point-spread function); "nuc" for resolved nucleus (small Sérsic with $n \leq 1$); "idisk" for inner disk (Sérsicwith $n \lesssim 1$), "bar" (Sérsic with $n \leq 1$, boxy isophotes; "spiral" for spiral arms (Sérsic modified by rotation function, optionally fourier and bending modes); "env" for envelope. The apparent magnitudes are uncorrected for extinction, and the radii given in arcseconds. Other component parameters, such as centre position (x_0, y_0), axis ratio $q = 1 - \varepsilon$ and position angle, are not shown here. Extinction-corrected absolute magnitudes from GALFIT decomposition are listed in Table 2.3, along with aperture magnitudes (§2.3.4) and magnitudes from the literature (bulge: Marconi & Hunt (2003), total: 2MASS database). Comparisons between standard and improved absolute magnitudes derived in our study, as comparisons with the literature value, are plotted Figures 2.1 and 2.2.

Galaxy	Bulge			Disk		Additional components			
	m_b	R_e ['']	n	m_d	R_s ['']	m_3	m_4	m_5	m_6
(1)	(2)	(3)	(4)	(5)	(6)	(7)	(8)	(9)	(10)
CygA	9.91 / –	18.4 / –	2.36 / –	– / –	– / –	–	–	–	–
IC1459	6.43 / 6.27	46.2 / 62.4	6.5 / 8.25	– / –	– / –	–	–	–	–
IC4296	7.13 / 6.68	39.9 / 97.8	5 / 8.24	– / –	– / –	–	–	–	–
NGC0221	5.01 / –	35.7 / –	3.4 / –	– / –	– / –	–	–	–	–
NGC0821	7.36 / 9.41	56.1 / 3.81	7.15 / 3.13	12.44 / 11.29	13.1 / 12.2	7.89 (env)	–	–	–
NGC1023	6.87 / 7.31	16.6 / 9.6	3.55 / 3.1	6.82 / 6.65	60 / 64.2	8.65 (bar)	–	–	–
NGC1300	9.86 / 9.55	4.08 / 10.4	1.34 / 4.3	7.40 / 8.03	64.8 / 65.4	13.86 (psf)	11.30 (idisk)	9.63 (bar)	8.74 (spir)
NGC1399	5.95 / 5.41	51.6 / 154	5.25 / 11.1	– / –	– / –	–	–	–	–
NGC2748	10.08 / 9.79	10.5 / 12.6	3.19 / 3.09	8.99 / 9.80	18.1 / 18.8	9.98 (spir)	–	–	–
NGC2778	10.18 / 10.46	4.14 / 2.75	4.6 / 3.98	10.16 / 9.99	11 / 10.7	13.83 (bar)	–	–	–
NGC2787	8.26 / 7.65	7.8 / 14.3	1.53 / 2.77	7.69 / 8.68	24.7 / 25.9	10.30 (bar)	10.22 (idisk)	12.69 (psf)	–
NGC3115	5.52 / 7.92	75 / 3.9	6.81 / 3.01	8.34 / 7.56	23.1 / 10.3	6.01 (env)	–	–	–
NGC3227	9.02 / 9.54	2.04 / 0.717	11.7 / 4.08	7.83 / 7.78	33.3 / 34.5	10.32 (bar)	–	–	–
NGC3245	8.94 / 9.50	3.54 / 1.95	2.27 / 1.6	8.24 / 8.20	20.4 / 20.5	9.91 (bar)	–	–	–
NGC3377	7.13 / 8.34	56.7 / 10.1	5.27 / 6.04	10.49 / 8.87	1.12 / 16.5	11.75 (idisk)	8.19 (env)	–	–
NGC3379	5.78 / 5.52	57.3 / 96.3	6.45 / 9.28	– / –	– / –	–	–	–	–
NGC3384	7.60 / 8.08	7.38 / 5.88	2.03 / 2.5	7.26 / 7.51	50.7 / 42.9	9.20 (idisk)	9.18 (bar)	10.25 (nuc)	–
NGC3608	7.40 / –	48.9 / –	6.6 / –	– / –	– / –	–	–	–	–
NGC3998	7.99 / 9.14	5.37 / 2.02	2.6 / 1.14	8.08 / 7.98	25.2 / 19.4	11.09 (bar)	8.90 (idisk)	11.75 (psf)	–
NGC4258	6.26 / 9.24	182 / 6.27	8.74 / 3.26	5.80 / 6.00	75 / 146	12.02 (psf)	9.82 (idisk)	8.23 (bar)	6.47 (spir)
NGC4261	6.95 / 6.65	37.5 / 68.4	4.67 / 6.49	– / –	– / –	–	–	–	–
NGC4291	8.09 / 7.96	17 / 21.3	6.79 / 8.55	– / –	– / –	–	–	–	–
NGC4342	9.69 / 10.21	1.59 / 0.99	5.25 / 1.94	9.76 / 9.64	5.61 / 4.98	10.95 (env)	–	–	–
NGC4374	5.65 / 5.40	84 / 139	6.28 / 8.3	– / –	– / –	–	–	–	–
NGC4473	6.97 / –	27.9 / –	5.11 / –	– / –	– / –	–	–	–	–
NGC4486	5.48 / 5.03	61.2 / 122	2.76 / 5.6	– / –	– / –	–	–	–	–
NGC4564	8.22 / –	13.5 / –	6.1 / –	9.18 / –	17.1 / –	–	–	–	–
NGC4649	5.54 / 5.18	51.9 / 95.7	3.41 / 5.81	– / –	– / –	–	–	–	–
NGC4697	5.59 / 8.57	154 / 6.27	6.32 / 2.11	11.24 / 8.24	20.6 / 22.9	12.38 (psf)	6.01 (env)	–	–
NGC5252	10.99 / 9.74	1.09 / 21.2	4 / 5.04	10.19 / 11.48	9.15 / 9.72	11.41 (psf)	–	–	–
NGC5845	9.08 / –	3.48 / –	2.77 / –	– / –	– / –	–	–	–	–
NGC6251	8.67 / –	20.6 / –	4.95 / –	– / –	– / –	–	–	–	–
NGC7052	8.26 / –	26.6 / –	4.15 / –	– / –	– / –	–	–	–	–
NGC7457	8.71 / 10.95	51.9 / 3	7.7 / 1.55	8.68 / 8.35	25.4 / 28.4	10.36 (bar)	13.40 (psf)	–	–
PGC49940	9.52 / –	16.7 / –	3.74 / –	– / –	– / –	–	–	–	–

Table 2.2: Basic GALFIT results for our galaxy sample. For details, see the preamble of §4.3.

Galaxy	core	disk	imp	$M_{t,2M}$	M_{24}	M_{ser}	$M_{t,std}$	$M_{t,imp}$	$M_{b,std}$	$M_{b,min}$	$M_{b,max}$	M_{sph}	M_{MH03}
CygA	no	no	no	-26.60	-27.02	-26.97	-26.97	-26.97	-26.97	-26.97	-26.97	-26.97	-27.28
IC1459	yes	no	yes	-25.46	-25.64	-25.84	-25.84	-26.00	-25.84	-26.00	-26.00	-26.00	-25.84
IC4296	yes	no	yes	-26.03	-26.39	-26.40	-26.40	-26.85	-26.40	-26.85	-26.85	-26.85	–
NGC0221	no	no	no	-19.40	-19.55	-19.48	-19.48	-19.48	-19.48	-19.48	-19.48	-19.48	-19.77
NGC0821	no	yes	yes	-23.95	-24.36	-24.48	-24.50	-24.24	-24.49	-22.44	-24.20	-24.20	-24.74
NGC1023	no	yes	yes	-23.99	-24.16	-24.38	-24.13	-24.15	-23.36	-22.92	-23.19	-22.92	-23.45
NGC1300	no	yes	yes	-23.83	-24.09	-23.57	-24.10	-24.14	-21.53	-21.84	-22.67	-21.84	–
NGC1399	yes	no	yes	-25.32	-25.70	-25.68	-25.68	-26.22	-25.68	-26.22	-26.22	-26.22	–
NGC2748	no	yes	yes	-23.18	-23.23	-23.40	-23.25	-23.24	-21.82	-22.11	-22.11	-22.11	–
NGC2778	no	yes	yes	-22.23	-22.32	-22.79	-22.33	-22.32	-21.56	-21.28	-21.33	-21.28	-22.94
NGC2787	no	yes	yes	-22.05	-22.15	-22.26	-22.12	-22.15	-21.05	-21.66	-21.85	-21.66	-21.23
NGC3115	no	yes	yes	-23.99	-24.25	-24.32	-24.43	-24.24	-24.35	-21.95	-24.03	-24.03	-24.34
NGC3227	no	yes	yes	-23.49	-23.64	-24.78	-23.61	-23.63	-22.11	-21.59	-22.02	-21.59	–
NGC3245	no	yes	yes	-23.68	-23.82	-24.20	-23.76	-23.79	-22.60	-22.04	-22.61	-22.04	-23.24
NGC3377	no	yes	yes	-22.75	-22.96	-23.35	-23.11	-22.97	-23.06	-21.85	-22.70	-22.68	-23.54
NGC3379	yes	no	yes	-23.79	-24.20	-24.28	-24.28	-24.54	-24.28	-24.54	-24.54	-24.54	-24.13
NGC3384	no	yes	yes	-23.51	-23.55	-23.52	-23.59	-23.55	-22.66	-22.18	-22.85	-22.18	-22.54
NGC3608	no	no	no	-23.64	-24.05	-24.34	-24.34	-24.34	-24.34	-24.34	-24.34	-24.34	-24.04
NGC3998	no	yes	yes	-23.35	-23.54	-23.51	-23.43	-23.41	-22.72	-21.57	-22.57	-21.57	–
NGC4258	no	yes	yes	-23.83	-23.93	-24.45	-24.04	-23.97	-23.03	-20.05	-21.61	-20.05	-22.40
NGC4261	yes	no	yes	-25.18	-25.17	-25.49	-25.49	-25.79	-25.49	-25.79	-25.79	-25.79	-25.54
NGC4291	yes	no	yes	-23.61	-23.88	-23.94	-23.94	-24.07	-23.94	-24.07	-24.07	-24.07	-23.84
NGC4342	no	yes	yes	-21.60	-21.73	-21.54	-21.65	-21.67	-20.93	-20.41	-20.85	-20.85	-21.04
NGC4374	yes	no	yes	-25.12	-25.53	-25.69	-25.69	-25.94	-25.69	-25.94	-25.94	-25.94	-25.72
NGC4473	no	no	no	-23.76	-23.88	-23.95	-23.95	-23.95	-23.95	-23.95	-23.95	-23.95	-23.74
NGC4486	yes	no	yes	-25.30	-25.86	-25.63	-25.63	-26.08	-25.63	-26.08	-26.08	-26.08	-25.68
NGC4564	no	yes	no	-23.07	-23.14	-23.23	-23.16	-23.16	-22.79	-22.79	-22.79	-22.79	-23.53
NGC4649	yes	no	yes	-25.34	-25.71	-25.54	-25.54	-25.90	-25.54	-25.90	-25.90	-25.90	-25.75
NGC4697	no	yes	yes	-24.12	-24.59	-24.90	-24.91	-24.70	-24.90	-21.92	-24.58	-24.58	-24.75
NGC5252	no	yes	yes	-25.17	-25.48	-25.80	-25.18	-25.58	-23.95	-25.20	-25.42	-25.20	-25.61
NGC5845	no	no	no	-22.90	-23.11	-22.93	-22.93	-22.93	-22.93	-22.93	-22.93	-22.93	-22.94
NGC6251	no	no	no	-26.12	-26.46	-26.48	-26.48	-26.48	-26.48	-26.48	-26.48	-26.48	-26.60
NGC7052	no	no	no	-25.58	-25.92	-25.89	-25.89	-25.89	-25.89	-25.89	-25.89	-25.89	-25.98
NGC7457	no	yes	yes	-22.36	-22.46	-23.30	-22.60	-22.45	-21.84	-19.60	-20.73	-19.60	-21.75
PGC49940	no	no	no	-25.94	-26.43	-26.41	-26.41	-26.41	-26.41	-26.41	-26.41	-26.41	–

Table 2.3: Absolute magnitudes of our target galaxies. All values have been derived from our WIRCam data, except for the total magnitude $M_{t,2M}$ (total magnitude from the 2MASS database) and M_{MH03} (bulge magnitude from MH03), which are corrected for our distances and listed for comparison. Aside from M_{24}, all magnitudes are based on GALFIT models (see Section 2.3). GALFIT-based magnitues are derived from single-Sérsic models (M_{ser}), bulge+disk models ($M_{t,std}$, $M_{b,std}$), or improved models ($M_{t,imp}$, $M_{b,min}$, $M_{b,max}$, M_{sph}). Columns "core" and "disk" indicate whether a core or a disk was detected, and "imp" whether an improved model (masked core or additional components) was established.

2.4.1 BULGE MAGNITUDES

In Figure 2.1 we compare bulge magnitudes derived from "standard" bulge(+disk) models ($M_{\rm b,std}$) with those from improved models ($M_{\rm b,min}$, $M_{\rm b,max}$ and $M_{\rm sph}$) which may include, as needed, nuclei, bars, spiral arms, inner (secondary) disks, envelopes and profile modifications as described in §2.3.3. For each galaxy with an improved model we derive three distinct bulge magnitudes. The "minimal" bulge magnitude, $M_{\rm b,min}$, is the magnitude of the improved model's bulge component alone, while $M_{\rm b,max}$ results from summing the flux of *all* components *except* the disk and, if present, spiral arms. Therefore, $M_{\rm b,min}$ and $M_{\rm b,max}$ represent a lower and upper limit, respectively, for the bulge magnitude. $M_{\rm b,min}$ reflects the conventional definition of the bulge (equation 2.1). It should be adopted as the "proper" $M_{\rm bul}$ except for the case of "edge-on lenticulars" (see 2.3.3), where the additional envelope component represents either an *ad hoc* component necessary to accurately model the outer part of the bulge, or a distict, "spheroidal" component. We therefore also introduce $M_{\rm sph}$ and include in it the flux of both "bulge" and "envelope" components. For galaxies without envelope, $M_{\rm sph} = M_{\rm b,min}$.

Not surprisingly, minimal and maximal bulge magnitudes sometimes differ considerably (by up to ≈ 1 mag) from one another, as well as from $M_{\rm b,std}$ (the bulge magnitude in the standard model). The sign of the difference, however, is not always what one might naively expect. In a few cases the bulge magnitude derived in the standard model, $M_{\rm b,std}$ is *fainter* than the conventional bulge magnitude in the improved model $M_{\rm b,min}$, despite the the fact that improved model include additional components that might be expected to "absorb" some of the bulge flux. Conversely, in numerous cases (NGC821, NGC1023, NGC2778, NGC3115, NGC3998, NGC4342, NGC4564, NGC4697, NGC7457), $M_{\rm b,std}$ is *brighter* than $M_{\rm b,max}$, the total minus the disk luminosity of the improved model. This confirms that ignoring additional components (bars, spiral arms, nuclei, etc..), and forcing a single Sérsic or Sérsic+exponential disk model to the data, can lead to severe (and unpredictable) biases in the derived bulge magnitude. We have labeled some of these cases in Fig.2.1 and discuss them in more detail below.

NGC5252 stands out as the galaxy with the largest negative difference $M_{\rm b,min} - M_{\rm b,std}$, i.e. the largest underestimate of bulge flux by a bulge+disk model. The galaxy has a bright nucleus in addition to a bulge and a disk component (see Chapter 3). Neglecting the nucleus, i.e. fitting a standard model to the profile, led to a best-fit Sérsic model for the bulge with unreasonably high n, and therefore we decided to fix the parameter (somewhat arbitrarily) to $n = 4$ (i.e. a deVaucouleurs profile). When including the nucleus in the improved model, the bulge Sérsic index converges to $n = 5.0$, close to the (fixed) value in the standard model. In the improved model, however, the bulge is brighter. We attribute this to a bias towards a small effective radius (an opposite bias would occur if the Sérsic index was not fixed) in the standard model, due to the luminous inner region. The improved model, which includes the nucleus, produces vastly

reduced residuals. Another case of bulge flux being *under*estimated by a bulge+disk model is NGC1300, for which as many as four components are present in addition to bulge+disk. Here though, the bias could be traced back to an unrealistic model of the exponential disk, which appears to fit the light of the large-scale bar. Further contribution to biased bulge parameters may come from the small, but bright, inner disk. For this galaxy, the Sérsic index *increases* (considerably!) when components other than bulge+disk are included in the model.

NGC7457 is an example of the more common situation in which the bulge flux in the standard model is overestimated, and is in fact larger than the upper limit on the bulge magnitude in the improved model. The galaxy has a bulge, a large scale disk, a bar and a nucleus. Ignoring the latter two components, and the bar in particular, leads to underestimate the disk's flux as well as its scale radius, and overestimating the bulge-R_e (see data and model profile of NGC7457 in Chapter 3). Effectively, in the standard model, the bulge over-extends to fit the large scale profile, which is in reality dominated by the disk, thus causing its magnitude to be overestimated. A similar situation occurs in NGC4258, where it is even more severe as the (main) disk, after experiencing a partial truncation at intermediate radii, continues with a larger scale radius at the largest radii. That this extension is not produced by bulge light may be inferred by the unrealistically high bulge Sérsicindex (≈ 8) in a corresponding standard model, but also by the low axis ratio at these radii. The bulge overestimate is here compounded by a bright, small and highly inclined inner disk, which supports a steep inner bulge profile, further biasing Sérsic index, effective radius and, as a consequence, bulge flux to high values.

A different situation occurs in edge-on lenticulars like NGC4697. In the standard model, the best-fit disk (which is forced to have an exponential profile) is too flattened and its flux therefore underestimated: as can be seen in Chapter 3, the best fit standard model does not provide a good match to the data. As discussed in §2.3.3, an additional component ("envelope") needs to be included to provide a good fit: without, $M_{b,std}$ is biased too high. In the particular case of NGC4697 (but also: NGC821), the inner Sérsic component is flatter that the outer. Yet it is probably not an inner disc, as its Sérsic index is > 2, and its axis ratio significantly greater than that of the exponential disc component.

The cases mentioned above are only examples; similar situations are encountered in the majority of galaxies harbouring a disk. For all of these, the inadequacy of a standard model is evident from a simple inspection of the residuals from the fits and comparison of the projected 1D model to the semi-major axis profiles of surface brightness, ellipticity, position angle and diskiness. However, the examples serve to illustrate the danger of applying a blind 2D decomposition to nearby galaxies: we found that inspection of the data and models, as well as careful supervision while running the code, were needed to provide not only a good fit, but also a realistic physical description of our targets.
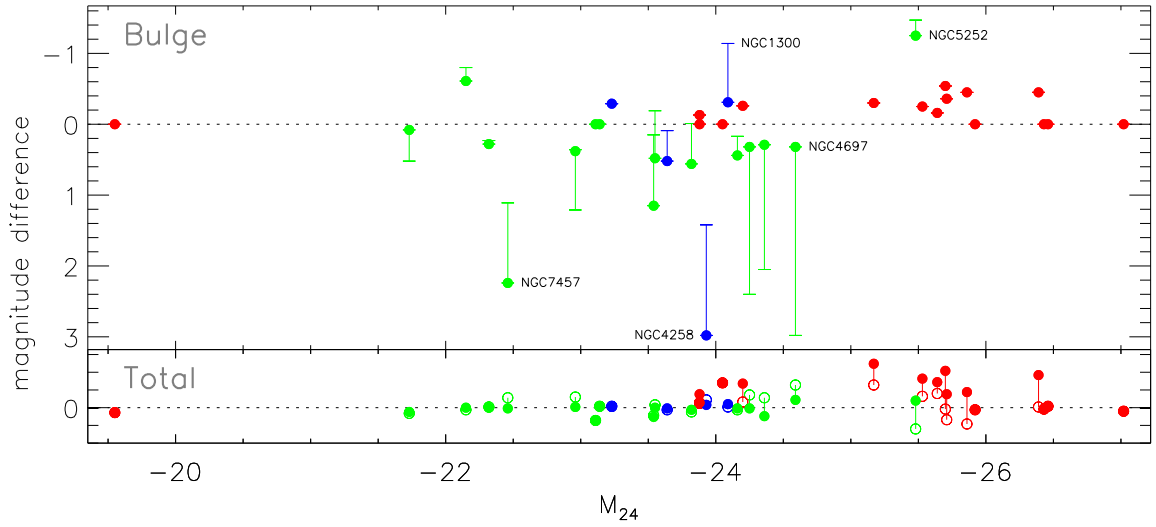
Figure 2.1: Comparison of different types of bulge (top panel) and total (bottom panel) magnitudes, all derived from our WIRCam data. Magnitude differences (y-axis) are plotted against our parameter-free estimate of total magnitude, M_{24}, with the same y-axis scaling in both panels. In the top panel, differences are between "standard" (bulge+disk) model bulge magnitudes and our three different definitions of bulge magnitude as measured by improved decomposition: $M_{sph} - M_{b,std}$, (filled circles), $M_{b,min} - M_{b,std}$ (lower limits) and $M_{b,max} - M_{b,std}$ (upper limits of the "error bars"). In all cases, the spheroid magnitude M_{sph} (nearly) coincides with either minimal ($M_{b,min}$) or maximal ($M_{b,max}$) magnitude, and their symbols thus overlap. The three improved magnitudes by definition coincide in case of elliptical galaxies; here any non-zero difference between standard and improved bulge magnitude arises from masking the core. Bottom panel: differences $M_{t,std} - M_{24}$ (open circles) and $M_{t,imp} - M_{24}$ (filled circles) between total magnitudes measured by fitting a model (bulge+disk: $M_{t,std}$, improved: $M_{t,imp}$) and parameter-free estimates (M_{24}). By comparing both panels, it is easily seen that total magnitudes are relatively invariant with respect to the applied photometric method, while standard and improved bulge magnitudes differ by up to a few magnitudes. For defintion of the magnitudes, please see Section 2.3 and §2.4.1. Labeled galaxies are discussed in 2.4.1. Linear relation fits to the plotted values are given in Table 2.4.

	$y = \Delta M$	$\langle x \rangle$	$a = \langle y \rangle$	b	r.m.s.
(1)	$M_{\mathrm{b,min}} - M_{\mathrm{b,std}}$	-24.23	0.36	0.14	1.01
(2)	$M_{\mathrm{sph}} - M_{\mathrm{b,std}}$	-24.23	0.13	0.13	0.73
(3)	$M_{\mathrm{b,std}} - M_{\mathrm{MH03}}$	-24.10	0.17	0.02	0.48
(4)	$M_{\mathrm{sph}} - M_{\mathrm{V12}}$	-23.88	-0.54	0.00	0.84
(5)	$M_{\mathrm{t,imp}} - M_{24}$	-24.23	-0.10	0.05	0.18
(6)	$M_{\mathrm{t,imp}} - M_{\mathrm{t,2M}}$	-24.23	-0.34	0.11	0.21

Table 2.4: Trends of absolute magnitude differences ΔM as plotted in Figures 2.1 and 2.2. Fitted are relations of the form $y = a + b(x - \langle x \rangle)$ with r.m.s. scatter in variable $y = \Delta M$ (first column). In all fits, $x = M_{24}$ (absolute isophotal magnitude). The x-offset, $\langle x \rangle$, is the average M_{24}, and therefore $a = \langle \Delta M \rangle$ is the average difference between the respective magnitudes. For the magnitude definitions, see Section 2.3 and §2.4.1. Notable is the large r.m.s. scatter for bulge magnitudes (lines 1-3), as well as the average offset between our "improved" and Vika et al. (2012)'s magnitudes (line 3), while the relation slopes b (trends with total magnitude) are relatively mild.

2.4.2 COMPARISON OF BULGE MAGNITUDES WITH LITERATURE VALUES

The upper panel in Figure 2.2 shows a comparison between our standard model bulge magnitudes, $M_{\mathrm{b,std}}$, and the bulge magnitudes given in Marconi & Hunt (2003). The latter were derived from 2MASS data by the *same* analysis software and the *same* model configuration (bulge+disk) as $M_{\mathrm{b,std}}$. The magnitude differences scatter considerably (r.m.s. of 0.5 mag around the average, see Table 2.4), with no obvious trend with magnitude or galaxy type (i.e. whether a disk was included or not). Our standard bulges are on average 0.17 mag fainter than MH03's. As mentioned in introduction, these results were somewhat anticipated given the uncertainties associated with the decomposition process that, in turn, originate in the limited depth of the 2MASS data and the applied background subtraction method.

Cases where M_{MH03} is much brighter than $M_{\mathrm{b,std}}$ from our WIRCam data are NGC5252, a lenticular galaxy with a bright nucleus, and NGC2778, a lenticular with a weak bar. The causes for these differences are not clear, but it is possible that NGC5252's very bright nucleus has biased the MH03 model to an unrealistically high Sérsic index, and that the NGC2778 disk might not have been recognized in the shallower 2MASS data. We note that the MH03 bulge magnitudes for NGC2778 is ~ 0.7 mag brighter than the *total* magnitude listed in the 2MASS database, and ~ 0.6 mag brighter than the *total* magnitude we estimate for this galaxy[5]. However, applying a single Sérsic model to the WIRCam data (i.e. omitting the disk) leads to a bulge (total) magnitude in reasonable agreement with MH03 (within 0.15 mag), giving credibility to our explanation that the disk component was neglected in the MH03 analysis.

The negative outlier in $M_{\mathrm{b,std}} - M_{\mathrm{MH03}}$ is NGC4258, a nucleated spiral galaxy. The galaxy hosts an

---

[5]Our data and analysis, on the other hand, leads to good agreement between $M_{\mathrm{t,std}}$, $M_{\mathrm{t,imp}}$ and M_{24}.

extended, low surface brightness disk that, if unaccounted for, might have biased the sky estimate in the 2MASS data, leading to oversubtraction. Notable is also CygA, which suffers from heavy stellar foreground contamination which, if insufficiently masked, could lead to an overestimate in the galaxy flux.

In the middle panel of Figure 2.2, we compare our spheroid magnitudes ($M_{\rm sph}$, bulge plus, if present, envelope flux) from improved models, to V12 spheroid magnitudes. The latter derive from data that allowed for modeling of nuclei, bars and cores. We find a remarkably large offset (our spheroid flux estimates are, on average, ~ 0.5 mag brighter) and considerable scatter in $M_{\rm sph} - M_{\rm V12}$, even more than for $M_{\rm b,std} - M_{\rm MH03}$ (see Table 2.4). We attribute part of this to the fact that V12 decompose NGC221 and NGC7052 into bulge+disk, where we do not find compelling evidence for a disk. Conversely, V12 do not account for the central disk of NGC4258, which probably leads to a bulge flux overestimate as explained in §2.4.1. In most other galaxies, ellipticals in particular, V12's model configuration agrees with ours. Yet, even after discounting the mentioned outliers, substantial offset and scatter between our and V12's magnitudes persist. Although the small sample overlap precludes a reliable assessment regarding a general cause, V12's method of sky level estimation, as described in §2.1 of their publication, might lead to deterioration of the galaxy flux, and contribute to the significant average underestimate (taking our results as reference). Moreover, we posit that the discrepancies cannot originate entirely in the treatment of the background. Instead, they highlight the uncertainty in bulge extraction that can be traced back to diffrences in data quality (resolution, depth), in addition to model complexity (a point which is also suggested in V12). The severity of the problem is highlighted considering that all but one of the galaxies used in this comparison are early-type (elliptical and lenticular).

2.4.3 TOTAL MAGNITUDES

Our analysis leads to three separate estimates of total magnitudes: $M_{\rm t,std}$ from the standard model (§2.3), $M_{\rm t,imp}$ from the improved model (§2.3.3) and M_{24} from a non-parameteric curve of growth analysis (§2.3.4). These are compared in the bottom panel of Figure 2.1. Differences between $M_{\rm t,std}$, $M_{\rm t,imp}$ and M_{24} are small, relative to the variance between bulge magnitudes (§2.4.1 and §2.4.2). In galaxies with disks, $L_{\rm tot}$ typically, but not always, decreases when improved models are used. The most notable exception to this trend is NGC5252, whose bulge Sérsic index has been fixed to $n = 4$ in the standard model (see §4.1). Magnitudes for elliptical galaxies are underestimated, by a few tenths of a magnitude, when cores are not masked while fitting a Sérsic profile.

Finally, $M_{\rm t,imp}$ is slightly brighter, on average, than M_{24}. This is to be expected given that, while
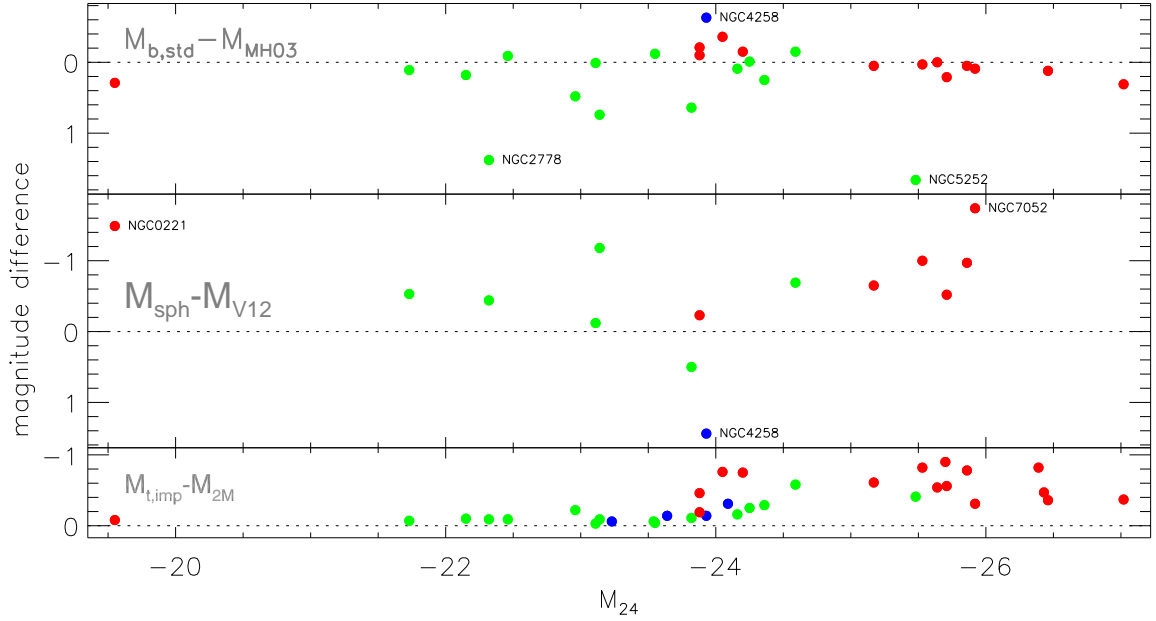
Figure 2.2: Comparison of absolute K-band magnitudes derived from our WIRCam data with literature values. Magnitudes from the literature are rescaled to our distances. Plotted are magnitude differences against our parameter-free estimate of total magnitude, M_{24}, with the same y-axis scaling in all panels. Colors indicate the galaxy type: elliptical (red), lenticular (green) and spiral (blue). Top panel: $M_{b,std} - M_{MH03}$, the difference between our standard model-based bulge magnitudes and corresponding bulge magnitudes as derived in Marconi & Hunt (2003), if available. Notably, while the underlying imaging data quality differs, the same mode of decomposition (bulge+disk) was applied. Yet, magnitude differences are often significant. Middle panel: $M_{sph} - M_{V12}$ differences between our "improved" spheroid magnitudes and those derived by Vika et al. (2012), whose models, like ours, account for nuclei, bars and and cores. The low number of points is a result of the small sample overlap. The scatter of this plot is remarkable, even after discounting the labeled galaxies (see §2.4.2). Bottom panel: difference between our best estimate of total magnitude ($M_{t,imp}$) and 2MASS total K-band magnitude ($M_{t,2M}$). Both magnitude estimates involve extrapolation of light, but we find that in comparison to our results, 2MASS data underestimate the flux, especially for elliptical galaxies. At the same time, the scatter in this plot is much smaller than in the upper two panels, indicating the relative robustness of measurements of total magnitude, in contrast to bulge magnitude. For magnitude definitions, please see Section 2.3 and §2.4.1. Labeled galaxies are discussed in 2.4.2. Linear relation fits to the plotted values are given in Table 2.4.

the former is exptrapolated to infinity, the latter reflects the flux within the isophote at which the surface brightness equals $24\,\mathrm{mag/arcsec^2}$. Comparison of $M_{\mathrm{t,imp}}$ with 2MASS total magnitudes (see Figure 2.2), which are derived similarly by extrapolaion of the profile, shows relatively small scatter, ($0.2\,\mathrm{mag}$), but 2MASS-based magnitudes are *always* fainter ($0.34\,\mathrm{mag}$ on average), the more so for the brightest and most extended (giant elliptical) galaxies. This is likely due to background oversubtraction, in the 2MASS images.

2.4.4 Magnitude uncertainties

The formal uncertainties of all our magnitudes measurements are very low - typically below 0.001. In case of galfit-derived values, these reflect the local change in χ^2 corresponding to the 1σ-confidence interval. The actual magnitude uncertainties are of course significantly larger (see also the discussion in Peng et al. 2010) and originate mainly in uncertainty in the appropriateness of the functional form of the component profiles, as well as the number of components in the model. This is exemplified in the differences between bulge magnitudes from standard and improved models, as well as in ambiguity in the interpretation of the various components for some galaxies (see §2.3.3). Total magnitudes are more robust: they show little dependency on the details of the modeling, and agree closely with the non-parametric curve-of-growth values. Additional, but less dominant, sources of uncertainty are in the background determination/subtraction, in the PSF model, the noise map, and the masks.

Quantifying such systematic uncertainty is very difficult. However, an educated guess can be gathered from the difference between the values derived using the standard and improved models and, in the latter case, between minimal and maximal values (see §4.1). The effect of magnitude uncertainties in the parametrization of the $M_\bullet - L_{\mathrm{bul}}$ relation will be discussed in chapter **??**. Here, we emphasize that the magnitudes we derive hold only under the condition that the *adopted* model (profile, number and types of components, and metadata) represent a valid physical description of the data.

In the case of isophotal magnitudes, we recognize that they necessarily represent lower limits, as we stop accounting for the galaxies' light at the measurement radius (R_{24}) at which $\mu = 24\,\mathrm{mag/arcsec^2}$. The uncertainty here originates in the unknown fraction of omitted flux, which in turn depends on the outer profile of a given galaxy, which we explicitly do not want to quantify in a parameter-free estimate. A general rough estimate, using the fundamental plane of Elliptical galaxies and assuming de Vaucouleurs' profile, indicates that the incurred magnitude error should be $\lesssim 0.1\,\mathrm{mag}$ even for giant elliptical galaxies ($M_K = -24\,\mathrm{mag}$). This agrees with the small systematic difference we observe between M_{24} and $M_{\mathrm{t,imp}}$ (§2.4.3 and Table 2.4).

2.5 DISCUSSION

Most of our non-elliptical target galaxies deviate significantly from the canonical Sérsic-bulge plus exponential-disk morphology. We emphasize that these deviations are not merely seen in the residual images once the best fit bulge+disk model is subtracted from the data, but are often noticeable in the original images and are reflected in the complexity of the one-dimensional profiles of surface brightness as well as isophotal parameters. It is worth remembering that dust obscuration is not a significant source of contamination in our analysis: except in case of the spiral galaxy NGC4258, where a small region near the galaxy centre is partially obscured, dust lanes/patches are not visible in any of our galaxies.

While the morphological complexity of the galaxies is perhaps not surprising as significant sub-structure is commonly seen in early-type galaxies with intermediate luminosity, (see, for instance, Ferrarese et al. 2006), what is noteworthy is the fact that ignoring such components can significantly bias the derived bulge magnitudes. Depth and spatial resolution are critical to accurately discern and model stellar nuclei, small nuclear disks, bars and the outer, low-surface brightness regions of galaxies. It follows that bulge parameters derived from data that do not permit an accurate characterization of the morphological diversity in nearby galaxies should be treated with caution. Case-by-case descriptions of the structure seen in our targets can be found in Chapter 3; here we summarize the most commonly observed effects of imposing Sérsic bulge (+ exponential disk) models on galaxies that deviate from such a simple morphology.

Cores in ellipticals: When a core, i.e. a depletion of light relative to the inner extrapolation of the Sérsic law that best fits the galaxy profile beyond a few arcseconds, is present and not accounted for (e.g. by masking), the resulting parameters of the Sérsic profile are biased such that luminosity, effective radius and Sérsic index n are all underestimated, sometimes drastically (up to a factor of 2-3, e.g. IC4296, NGC1399, M87, M60). The change in n is not surprising, as a model with lower Sersic index n features a fainter and less steep profile at small radii compared to a high-n model with the same total flux. At the same time, the total flux decreases since a profile with low n is steeper in the outer parts than a profile with high n. For example, for a Sérsic model with $n = 10$, $\sim 8\%$ of the total flux is at radii $r > 20R_e$, whereas for $n = 4$ (de Vaucouleurs) this fraction is less than 1%.

Nuclear (point-)sources: Here the same mechanisms as for cores is at play, albeit with opposite effect: bright nuclei *increase* the Sérsic index of the bulge component (in the most extreme case, the solution diverges[6] if the n is not fixed, see e.g. NGC5252). A profile with high n is steeper in the inner parts (thus providing a better fit for the nuclear component) but shallower (more extended) in the outer parts, leading to an artificially bright magnitude. This effect is compounded

---

[6]the fitted image region is limited in practice and, in this case, not large enough to mediate the n-divergence

if a large-scale disk is present (e.g. NGC7457): then, the latter may be degenerate with the Sérsic profile in the outer parts, and the best-fit solution may evolve to an entirely different configuration, in which, boosted by the artificially high n, the bulge component dominates again at the largest radii.

Bars and Inner Disks: If unaccounted for, these components may also bias the bulge parameters. Apart from contributing flux that should not be attributed to the bulge, they may bias R_e and n to both higher and lower values. The effect may become amplified due to the bulges' overlap, and therefore partial degeneracy, with the disk.

Finally, we comment here briefly on the possible distinction between classical and pseudo-bulges, in view of recent claims that black hole scaling relations might differ depending on the "class" to which the hosting bulge belongs (e.g., Hu 2008; Greene et al. 2008; Nowak et al. 2010; Sani et al. 2011; Kormendy et al. 2011, but see also Greene et al. (2010) for an alternative interpretation). Typically, pseudo-bulges are defined as having low Sérsic index ($n < 2$) and for being associated with distinct morphological features, including nuclear bars, spiral structures, dust, and flattening similar to the disk (Kormendy et al. 2011)).

We apply those criteria to our imaging data. As mentioned at the beginning of this subsection, none of our targets exhibits dust lanes in the K-band. At our resolution of $\sim 0\rlap{.}''8$, we observe neither spiral structures nor bars in the nuclear regions. All of our bulges appear less flattened than the respective disks. Although in a number of galaxies, we *do* identify (and model) inner disks – Sérsic components with flattening similar to the disk's and $n < 2$ (in fact, $n \lesssim 1$ all cases) – these are seen in *addition* to a bulge component, they do not *replace* it. Therefore, we fail to identify pseudo-bulges in our data based on morphological features alone. When we consider the Sérsic index, if we restrict ourselves to the bulge+disk decomposition, three galaxies have $n < 2$: NGC1300, NGC2787 and NGC3384. However, in all three cases, when improved models are used, the Sérsic indices of the bulges increase above $n = 2$ ($n = 4.3$, 2.8 and 2.5 specifically). Using the improved models, four galaxies (for which $n > 2$ when bulge+disk models are used) are best described by bulges with $n_{bul} < 2$ (these are NGC3245, NGC3998, NGC4342 and NGC7457). For the first three of them, however, the improved model is not a perfect fit to the data, suggesting that the bulge parameters are likely quite uncertain.

In conclusion, with our data and using improved models that fare better at avoiding biased bulge parameters, there are only 4 candidate galaxies that may not harbour a "classical" bulge. Yet, even in those cases the classification as pseudobulge is tentative and based on $n < 2$ only. All other galaxies feature bulges with $n > 2$. We conclude that a morphologically based classification of bulges into two separate classes is shaky at best, and do not support it.

2.6   Summary and conclusions

Using the wide field of view WIRCam imager at CFHT, we have obtained deep, high spatial resolution near-IR (*K*-band) images for 35 nearby galaxies with securely measured supermassive black hole masses $M_\bullet$. Our goal is to study and characterize the NIR $M_\bullet - L_{\mathrm{bul}}$ and $M_\bullet - L_{\mathrm{tot}}$ relations using a homogeneous imaging data set that supersedes the quality of *K*-band data previously available for our sample galaxies. In particular, we required 1) increased imaging depth to reduce component degeneracy and to allow for reliable bulge parameter estimates; 2) a dedicated dithering and data reduction strategy to improve subtraction of the strong and variable NIR-sky background; and 3) high spatial resolution to resolve and model small components, such as stellar nuclei or inner disks which, if unaccounted, can potentially bias the derived bulge parameters. These criteria are not met by 2MASS data, which formed the basis of the first NIR $M_\bullet - L_{\mathrm{bul}}$ relation (MH03). Likewise, the UKIDDS *K*-band images used by Vika et al. (2012) still suffer from residual background fluctuations and include only a fraction of our BH-host galaxy sample.

We described a dedicated data reduction procedure designed specifically to provide accurate modeling of the background, a task that is significantly aided by the wide field of view ($20' \times 20'$) of WIRCam. Our iterative procedure exploits the fact that the background can be characterized as two independent components: a spatially invariant (on the scale of a single CCD), time dependent component, and a spatially complex, but time-invariant pattern. Using the 2D software GALFIT3, we found that while 17 galaxies (all classified as ellipticals) can be adequately modeled by a single Sérsic profile, all other galaxies (including 3 targets classified as elliptical in the RC3) required the addition of (at least) an exponential disk. The resulting bulge magnitudes, $M_{\mathrm{b,std}}$, typically differ by several tenth of a magnitude from the values published by MH03 and based on 2MASS.

However, we found that such "standard" bulge+disk models do not generally provide good fits to the data. Such discrepancies can be resolved by the inclusion of additional components, most commonly bars (8 galaxies), galactic nuclei (8 galaxies) and inner disks (6 galaxies). Making use of the flexibility offered by GALFIT, we also model evident spiral arms (4 galaxies) and rings (2 galaxies). Moreover, in 5 early-type systems with highly inclined disks, we found it inevitable for an adequate fit to introduce, in addition to the bulge, a second large-scale component with Sérsic profile ($n \gtrsim 1$). It is unclear whether such "envelope" is simply needed to account for deviations from a Sérsic model in the outer part of the bulge, or whether it constitutes a separate stellar component, distinct from the bulge. Finally, we observe a central light deficit (measured relative to the inner extrapolation of the Sérsic law that best fits the outer profile) in 9 elliptical galaxies: for these, the core region was masked when fitting the data.

While the total magnitudes we derived are largely independent on the details of the modeling

(e.g. the number of components used), and agree well with the estimate obtained from a non-parametric curve-of-growth analysis, the bulge magnitudes vary significantly according to the specifics of the model used to represent the galaxy. For galaxies requiring additional components, bulge magnitudes are on average 0.36 mag fainter than derived using a simple bulge+disk decomposition. This serves as a warning that careful analysis and supervision must be applied when fitting nearby galaxies to avoid biases and systematics in the derived bulge magnitudes.

In chapter 4, the bulge and total magnitudes will be used to provide a detailed characterization of the NIR $M_\bullet - L_{\mathrm{bul}}$ and $M_\bullet - L_{\mathrm{tot}}$ relations for supermassive black holes.

2.A   ESTIMATING $\Delta\chi^2$ FOR SINGLE-PARAMETER CHANGES AROUND THE GALFIT SOLUTION

This appendix investigates the way that different image regions constrain the best-fit solution rendered by a profile fitting code like GALFIT, by analyzing the local dependency of χ^2 with respect to single-parameter changes around its minimum. It briefly discusses the distinction between the projection of the χ^2-contours and their intersection with the axes of constant parameters. It is demonstrated that the local χ^2-derivative, as opposed to the χ^2-value itself, is relevant for constraining the model parameters, and that therefore identication of "sensitive" radial ranges on the basis of χ^2, as suggested by Sani et al. (2011), is misguided. Finally, it is shown that, also in contrast to the mentioned publication's claims, significant constraints are placed on the best-fit solution at all radii, resulting in the recommendation to include a large area in the fit.

2.A.1   PROJECTION OF $\Delta\chi^2$

Around the optimal (minimum-χ^2) solution provided by GALFIT, consider $\Delta\chi^2$ as a function of the variations δp_i, $i = 1, ..., M$, of the parameters of this model around their least-χ^2-values. For example, there are $M = 7$ parameters for a Sersic model: x_0, y_0, m, R_e, n, q and PA.

Now, we want to find the $\Delta\chi^2$ effected by a certain variation in only *one* of these parameters, say δp_ν. Equivalently, one could state the problem the other way around: Given a fixed value of $\Delta\chi_0^2$, what is the variation δp_ν needed? Therefore, we must consider the *projection* of $\Delta\chi^2$ onto the axis of p_ν. A mere intersection of $\Delta\chi^2$ along the p_ν-axis, i.e. evaluating $\Delta\chi^2(0, 0, .., p_\nu, 0, ..., 0) = \Delta\chi_0^2$ does not suffice: what we in fact want to know are the boundaries of the M-dimensional region containing $\Delta\chi^2(\{p_i\}) < \Delta\chi_0^2$, specifically its extent $[-\delta p_\nu, \delta p_\nu]$ in the p_ν-direction[7]. As illustrated in Press et al. (1992, p.689), this amounts to finding the set of parameters $\{\delta p_i\}_{i \neq \nu}$ minimizing $\Delta\chi^2$ while δp_ν is kept fixed. This can be done analytically (see Press et al. 1992, p.691) once all second derivatives $\frac{\partial(\Delta\chi^2)}{\partial p_i \partial p_j}$ and the inverse of the resulting Hessian matrix are known. Luckily, we can forego (numeric) calculation of the derivatives here and simply use GALFIT to minimze χ^2 under the condition of keeping parameter ν fixed at the desired variation δp_ν.

The resulting $\Delta\chi^2$ then can serve to calculate the confidence of a given parameter interval. Since $\Delta\chi^2 = \sum_{x,y} \Delta\chi^2(x, y)$, one can map the spatial distribution of the χ^2 increase incurred by a given amount of deviation from the best-fit model. This way, one can identify the regions where the solution is most sensitive to parameter changes, and hence the largest power in narrowing down

---

[7]we assume $\Delta\chi^2$ to be even in the $\{p_i\}$, which indeed holds in a sufficiently small region around the best-fit model.

the confidence intervals lies. In particular, when allowed a small total change in the input *data*, this gives the way one would distribute it in order to achieve the largest possible change in the fitted model magnitude.

2.A.2 The case of bulge+disk models

While the confidence interval of the *bulge* magnitude (m_b) in a model with disk component is found in just the same way, by simultaneously optimizing the additional disk parameters including the disk magnitude m_d, the question of how to obtain the confidence (that is, $\Delta\chi^2$) of a given local change in *total* magnitude (m_t) requires yet more consideration. The reason simply is because m_t is not a parameter of the model, but rather a function thereof:

$$m_t = -2.5 \log\left(10^{-m_b/2.5} + 10^{-m_d/2.5}\right) \tag{2.2}$$

The solution to this problem would be exeedingly simple if the contraints modes of GALFIT were to allow for sums and functions of parameters to be equated.

Since this is to my knowledge not the case, the way to go is to consider the projection in two steps. First, project $\Delta\chi^2$ from the space of all M parameters onto the (m_b, m_d)-plane. Following the agrument in §1 for changes in one parameter, this is done by specifying ($\delta m_b, \delta m_d$) and letting GALFIT optimize χ^2 over all other parameters.

Second, consider from here and on as if we had $\Delta\chi^2$ depending on only two parameters to begin with. We want to seek out the parameter combination along the line of constant m_t that minimizes $\Delta\chi^2$ - which is equivalent to projecting the elliptical region containing a given $\Delta\chi_0^2$ along lines of constant δm_t. The $\pm\delta m_t$ probed this way will be the one tangent to the ellipse of constant $\Delta\chi_0^2$. Equivalently, one may also proceed the other way around: specifying δm_t and seeking the combination ($\delta m_b, \delta m_d$) that yields the smallest possible $\Delta\chi^2$ while keeping (2.2) constant.

$\Delta\chi^2$ can be locally approximated by a Taylor expansion around the original solution ($\delta m_b = \delta m_d = 0$):

$$\Delta\chi^2 \approx \frac{1}{2}\chi_{bb}^2 \cdot (\delta m_b)^2 + \chi_{bd}^2 \cdot (\delta m_b)(\delta m_d) + \frac{1}{2}\chi_{dd}^2 \cdot (\delta m_d)^2 + ... \tag{2.3}$$

where the subscripted χ^2 denote the partial derivatives with respect to m_b and m_d. We have also used the exchangeability of the partial derivatives and that the first derivatives of χ^2 (and of $\Delta\chi^2$) vanish at its minimum. We now insert (2.2) and choose one of the two parameters, e.g. δm_d, to be eliminated in favor of δm_t. As (2.2) is nonlinear, we resort to its linear approximation in order

to solve (2.3):

$$
m_t(m_b + \delta m_b, m_d + \delta m_d) \;\approx\; m_t(m_b, m_d) + \frac{\partial m_t}{\partial m_b} \cdot \delta m_b + \frac{\partial m_t}{\partial m_b} \cdot \delta m_b + \ldots
$$

$$
\implies \quad \delta m_t \;\approx\; \frac{\partial m_t}{\partial m_b} \cdot \delta m_b + \frac{\partial m_t}{\partial m_d} \cdot \delta m_d \tag{2.4}
$$

After substituting (2.4) into (2.3), one may now obtain the relationship between $\Delta\chi_0^2$ and δm_t by searching for the line $\delta m_t = const.$ that is tangent to $\Delta\chi^2 = const. = \Delta\chi_0^2$, which is done by demanding the quadratic equation for $\Delta\chi^2 = \Delta\chi^2(\delta m_b; \delta m_t = const.)$ to have a unique solution in δm_b. As mentioned above, likewise one may specify δm_t, then set $\frac{\partial \Delta\chi^2}{\partial(\delta m_b)} = 0$ at its minimum and thus obtain the optimal value $(\delta m_b)_{opt}$. Substituting $(\delta m_b)_{opt}$ back into (2.4) gives $(\delta m_d)_{opt}$.
I performed the calculation both ways, with unsurprisingly identical results:

$$
(\delta m_b)_{opt} \;=\; \frac{\gamma_b \chi_{dd}^2 - \gamma_d \chi_{bd}^2}{D} \cdot \delta m_t \tag{2.5}
$$

$$
(\delta m_d)_{opt} \;=\; \frac{\gamma_d \chi_{bb}^2 - \gamma_b \chi_{bd}^2}{D} \cdot \delta m_t \tag{2.6}
$$

$$
\overset{(2.3)}{\implies} \quad \Delta\chi^2 \;=\; \frac{\chi_{bb}^2 \chi_{dd}^2 - (\chi_{bd}^2)^2}{2D} \cdot (\delta m_t)^2 \;, \tag{2.7}
$$

where

$$
\gamma_b \;=\; \frac{\partial m_t}{\partial m_b} = \frac{1}{1 + 10^{(m_b - m_d)/2.5}}
$$

$$
\gamma_d \;=\; \frac{\partial m_t}{\partial m_d} = \frac{1}{1 + 10^{(m_d - m_b)/2.5}}
$$

$$
D \;=\; \gamma_b^2 \chi_{dd}^2 - 2\gamma_b \gamma_d \chi_{bd}^2 + \gamma_d^2 \chi_{bb}^2 \;.
$$

One has to be careful when taking the partial derivatives of m_t in that the derivative of $\log(y)$ is $(\ln 10)^{-1} \cdot (y'/y)$, *not* simply y'/y.
Close inspection of (2.7) shows that the numerator is the determinant of the Hesseian matrix $\mathbf{H} = \mathbf{H}[\Delta\chi^2(m_b, m_d)]$, and (2.5)-(2.7) could be rewritten as

$$
\begin{pmatrix} \delta m_b \\ \delta m_d \end{pmatrix}_{opt} \;=\; \frac{\mathbf{H}^{-1}\vec{\gamma}}{\vec{\gamma}^T \mathbf{H}^{-1} \vec{\gamma}} \cdot \delta m_t
$$

$$
(\delta m_t)^2 \;=\; 2\vec{\gamma}^T \mathbf{H}^{-1} \vec{\gamma} \cdot \Delta\chi^2 \;,
$$

where $\vec{\gamma} = \vec{\nabla}m_t$ is the gradient with respect to m_b and m_d.

We have thus arrived at a formula to evaluate the change in $\Delta\chi^2$ given an amount δm_t of change in total magnitude while optimizing over all other parameters - that is, we know the "proper" change m_b and m_d away from the original solution that we have to set fixed in order to find the unique $\Delta\chi^2$-surface that is tangent to $\delta m_t = const$.

For completeness, I will lastly give a suggestion for obtaining the second derivatives of $\Delta\chi^2$. I use the approximation of the gradient in a symmetrized form. For an arbitrary, yet continuous and continuously differentiable function $f(x)$, and a small but finite interval Δx around the argument,

$$f_x \approx \frac{f(x + \Delta x) - f(x - \Delta x)}{2\Delta x} \ .$$

Thus for second derivatives, and for functions $f(x, y, ...)$ depending on more than one variable:

$$f_{xx} \approx \frac{f(x + \Delta x, y) - 2f(x, y) + f(x - \Delta x, y)}{(\Delta x)^2}$$

$$f_{xy} \approx \frac{1}{4(\Delta x)(\Delta y)} \cdot \big[f(x + \Delta x, y + \Delta y) - f(x + \Delta x, y - \Delta y) \\ - f(x - \Delta x, y + \Delta y) + f(x - \Delta x, y - \Delta y) \big]$$

In the context of §2, where f, x and y get replaced by $\Delta\chi^2$, m_b and m_d, it is important to keep in mind again that $\Delta\chi^2$ is already evaluated by optimizing over all other model parameters. Inserting (2.7) into the above approximations, and considering $\Delta\chi^2 = \Delta\chi^2(\delta m_t)$ gives

$$\frac{\mathrm{d}^2\Delta\chi^2}{\mathrm{d}m_t^2} = \frac{\chi_{bb}^2\chi_{dd}^2 - (\chi_{bd}^2)^2}{\gamma_b^2\chi_{dd}^2 - 2\gamma_b\gamma_d\chi_{bd}^2 + \gamma_d^2\chi_{bb}^2} = \left(\vec{\gamma}^T \mathbf{H}^{-1} \vec{\gamma}\right)^{-1} \tag{2.8}$$

Subsequently, the change in χ^2 for *any* given (but small) change in m_t may be calculated as $\Delta\chi^2(\delta m_t) \approx \frac{1}{2}\frac{\mathrm{d}^2\Delta\chi^2}{\mathrm{d}m_t^2} \cdot (\delta m_t)^2$ according to the Taylor expansion - which is, of course, identical with (2.7).

Another comment should be made about equations (2.7) and (2.8) : It is *not* permissible to compute (2.7) pixel-by-pixel directly from the $\Delta\chi_{bb}^2$, $\Delta\chi_{bd}^2$ and $\Delta\chi_{bb}^2$ images of the second derivatives. This is a consequence of the nonlinearity in (2.7):

$$\frac{(\sum_i \chi_i^2)_{,bb}(\sum_i \chi_i^2)_{,dd} - \left[(\sum_i \chi_i^2)_{,bd}\right]^2}{\gamma_d^2(\sum_i \chi_i^2)_{,bb} + \gamma_b^2(\sum_i \chi_i^2)_{,dd} - 2\gamma_b\gamma_d(\sum_i \chi_i^2)_{,bd}}$$

$$= \frac{(\sum_i \chi_{i,bb}^2)(\sum_i \chi_{i,dd}^2) - (\sum_i \chi_{i,bd}^2)^2}{\gamma_d^2 \sum_i \chi_{i,bb}^2 + \gamma_b^2 \sum_i \chi_{i,dd}^2 - 2\gamma_b\gamma_d \sum_i \chi_{i,bd}^2}$$

$$\neq \sum_i \frac{\chi_{i,bb}^2\chi_{i,dd}^2 - (\chi_{i,bd}^2)^2}{\gamma_d^2\chi_{i,bb}^2 + \gamma_b^2\chi_{i,dd}^2 - 2\gamma_b\gamma_d\chi_{i,bd}^2}$$

Hence, one has to consider the derivatives of the full (total) χ^2. If one wants to calculate the corresponding *images* of $\Delta\chi^2$ and its derivatives regarding the total magnitude, one cannot bypass (2.5) and (2.6) but must use the optimal parameter set $\{(\delta m_b)_{opt}, (\delta m_d)_{opt}\}$ to construct the two models with $\pm\delta m_t$ and measure local χ^2 deviations from them.

Figure 2.3 shows two examples (CygA, a giant elliptical galaxy, and NGC2778, which harbours a disk component) of the behaviour of $\Delta\chi^2$ under changes of several parameters. Generally, one can see that despite having a much higher amplitude (average value per pixel) at small radii, at least half of the total χ^2 change incurs outside of the effective radius. In particular, for the respective total magnitudes, roughly 70% of the total $\Delta\chi^2$ accumulates there. This translates directly into the fact that the region outside of $1\,R_e$ places at least as much constraint on the fitted magnitude than the region within $1\,R_e$. For the observer, this suggests that in order to measure magnitudes of typical galaxies, both early- and late-type, it is advantageous to

1. include a large enough image region in the fit - if available, extending at least as far as $\sim 10\,R_e$ from the galaxy centre[8]

2. determine and subtract the background as precisely and reliably as possible, and avoid overestimates that tend to occur from the inclusion of unrecognized low-surface brightness (LSB) regions. In particular,

   - *generously* mask extended sources, prominently the target galaxy

   - use off-target exposures when the target galaxy is large compared to the field-of-view (FOV), or when the latter is otherwise contaminated by LSB sources

   - do *not* use off-target exposures unnecessarily, especially when sky level is highly variable[9]

   - do not fit polynomials (as unfortunately done for the 2MASS LGA) or other higher-order functions

   - avoid using the "sky" component offered by GALFIT, as it becomes increasingly degenerate with the galaxy model's profile in its outer parts

   - detect and exclude as many back- and foreground sources as possible, or at least do so in a consistent manner[10]

---

[8]this agrees with the suggestion given in the GALFIT manual
[9]because of the time gap between on-target and sky exposures
[10]that is, with the same detection method and threshold when estimating the sky and when running GALFIT
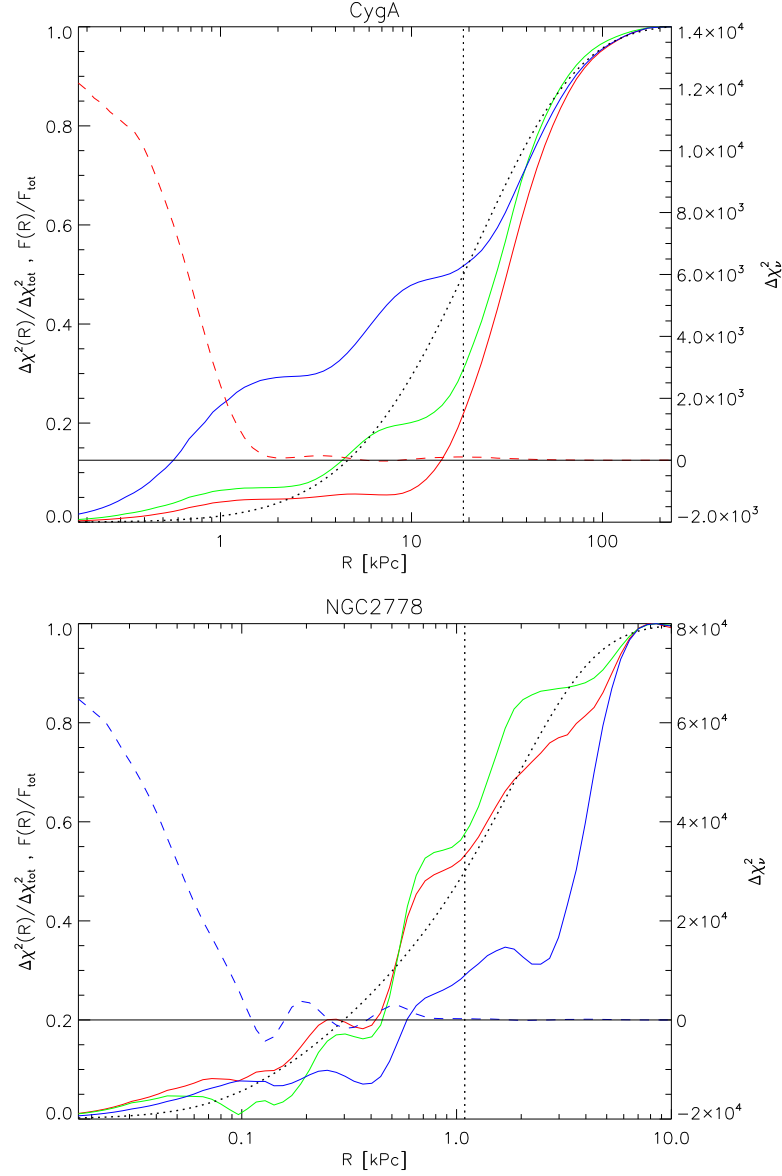
Figure 2.3: Figures showing exemplary radial distributions of projected $\Delta\chi^2$ under local (small) changes of various model parameters. The responses were symmetrized and normalized, and are thus equal to the corresponding second derivatives. The cumulative $\Delta\chi^2(< R)$ is represented by the solid curves. Dotted curves show the cumulative K-band flux $F(< R)$ and dashed curves the $\Delta\chi^2_\nu(R)$ for comparison. The effective radius is indicated by the vertical line. ***Upper panel:*** CygA, a giant elliptical galaxy modeled by a single Sérsic component. Shown derivatives are with respect to $m_b = m_t$ (red curves), R_e (green) and Sérsic index n (blue). ***Lower panel:*** NGC2778, a late-type modeled by a Sérsic bulge plus exponential disk. Shown derivatives are with respect to bulge (m_b, red), disk (m_d, green) and total (m_t, blue) magnitudes. For $\partial\Delta\chi^2/\partial m_t$, the recipe described in §2 was used.

INDIVIDUAL GALAXY DECOMPOSITIONS[*]

ABSTRACT

This chapter presents detailed notes and diagnostic plots pertaining to the galaxy image decompositions which led to the bulge and total magnitudes presented in Chapter 2. We intend to demonstrate the intricacies and uncertainties often inherent in extraction of bulge light from a galaxy image, the importance of an accurate identification of distinct morphological components to obtain unbiased structural parameters, and the frequent unsuitability of bulge+disk models in particular. This chapter should also serve to highlight the abundance and variety of morphological features revealed by our high-quality imaging data, even in the majority of the galaxies in which spiral arms are not present.

3.1 GUIDE FOR THE NOTES AND FIGURES

We here describe the photometric characteristics and the corresponding decomposition strategies *individually per galaxy*. For a summary description and general discussion thereof, as well as the data acquisition, data reduction and resulting photometric parameters, see Chapter 2.

The notes and figures appear in ascending alphanumeric order of the galaxy identifier (for the full list, see Table 2.1). They are accompanied by a figure that includes the original image, the residual image, and the radial surface brightness profile of both data and model, including individual components where present. For galaxies with disk, we also include the curve-of-growth, the ellipticity profile, and a profile of either position angle (PA) or diskiness ("B4", the amplitude

---

[*]This chapter is adapted from the paper Läsker, Ferrarese & van de Ven (2013, in prep.)

45

of the 4th-order isophotal harmonic), depending on which better serves to reveal the galaxy's characteristics. All but one of the disk galaxies required an "improved model" (components apart from bulge and disk), which we plot alongside the "standard" (bulge+disk) model for comparison. Sometimes the single-Sérsic model is included as well, in order to show how in these galaxies the addition of an exponential profile to the single-Sérsic model is unable to account for the *disk*, unless at least one further component, typically an "envelope", is included. In all profile plots, the point-spread function's *radius* at half-maximum (not the FWHM) is indicated by the dotted, and the effective radius by the solid vertical line. The latter is measured from the curve-of-growth, and therefore not always equal to the effective radius of the 2D-Sérsic profile shown in Table 2.2. Where a core is present, its size is indicated by the shaded area, commensurate with the area we mask to get an improved model. The horizontal dashed line in the surface brightess plots indicates the dynamic range of the residual image, that is, a surface brightness of $m = m_{ZP} - 2.5 \log F_{\mathrm{pix}}^{(\mathrm{max})}$, where $F_{\mathrm{pix}}^{(\mathrm{max})}$ is the flux per pixel that saturates the greyscale (white), while zero flux is plotted in grey and $F_{\mathrm{pix}}^{(\mathrm{min})} = -F_{\mathrm{pix}}^{(\mathrm{max})}$ leads to negative saturation (black). Note that the greyscale of the residual image is linear in Flux/pixel, while the science image greyscale is proportional to the logarithm of surface brightness. Note also when inspecting the figures, that the semimajor-axis range of plotted profiles is typically much larger than the displayed image area. the latter is chosen as a compromise, while the data (the co-added .fits files) provide both much more detail, as well as much more area coverage, than what can be displayed here.

3.2   GALAXY-SPECIFIC NOTES AND FIGURES

CygA (Fig. 3.1) is the most distant ($d \sim 240$Mpc), largest ($R_e \sim 20$ kpc) and most luminous ($L_K \sim 1.3 \times 10^{12} L_\odot$) object in our sample. Photometric measurements are more difficult here as this galaxy is located in a dense field of foreground stars. At the same time, this means that the resolution and depth of our WIRCam data are particularly useful here, not only to resolve the object itself, but also to reliably mask the numerous stellar sources overlapping it. The latter also required constructing a "2nd-pass" object mask from the initial residual image. A Sérsic profile fits CygA exceptionally well at all radii. Despite clearly being a giant elliptical galaxy, we cannot identify a core, possibly owing to an unresolved nuclear source.

IC1459 (Fig. 3.2) has the appearance of an elliptical galaxy, but the residual image from a single-component model reveals some deviations from a 2D-Sérsic profile. Apart from an ample core, which we accordingly mask for improved modeling, IC1459 exhibits a relatively strong isophotal tiwst ($\sim 15°$), indicative of triaxiality. Despite the central light deficit, the central surface brightness is notably higher than we observe in other cored ellipcticals, and the residuals barely
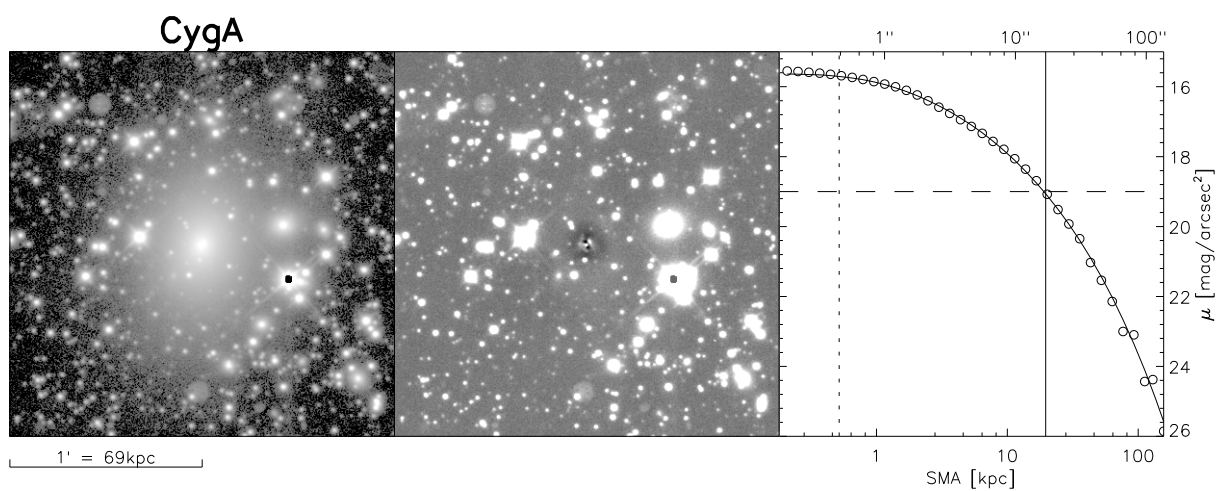
Figure 3.1: Panels showing cutout of co-added image (left), residuals from the single-Sérsic model obtained by GALFIT (middle), and surface-brightness profiles (right) of data (open circles) and model (solid line). The solid vertical line indicates the galaxy effective radius as determined from the curve-of-growth on circular apertures (not shown here). The dotted vertical line corresponds to the FWHM of the image point-spread function. The dashed horizontal line indicates the saturation limit of the residual image, both for positive (bright) and negative (dark) residual flux. The residual image greyscale scales linearly with flux (grey corresponding to zero), while the data image is displayed on a logarithmic scale.
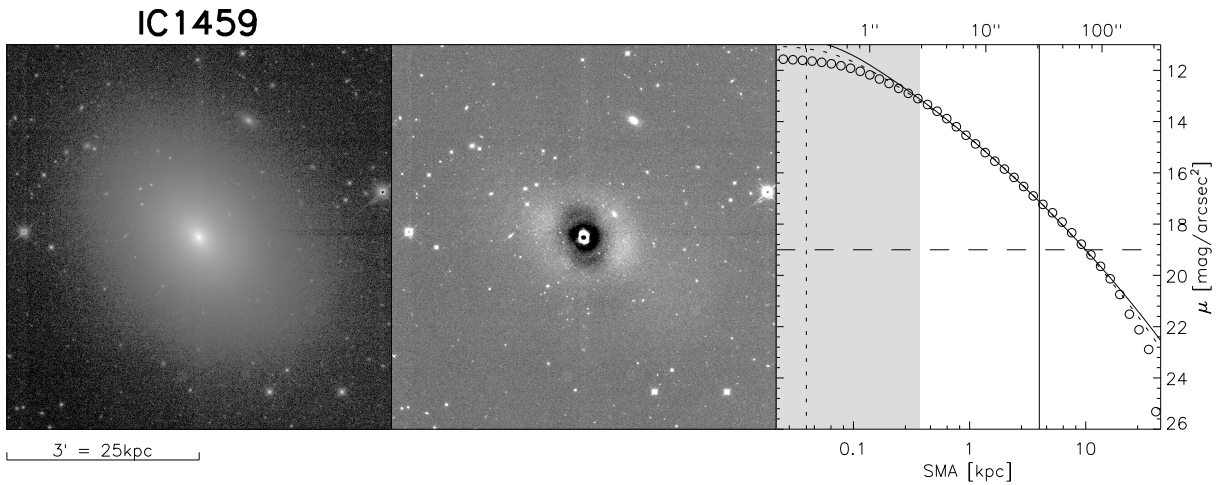
Figure 3.2: Description as for Figure 3.1, but now the Sérsic model has been fitted after masking the core. The radial extent of the core mask is indicated by the shaded region in the figure on the right. For comparison, the profile from a model fitted without core masking is shown as a dotted curve.

improve after core-masking. Furthermore, outside of $R \sim 100''$, the observed surface-brightness is mildly but consistently below the Sérsic-profile. Yet, while multi-component models improved the rersiduals, they were inconsistent with the presence of an exponential disk. A disk is also not supported by the ellipticity profile and isophotal harmonic modes, and we thus retain the single-Sérsic model for this galaxy.

IC4296 (A3565-BCG, Fig. 3.3) is an elliptical galaxy with very low flattening, and well modeled by a Sérsic profile outside of the core radius.

NGC221 (M32, Fig. 3.4) requires special treatment as it overlaps with M31's outer disk, leading to an unavoidable degeneracy. Additionally, at $R \gtrsim 100''$, the image resolves many of both system's stars, preventing us from masking stellar sources without compromising M32's photometry. We therefore simultaneously account for galactic foreground and M31 by including GalFit's tilted "Sky" component in the model, and find a reasonably good fit to M32 by a single Sérsic profile. We chose not to account for profile deviations from a Sérsic at large radii, because the degeneracy with the sky component is expected to render the results unreliable. M32 has a very bright centre which saturates even in the shortest (2.5 second) exposures. As far inward as reliable data exists, the profile remains steep and even shows signs of steepening, indicating a resolved nucleus. Regardless, it does not effect our fit as most of it is masked due to the saturation.
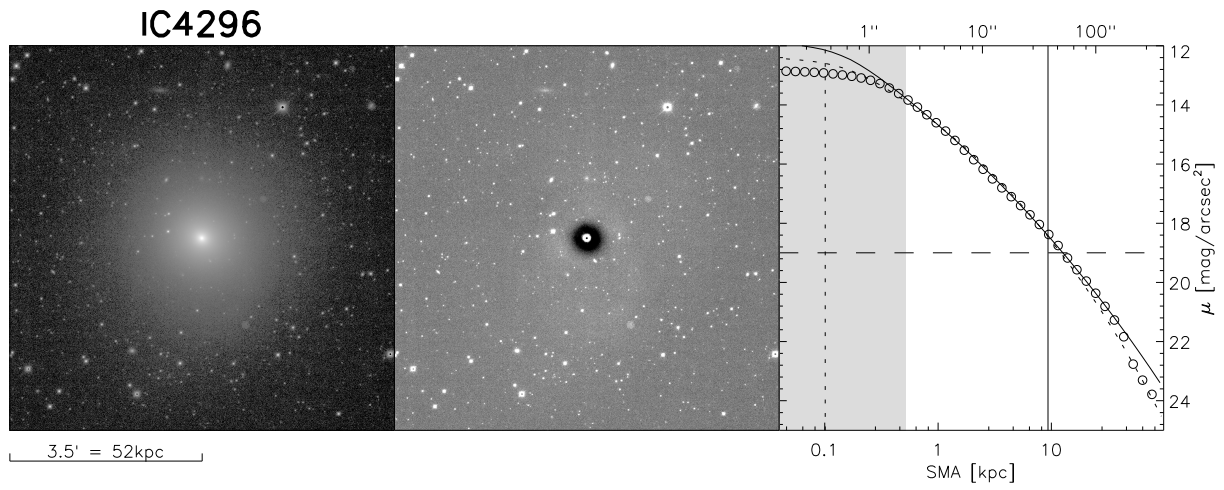
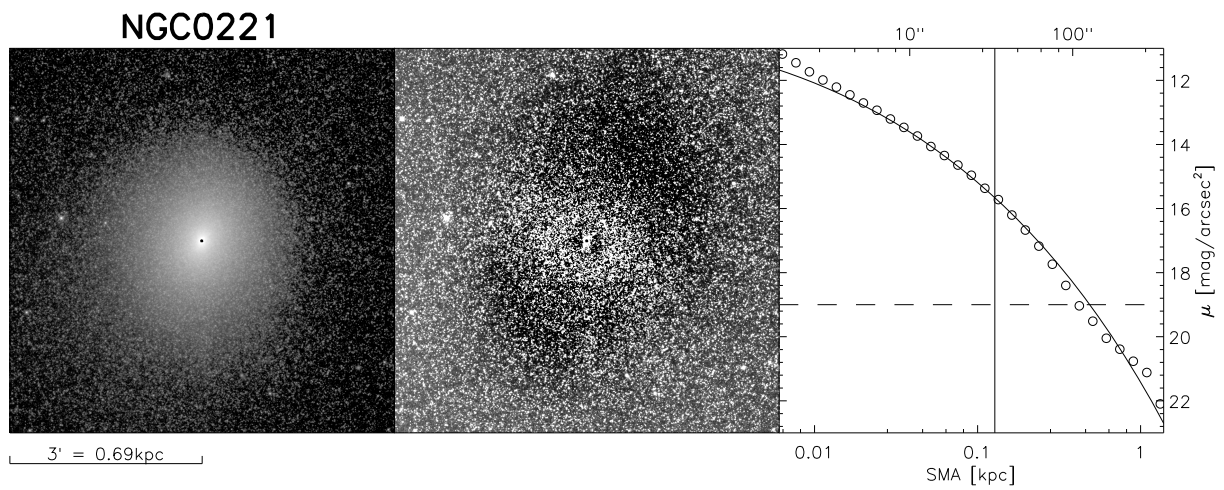**Figure 3.3:** For description, please see Figure 3.2.

Figure 3.4: For description, please see Figure 3.1.

NGC821 (Fig. 3.5)is a typical representative of a lenticular galaxy with highly-inclined embedded disk (see §2.3.3). The disk is discernible visually, from the profiles of ellipticity and B4 harmonic coefficient, as well as the single-Sérsic residual image. While modeling this galaxy clearly necessitates a (very flat) disk component, the "standard" bulge+disk configuration is fraught with problems that, as we find, can *not* be solved by using an "edge-on disk" profile (instead of exponential). The best-fit bulge+disk model is not unique as there exist two solutions with equivalent χ^2. Both have extreme disk flattening: in one case rounder than the bulge (and therefore discarded by us as "unphysical"), in the other case too flattened ($q = 0.09$) to reproduce the observed disk shape. In the latter case, the disk component proves to deviate from exponential, that is, if modeled by a Sérsic-profile, its Sérsic index is best-fitted by $n_d \sim 0.5$. Lastly, the bulge Sérsic index is unusually high or a galaxy of this size and luminosity (≈ 7, almost the same as for the single-Sérsic model), further suggesting unsuitability of the standard model.

Addition of an "envelope" (Sérsic-profile, $n = 2.5$, axis ratio intermediate between disk and bulge) addresses those issues and strongly reduces residuals, although some remain. More complex models that include a central point source or a secondary (inner) disk provide only minimal χ^2-reduction. We thus adopt the bulge+disk+envelope model, because it allows for a robust exponential disk extraction and no other components, apart from a contingent weak nucleus, are discernible in the residual image. In this model, it is not clear whether the envelope, represents the outer part of the bulge, or a separate stellar component. In any case, it appears to belong to the *spheroidal* population, especially as it is even less flattened than the model's bulge component. Conversely, it can also not be excluded that the latter comprises part of the disk light. Therefore, NGC821 is a case of an *early-type* galaxy in which the "Sérsic-bulge + exponential-disk" representation is inadequate, and the spheroidal component is not well described by a single Sérsic profile.

NGC1023 (Fig. 3.6) clearly is a lenticular that clearly contains a bar, which in this case is not aligned with the disk. Attemepts to fit the isophotal twists with coordinate rotations in disk or bulge proved ineffective, verifying the extra component. A nuclear point source can be fitted, but we omit it in our adopted model as it is only weak and has little influence on the bulge parameters.

NGC1300 (Fig. 3.7)is a grand-design spiral, with dominant bar and spiral arms. A conventional bule+disk model is created for the sake of completeness but is clearly inadequate here. Its "disk" component mostly follows the bar's light, making it much more flattened than (outer) disk and effectively excluding the flux of the disk (as well as spiral arm) flux from the model.

This is the most complex galaxy in our sample. As a consequence, we require an "improved model" with 6 components for an adequate fit: bulge, disk, bar, spiral arms, inner disk and
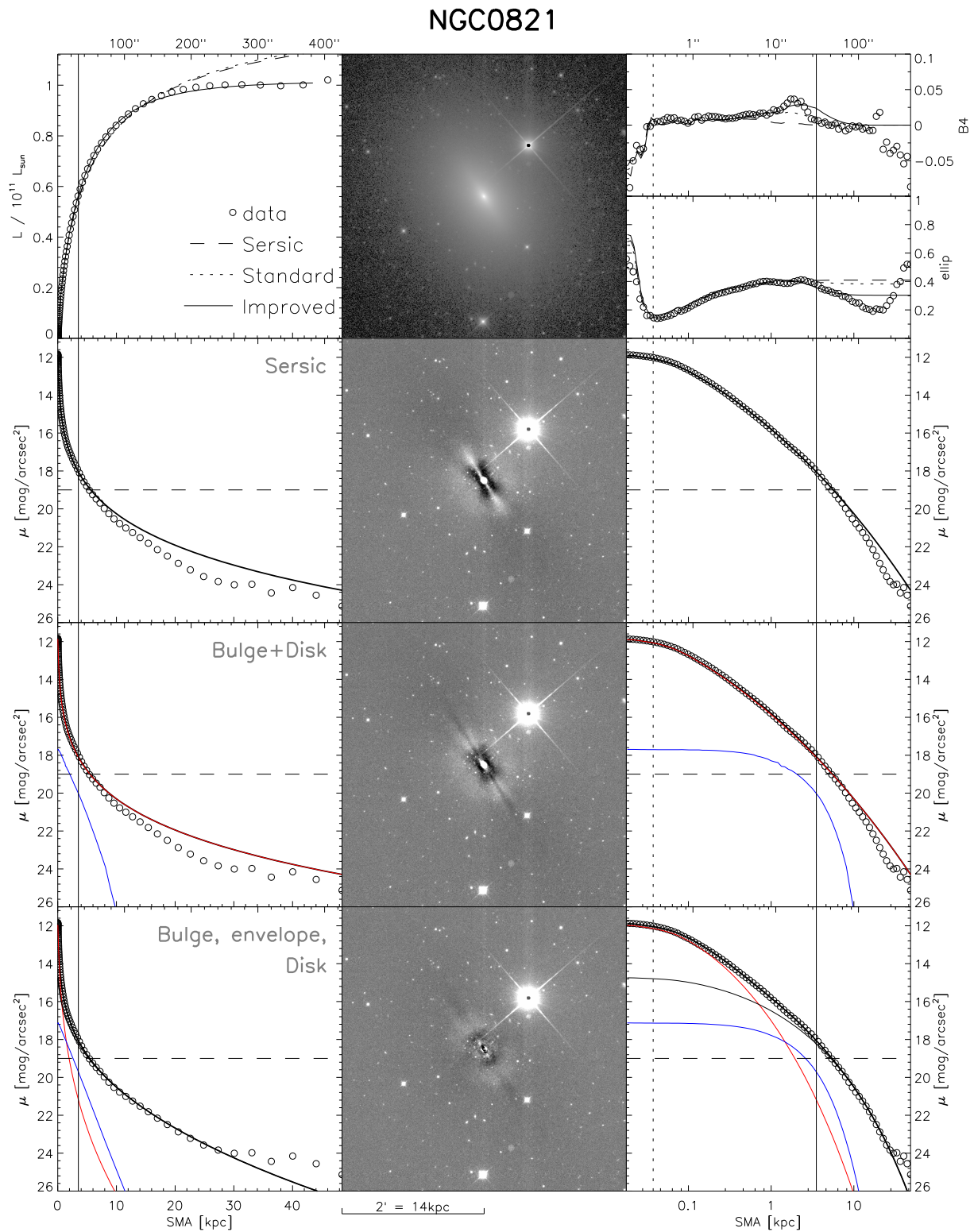
Figure 3.5: For description, please see Figure 3.6, with respect to which we have added the single-Sérsic model (second row) to show the embedded disk more clearly.
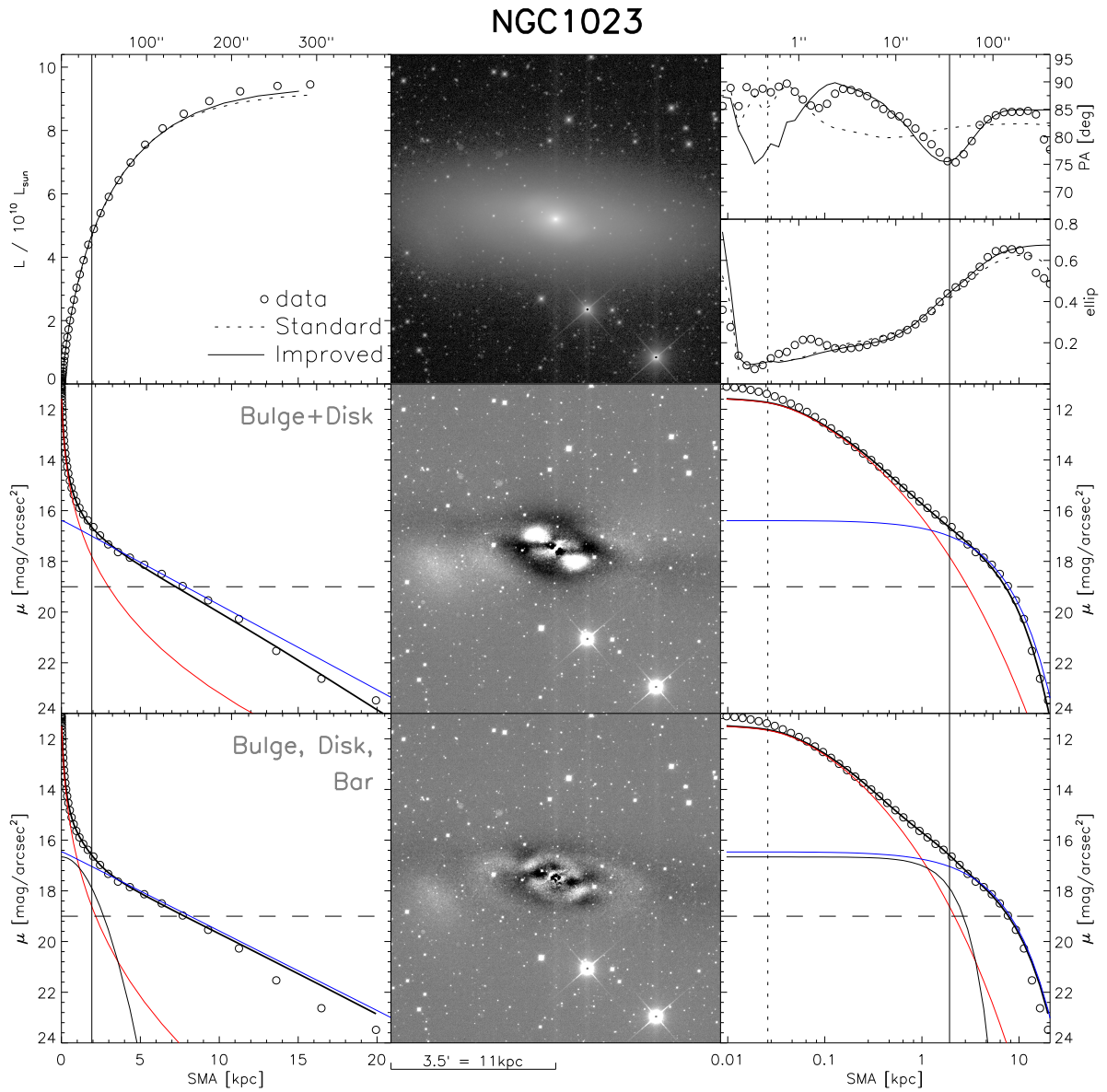
Figure 3.6: Comparison of "standard" (bulge+disk) and improved models. The top row presents the data image (left), and curves-of-growth (right figure). The middle and bottom rows show the residual image (left figure) and surface brightness profiles (middle and right figure), respectively for both models. Image scalings, as well as vertical and horizontal lines in the surface brightness profiles, are defined as in Figure 3.1. The surface brightness profile is shown on a linear radial scaling (middle figures) in order to allow for comparison with an exponential decline (straight line). With respect to Figure 3.1, the component profiles have been added (thick red and blue curves: bulge and disk, thin black curves: additional components). Components are listed in the top-centre panel, ordered by decreasing central surface brightness. Curves-of-growth (top-right figure) are shown as measured on data image (open circles) and model images (dotted line: bulge+disk, solid line: improved model).

nucleus. The disk light is a superposition of an exponential profile (diffuse light) and the spiral arms. The "maximum bulge" magnitude in this case is calculated by excluding the light of both the disk and spiral arms, while, as usual, the fluxes of bulge and all other additional components are summed in order obtain the upper limit of the bulge magnitude that assumes contingent profile mismatch or spurious components.

The spiral arms are reproduced by employing coordinate rotation, and refined by bending and fourier modes that account for their asymmetric strength and shape. Spiral arms and bar could not be modeled from the same component as intended by GALFIT3's "bar radius", due to a discontinuity in the surface-brightness profile, the relation between arm and bar width, and the complexity of the rotational pattern. The spiral component accordingly requires an inner truncation.

Aided by the high image quality (PSF FWHM = $0.''5$), a bright small-scale disk can be identified and clearly distinguished from bulge and bar. It is sharply truncated, which upon close visual inspection creates the impression of ring and requires either introduction an (outer) truncation function or a Sérsic profile with low (≈ 0.2) Sérsicindex. We adopted the latter because the fit converges faster and more robustly than when using the trucation, while providing equally low residuals. Inclusion of the inner disk proves essential for unbiased bulge parameters.

NGC1300 provides a good example of the bulge's flux and Sérsic index being *under*estimated unless additional components can be resolved and modeled: it changes from 1.3 (standard) to 4.3 (improved model), despite the latter's inclusion of a central point source (nucleus). Therefore, from simplistic modeling this galaxy would be interpreted to posess a *pseudobulge* (according to Sérsic index), while in fact it harbours a "classical" bulge *and* an inner disk, which together with the nucleus resembles a small-scale late-type galaxy in this case.

NGC1399 (Fig. 3.8) is a giant Elliptical with a large core ($R_c \sim 6''$), masking of which significantly changes the parameters of the Sérsic model, including its magnitude.

NGC2748 (Fig. 3.9) is a spiral galaxy seen at high inclination. The spiral arms appear tightly wound and can be visually traced across a semimajor-axis interval of $\sim 6...40''$, undergoing a $\sim 360°$ rotation. Inside $6''$ they are not well defined. The disk appears asymmetric (lopsided), and a faint plume-like distribution of stellar light is seen to extend from the centre outwards along the minor axis. The radial profile is very close to exponential over an unusually large range, $\sim 6...120''$, except for a "bump" at $30''$ that can be ascribed to the spiral arms.

The bulge+disk model overestimates the disk's flux and scale radius, likely due to the presence of the spiral arms. The the disk profile, if modeled by a Sérsic, significantly deviates from exponential, $n_d \rightarrow 0.5$. Significant residuals also originate in the asymmetry. Although generally
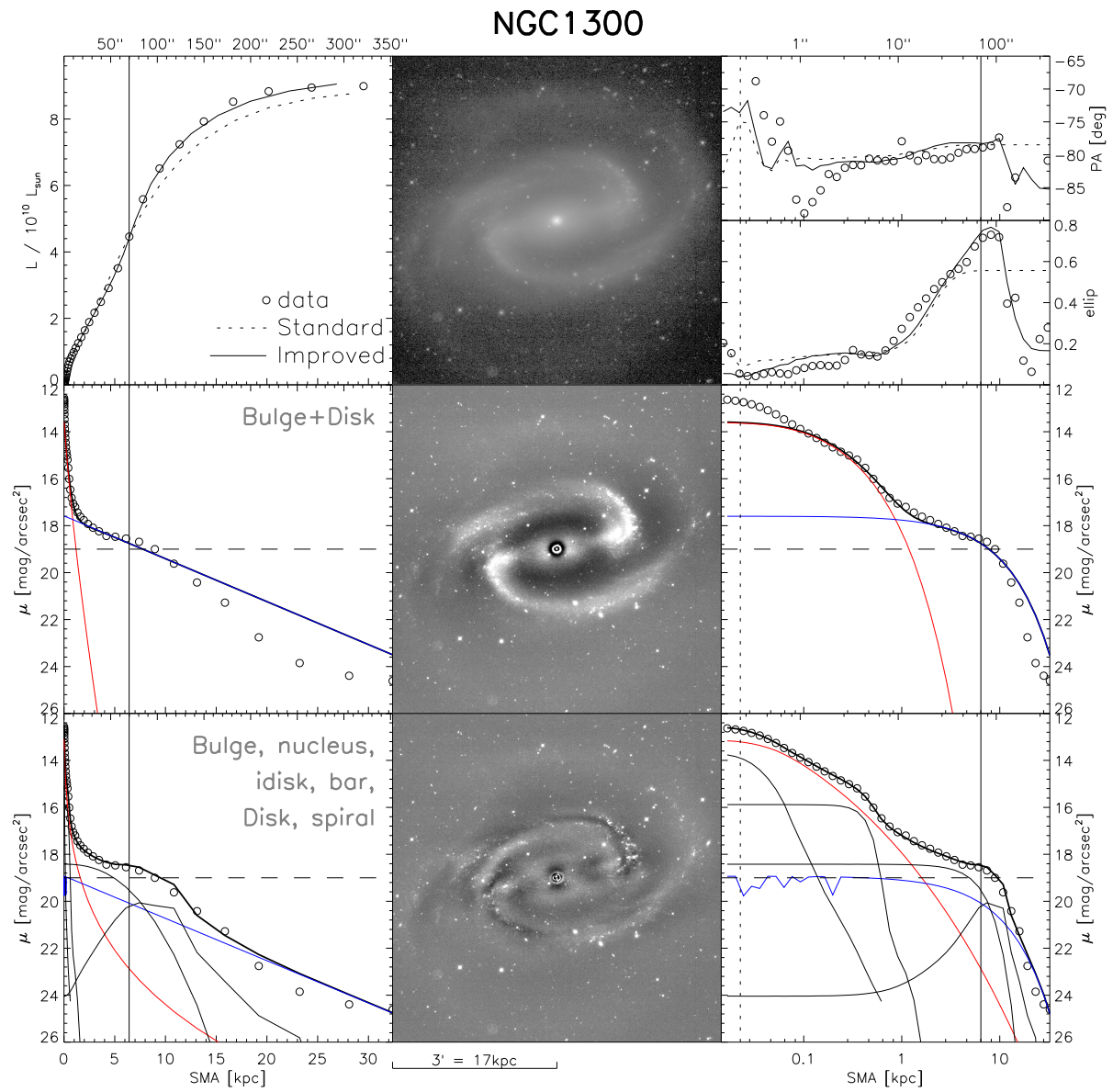
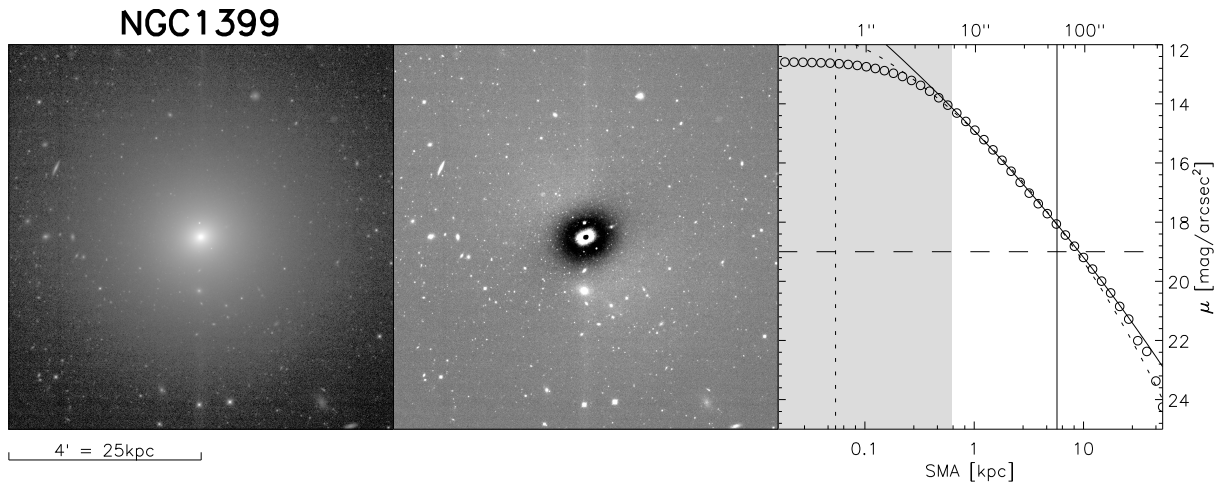**Figure 3.7:** For description, please see Figure 3.6.

Figure 3.8: For description, please see Figure 3.2.

not allowed in a "standard" model, we have tested adding perturbations by inclusion of fourier mode F1 and bending mode B2, and found only a small impact on the standard model parameters.

We provide the warranted improved decomposition by introducing a component for the spiral arms. These are difficult to model here, because they are seen at high inclination and appear intermittent and flocculent. We could not establish a rotation-function for the profile that reproduces to the observed pattern well, even when azimuthal fourier modes and bending were used in addition. The arms thus still are present in the residual image, but their light contribution, especially with respect to its radial distribution, is approximately reproduced. There is some uncertainty as to the best way of accounting for the asymmetries: First, it is not clear whether it is the disk or the spiral component, or both, that should by accordingly modified. Second, asymmetries may be modeled by harmonic perturbations, bending modes, relative shifts of component centres, or any combination thereof. We tested all and find that the various configurations imply different best-fit parameters, but often also slow or unstable convergence behaviour. We eventually adopt a configuration in which all component centres are aligned, and asymmetric distortions are ascribed to the spiral component only, in form of a first-order harmonic perturbation. Some models with higher-order perturbations or independent component centres provide improvements in χ^2, but they suffer from non-unique convergence or non-exponentiality of the disk when its profile was generalized to a SérsicWe have not separately accounted for the plumes emanating from NGC2748's centre, as they are very faint, have no known or probable functional form of surface-brightness profile, and would cause an undesirable degree of degeneracy with the other components.

Interestingly, despite *adding* a component (the spiral arms), the improved model's bulge is

brighter than the standard model's.

NGC2778 (Fig. 3.10) is classified as an Elliptical in the RC3(1999) catalog, but we find a large-scale disk to be unambiuously present. Furthermore, the profiles (surface-brightness inflection and ellipticity peak at $\sim 6''$) and residual image reveal a bar. Although χ^2 decreases only slightly from inclusion of the latter, we adopt such an extended model on grounds that the bulge flux is overestimated by $\sim 30\%$ when the bar is omitted. The adopted model does not fully account for the flux in the data at $R \gtrsim 60''$, but the surface brightness is very low here and the contribution to the total flux marginal, as indicated by the curve-of-growth.

NGC2787 (Fig. 3.11) is a lenticular galaxy which shows a strong ring and large bar, necessitating an improved model. Already suggested upon visual inspection of the image, comparing corresponding model configurations confirms that the bar does not extend all the way through the centre. It thus requires an inner truncation. The same applies to the (large-scale) disk in order to model the ring.

Inside the ring, an additional component needs to be introduced and may be interpreted as the inner continuation of the outer disk or as a separate inner disk / pseudobulge. Its best-fit axis ratio is equal to the outer disk's. We find the best residuals and convergence behaviour by dispensing with an outer truncation of the exponential profile, and instead model the inner disk by a Sérsic component. Its fit converges to $n \rightarrow 0.25$, which leads to the required steep decline at the ring radius.

NGC2787 also harbours a nucleus, which we model by a PSF profile. In this case, our images marginally resolve the nucleus. Corresponding models with Sérsic and King profile converge, but lead to a very similar magnitude and no not change the other components' parameters.

NGC3115 (Fig. 3.12) is a lenticular galaxy with almost edge-on embedded disk and elongated appearance (q 0.5). The major-axis surface-brightness profile has a near-exponential decline between $\sim 70...270''$, but this may be a "conspiracy" between components: the maximum ellipticity ($e \sim 0.6$) occurs at $R \sim 70''$ and decreases again in the exponential regime of the surface brightness profile. There is another, weaker, ellipticity peak at $R \sim 30''$ that suggests a smaller "inner disk".

NGC3115's disk is easy to identify visually, but difficult to. A bulge+disk model is iinadequate, as evidenced by the radial profiles, residual image, and a non-exponential disk profile. The adopted improved model includes an envelope (Sérsicindex $n = 2.1$) and benefits from azimuthal fourier modes (similar to diski-/boxiness) allowed for all components. The envelope's
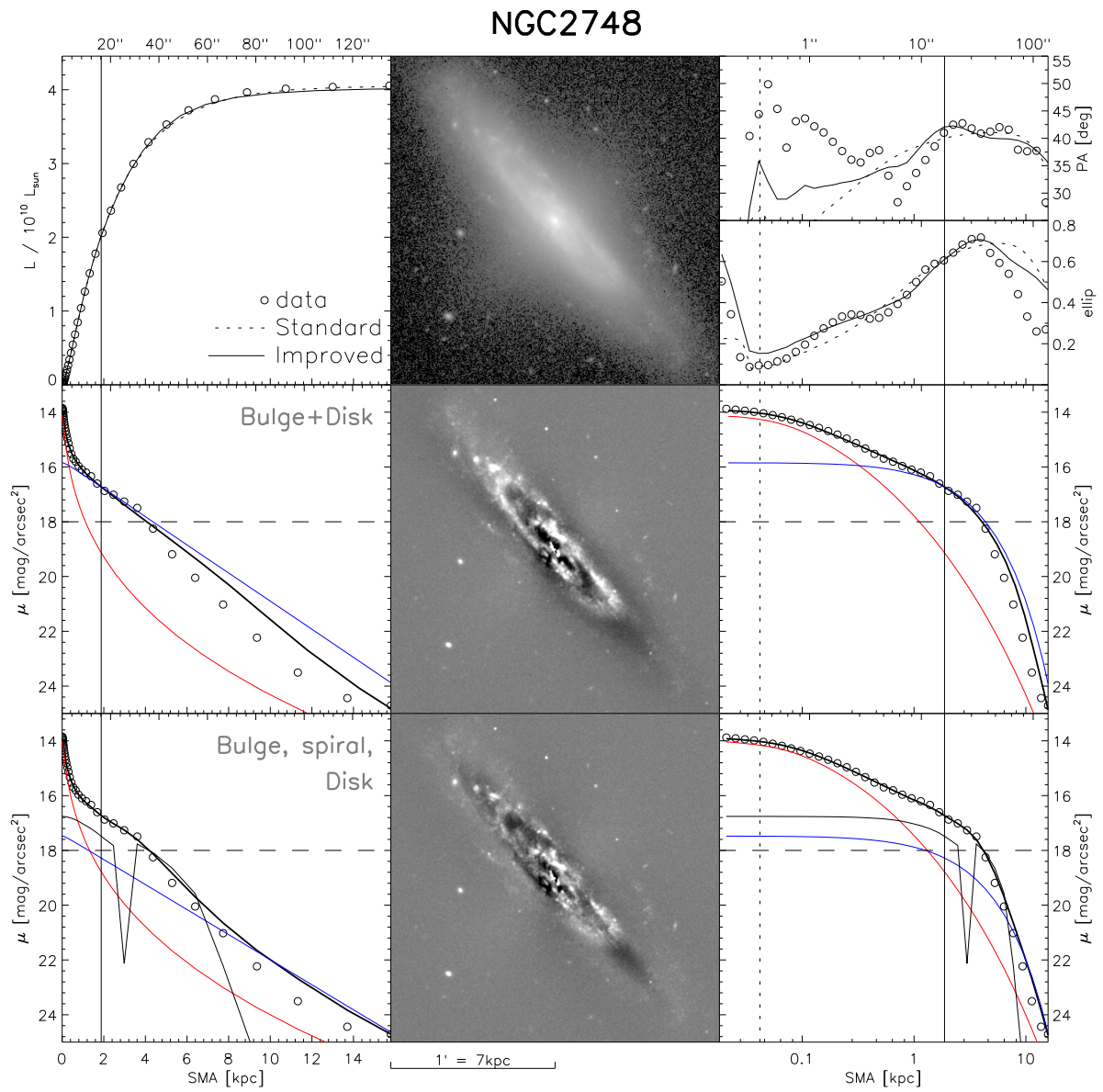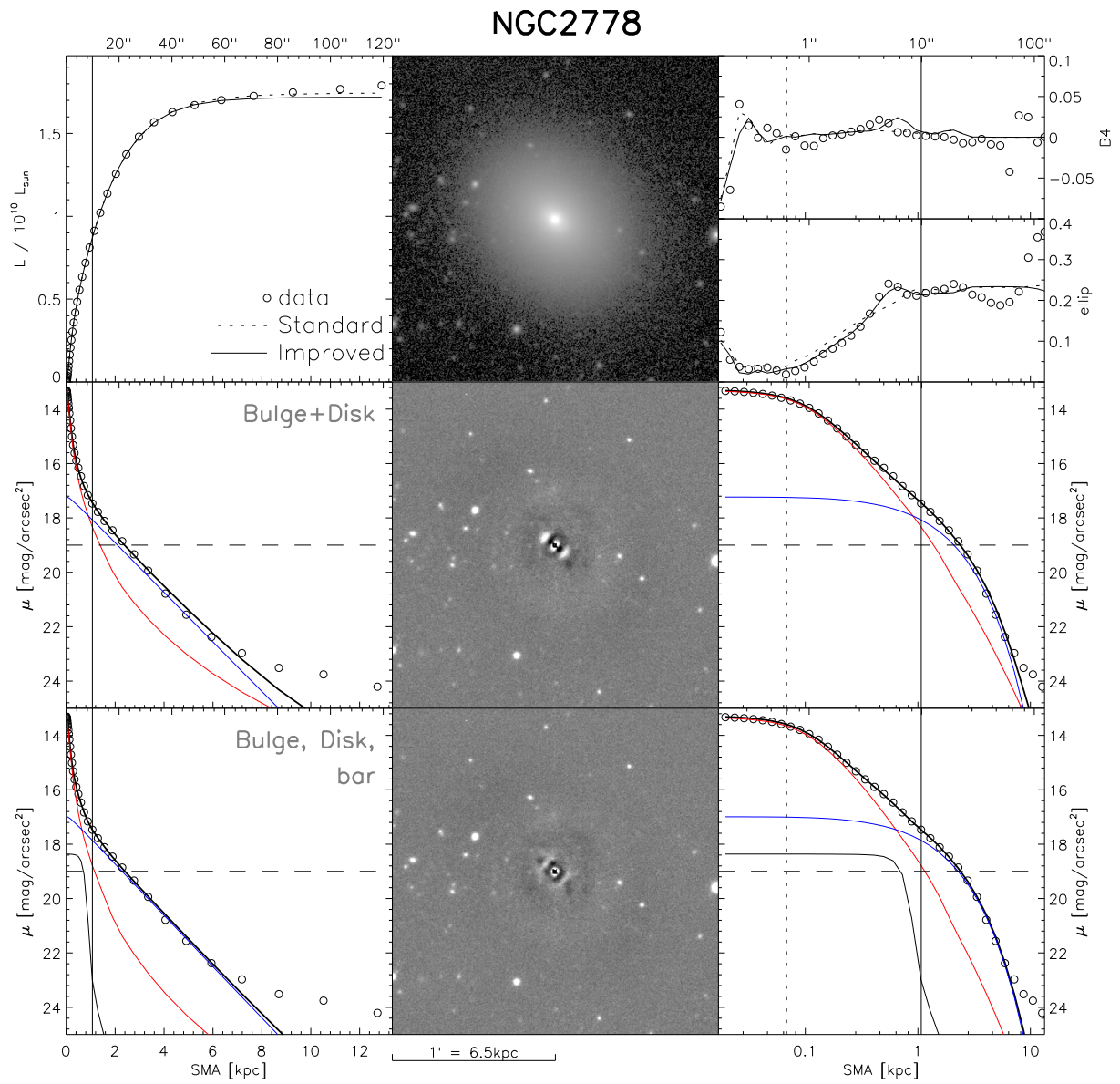
Figure 3.9: For description, please see Figure 3.6.

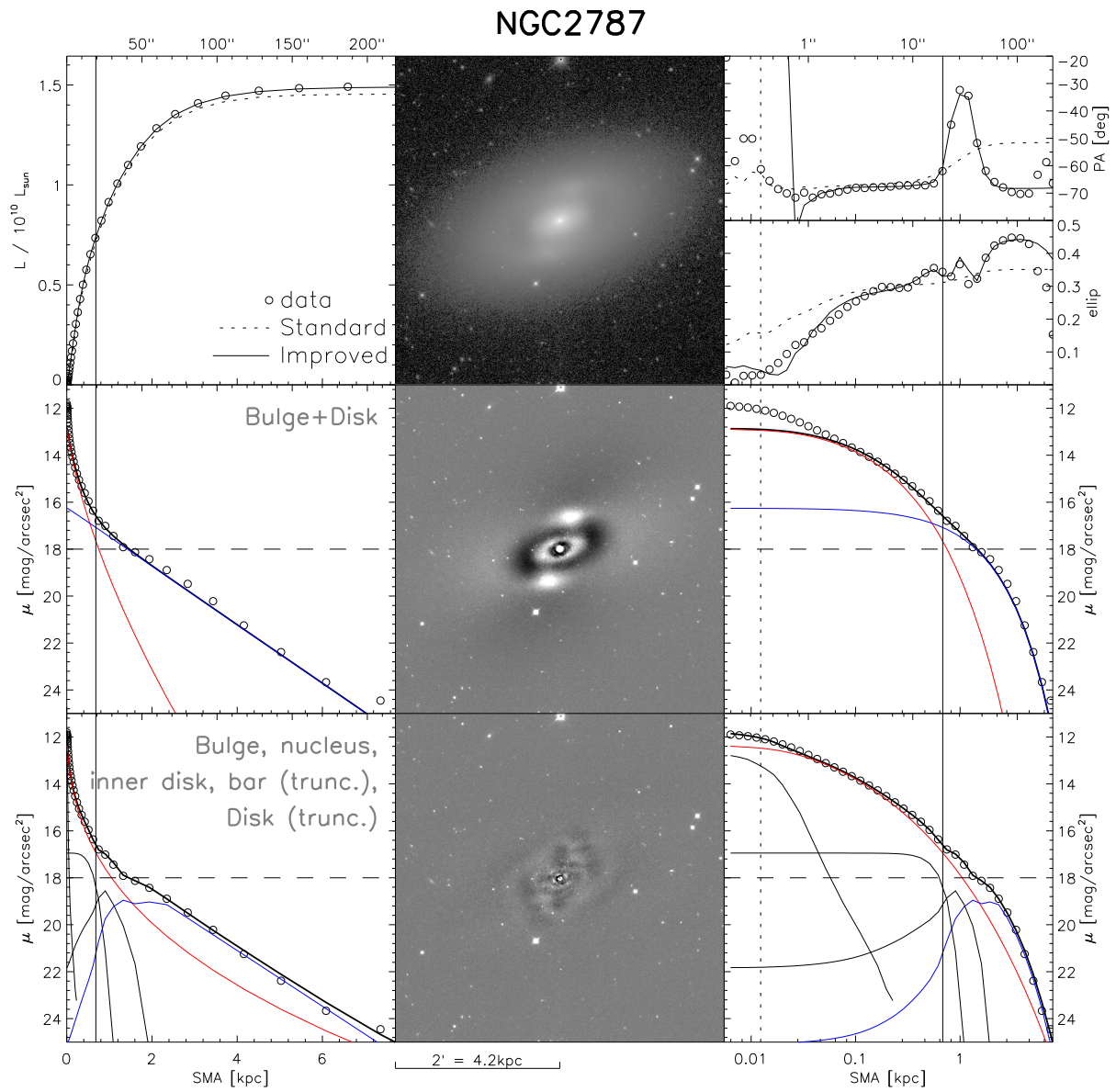**Figure 3.10:** For description, please see Figure 3.6.

Figure 3.11: For description, please see Figure 3.6.
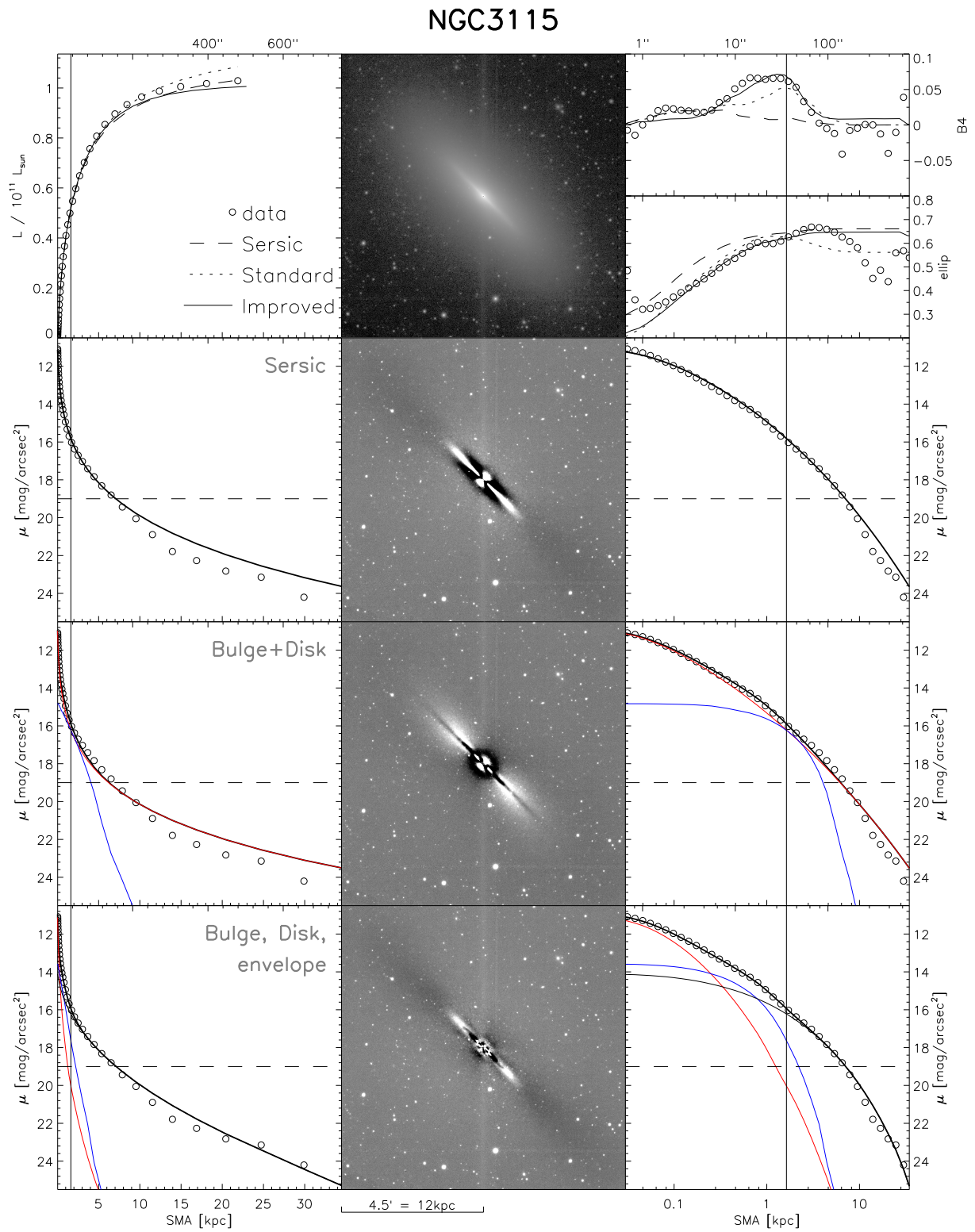
NGC3115

Figure 3.12: For description, please see Figure 3.6.

axis ratio is intermediate between bulge and disk. It may therefore be interpreted as either the more flattened outer part of the spheroid, or as a separate thick ("hot") disk. The 3-component model reproduces the observed profiles much better than the standard model. Even so, moderate residuals remain and hint at either profile mismatches or additional components to be present (e.g. the mentioned secondary disk). Yet, we could not find a corresponding (4-component) non-degenerate model with Sérsic bulge and exponential disk.

NGC3227 (Fig. 3.13) poses a challenge to decomposition not only due to the presence of two spiral arms, but also because it is partially superposed with an elliptcial galaxy, NGC3226. The proximity, size and brightness of NGC3226 practically prevents masking. It therefore requires its inclusion in the model (single-Sérsic profile) and induces degeneracy with the disk of NGC3227's. The latter's profile consists of two exponential parts, both with about the same scale radius but with a relative brightness offset. The transition occurs between 70...90″, which corresponds to the radial range where the two spiral arms are seen to end in the image. The spiral arms exhibit a smooth light distribution and could perhaps be a result of tidal interactions with NGC3227 rather than active star formation, a view supported by the two faint extended light distributions that resemble stripped material and are found along the minor axis direction some distance away from the visual boundary of the disk.

NGC3227's has a very high central surface brightness but a small bulge that dominates only inside $\sim 20''$ (compared to $\sim 300''$ out to which we can measure the disk profile). Yet, a bulge+disk model produces a best-fit bulge Sérsic-index of $n = 12$ (!), which, together with the visual impression of the image, suggests the presence of a nucleus. Naturally, the standard model can also not reproduce the spiral shape.

For these reasons we establish an improved model with nucleus, a bar (which may also be viewed as the inner part of the spiral arms) and coordinate rotation of the disk. Perhaps surprisingly, the nuclear component of the best-fit is weak, with lower central surface-brightness than the bulge component. If we subsequently omit the former, the bulge Sérsic index remains almost constant at ~ 4. Hence, we adopt a "bulge+bar+disk" model. We caution though that at such a small bulge effective radius of about 1″, even slight misrepresentation of the point-spread-function may alter the bulge parameters, as well as the significance of a putative central point source.

NGC3245 (Fig. 3.14) has a strong disk component (exponential profile), but lacks obvious spiral structure. Besides the bulge and the exponential disk, the radial profile shows that the disk is partially truncated beyond $R \sim 60''$, followed by a low-surface-brightness extended disk (or halo) beyond $R \sim 120''$, as well as a small inflection around $\sim 15''$, suggesting a bar. The bulge+disk model shows considerable residuals between R 6...20″ along the major axis, confirming the bar.
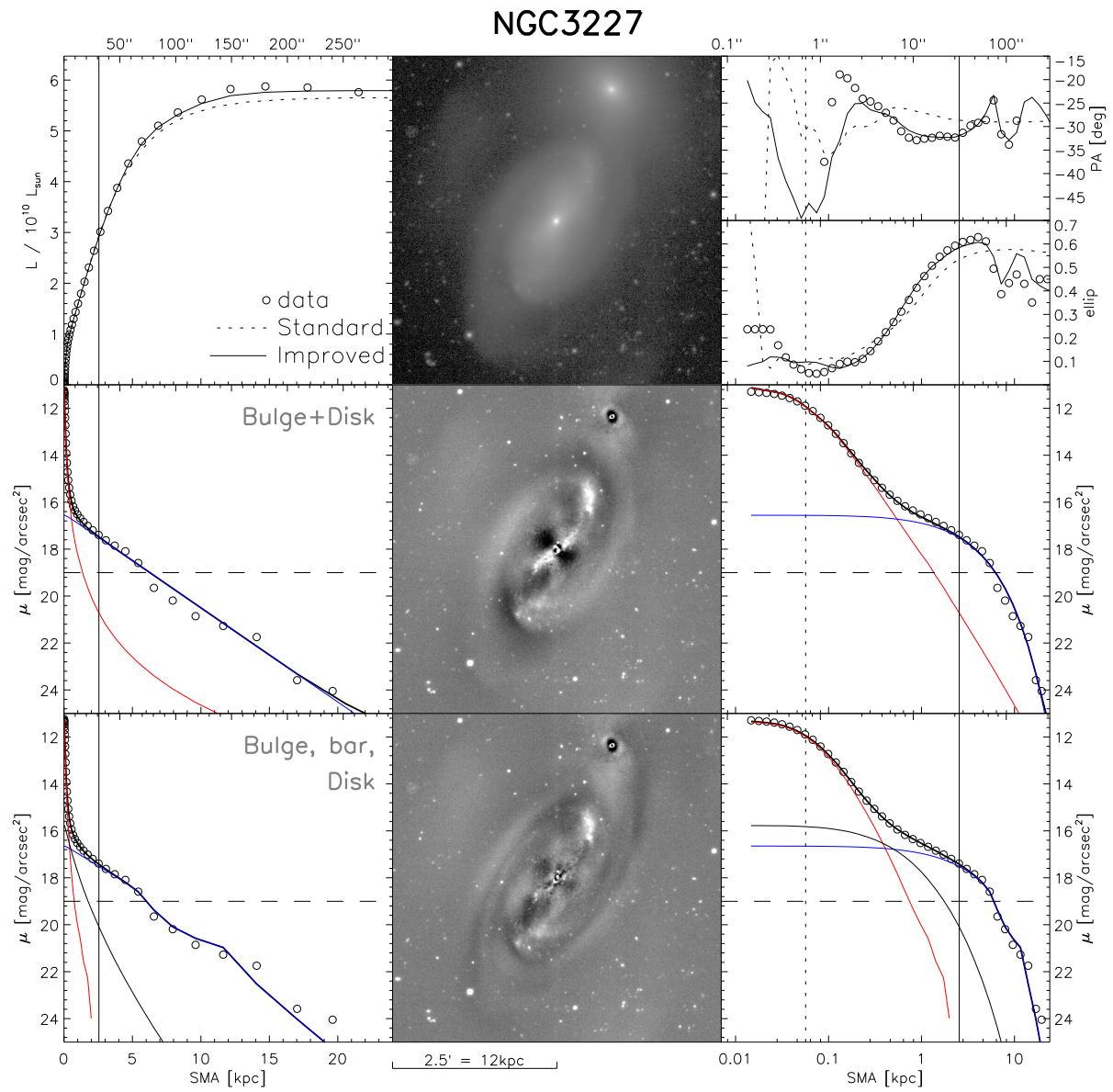
Figure 3.13: For description, please see Figure 3.6.

The standard model's disk is also not exponential ($n \rightarrow 0.5$ if modeled by a Sérsicprofile).

Inclusion of a bar solves both of these issues, but we could not establish a suitable improved model that accounts for the extended profile at the largest radii. Furthermore, residuals remain in the central regions and indicate either a nucleus, an inner disk, a bulge isophotal twist (triaxiality), or a spiral structure. Yet, we could not identify and fit any of these features unambiguously, and the corresponding models do not converge robustly. This unsatisfactory situation arises not only because our resolution is still insufficient at these small spatial scales, but becuase the suitable profile and morpholgy of the putative additional component(s) and modifications are unknown and degenerate with other model parameters.

NGC3377 (Fig. 3.15) appears to be an elliptical galaxy, and is classified accordingly as E5 in the RC3 catalogue. Yet, the surface-brightness profile exhibits an exponential decline at radii $R > 60''$, and closer inspection of ellipticity and B_4 (diskiness) profiles reveal respective peaks at $R \sim 8''$ and $R \sim 30''$ that suggest two embedded disks. A single-Sérsic model not only produces quadrupole residuals, but also a very high (considering the luminosity) Sérsic index of 8.7. Its surface brightness profile shows a strong overestimate of flux at large radii, which we suspect to result from the steep inner profile. The latter is due to a bright small-scale disk which can be identified in the residual image. Bulge+disk models produce similar results, independent of whether the disk component is adjusted (by choosing the initial parameters) to fit the inner or the outer disk. Hence, we require an improved model here, which includes 4 components (bulge, disk, inner disk and envelope). 3-component models did not adequately fit this galaxy, because even with two disk components in place, the bulge component cannot account for the near-exponential decline and low ellipticity at the largest radii.

NGC3379 (M105, Fig. 3.16) appears to be a typical giant elliptical, with the logarithmic brightntess profile showing a core ($R < 3''$) and no conclusive sign of a disk. We thus fit it by a single-Sérsic model while masking the core. Despite a corresponding mask, a light contribution from the neighbouring NGC3384 is seen in the profile beyond $\sim 300''$. Ellipticity is nearly constant at 0.1. NGC3379 also exhibits a smooth isophotal twist of ($\sim 10°$) overall. The diskiness is zero within the noise limits.

NGC3384's surface brightness profile (see Fig. 3.17) reveals a large-scale exponential disk that is modified by a step in the profile between $R \sim 100...160''$, beyond which the scale radius appears to be slightly larger than in the inner part. Alternatively, the outer profile may deviate from exponentiality. Out depth is not suffient to trace the profile far enough out to draw an unambigous conclusion on this matter. As is the case in a few other galaxies of our sample, the disk can thus be considered to either consist of two parts, or as being truncated with an additional
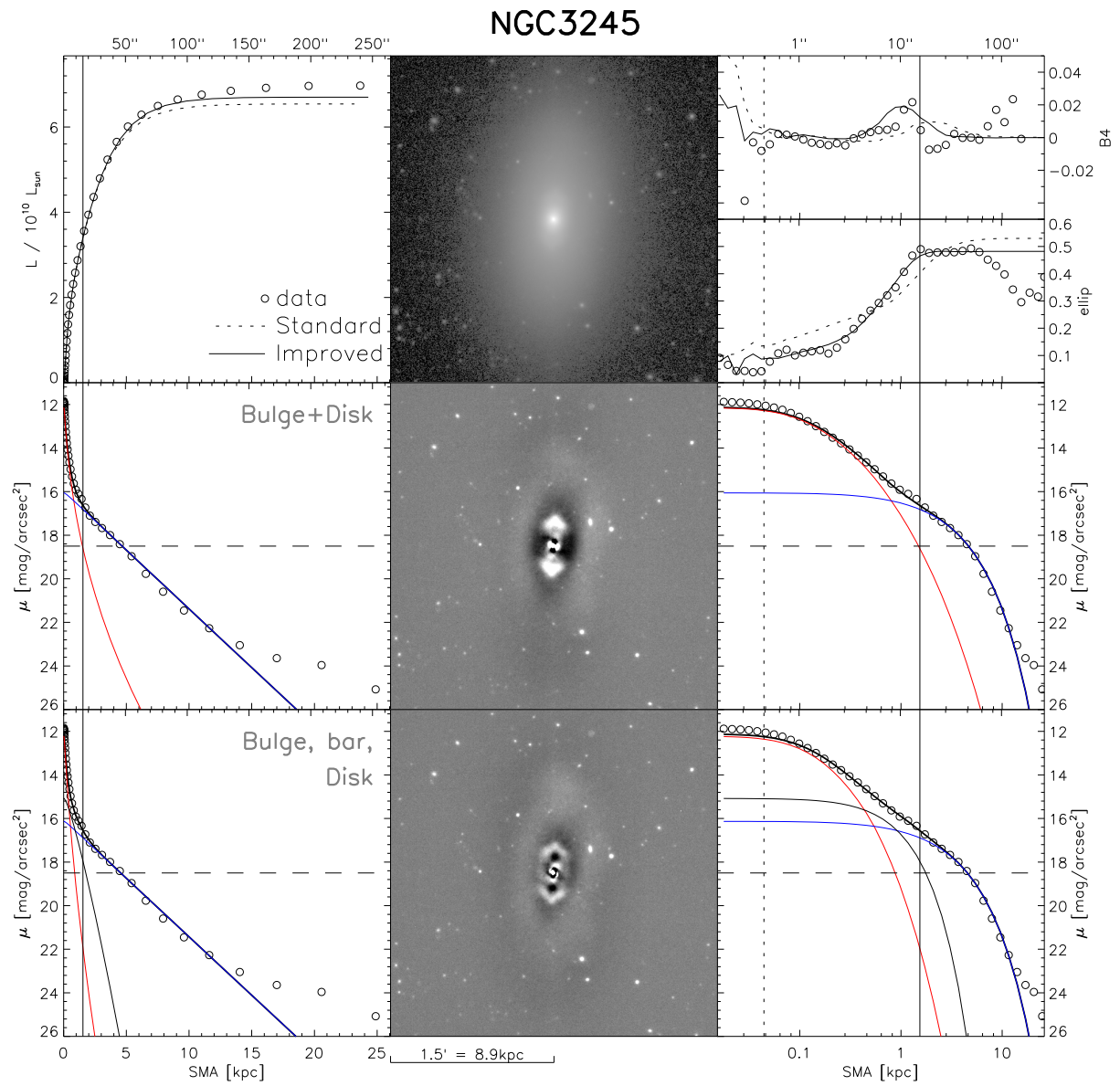
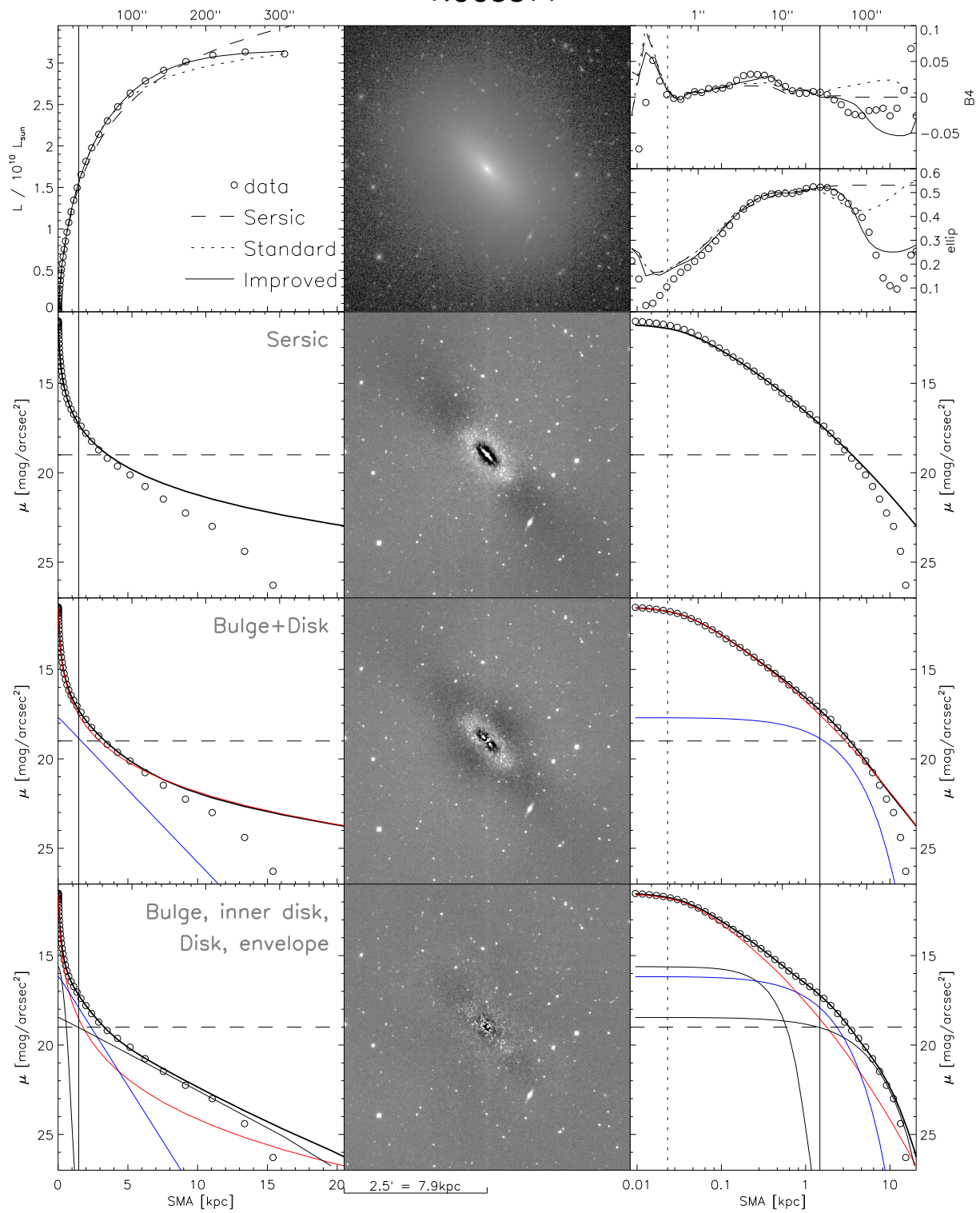**Figure 3.14:** For description, please see Figure 3.6.

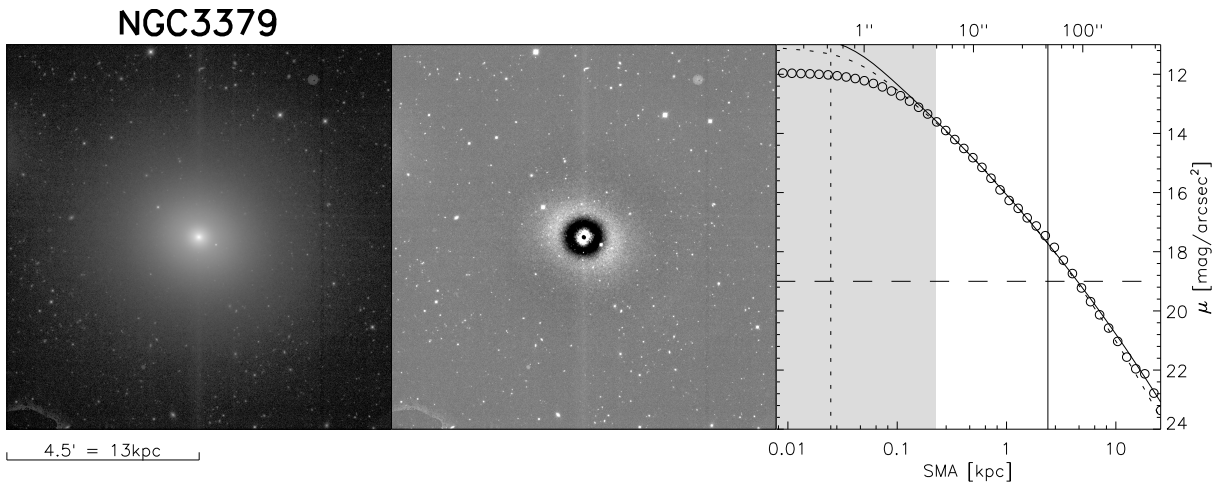**Figure 3.15:** For description, please see Figure 3.6.

Figure 3.16: For description, please see Figure 3.2.

component (envelope, halo) accounting for the flux at the largest radii.

Unfortunately, the standard model's disk is not robustly exponential: if modeled by a Sérsic profile, n_d drops to almost 0.5 (instead of remaining at ≈ 1 for exponential). Moreover, after fitting NGC3384 with this bulge+disk model, strong and characteristic residuals remain: a bright and highly flattened small-scale structure ($R \lesssim 10''$), which is aligned with the disk major axis and reminiscent of an inner edge-on disk; a compact octupole pattern at intermediate radii which resembles a bar that is approximately orientented along the image's minor axis; and a dark ring at the radius of the above-mentioned transition in the disk profile.

We establish an improved model that accounts for these features. The bar and central edge-on disk feature are modeled by a Sérsic profile, respectively. Inclusion of the bar component is prerequisite to fitting the small disk, or the parameters would converge to the values of the bar anyway as the latter is the "stronger" feature. Regardless, the cetral disk is required for satisfactory residuals. These additional components, as well as the bulge, benefit notably from allowing modified (disky/boxy) isophotal shapes. We find the step in the porifle of the main disk to be well reproduced by using an exponential disk with large scale radius, and superposing it with a more compact intermediate-scale component, to the effect that the latter increases the surface brightness at radii inside the disturbance, but not outside of it. Equivalenly low residuals can be achieved by using two different profiles for this compact disk component: either a Sérsic with $n < 1$, or an exponential profile with outer truncation. In both cases, we first fix the two disk parts' position angle and ellipticity to the same value during the fitting. Even when then allowed to vary independently, they become fi to the same values, supporting the view that they both model different parts of the same disk. We eventually adopt the configuration in which the

inner part of the main disk is a Sérsic profile, since it converges faster than a disk with truncation, and the best-fit parameters are less sensitive to the initial values.

We also tested other model configurations that are aimed at modeling the break in the disk profile, but found them to be less suitable. The adopted improved model is thus composed of a bulge, central disk, bar and a two-component main disk, which is now also "truly" exponential (Sérsic index of 0.9).

NGC3608's surface-brightness profile (see Fig. 3.18) shows slight deviations from a Sérsic at intermediate radii, but ellipticity variations are only weak. We hence fit it by a single Sérsic component. In our image, we cannot discern a core. NGC3608 is a relatively close neighbour of another (larger) elliptical galaxy. As their light distributions overlap, even if slightly, we simultaneously fit the neighbour, also by a Sérsic profile.

NGC3998 (Fig. 3.19) appears to be a lenticular galaxy, but the radial profiles of surface brightness, ellipticity and position angle indicate deviations from a bulge+disk composition.

The surface brightness profile exhibits an inflection between $\sim 10...40''$ (best seen when scaling the radial coordinate logarithmically), which corresponds to the ring that one can discern in the science image upon closer inspection. This inflection is located in between the bulge- and disk-dominated regimes, and its surface brightness is lower than the inward extrapolation of the exponential part of the profile ($R \gtrsim 50''$). Further, at $R \gtrsim 150''$, there is a light excess with respect to the exponential disk profile, indicative of an extended outer disk (see Minchev et al. 2012 and references therein). The ellipticity generally behaves as expected, virtually vanishing in the central regions and having a higher, roughly constant value outside $\sim 15''$ due to the disk'l lower axis ratio with respect to the bulge's. Yet, in the trasition between those two regimes, at $\sim 8''$, there is an ellipticity peak which the bulge+disk residual image reveals to be the signature of a relatively small-scale bar. The position angle shows an extremum at the same radius, in addition to some isophotal twist in the innermost (bulge-dominated) regions.

Overall, strong residuals from ring and bar remain if a simple bulge+disk model is fitted, as well as residuals from a nucleus (not discernible in Figure 3.19). These command an improved model, which comprises the bulge, a bar, an inner disk that is best-fitted by a compact ($n \sim 0.6$) Sérsic profile, the main (outer) disk, and a central point source. The main disk is modified by an inner truncation. The best-fit truncation parameters effecting only a partial truncation, that is the disk's central central surface brightness is merely ≈ 1 mag lower than the extrapolation of the outer exponential profile to the centre. However, models without an inner disk component could be ruled out, as well as models that dispense with the disk's inner truncation. The additional inner disk component may thus be interpreted as either a modified continuation of the outer disk
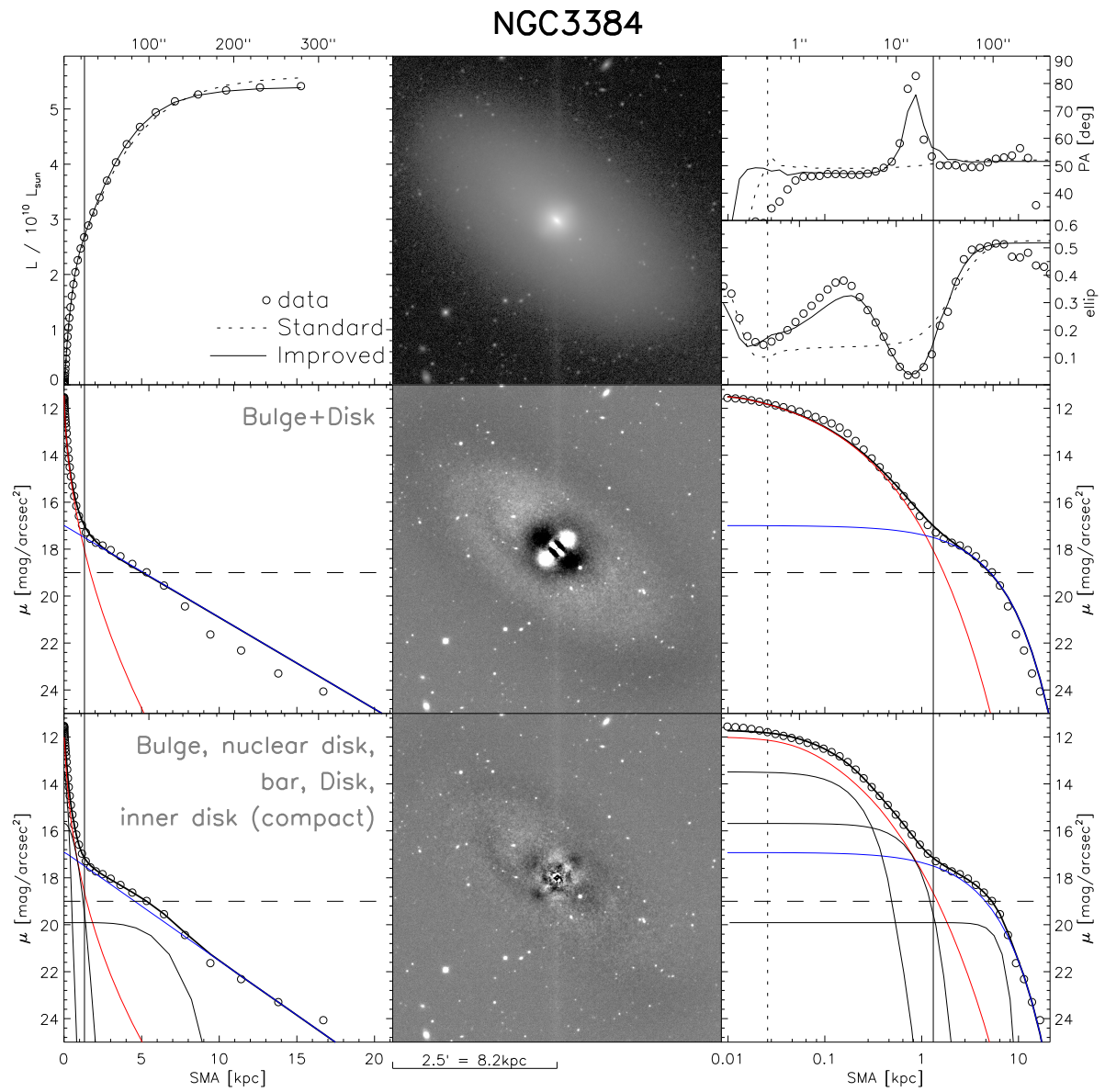
Figure 3.17: For description, please see Figure 3.6.
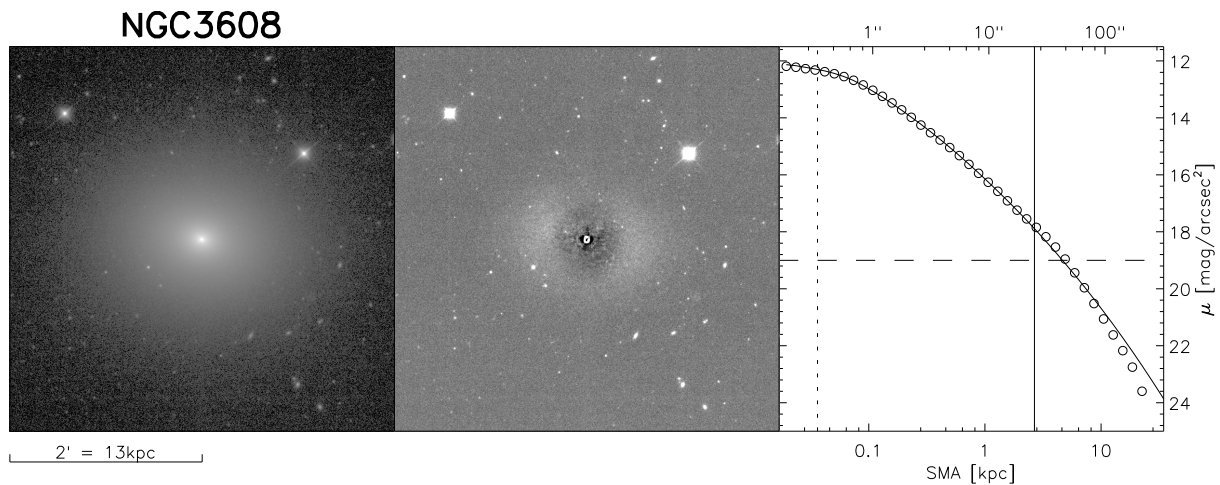
NGC3608

2' = 13kpc

Figure 3.18: For description, please see Figure 3.1.

that helps to reproduce the ring, or as a separate stellar component, for example a "pseudobulge".

NGC4258 (M106, Fig. 3.20) is, within our survey, one of the objects with the largest apparent size. Apart from the spiral arms, it shows a number of irregular features.

The disk profile is divided into an inner part (wich we will call "main disk") that terminates at about the same radius ($\sim 200''$) as the spiral arms, and an outer disk with larger scale radius. The outer disk is visible[1] out to $R \sim 600''$ and exhibits mild warping and asymmetry (lopsidedness), as well as a relatively sharph truncation at the visibility radius. The two spiral arms appear not well defined at all radii, and can hardly be traced inside $\sim 100''$, where they weaken and broaden. Their knotty (presumably star-forming) regions are located mainly in two narrow regions near the edge of the main disk. The northern arm appears brighter than the southern arm. Both data and residual image from a bulge+disk model *suggest* an additional pair of (weaker) minor-axis arms, but this structue may also result from a bar or other irregularities in the disk. Besides a nucleus, there appears to be a small, bright and elongated structure near the galaxy centre (difficult to discern in Fig. 3.20), resembling an edge-on disk that is inclined with respect to the main disk. It can be identified not only by means of the images, but also the profiles of ellipticity and diskiness, which are elevated between $\sim 5...15''$ ($\sim 100...300\,$pc).

A standard bulge+disk model has been created, but naturally it does not account for any of the above-mentioned features. Additionally, its best-fit bulge Sérsic index assumes a very high value

---

[1]not in Figure 3.20 due to the smaller size of the displayed image, which covers mostly the main (inner) part of the disk
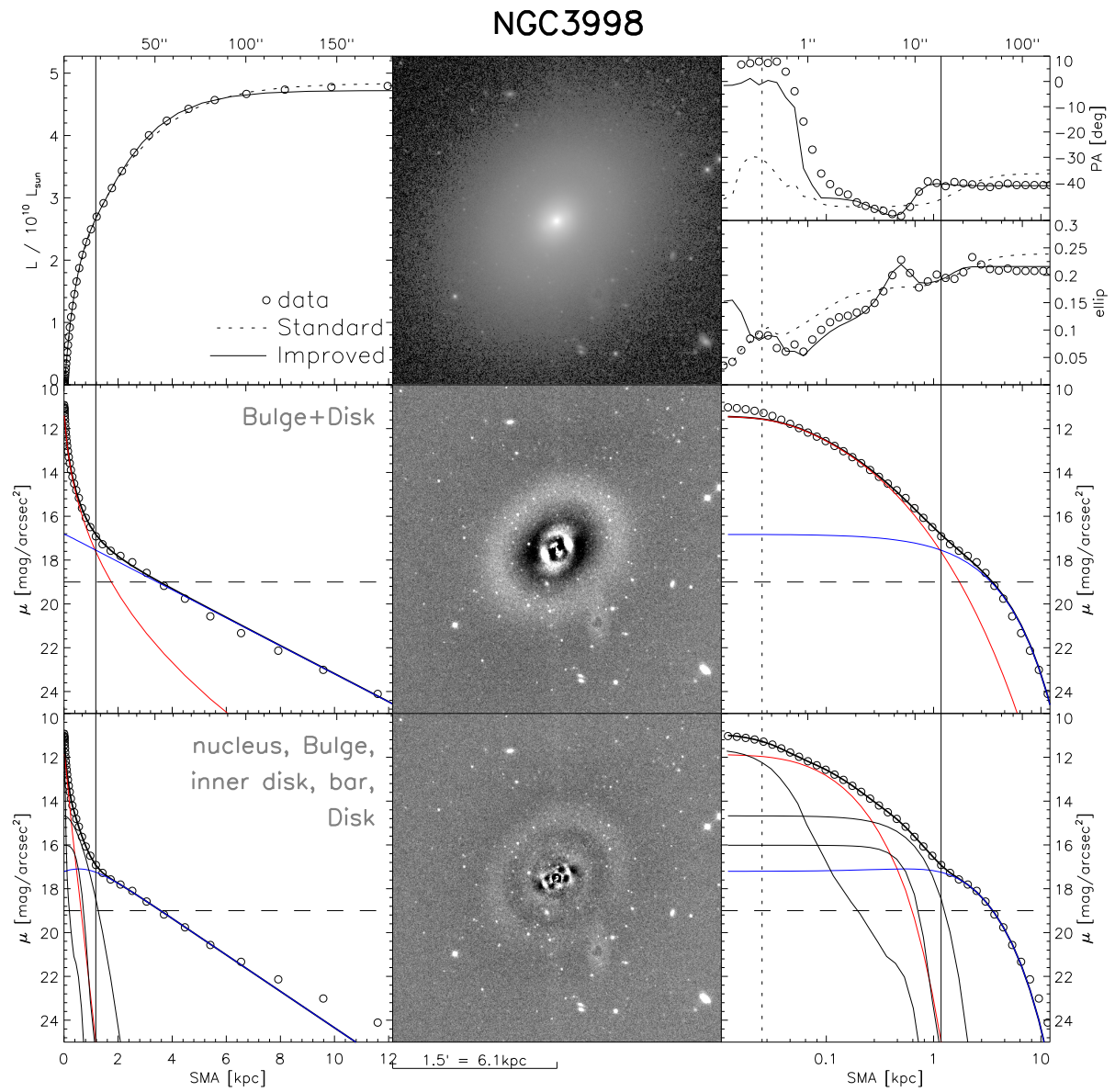
Figure 3.19: For description, please see Figure 3.6.

($\sim$ 8.7), and consequentially the bulge component dominates the model's surface brightness in the outer disk regime. We suspect that the bulge parameters are biased by the bright central disk, and that the bulge flux is greatly overestimated in this simple model.

The main concerns arising during the creation of the improved model were the mixing of main disk and spiral arms, the latter's asymmetry and ambiguous morphology in the inner parts, and the degeneracy of bulge, spiral arms, main disk and edge-on central disk. The configuration we eventually adopt is by no means exclusive, and the bulge parameters may vary greatly if other component configurations are applied.

We account for the spiral arms and part of the main disk by a compact Sérsic ($n \sim 0.5$) profile component, modified by rotation and 1st-order bending modes to reproduce the main spiral arm pair, as well as 2nd- and 4th-order fourier modes to reproduce part of the more diffuse main disk light. An exponential profile component then accounts for the remaining main disk light and the outer/extended disk. This way, the truncation of spiral arms and main disk is represented approximately, while the outer disk's truncation remains unaccounted-for. Yet, application of a corresponding truncation function(s) unfortunately leads to a degenerate model, i.e. slow and unstable convergence of the fit. Similarly, we dispense with uneven fourier modes or independent component centres with which we attempted to account for the outer disk's asymmetries, as otherwise degeneracy ensues with bulge and other central components.

To model the inner part of NGC4258, we use 4 components, of which we have already mentioned the bulge, the nucleus, and the central edge-on disk. When fitting only those three, the central flat component has higher central surface brightness than the bulge, and the latter's profile is almost exponential. The best-fit parameters of this configuration produce a data-model profile mismatch inside $\sim 3''$, that is, a relatively strong light exess of the model in the very centre and a deficit (positive residuals) in a few arcsecond-sized region around it. Analysis of the components' profiles reveals that the point source of the model is too birght, and that probably the fitting algorithm attempts to "use" the point source to account for *extended* (resolved) spheroidal flux. Supporting this interpretation is the central disk component's axis ratio: it exceed's the measured axis ratio, even though the latter is already seeing-convolved. The reason is probably that the model's edge-on central disk component is also influenced by, and accounting for, part of a round centrally concentrated light distribution. We therefore introduce another Sérsic component, initialized with $R_e = 0''5$ (0.5 pix) and $n = 0.5$ (compact profile), which GALFIT3 readily optimizes to $R_e = 6''3$ (220 pc), $n \sim 3.3$ and high axis ratio, as expected for a "classical" bulge. We accordingly identify this as the bulge component. Unfortunately now the interpretation of the other Sérsic component (the previous model's "bulge") is unclear. It is not aligned with the galaxy major axis, but rotated towards the direction of the minor-axis structure in the disk. It may thus represent, as described above, (part of) the light of a putative bar or minor-axis spiral arms. It is also possibly to some degree degenerate with the main disk and the bulge, as its axis

ratio is higher than the disk's. In summary, we cannot draw reliable conclusions with respect to the nature of this component, but tentatively term it "bar".

NGC4261 (Fig. 3.21) is a giant elliptical galaxy as indicated by its core and low curvature of the $\mu - \log R$ profile. Yet, the residual image shows at least two peculiarities: the high-ellipticity region directly sourrounding the core ($R \sim 3..15''$), and strong boxiness between $R \sim 3...45''$, while isophotes are perfectly elliptical at all other radii. Interestingly, the boxiness peak concides with the ellipticity peak. The central structure in the residual image resembles a bar. Therefore, we tested various multi-component models, but none of them remove those features and includes a clearly-identifiable bulge and exponential disk simultaneously. We therefore retain the core-masked single-Sérsicmodel.

NGC4291 (Fig. 3.22) appears to be a giant Elliptical due to its flattened core and low profile curvature, but is relatively small ($R_e \sim 2\,\mathrm{kpc}$). Ellipticity varies and peaks at $R \sim 15''$, followd by a minimum at $R \sim 45''$ and another increase at the largest radii. The second ellipticity peak may be due to the nearby bright star, despite its generous masking, although the peak's location does not agree precisely with the star's distance from the galaxy centre. NGC4261's diski-/boxiness is very close to zero. Just as with NGC4261, the residuals from a single-Sérsic model produce some peculiar structure, in this case a ring (bright residuals between $R \sim 15...20''$), which becomes reduced, but not removed, when the fit is performed while masking the core. Yet, we do not find a multi-component to be appropriate for this galaxy.

NGC4342 (Fig. 3.23) appears to be a lenticular galaxy seen at high inclination. As the other edge-on lenticulars, it poses a challenge to "proper" fitting, in this case amplified by its small apparent size and the resulting relative lack enough information in the data, hindering a robust fit of the multiple additional components that are required for reduced residuals.

NGC4342's profile shows an extended range of exponential decline ($R \sim 7..35''$) and significant diskiness at most radii, indicating the (main) exponential disk, and possible further (secondary, embedded) disks. The bulge+disk model produces strong residuals, suggesting that the disk in this model is too flattened, while overestimating flux the central regions. The disk is not "robust", as using a Sérsicinstead of an exponential profile shows. The standard model also fails to account for light in the outer "envelope"(or: halo), which is discernible in the profiles of surface brightess and ellipticity.

We tried to account for the mismatch by introducing a (Sérsic-) envelope (see §2.3.3, a nucleus, an inner truncation of the disk, and experimented with implementing a bulge ellipticity gradient by means of symmetric truncation functions.
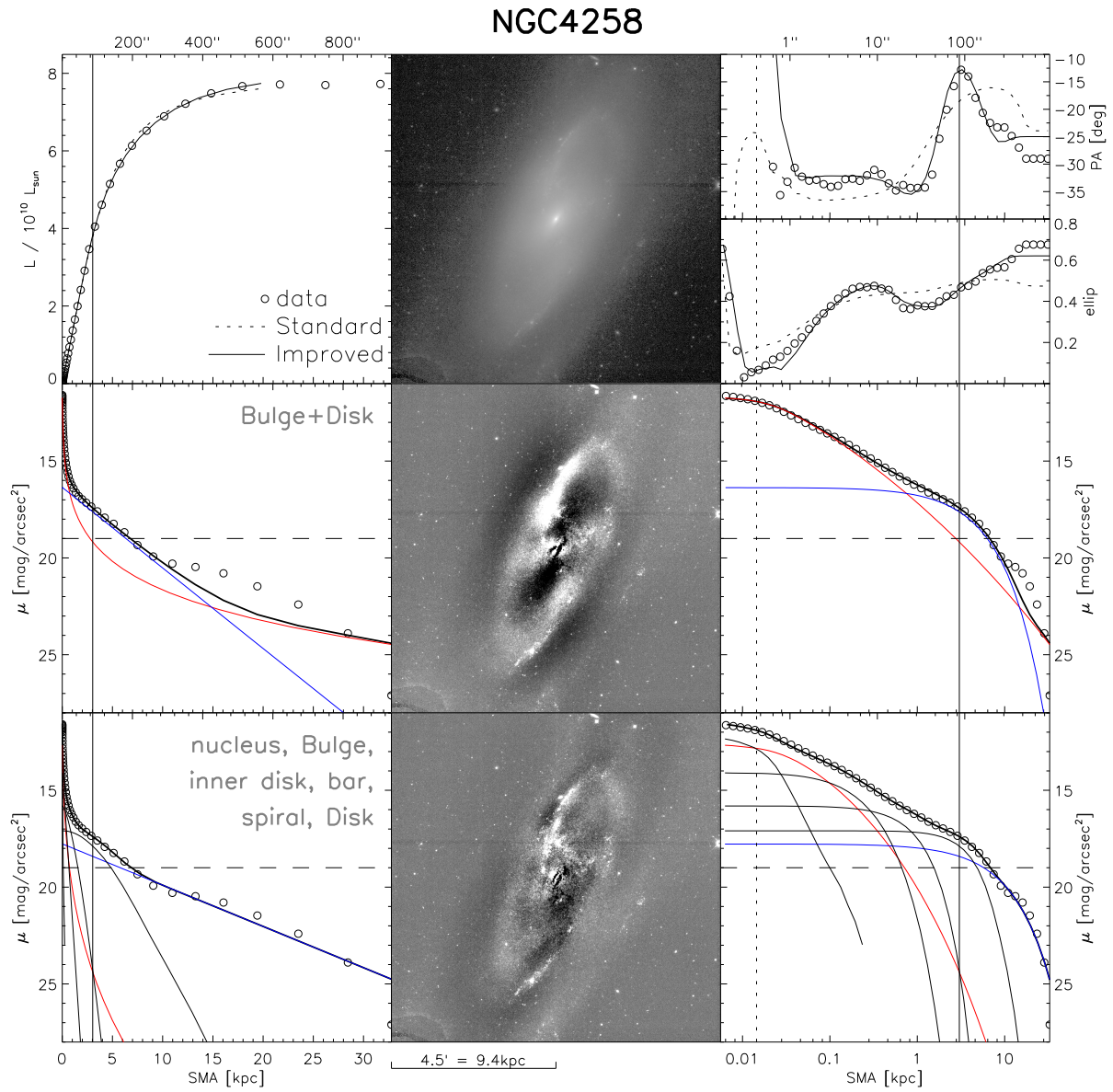
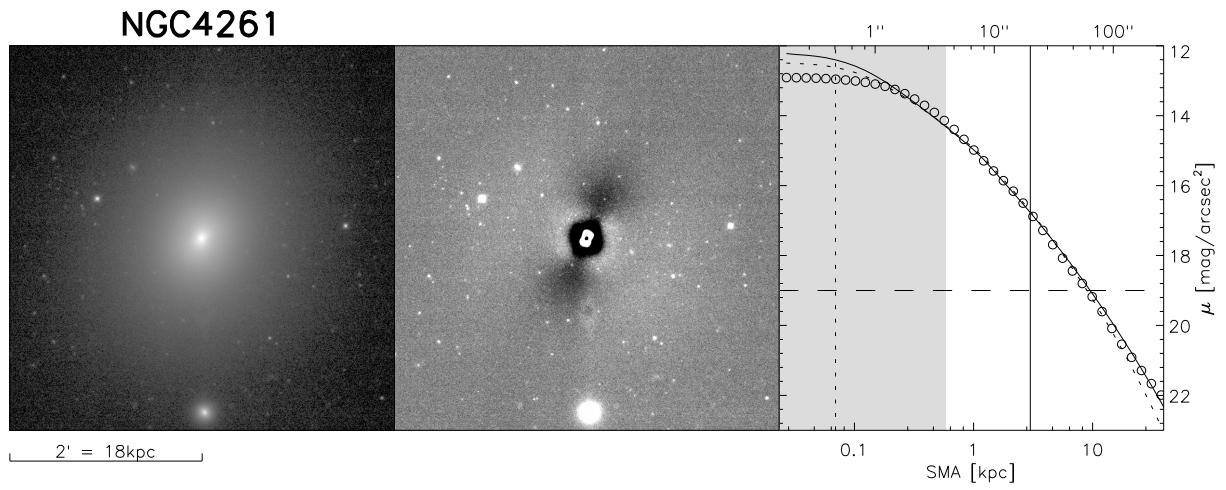**Figure 3.20:** For description, please see Figure 3.6.

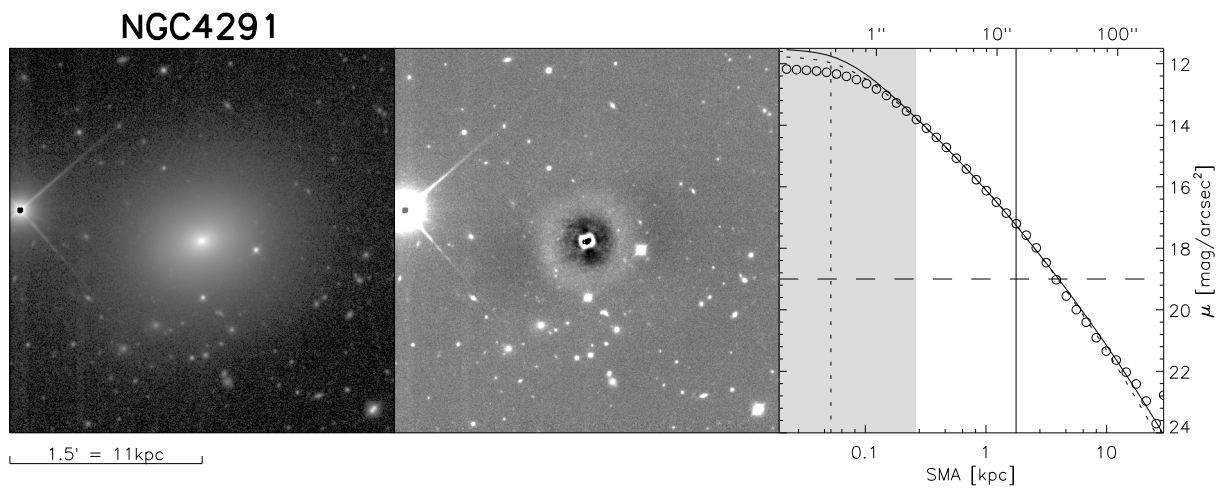**Figure 3.21:** For description, please see Figure 3.2.

Figure 3.22: For description, please see Figure 3.2.

As for other highly flattened E/S0 galaxies, the "envelope" sems to be an essential ingredient of a descriptive model (Bulge+Disk+Envelope, see the image in the bottom-left panel of Figure **??**). This model's disk component is exponential as desired ($n_d \rightarrow 0.9$). Yet, characteristic residuals remain. We therefore introduce a nuclear component with the aim to account for this model's light deficit in the innermost arcsecond. This component, if modeled by a finite-sized (Gaussian, Sérsic-n = 0.5), will expand during the fit broadened once its effective radius is not fixed. If allowing its Sérsicindex as a free fit parameter, it assumes the size, Sérsic index and axis ratio typical of a bulge. The component that represented the bulge in the Bulge+Disk+Envelope model now has best-fit parameters intermediate between a bar and a disk. We allow generalized ellipses here, and find boxy isophotes best. Unfortunately, the octupole residuals seen in the 3-component model at intermediate ($R \sim 4''$ along the SMA) radii barely reduce. The remaining residuals are suggestive of both a bar and a (secondary) embedded disk, and would thus require introduction of yet another component.

As mentioned above, we find that our data hardly support robust convergence of such a model, and while the components themselves may not be spurios, we surmise that their interpretation (bar, inner disk) is shaky. We therefore retain the Bulge+Disk+Envelope model, not without mentioning that assessment of structure, including bulge magnitude, is probably incomplete in this galaxy and would require additional (improved) data to be reliable.

NGC4374 (M84, Fig. 3.10) is a giant elliptical galaxy with an ample core. Ellipticity is low (about 0.2) at small radii and decreases to almost zero outside of $\sim 100''$. Isophotes are boxy throughout. There are no signs of any subcomponents. We hence model this galaxy by a single Sérsic profile and mask its core for the improved model fit.

NGC4473 (Fig. 3.25) is a flattened ($q \approx 0.5$) early-type galaxy with disky isophotes. Its surface-brighntess profile suggests a mild mismatch with a single-Sérsic model, and the ellipticity profile peaks twice, at $R \sim 3''$ and $R \sim 45''$, suggesting two disks. The putatuve inner disk is clearly seen in the residuals from a single-Sérsic model. Yet, we were unable to fit a model that includes an *exponential* disk, whether only in conjunction with a bulge or also adding a secondary disk. Thus, the interpretation of such a model is not possible within the scheme adopted throughout our analysis, and we treat this galaxy as an Elliptical. Although the Sérsic profile overfits the central regions, we do not interpret this mismatch as a core, but rather a result of (unaccounted-for) substructure. We hence do not mask it.

NGC4486 (M87, Fig. 3.26) is a cD galaxy, and therefore unsurprisingly shows large ($R \sim 8''$) core in our K-band imaging. Within our sample, this is also the galaxy with the largest (appar-
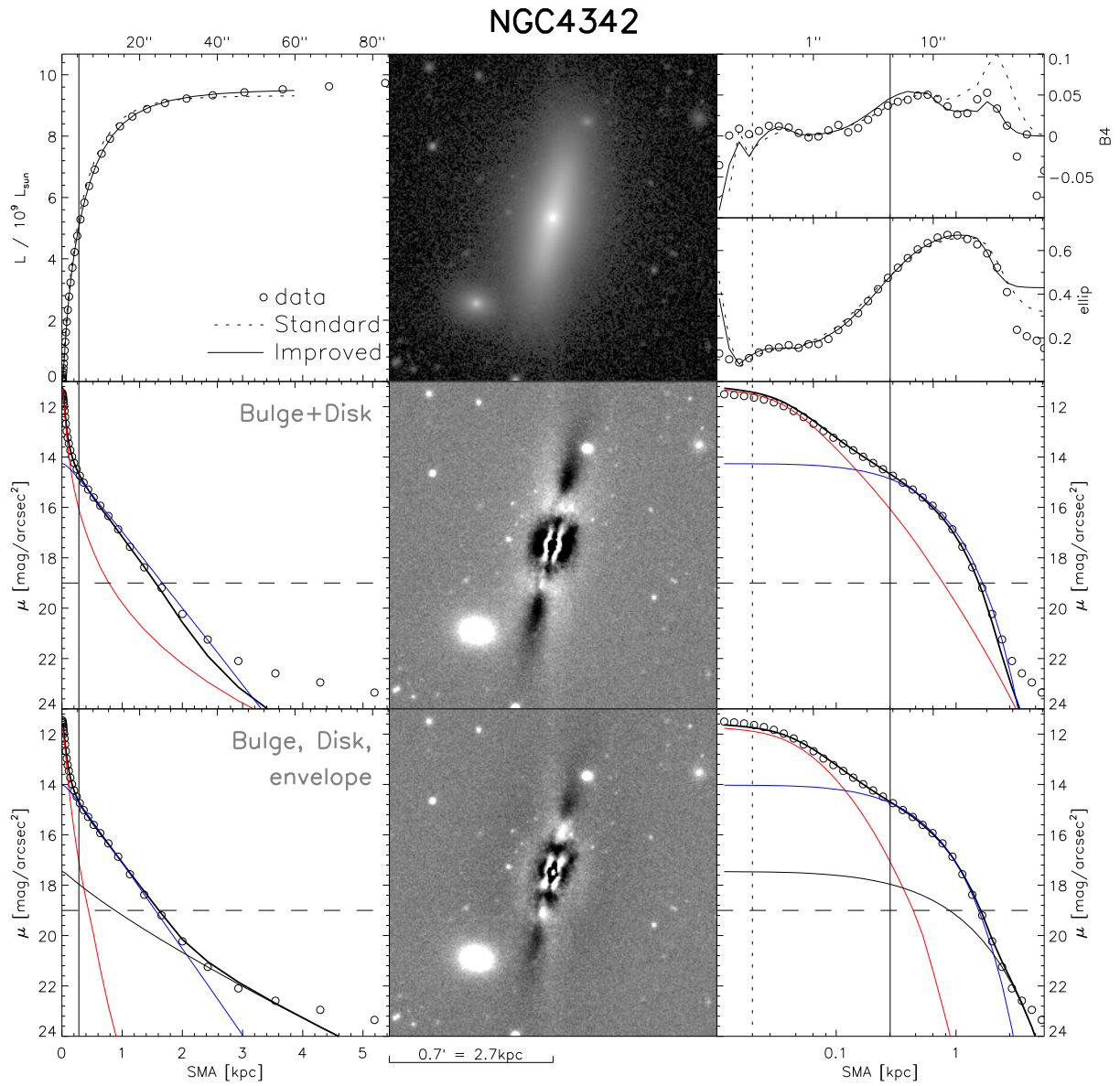
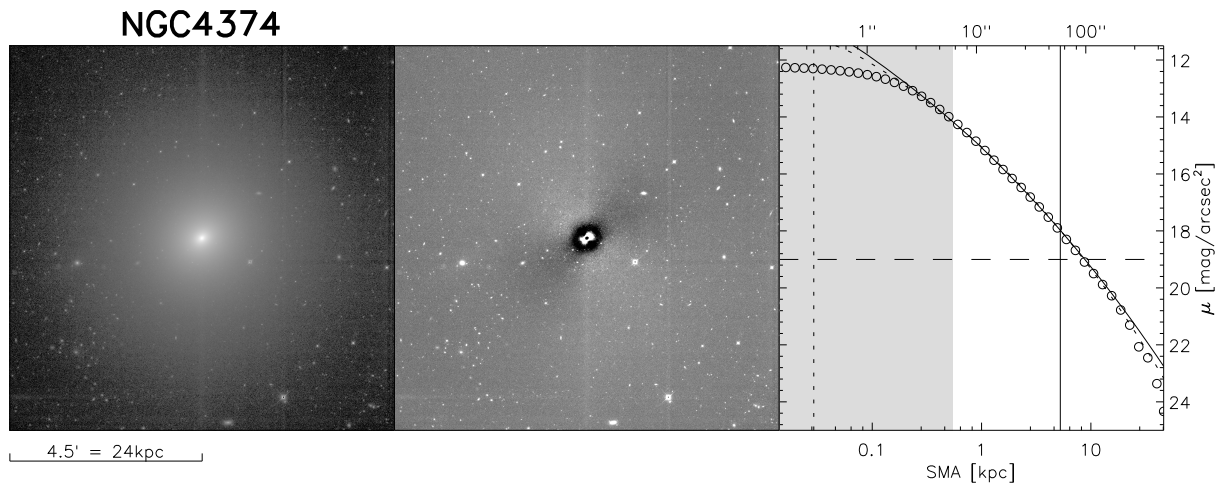**Figure 3.23:** For description, please see Figure 3.6.

NGC4374

4.5' = 24kpc

Figure 3.24: For description, please see Figure 3.2.
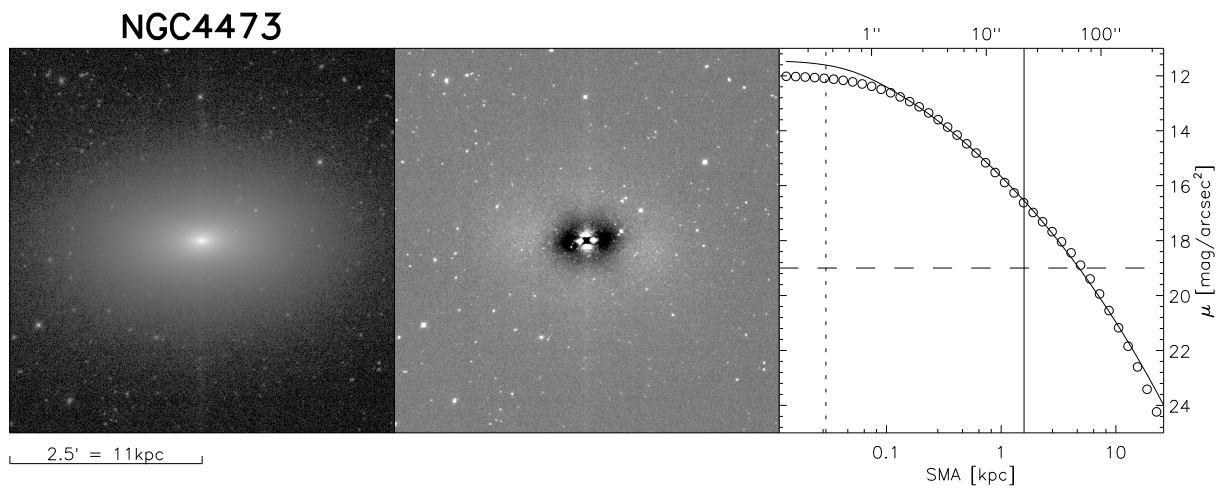

NGC4473

2.5' = 11kpc

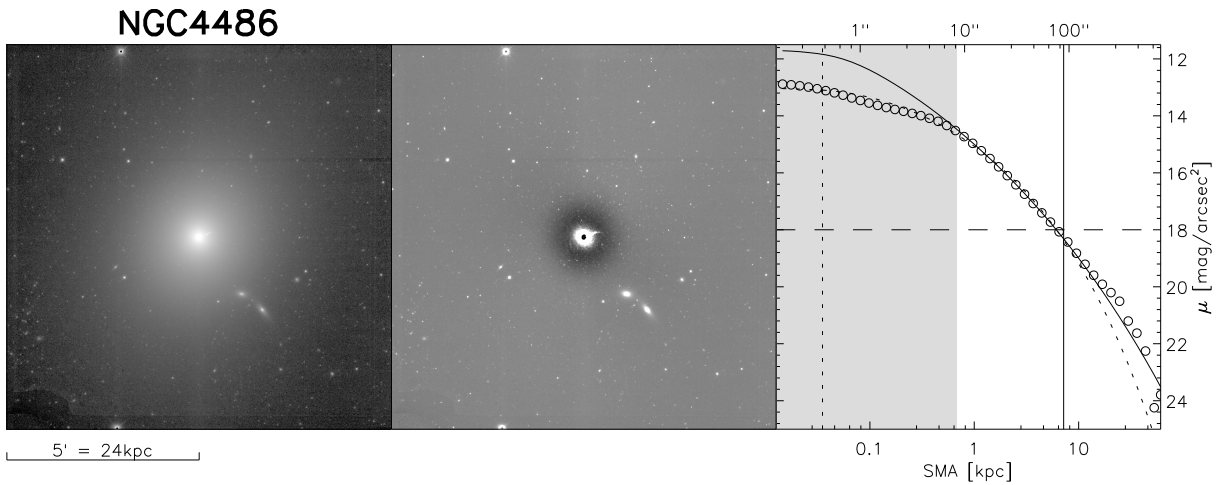**Figure 3.25:** For description, please see Figure 3.1.

Figure 3.26: For description, please see Figure 3.2.

ent) effective radius - 122″ from the improved model, in which the core is routinely masked. The improved model fits the outer profile much better than the model with unmasked core. The well-known jet is clearly visible, and we found that it also needs to be masked in order not to disturb the analysis. M87's AGN is discernible in the radial profile, and even visually on the image. The radial ($\mu - \log R$)-profile is close to a powerlaw (i.e., has low curvature) outside the core. It appears to have a "knee" with subsequent steeper decline at very large radii ($\approx 400''$), but this observation is tentative as the profile becomes noisy and thus untraceable at even larger radii. We suspect that this feature may also be due to background uncertainties or oversubtraction, as we reach a limit in apparent size here at which our adopted sky subtraction procedure becomes biased. Yet, we note that simliar (but likewise tentative) features have been seen in other elliptical galaxies at low ($> 24\,\mathrm{mag/arcsec^2}$) surface brightnesses. Regardless, this feature does not significantly affect the fit, as our field-of-view, and hence the fitted area, does not extend far beyond it.

NGC4564 (Fig. 3.27) is an early-type galaxy with high average ellipticity and exhibits strong indications of a disk (exponential decline between $R \sim 30...75''$, maximum of ellipticity and significant diskiness at the same radii). Yet, like other flat early-types in our sample, it resists a "clean" bulge+disk decomposition. The standard model does not fully account for the ellipticity gradient, and a bar-like structure can be seen in the residuals in the inner regions. Tests with using the "edgedisk" profile effected little improvement, as did 2nd- and 4th-order harmonic modes of the ellispoidal shape. Yet, in contrast to the other edge-on lenticulars, the disk is "robust" ($n_d \rightarrow 1.2$), and residuals are reltively moderate. Furthermore, introduction of a 3rd
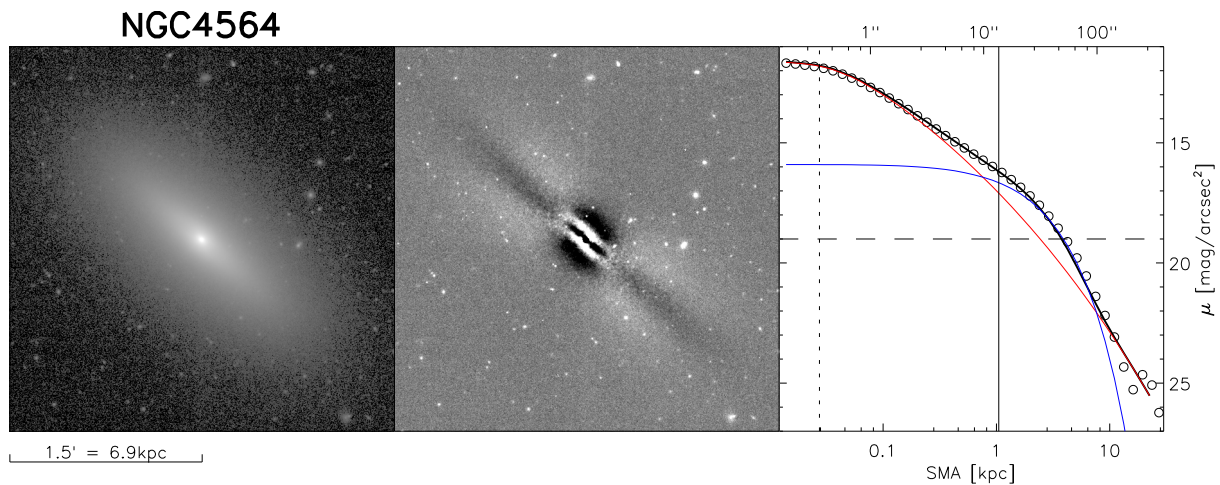
Figure 3.27: For description, please see Figure 3.6.

component (either in form of a bar with compact profile, or an "envelope" with low ellipticity and large effective radius) only slighty reduces residuals, but results in models in which netiher component can be reliably identified as the exponential disk. We therefore decide to adopt the bulge+disk model, leaving this galaxy as the only sample member with disk for which no improved model is required.

NGC4649 (M60, Fig. 3.10) is a cored elliptical galaxy. While fitting it with a single Sérsic profile, the interloper (apparently a spiral galaxy) is masked out since it would be nearly impossible to model it simultaneously without biasing the fit for N4649. Furthemore, the influence of some possibly unmasked outer disk light is very likely benign due to its small total flux compared to NGC4649. As usual with cored (giant) ellipticals, the Sérsic component fits the outer profile much better when the core is masked out, which is why we adopt the resulting Sérsic parameters as our improved model.

NGC4697 (Fig. 3.29) is an early-type galaxy that, according to our data, harbours a highly flattened embedded disk. Its ellipticity and diskiness profiles even show two distinct peaks. The diskiness of isophotes at small and intermediate radii is also readily recognized on the science image.

The residual image from single-Sérsic model, applied in concordance with NGC4697's Hubble classification, supports the existence of two disks, with residuals along the major axis being positive at intermediate radii and negative at the largest radii. Apparently, the Sérsic model is
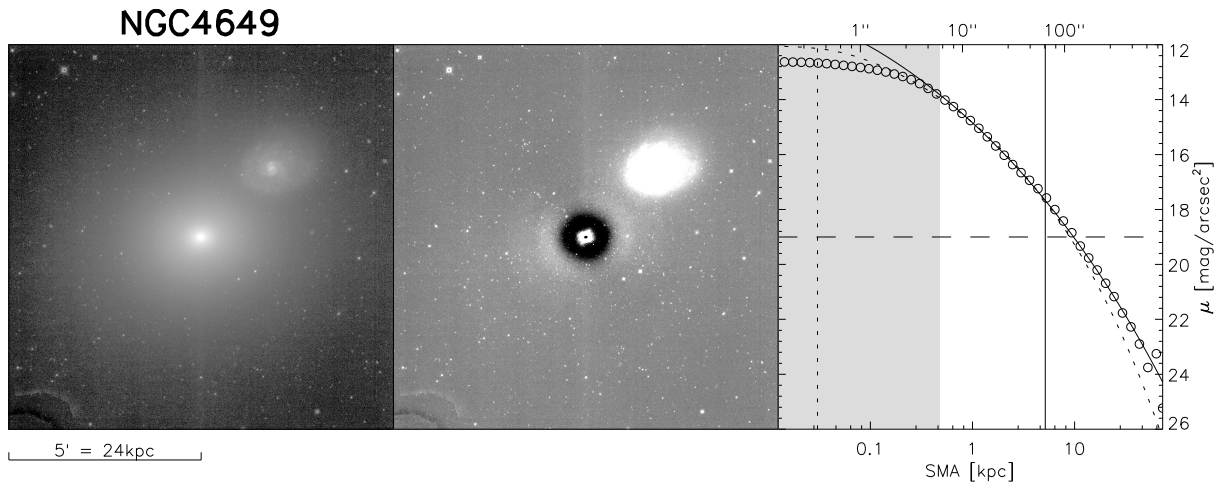
Figure 3.28: For description, please see Figure 3.2.

biased to a higher flattening by the embedded disk, making it too flattened to match the data at the large radii. There is a similar small, but bright, residual structure at the smallest radii (< 10").

The standard model fares very poorly in removing those residuals and accounting for the disk. Similar to other edge-on E/S0 galaxies in our sample, the additional exponential disk component converges to an extremely flattened ($q \sim 0.07$) and faint ($m_d = 11.34$, compared to $m_b = 5.69$) solution. Moreover, when replaced by a Sérsiccomponent, its best-fit parameters completely diverge from an exponential ($n \rightarrow 5.9$).

The indispensable improved model features a second Sérsiccomponent, which converges to intermediate (between disk and bulge) flattening but much small size ($R_e \sim 7$") than both disk ($R_{e,d} \sim 38$") and bulge ($R_{e,b} \sim 130$"). We interpret it as a small-scale disk due to the high flattening. It shows significant deviation from an exponential ($n \sim 2.1$). This, and the still remaining (weak) residuals, may indicate that this "Sérsicdisk" is really composed of two or more (sub-)components. We were not able to reliably decompose further, due to degeneracy of the emerging solutions. It is also well possible that it comprises part of the bulge's light, if the bulge shows a negative radial ellipticity gradient. This ambiguity is taken into account by including the extra component's flux in the "maximal bulge" magnitude, $M_{b,max}$.

We finally add a nuclear point source to our improved model. Despite comprising little flux (< 1% of the total), this was motivated by the nucleus being apparent in both science and residual images. Also, it reduces the Sérsicindex of the fitted extra component, which is otherwise biased to a high value (~ 3.1) in accounting for the light concentration in the centre.

NGC5252 (Fig. 3.30) is a lenticular galaxy that harbours a prominent nucleus (AGN) which is
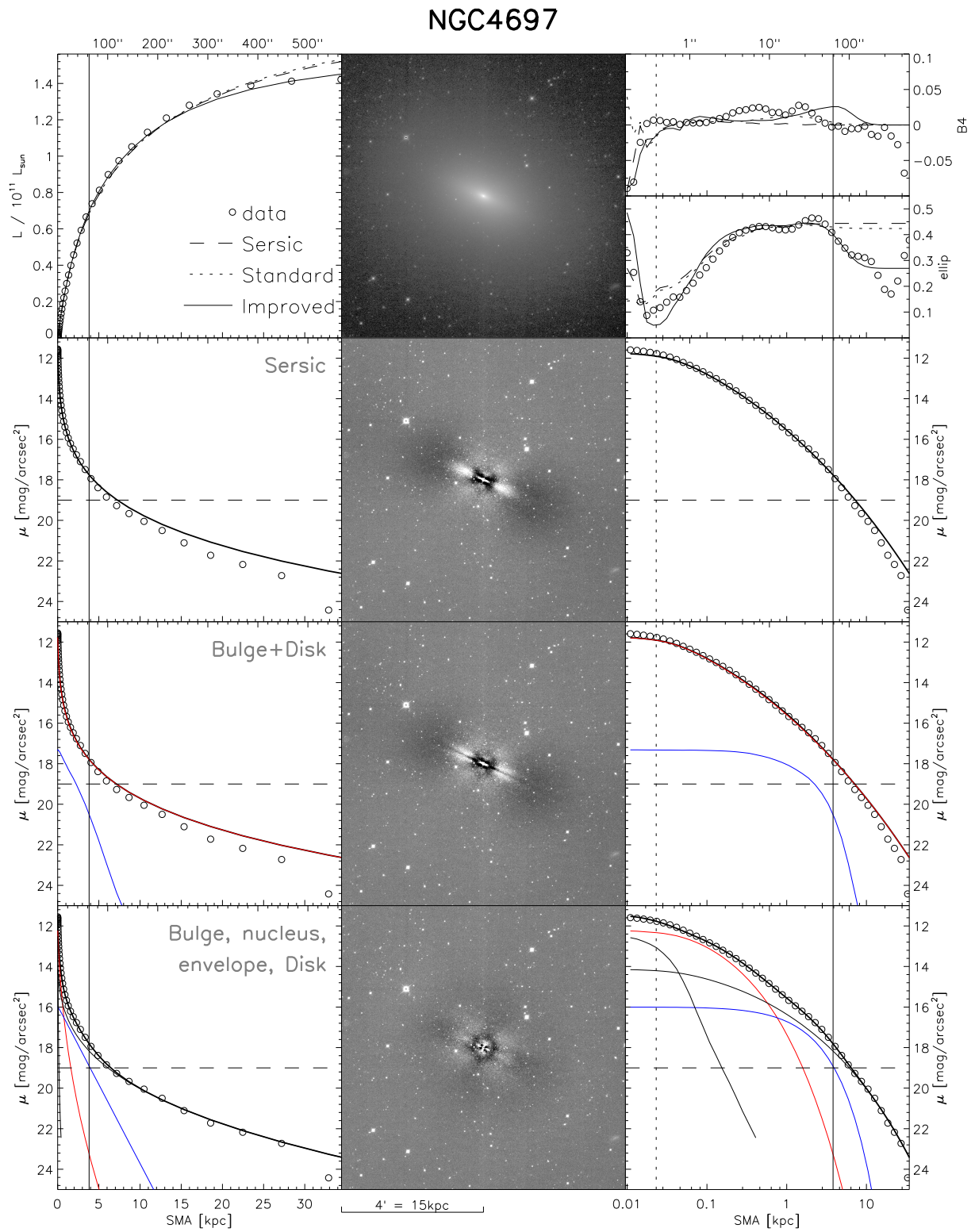
Figure 3.29: For description, please see Figure 3.6.

so bright that the Sérsic index in a bunlge+disk fit tends to diverge and assumes a value well into two-digit values. This can be explained by the finite size of the fitted image area (field-of-view). The mismatch (overestimate of flux) here occurs at extremely large radii, at which a high-n Sérsic profile still includes a significant fraction of the flux, but which are unavoidably excluded from the χ^2-computation. Therefore, in the standard model fit we fix the Sérsic index to $n = 4$, which unfortunately results in a best-fit with an unrelaistically small bulge component. The required improved model includes the obvious central point source and fits this galaxy image extremely well. This is remarkable considering that NGC5252's disk is quite flattened, and that residuals of other galaxies wth similar morpholgy are typically high.

NGC5845 (Fig. 3.31) is a galaxy that we find difficult to classify and fit. The data are unusual here in several ways. NGC5845 is one of the smallest targets in our sample, implying low relative resolution. A very large and bright nearby elliptcial galaxy (NGC5846) requires a separate model, as its extended low-surface brightness flux otherwise contaminates the area used to fit our target. NGC5845's profile shows a distinct inflection ("dip") at $R \sim 35''$ and low surface brightness ($\sim 22\,\mathrm{mag/arcsec^2}$), with a very shallow decline beyond this radius. This extended outer profile can *not* be attributed to the mentioned neighbour, as it persists after modeling the latter. The radial profiles of e, PA and $B4$ show numerous fluctuations, which probably originate in both actual substructure on the one hand (e.g., the isophotal twists are visually discernible on the image), and noise due to the low total flux and small angular extent on the other hand.

The inflection at $\sim 35''$ may be interpreted in several, not mutually exclusive, ways: as resulting from an embedded disk that contributes to the profile mostly at intermediate radii, inside the inflection (which is supported by the profiles of ellipticity and diskiness); as a large-scale ring; or as evidence of a distict outer envelope/halo. These scenarious still do not explain the isophotal twist, that may result from a triaxial spheroid, or a bar (for which we otherwise find no conclusive evidence). Further, we note that the residual image from single-Sérsic and bulge+disk models suggest a small-sale edge-on disk.

The data, in concert with the flexible GALFIT3 fitting code, unfortunately do not allow us to discriminate these scenarios reliably. A bulge+disk model produces ample residuals that are barely an improvemnt over those resulting from a single-Sérsic model. Its "disk" component is not exponential when a Sérsic profile is used, and it converges to high axis ratio (higher than the "bulge" axis ratio), unless the initial parameters are carefully tuned. Other multi-component models did not allow for unambiguous physical interpretation, either.

Thus, while it appears to be different from a "normal" Eliiptical, and single-Sérsic model residuals reveal ample substructure, we did not succeed at fitting a unique solution with exponential disk, low residuals and a clear interpretation of all components. We suspect that this galaxy may
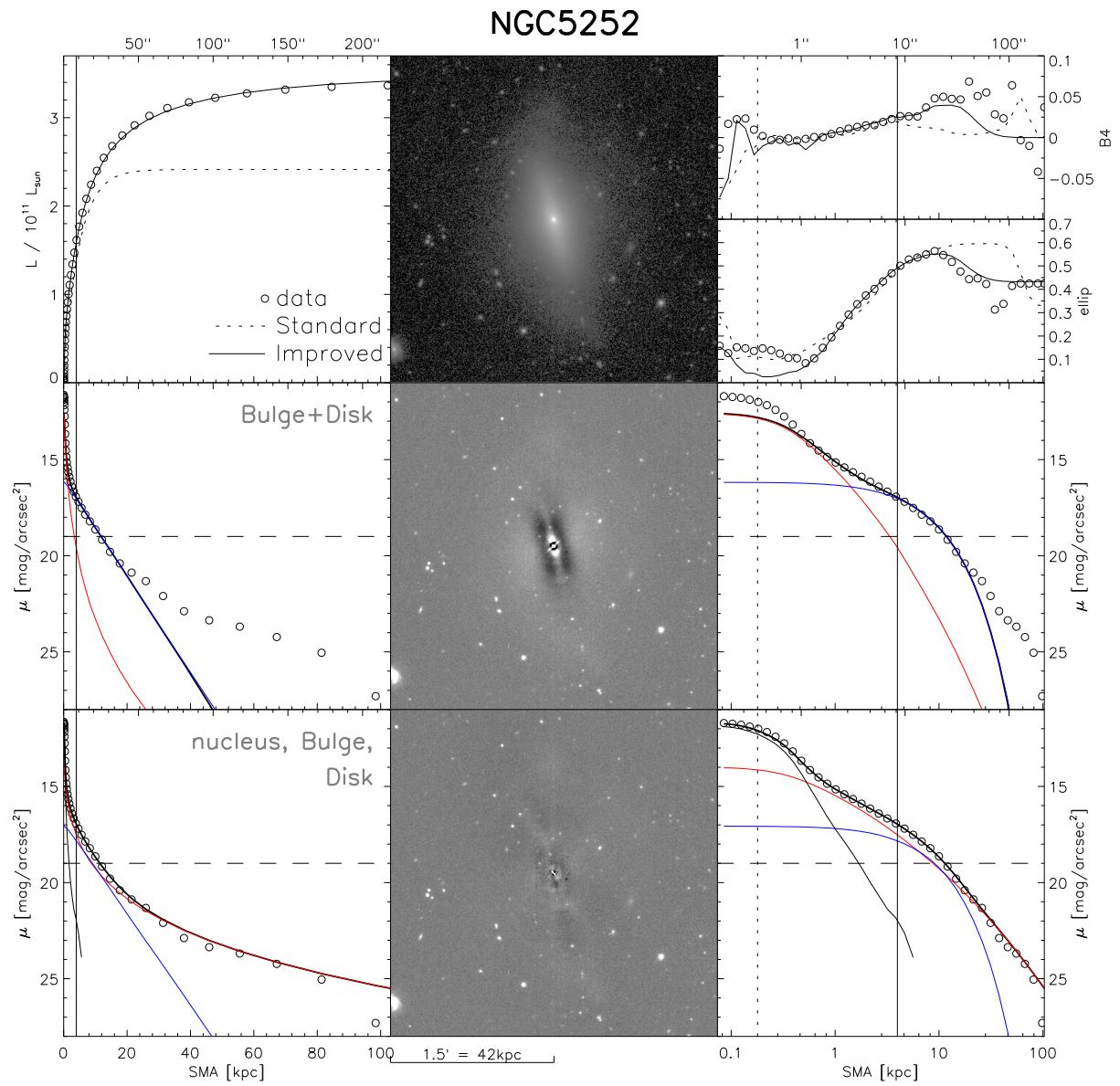
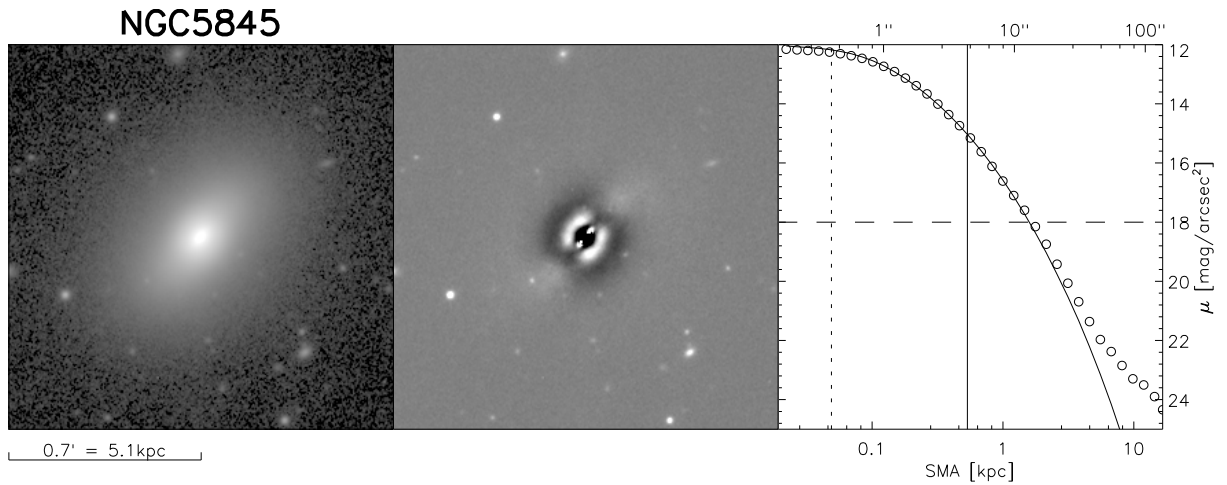**Figure 3.30:** For description, please see Figure 3.6.

Figure 3.31: For description, please see Figure 3.1.

be another representative of the "edge-on lenticular" galaxies with embedded disk(s), strong ellipticity gradient in the spheroid and/or additional envelope, plus possibly a bar in this particular case. Yet, from our data the evidence is inconclusive and bulge photometry from such models highly uncertain. We hence adopt a single-Sérsic model here, not without cautioning that such a model significantly underestimates flux at radii outside $\sim 30''$.

NGC6251 (Fig. 3.32) is a very luminous early-type galaxy, yet we cannot discern a core. The slight "knee" in the profile at $R \sim 50''$ may indicate an outer disk, and a corresponding fit indeed produces a somewhat decreased chi^2. Yet, this may merely be a result of the increased number of parameters. We find no indication of a disk in profiles of ellipticity and diskiness. If this galaxy is seen at very low inclination, this is not surprising. Still, the data do not justify introduction of a disk component overall, as residuals from a single-Sérsic model are already quite low.

NGC7052 is a very elongated elliptical galaxy. The stellar foreground is dense, such that a "second-pass" object mask is necessary, which is derived from the residual image. NGC7052 shows a strong ellipticity gradient ($e \approx 0.2$ in the centre, and ≈ 0.6 outside of $R \sim 30''$). Unusually, despite its relatively high flattening, ispohotes are predominantly boxy, with very strong boxiness outside $R \sim 30''$. We cannot discern a disk here, but residuals strongly decrease upon introduction of a second compoent. This component's Sérsic index is > 2, again refuting the disk but instead implying that the ellipticity gradient alone is responsible for the residuals seen in the single-Sérsic model. Trials in accounting for the ellipticity gradient by using a truncation function to join two Sérsic components with shared parameters, except for ellipticity and disky-
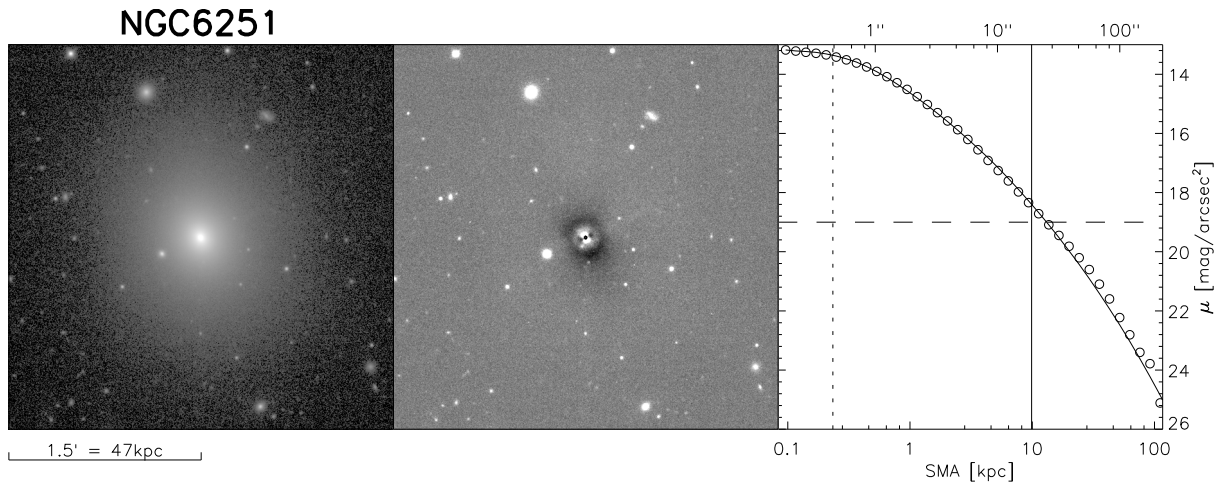
Figure 3.32: For description, please see Figure 3.1.

/boxiness, converged very slowly and did not improve residuals as much as hoped. Therefore, we choose to fit this galaxy by a single 2D-Sérsic profile.

NGC7457 (Fig. 3.34) is clearly a lenticular galaxy with a strong large-scale disk component. The residuals from a standard model are already relatively good, but show signs of a bar (not aligned with disk and bulge and a nucleus. More justification for applying a more complex model is provided by the profiles of the composite model and the components: the bulge is clearly too extended and overpredicts the data at large radii ($\gtrsim 120''$). At these distances from the centre, the bulge component again dominates the surface brightness (as it doesn in the centre), and the model follows a Sérsic profile, while the data clearly are follow an exponential profile (i.e., are dominated by the disk). It is not then surprising bulge of this model has a very high $n = 7.7$ (!), probably being boosted by the nucleus.

Indeed, the improved model, which includes a central point source and bar leads to a much lower bulge Sérsic index and an exponential outer profile. The bar component in this model is quite large, aside from modeling the isophotal twist at intermediate radii, needed to achieve the improvement in bulge parametrization. It also provides for a disk profile that is quite close to exponential.

We find that the bar may be equally well modeled by a modified Ferrer profile instead of a Sérsic. Interestingly, while the resulting chi^2 is virtually the same in both cases, the respective bulge parameters differ: the bulge is brighter and has Sérsic index $n > 2$, instead of ~ 1.5 as in case of a bar with Sérsic profile. This highlights our overall conclusion that bulge parameters are quite
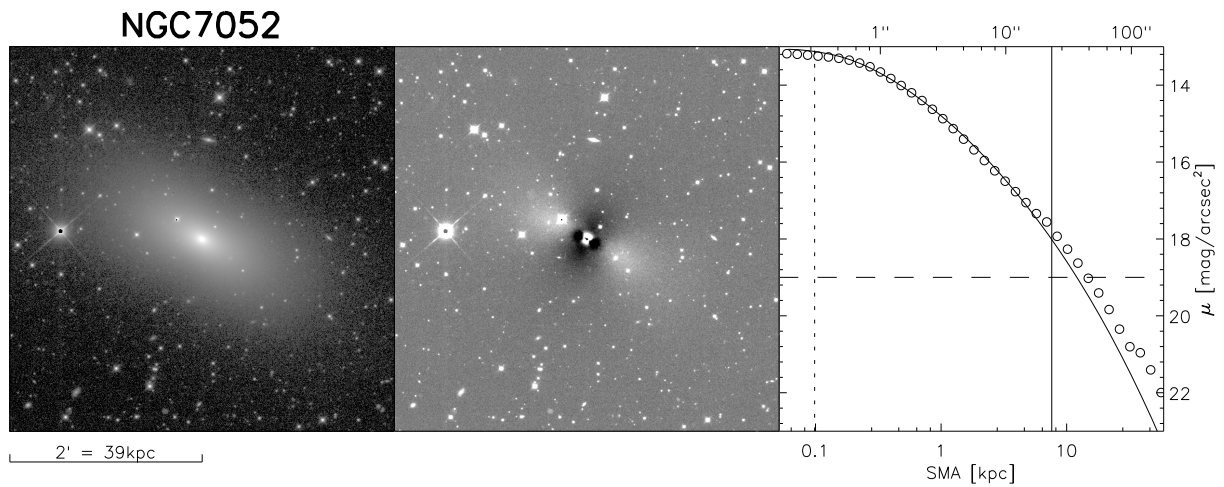
Figure 3.33: For description, please see Figure 3.1.

sensitive to details of the decomposition. We eventually adopt a Sérsic profile for NGC7457's bar, as we do for all other barred galaxies.

PGC49940 (A1836-BCG, Fig. 3.10) is a luminous elliptical galaxy, seen at a relatively large distance (153 Mpc). Yet, a core cannot be discerned in the surface-brightness profile, and is, at best, weak as suggested by the residuals from a single-Sérsic model. We therefore apply no corresonding mask. Although the Sérsic profile mildly unerestimates the flux at $R \gtrsim 30''$, where $\mu \lesssim 22$ mag/arcsec^2, we find no justification for introduction of a large-scale disk here.
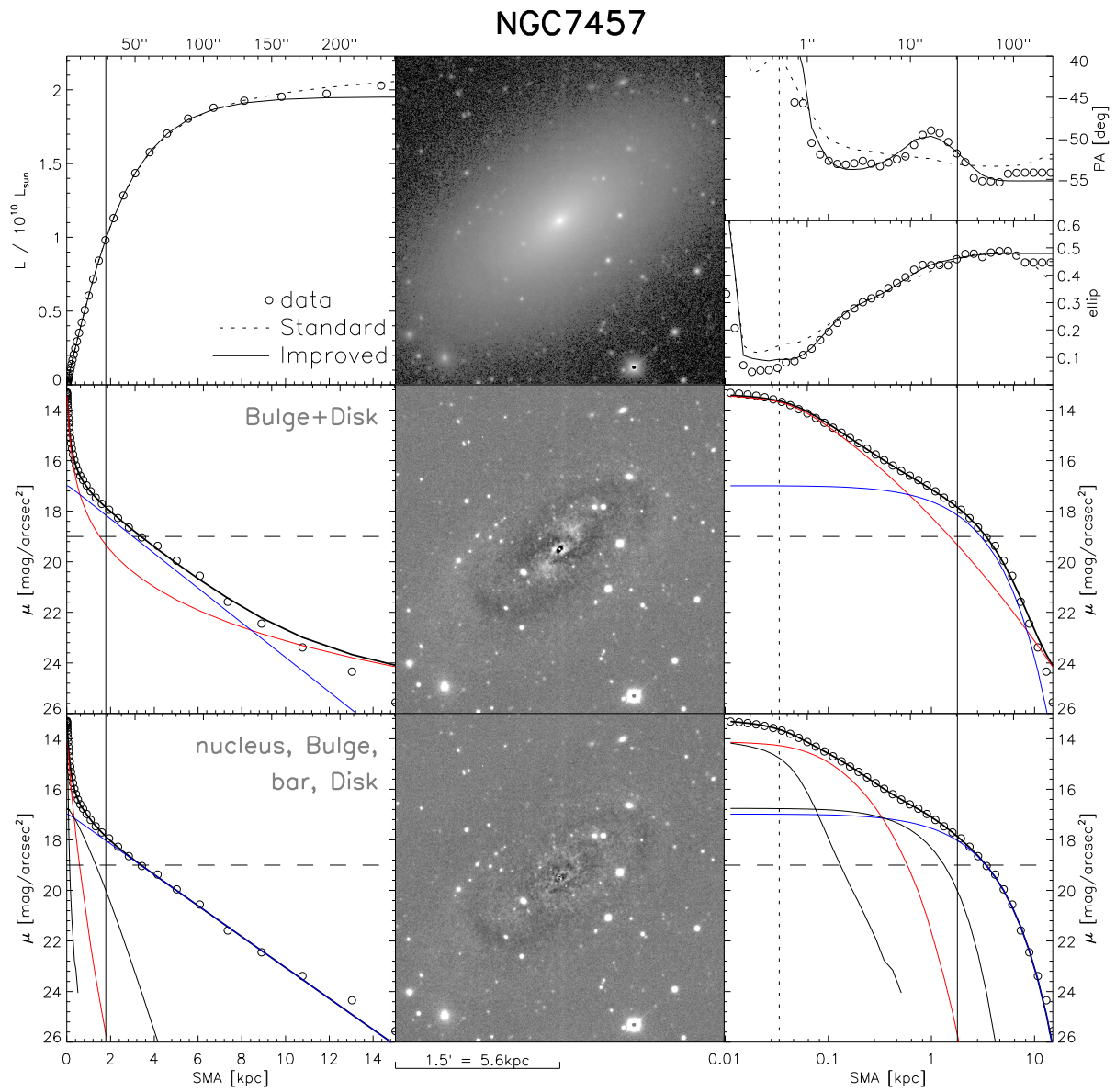
Figure 3.34: For description, please see Figure 3.6.
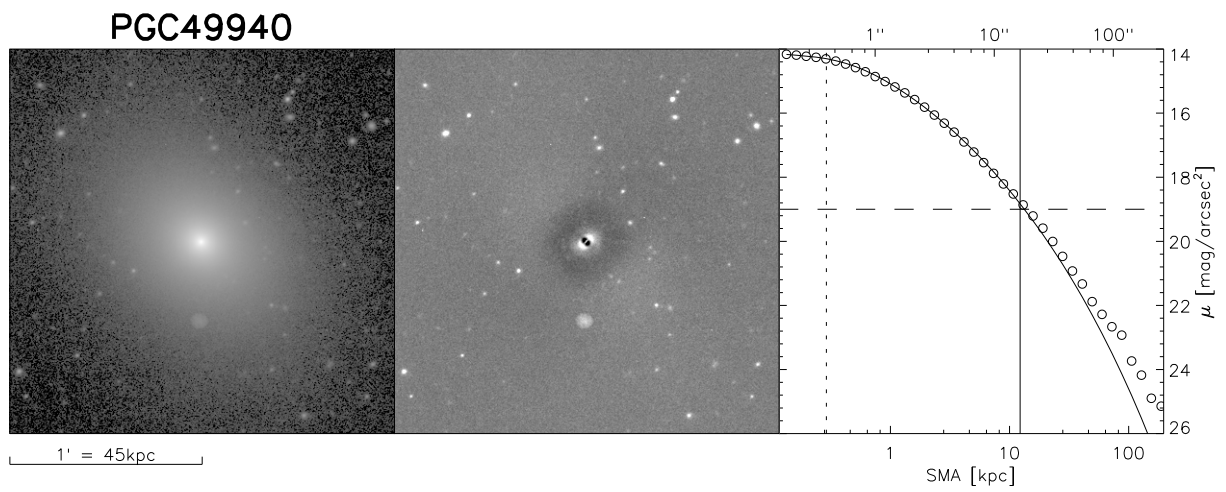
Figure 3.35: For description, please see Figure 3.1.

4

THE CORRELATION OF $M_\bullet$ WITH NEAR-INFRARED LUMINOSITIY REVISITED[*]

ABSTRACT

We present an investigation of the scaling relations between Supermassive Black Hole (SBH) masses, $M_\bullet$, and their host galaxies' K-band bulge (L_{bul}) and total (L_{tot}) luminosities, based on new high-resolution imaging, obtained with the wide-field WIRCam imager at the Canada-France-Hawaii-Telescope (CFHT), that represents the deepest homogeneous near-infrared data set of BH host galaxies currently available. From a sample of 35 galaxies with securely measured $M_\bullet$, selected irrespective of Hubble type, we derive bulge and total magnitudes via two-dimensional profile fitting and account for cores, bars, nuclei, rings, small-scale disks, envelopes and spiral arms when necessary, in addition to the canonical bulge and large-scale disk. Contrary to previous claims, we find that the present-day $M_\bullet - L_{\mathrm{bul}}$ and $M_\bullet - L_{\mathrm{tot}}$ relations have consistent intrinsic scatter, suggesting that $M_\bullet$ correlates equally well with bulge *and* total luminosity of the host. Our analysis provides only mild evidence of a decreased scatter if the fit is restricted to elliptical galaxies. We measure a log-slope of 0.77 ± 0.09 for our best characterization of $M_\bullet - L_{\mathrm{bul}}$, and 0.95 ± 0.14 for the $M_\bullet - L_{\mathrm{tot}}$ relation, implying that $M_\bullet$ is proportional to L_{tot} rather than L_{bul}. Moreover, the slope of $M_\bullet - L_{\mathrm{bul}}$ appears to be sensitive to the detail of the image decomposition, while characterization of $M_\bullet - L_{\mathrm{tot}}$ is robust with respect to the photometric method. Given the difficulties and potential ambiguities intrinsic to a bulge/disk (or more) decomposition, our results indicate that L_{tot} is in practice a more suitable quantity than L_{bul} as SBH mass indicator, and that its correlation with $M_\bullet$ should be used as a constraint in the context of modeling SBH-galaxy co-evolution.

4.1 INTRODUCTION

The correlation between supermassive black hole (BH) masses, $M_\bullet$, and luminosities of their host galaxies' bulges, L_{bul}, is significant for at least two reasons.

First, there is to this date no obvious nor unique theoretical framework that satisfactorily explains its existence and characteristics. On the other hand, understandin this, and other correlations between BHs and host galaxy properties, has important implications for understanding the origin of BHs and the formation of galaxies. Models of BH-galaxy-coevolution include mergers of galaxies and their BHs, but typically also invoke an interaction ("feedback") between BHs and their hosts (e.g., Silk & Rees 1998; Granato et al. 2004; Hopkins et al. 2006; Croton et al. 2006; Shankar et al. 2006; Volonteri et al. 2011). The relative importance of mergers and feedback, their timescales, efficiencies and frequencies, may be constrained by comparing model predictions with the observed $M_\bullet - L_{bul}$ relation.

Second, the $M_\bullet - L_{bul}$ relation allows to infer BH masses, which are difficult to measure directly, from observationally much more accessible luminosities. This is used, for example, in the context of establishing the black hole mass function (BHMF) and its redshift evolution. Furthermore, the $M_\bullet - L_{bul}$ relation derived from dynamically measured BH masses is also an indispensable tool to calibrate secondary methods of measuring $M_\bullet$ in active galaxies, namely the reverberation mapping and the empirical photoionization method (e.g. Onken et al. 2004; Ferrarese & Ford 2005; McGill et al. 2008). The latter is frequently used to investigate the redshift evolution of BH masses and BH-galaxy scaling relations (e.g., Shankar et al. 2009a; Bennert et al. 2011).

The $M_\bullet - L_{bul}$ relation shares both theoretical significance and predictive power with other correlations between BH mass and host galaxy properties, most notably the the bulge stellar velocity dispersion, σ_v, as well as the closely related (derived) stellar and dynamical mass, $M_{\star(,bul)}$ and $M_{dyn(,bul)}$. Of special interest in this context is the correlations' intrinsic scatter, ϵ, since a relation with low scatter will allow more precise $M_\bullet$ inferences, provided that the correlating quantity is observationally accessible with adequate precision. Yet, aside from desiring a "tight" relation as predictive tool, it is worthwhile to note that from a theoretical perspective, all correlations, not only the one with the lowest scatter are of interest, since they serve as an additional constraint to evolutionary models. Consequently, it is imperative for the calibration of these relations to be as precise and unbiased as possible. For example, the models of Jahnke & Macciò (2011), where merging is the main driver behind the emergence of the $M_\bullet - M_\star$ relation at $z = 0$, predict a lower scatter than observed unless star formation, black-hole accretion and disk-to-bulge conversion are included.

Unfortunately, the present characterization of the $M_\bullet - L_{bul}$ relation and its intrinsic scatter is far from secure. Published parameter values range from ~ 0.9 to ~ 1.3 for the slope, and ~ 0.3 to

~ 0.6 for ϵ, with a typical 1σ-uncertainty of $\sim 10\%$[1]. Of particular interest is the relation at near-infrared (NIR) wavelenghts, since, compared to optical, NIR luminosities are a better tracer of stellar mass and are less affected by dust extinction. The first study of $M_\bullet - L_{bul,NIR}$ relations was based on 2MASS J, H and K-band data (Marconi & Hunt 2003MH03 hereafter). The authors estimated the scatter in the relation, ϵ, to be between 0.5 and 0.3, the former obtained using the full sample of $M_\bullet$ available at the time, the latter (smaller) using a subsample of 27 galaxies, deemed to have reliable estimates of $M_\bullet$. Surprisingly, MH03 found the intrinsic scatter in the NIR to be equivalent to the scatter in the optical (B-band) for the same sample, despite the former's expected advantage with respect to dust and stellar population effects. One may suspect the relatively low resolution and shallow nature of the 2MASS images, which hamper reliable decomposition and bulge photometry, to be partially responsible.

Several years later, (Vika et al. 2012V12 hereafter) presented an updated relation using data from the UKIDSS survey. The improved spatial resolution and depth of the data allowed them to account for nuclei, bars and cores when modeling galaxy images (while MH03 restricted their analysis to a bulge+disk decomposition). Based on a sample of 29 galaxies, V12 found a characterization of the relation in agreement with MH03 (see Graham 2007), but noted that the scatter increased to 0.5 dex (0.4 dex if barred galaxies were excluded), in spite of the clearly improved quality of the photometric data and analysis. Given these discrepancies, the importance of the $M_\bullet - L_{bul}$ relation, and the challenges of working with NIR bands, a devoted study to more firmly establish the relation in these bands is required.

To further investigate the K-band $M_\bullet - L_{bul}$ relation, we used the WIRCam instrument at CFHT to conduct a dedicated imaging survey, resulting in the deepest currently available homogeneous NIR-data set of known BH host galaxies with reliable direct $M_\bullet$ measurements. Since our goal is to perform an accurate decomposition of each galaxy into separate morphological components, we required $\lesssim 1''$ image resolution. In order to further reduce photometric uncertainties, we placed special emphasis on developing an observation strategy and data reduction pipeline that reliably accounts for the high and variable NIR backgound. Using the latest GALFIT profile fitting code (GALFIT3, Peng et al. 2010), we find that most galaxies require components in addition to a canonical bulge and disk, and demonstrate the large impact on the resulting bulge magnitudes. We additionally characterize the $M_\bullet - L_{tot}$ relation with total galaxy luminosity and compare with the parameters of $M_\bullet - L_{bul}$.

Details of the data acquisition and analysis, as well as a detailed discussion of each galaxy, are presented in Chapters 2 and 3. In the current chapter, we focus on the derivation of the $M_\bullet - L$ scaling relations. It is organized as follows: In §4.2 we describe the sample selection and summarize data quality and analysis leading to our bulge and total luminosity measurements.

---

[1] in case of ϵ, the confidence interval was characterized only by a few recent publications

§4.3 presents the ensuing scaling relations, including comparison with previous publications. We discuss our results in §4.4 and draw conclusions in §4.5. We elaborate on the correlation fitting method and the treatment of data uncertainties in the appendix.

4.2 BULGE AND TOTAL LUMINOSITIES FROM SUPERIOR NEAR-INFRARED IMAGING

4.2.1 SAMPLE OF BH HOST GALAXIES

Our sample of BH host galaxies comprises all secure $M_\bullet$ measurements available at the time of observing proposal submission (March 2008), regardless of the Hubble type of the host galaxy. The sample comprises only galaxies for which the BH mass is derived based on dynamical analysis of the spatially resolved kinematics of gas or stars. We threfore do not consider targets where only upper limits on $M_\bullet$ are available. We also exclude measurements from gas kinematics based on models with fixed disk inclination (e.g. NGC4459 and NGC4596, Sarzi et al. 2001), irregular disks that did no permit clean modeling (M81, Devereux et al. 2003), measurements based on isotropic stellar dynamical models (NGC4594, Kormendy et al. 1988; NGC4486b, Kormendy et al. 1997), measurements flagged as being particularly uncertain in the original papers (M31, Bacon et al. 2001; NGC1068, Greenhill et al. 1996; Circinus, Greenhill et al. 2003), and the unpublished BH mass of NGC4742 (initially used in Tremaine et al. 2002). NGC5128 (CenA) has been excluded because of declination constraints. This means that with respect to MH03's "group 1" sample of host galaxies with secure $M_\bullet$, we exclude NGC5128, NGC4594, NGC4742, as well as M31, NGC1068, NGC4459 and NGC4596 which were only used by MH03's for their "group 2" results. Conversely, we include several galaxies that had their $M_\bullet$ published since: IC4296, NGC1300, NGC1399, NGC2748, NGC3227, NGC3998, and PGC49940 (A1836-BCG). V12's sample is quite different from ours, since only 14 of their 25 galaxies[2] meet our criteria, while several were not measured yet at the data of our proposal submission.

The above selection results in the sample of 35 galaxies listed in Table 4.1. Distances are measured using Surface Brightness Fluctuations when available[3] or otherwise estimated from the systemic velocity assuming $H_0 = 72 \pm 8$ km/s, (Freedman et al. 2001). All SBH masses, which are taken from the literature, have been rescaled to the new adopted distances. Galactic foreground extinctions are taken from the NED database. K-band luminosities, as derived from our images, are also given.

---

[2] 4 of the orginal 29 galaxies were already flagged by V12

[3] A constant of 0.06 mag has been subtracted from the distance moduli as given in Tonry et al. (2001) to account for the updated Cepheid distances presented in Freedman et al. (2001).

Galaxy	Hubble type	D [Mpc]	$M_\bullet$ [10^8 $M_\odot$]	$\Delta M_\bullet$ (+ / −)	L_K [10^{11} $M_\odot$]	R_e [kpc]	Ref.
(1)	(2)	(3)	(4)	(5)	(6)	(7)	(8)
CygA	E	238.0	26.5	6.4 / 6.4	13.2	19.6	2−1
IC1459	E3	28.4	24.4	2.8 / 2.8	3.71	3.98	1−2
IC4296	E	50.8	13.4	2.1 / 1.9	7.39	9.33	7−3
NGC0221	cE2	0.791	0.028	0.006 / 0.006	0.0136	0.128	1−4
NGC0821	E6	23.4	1.65	0.74 / 0.74	1.13	3.51	1−5
NGC1023	S0	11.1	0.42	0.04 / 0.04	0.944	1.92	1−6
NGC1300	SBbc	19.0	0.67	0.64 / 0.32	0.889	6.42	2−7
NGC1399	E1pec	21.2	5.1	0.7 / 0.7	3.89	5.72	8−8
NGC2748	SAbc	24.0	0.45	0.36 / 0.37	0.402	1.87	2−7
NGC2778	S0	22.3	0.129	0.1 / 0.1	0.174	1.07	1−5
NGC2787	SB(r)0	7.28	1.04	0.36 / 0.64	0.149	0.683	1−9
NGC3115	S0	9.42	8.85	2.8 / 2.8	1.03	1.63	1−10
NGC3227	SAB(s)pec	16.8	0.13	0.06 / 0.06	0.586	2.55	2−11
NGC3245	SB(s)b	20.3	2.04	0.49 / 0.49	0.691	1.54	1−12
NGC3377	E5	10.9	1.77	0.93 / 0.93	0.312	1.47	1−5
NGC3379	E1	10.3	4.0	1.0 / 1.0	0.980	2.39	1−13
NGC3384	SB(s)0-	11.3	0.106	0.048 / 0.048	0.539	1.32	1−5
NGC3608	E2	22.3	4.55	0.97 / 0.97	0.854	2.67	1−5
NGC3998	SA(r)0	13.9	2.2	2.0 / 1.6	0.534	1.18	1−14
NGC4258	SAB(s)bc	7.21	0.39	0.01 / 0.01	0.768	3.03	4−15
NGC4261	E2	30.8	5.02	1.0 / 1.0	2.39	3.00	1−16
NGC4291	E3	25.5	9.37	3.0 / 3.0	0.728	1.78	1−5
NGC4342	S0	13.3	2.7	1.5 / 1.0	0.101	0.282	2−17
NGC4374	E1	18.5	10.3	18.0 / 6.0	3.34	5.25	5−18
NGC4473	E5	15.3	0.899	0.45 / 0.45	0.734	1.58	5−5
NGC4486	E0pec	16.7	61.5	3.7 / 3.7	4.54	7.18	5−19
NGC4564	S0	15.9	0.88	0.24 / 0.24	0.369	1.05	5−5
NGC4649	E2	16.4	47.1	10.0 / 10.0	3.94	5.16	5−20
NGC4697	E6	12.5	2.02	0.51 / 0.51	1.41	3.82	1−5
NGC5252	S0	97.3	10.0	15.0 / 4.7	3.20	3.97	2−21
NGC5845	E*	25.2	4.75	1.5 / 1.5	0.359	0.534	1−5
NGC6251	E	107.0	6.0	2.0 / 2.0	7.88	9.88	2−22
NGC7052	E	67.6	3.7	2.6 / 1.5	4.80	7.60	2−23
NGC7457	SA(rs)0-	12.9	0.092	0.055 / 0.055	0.198	1.79	1−5
PGC49940	E	153.0	37.6	4.3 / 5.2	7.67	12.3	2−3

Table 4.1: BH host galaxy sample. Columns (1) and (2) give the name and Hubble type of each sample member. Distances (in Mpc) given in column (3) are based on surface brightness fluctuations (SBF) when available. Our adopted BH masses and errors are given in columns (4) and (5), which include the updated masses derived by Schulze&Gebhardt(2011). Columns (6) and (7) list galaxy luminosities and effective radii as derived from our WIRCam data via aperture photometry. Distance references in column (8, first digit) are 1: Tonry et al. (2001), 2: redshift distances (NED), 4: Herrnstein et al. (1999), 5: Mei et al. (2007), 7: Jensen et al. (2003), and 8: Blakeslee et al. (2009). For details on the distance scale homogenization, see Table 2.1. $M_\bullet$ references (second digit) are 1: Tadhunter et al. (2003); 2: Cappellari et al. (2002); 3: Dalla Bontà et al. (2009); 4: Verolme et al. (2002); 5: Schulze & Gebhardt (2011); 6: Bower et al. (2001); 7: Atkinson et al. (2005); 8: Gebhardt et al. (2007); 9: Sarzi et al. (2001); 10: Emsellem et al. (1999); 11: Davies et al. (2006); 12: Barth et al. (2001); 13: van den Bosch & de Zeeuw (2010); 14: de Francesco et al. (2006); 15: Herrnstein et al. (2005); 16: Ferrarese et al. (1996); 17: Cretton & van den Bosch (1999); 18: Bower et al. (1998), but see Maciejewski & Binney (2001) for a different estimate; 19: Gebhardt et al. (2011); 20: Shen & Gebhardt (2010); 21: Capetti et al. (2005); 22: Ferrarese & Ford (1999); 23: van der Marel & van den Bosch (1998).

4.2.2 DATA ANALYSIS AND GALAXY DECOMPOSITION

Full details of the data reduction and analysis are given in Chapter 2. All data were obtained
with WIRCam at the Canada-France-Hawaii-telescope, have subarcsecond resolution (median
$0\overset{''}{.}8$ on the final image stack, a factor of 2-3 higher than 2MASS), and signal-to-noise ratio of
S/N=1 at 24mag/arcsec^2, a factor of 40 (or 4 magnitudes) deeper than 2MASS data as well as
2 mag deeper that the UKIDSS data used in V12. Importantly also, observing strategy and data
reduction were optimized to reduce both random and systematic uncertainty in the high and
variable NIR background.

Our measurements of apparent magnitudes are based on two-dimensional (2D) image decompo-
sition performed with GALFIT3 (Peng et al. 2010). We here present an overview of the approach
we took to derive bulge and total luminosities. §2.3 discusses the details of the decomposition,
including a table of derived bulge parameters and discussion of the magnitude differences arising
from the varying complexity of the models.

In brief, we require each galaxy model to contain a "bulge" component with a Sérsic radial
surface brightness profile (Sérsic 1963). When necessary (as evidenced by large redisuals when
only a single Sérsic component is fitted), we also add a "disk" component with exponential radial
profile (equivalent to a Sérsic profile with index $n \equiv 1$). Such Sérsic bulge (+ exponential disk)
models have been applied in most previous studies, and we refer to them as "standard" models.

After fitting all images with standard models, and measuring the corresponding bulge and total
magnitudes, most (30 out of 35) galaxies showed characteristic residuals in the model-subtracted
images. While large residuals are expected for spiral galaxies, they are instead observed in *all*
galaxies with a disk component, and even in some ellipticals. This led us to perform more de-
tailed and complex fits to account for additional components (bars, nuclei, inner disks, envelopes,
spiral arms), necessary profile modifications, such as diski-/boxiness and truncations, and mask-
ing of giant ellipticals' cores. To decide whether to include additional components as well as
profile modifications in our analysis, we take a multi-prong approach, based on the radial pro-
files, the χ^2 of the fit, and a visual analysis of the residual image. To judge the model suitability,
we also routinely replace the disk's exponential by a Sérsic profile, and observe how far the best-
fit Sérsic index deviates from $n = 1$. Models should additionally be non-degenerate, converging
quickly to a best-fit (minimum-χ^2) solution that does not sensitively depend on the initial param-
eters. We refer to these more complex models (i.e. including components in addition to bulge
and disk) as "improved" models.

Luminosity	Short name	Definition
$L_{b,std}$	"standard bulge"	bulge component luminosity from a standard Sérsic-bulge(+exponential disk) model
$L_{b,min}$	"miminimal bulge"	bulge component luminosity from an improved (additional components or masked core) model
$L_{b,max}$	"maximal bulge"	total minus disk and (if present) spiral arm luminosity of the improved model
L_{sph}	**"spheroid"**	**luminosity of bulge component plus envelope (if present) in the improved model**
L_{ser}	"Sérsic"	luminosities of single-Sérsic models (all galaxies)
$L_{t,std}$	"standard total"	sum of bulge and disk luminosity of a standard model
$L_{t,imp}$	**"improved total"**	**sum of all component luminosities from an improved model**
L_{24}	"isophotal"	luminosity within aperture delimited by the 24 mag/arcsec^2-isophote
$L_{\{\cdot\}}^{(ell)}$	"ellipticals"	luminosties of elliptical galaxies

Table 4.2: Overview of luminosities used to fit the scaling relations. The method of fitting standard and improved models to the *K*-band galaxy images is presented in Section 4.2 and Chapter 2. L_{ser} is evidently not a good estimate of luminosity for all galaxies with multiple components, but has been included in the analysis to demonstrate the effect of model mismatch, expected to occur if imaging depth and resolution is insufficient to extract galaxy components.

4.2.3   BULGE AND TOTAL LUMINOSITIES

An overview of the luminosities derived by applying standard and improved decompositions is given in Table 4.2.

For all galaxies, we measure $L_{b,std}$, the luminosity of the bulge component in a "standard" bulge(+disk) model. For galaxies requiring components in addition to a bulge and disk, we derive three distinct improved bulge luminosities: the "minimal" bulge luminosity ($L_{b,min}$) is the luminosity of the improved model's bulge component alone; the "maximal" bulge luminsoity is derived by summing the flux of *all* all components *except* the disk and, if present, spiral arms. Therefore, $L_{b,min}$ constitutes a lower, and $L_{b,max}$ an upper, limit estimate for the bulge luminsosity. $L_{b,min}$ and $L_{b,max}$ sometimes differ considerably from one another, as well as from $L_{b,std}$. For several galaxies, the latter is outside of the range defined by $L_{b,min}$ and $L_{b,max}$, confirming that ignorance of additional components can significantly bias the results. The third estimate of the bulge luminosity derived by us, the "spheroid luminosity" (L_{sph}), includes the flux of the envelope component, in addition to the bulge component. As detailed in Chapter 2, interpretation of the envelope is not straightforward, but it most likely represents part of the *spheroidal* stellar distribution, which is not well fit by a single 2D-Sérsic profile. This of course applies only to galaxies in which such an envelope is identified and required to obtain a suitable fit; for all other targets, $L_{sph} = L_{b,min}$.

Combining the luminosities of all components provides the total luminosity, $L_{\text{t,std}}$ and $L_{\text{t,imp}}$, of standard and improved model. Naturally, for elliptical galaxies (fit by a single Sérsic profile), the total equals the bulge luminosity. If a core is present, we mask it to obtain $L_{\text{t,imp}}$; for all other ellipticals, also $L_{\text{t,imp}} = L_{\text{t,std}}$. In addition, we derive a non-parametric total luminosity from aperture photometry. The resulting isophotal luminosity, L_{24}, accounts for the flux inside R_{24}, the radius at which the surface brightness of circular annuli drops below 24 mag/arcsec^2. Differences between $L_{\text{t,std}}$, $L_{\text{t,imp}}$ and L_{24} are relatively small compared to the variance between bulge luminsosities.

We retain luminosities resulting from standard models, even when such models are clearly inadequate, to investigate the impact that the modeling complexity has on the BH scaling relations, and to provide relations for estimating BH masses in situations where the detailed decompositions are not feasible. Naturally, in galaxies where a bulge(+disk) model suffices and no core is present (in our sample, 1 lenticular and 8 elliptical galaxies), we adopt the standard model luminosity throughout. All luminosities are given in units of solar luminosity and have been converted from the absolute magnitudes given in Table 2.3, using the absolute K-band magnitude of the Sun [4], $M_{K,\odot} = 3.28$.

4.3   RESULTING SCALING RELATIONS

We derived bulge K-band luminosities, $L_{\text{bul}} = \{L_{\text{b,std}}, L_{\text{b,min}}, L_{\text{b,max}}, L_{\text{sph}}\}$, and total K-band luminosities, $L_{\text{tot}} = \{L_{\text{t,std}}, L_{\text{t,imp}}, L_{24}\}$. As described briefly in Section 4.2 and explicitly in Chapter 2, their values are obtained either via fitting bulge(+disk) components only ("standard" models: $L_{\text{b,std}}$ and $L_{\text{t,std}}$), or allowing for additional components and modifications ("improved" models: $L_{\text{b,min}}$, $L_{\text{b,max}}$, L_{sph} and $L_{\text{t,imp}}$). By contrast, L_{24} is a parameter-free measurement of total luminosity. A summary of the definitions of luminosity we have applied is given in Table 4.2.

We plot the luminosities, $\tilde{L}_{\{\cdot\}} = \log\left(L_{\{\cdot\}}/L_\odot\right)$ (see Table 4.3) for all sample galaxies against BH mass, $\tilde{M}_\bullet \equiv \log\left(M_\bullet/M_\odot\right)$, and fit a correlation with a ridgeline

$$\tilde{M}_\bullet = a + b(\tilde{L}_{\{\cdot\}} - 11) , \tag{4.1}$$

including Gaussian[5] intrinsic scatter $\epsilon_\bullet$ in the direction of $\tilde{M}_\bullet$ (y-axis) and $\epsilon_\perp$ in the direction perpendicular to the ridgeline. We choose to pivot all relations around $L = 10^{11} L_\odot$ since this value is approximately equal to the mean luminosity, reducing the covariance between a and b. In the remainder of this section, we yllanoitidda use the notation $\epsilon \equiv \epsilon_\bullet$, as opposed to $\epsilon_\perp$,

---

[4]as taken from: http://www.ucolick.org/ cnaw/sun.html
[5]this chioce of distribution is justified in Gültekin et al. (2009)

Galaxy	class.	log $M_\bullet$	$L_{t,2M}$	L_{24}	L_{ser}	$L_{t,std}$	$L_{t,imp}$	$L_{b,std}$	$L_{b,min}$	$L_{b,max}$	L_{sph}	L_{MH03}
CygA	1	9.42 ± 0.11	11.95	12.12	12.10	12.10	**12.10**	12.10	12.10	12.10	**12.10**	12.22
IC1459	1	9.39 ± 0.05	11.50	11.57	11.65	11.65	**11.71**	11.65	11.71	11.71	**11.71**	11.65
IC4296	1	9.13 ± 0.06	11.72	11.87	11.87	11.87	**12.05**	11.87	12.05	12.05	**12.05**	–
NGC0221	1	6.45 ± 0.09	9.07	9.13	9.10	9.10	**9.10**	9.10	9.10	9.10	**9.10**	9.22
NGC0821	2	8.22 ± 0.21	10.89	11.05	11.10	11.11	**11.01**	11.11	10.29	10.99	**10.99**	11.21
NGC1023	2	7.62 ± 0.04	10.91	10.98	11.06	10.97	**10.97**	10.65	10.48	10.59	**10.48**	10.69
NGC1300	3	7.83 ± 0.29	10.84	10.95	10.74	10.95	**10.97**	9.92	10.05	10.38	**10.05**	–
NGC1399	1	8.71 ± 0.06	11.44	11.59	11.59	11.59	**11.80**	11.59	11.80	11.80	**11.80**	–
NGC2748	3	7.65 ± 0.50	10.58	10.60	10.67	10.61	**10.61**	10.04	10.15	10.15	**10.15**	–
NGC2778	2	7.11 ± 0.46	10.20	10.24	10.43	10.24	**10.24**	9.94	9.83	9.85	**9.83**	10.49
NGC2787	2	8.02 ± 0.27	10.13	10.17	10.22	10.16	**10.17**	9.73	9.98	10.05	**9.98**	9.81
NGC3115	2	8.95 ± 0.14	10.91	11.01	11.04	11.08	**11.01**	11.05	10.09	10.93	**10.93**	11.05
NGC3227	3	7.11 ± 0.22	10.71	10.77	11.22	10.76	**10.76**	10.15	9.95	10.12	**9.95**	–
NGC3245	2	8.31 ± 0.11	10.78	10.84	10.99	10.82	**10.83**	10.35	10.13	10.35	**10.13**	10.61
NGC3377	2	8.25 ± 0.25	10.41	10.49	10.65	10.55	**10.50**	10.54	10.05	10.39	**10.38**	10.73
NGC3379	1	8.60 ± 0.11	10.83	10.99	11.03	11.03	**11.13**	11.03	11.13	11.13	**11.13**	10.97
NGC3384	2	7.03 ± 0.21	10.72	10.73	10.72	10.75	**10.73**	10.38	10.18	10.45	**10.18**	10.33
NGC3608	1	8.66 ± 0.09	10.77	10.93	11.05	11.05	**11.05**	11.05	11.05	11.05	**11.05**	10.93
NGC3998	2	8.34 ± 0.42	10.65	10.73	10.72	10.68	**10.67**	10.40	9.94	10.34	**9.94**	–
NGC4258	3	7.59 ± 0.01	10.84	10.89	11.09	10.93	**10.90**	10.52	9.33	9.96	**9.33**	10.27
NGC4261	1	8.70 ± 0.09	11.38	11.38	11.51	11.51	**11.63**	11.51	11.63	11.63	**11.63**	11.53
NGC4291	1	8.97 ± 0.14	10.76	10.86	10.89	10.89	**10.94**	10.89	10.94	10.94	**10.94**	10.85
NGC4342	2	8.43 ± 0.20	9.95	10.00	9.93	9.97	**9.98**	9.68	9.47	9.65	**9.65**	9.73
NGC4374	1	9.01 ± 0.41	11.36	11.52	11.59	11.59	**11.69**	11.59	11.69	11.69	**11.69**	11.60
NGC4473	1	7.95 ± 0.24	10.82	10.87	10.89	10.89	**10.89**	10.89	10.89	10.89	**10.89**	10.81
NGC4486	1	9.79 ± 0.03	11.43	11.66	11.57	11.57	**11.75**	11.57	11.75	11.75	**11.75**	11.58
NGC4564	2	7.94 ± 0.12	10.54	10.57	10.60	10.58	**10.58**	10.43	10.43	10.43	**10.43**	10.72
NGC4649	1	9.67 ± 0.10	11.45	11.60	11.53	11.53	**11.67**	11.53	11.67	11.67	**11.67**	11.61
NGC4697	2	8.31 ± 0.11	10.96	11.15	11.27	11.28	**11.19**	11.27	10.08	11.15	**11.14**	11.21
NGC5252	2	9.00 ± 0.34	11.38	11.50	11.63	11.38	**11.54**	10.89	11.39	11.48	**11.39**	11.56
NGC5845	2	8.68 ± 0.14	10.47	10.55	10.48	10.48	**10.48**	10.48	10.48	10.48	**10.48**	10.49
NGC6251	1	8.78 ± 0.15	11.76	11.90	11.90	11.90	**11.90**	11.90	11.90	11.90	**11.90**	11.95
NGC7052	1	8.57 ± 0.23	11.54	11.68	11.67	11.67	**11.67**	11.67	11.67	11.67	**11.67**	11.70
NGC7457	2	6.96 ± 0.30	10.26	10.30	10.63	10.35	**10.29**	10.05	9.15	9.60	**9.15**	10.01
PGC49940	1	9.58 ± 0.06	11.69	11.88	11.88	11.88	**11.88**	11.88	11.88	11.88	**11.88**	–

Table 4.3: Summary of bulge and total luminosities, expressed as $\log(L/L_\odot)$, alongside logarithmic BH masses (with error bars symmetrized) and our galaxy classification (1: elliptical, 2: lenticular, 3: spiral galaxy), to be used directly towards plots shown in Figures 4.1-4.3. Printed in boldface are the bulge and total luminosities used in our adopted scaling relations. All luminosities have been derived from our WIRCam data, except for $L_{t,2M}$ (total luminosity derived from the 2MASS database) and L_{MH03} (derived from bulge magnitudes given in MH03), both of which corrected for our distances. Aside from L_{24}, all luminosities are based on GALFIT models (see §4.2.2). For a summary of the definitions used to derive luminosities in our study, see Table 4.2 and Chapter 2.

	Luminosity	a_0	Δa	b_0	Δb	$\epsilon_{\bullet,0}$	$\Delta\epsilon_\bullet$	$\epsilon_{\perp,0}$	$\sigma(\epsilon_\perp)$	r
	(1)	(2)	(3)	(4)	(5)	(6)	(7)	(8)	(9)	(10)
(1)	$L_{b,std}$	8.508	±0.090	0.875	±0.120	0.463	+0.093/ − 0.042	0.348	0.043	0.794
(2)	$L_{b,min}$	8.598	±0.093	0.723	±0.098	0.460	+0.093/ − 0.041	0.373	0.044	0.800
(3)	$L_{b,max}$	8.489	±0.084	0.856	±0.104	0.424	+0.087/ − 0.039	0.322	0.043	0.833
(4)	$\mathbf{L_{sph}}$	**8.566**	**±0.084**	**0.773**	**±0.093**	**0.421**	**+0.083/ − 0.039**	**0.333**	**0.034**	**0.833**
(5)	L_{ser}	8.328	±0.106	0.920	±0.170	0.555	+0.111/ − 0.049	0.408	0.061	0.698
(6)	$L_{t,std}$	8.365	±0.097	0.975	±0.154	0.508	+0.101/ − 0.045	0.364	0.048	0.754
(7)	$\mathbf{L_{t,imp}}$	**8.339**	**±0.095**	**0.946**	**±0.141**	**0.490**	**+0.098/ − 0.044**	**0.356**	**0.046**	**0.772**
(8)	L_{24}	8.378	±0.095	0.995	±0.151	0.495	+0.099/ − 0.044	0.351	0.046	0.766
(9)	$L_{std}^{(ell)}$	8.501	±0.132	0.971	±0.169	0.392	+0.142/ − 0.039	0.281	0.053	0.850
(10)	$L_{imp}^{(ell)}$	8.438	±0.132	0.952	±0.157	0.380	+0.131/ − 0.038	0.275	0.045	0.862
(11)	$L_{24}^{(ell)}$	8.515	±0.126	0.977	±0.162	0.377	+0.134/ − 0.038	0.270	0.046	0.858

Table 4.4: Scaling relations resulting from our WIRCam data and 2D-image analysis by fitting eqn. (4.1). Column (1) indicates the type of luminosity correlated with $M_\bullet$ (see Table 4.2). Columns (2), (4), and (6) contain the best-fit parameter values $(a, b, \epsilon_\bullet)_0$ of each relation, as derived via the maximum-likelihood method. Columns (3), (5) and (7) give relative location of the central 68%("1-σ")-confidence interval, as derived from the posterior probability distribution. Column (8) gives the orthogonal intrinsic scatter, calculated from b and $\epsilon_\bullet$, and column (9) the standard deviation of its probability distribution as obtained via bootstrap resampling. Finally, column (10) indicates each relation's Pearson correlation coefficient. For more details about the fitting method, please see appendix 4.A. Note that the confidence interval of $\epsilon_\bullet$ is asymmetric with respect to the best-fit value because (i) after marginalizing the 3D-distribution over a and b, $\epsilon_\bullet$ closely follows a lognormal distribution, i.e. the median (and mean) are larger than the maximum, which is (ii) itself larger than $\epsilon_{\bullet,0}$ due to positive correlation of $\epsilon_\bullet$ with $|a − a_0|$ and $|b − b_0|$.

the intrinsic scatter perpendicular to the relation's ridge line. We also introduce the shorthand notation $\{p\}_{\{\cdot\}}^{(ell)}$, where $p \in \{a, b, \epsilon\}$ may be any of the model parameters, the subscript $\{\cdot\}$ indicates the type luminosity measurement used, and (ell) the restriction to elliptical galaxies in fitting the relation.

The parameter estimates are performed by calculating the three-dimensional posterior probability distribution of the parameters (a, b, ϵ) on a dense grid. The maximum of the likelihood function corresponds to the adopted parameters, while the quoted uncertainties correspond to the central 68%-confidence interval of the marginalized distributions. We supplement our statistical analysis by estimates from bootstrap-resampling and find the results to be consistent. For more details on the choice of the fitting method, and the treatment of uncertainty in the data, please see Appendix 4.A. A selection of all fitted scaling relations is given in Table 4.4.
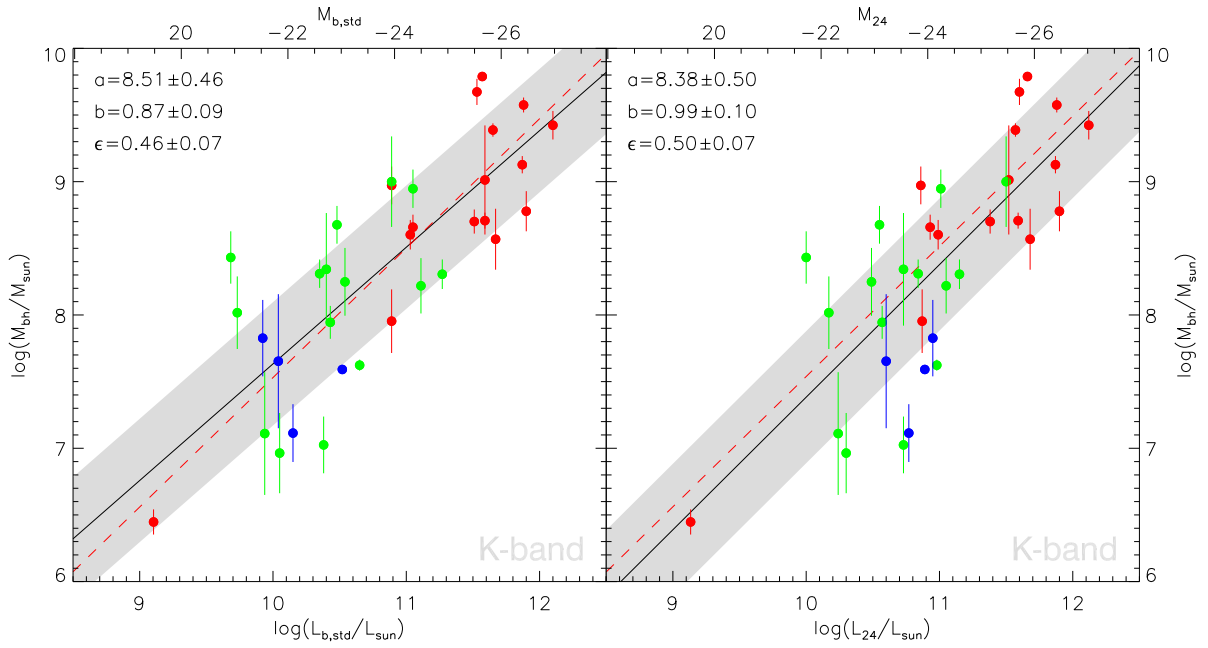
Figure 4.1: Correlations of $M_\bullet$ with "standard" bulge ($L_{b,std}$, left panel) and paremeter-free total (L_{24}, right panel) luminosity. The filled circles correspond to elliptical (red), S0 (green) and spiral (blue) galaxies. Vertical solid bars indicate the 1σ-uncertainties in $M_\bullet$. The black solid lines are the corresponding best-fit linear relations of the form $\log M_\bullet = a + b \log L$. The shaded area has a width of $2\epsilon_\bullet$ in the direction of $M_\bullet$. As expected, the best-fit slope b is steeper for total luminosities. Crucially, the intrinsic scatter ϵ of both relations is consistent. The red dashed lines are the relations of elliptical galaxies only (see §3.1).

4.3.1   BULGE VERSUS TOTAL LUMINOSITY

Comparing the correlations of $M_\bullet$ with L_{bul} and L_{tot} in the K-band, we find that

1. **bulge and total luminosities lead to similarly tight correlations with comparable intrinsic scatter,**

2. **the slope of the $M_\bullet - L_{bul}$ relation is significantly < 1, while the $M_\bullet - L_{tot}$ relation is consistent with being linear, and**

3. **the characterization of $M_\bullet - L_{tot}$ is more robust with respect to the photometric method.**

These results hold for all our applied methods of luminosity measurement (standard, improved, isophotal). Our findings are quantified in Table 4.4, as well as the tables in Appendix 4.B. We illustrate (i) and (ii) in Figure 4.1 using $L_{b,std}$ and L_{24}, as these represent the simplest available estimates of bulge and total luminosity, respectively. Figure 4.2 demonstrates (iii), i.e. the dependency of $M_\bullet - L_{bul}$ on modeling complexity and potential ambiguities inherent in the bulge photometry.

More specifically, the intrinsic scatter $\epsilon_{b,std} = 0.46^{+0.09}_{-0.04}$ (bulge luminosities from standard decomposition) is virtually identical to $\epsilon_{b,min}$ (improved decompositions), despite the improved decompositions used in deriving the latter, the presumed increase in photometric accuracy, and the often large differences in resulting bulge luminosity (cf. Chapter 2). ϵ decreases by 0.04 dex when envelopes are included in the improved bulge luminosity (L_{sph}), or when using $L_{b,max}$ (inclusion of all components other than disk and spiral arms), although this change is well within the parameter uncertainty. If total magnitudes are used, likewise all estimates lead to $\epsilon_{tot} \approx 0.5$, again consistent with $\epsilon_{b,std}$. In other words, no matter whether bulge or total magnitudes are used, and regardless of the specifics of the decomposition or photometric analysis, *all* ϵ agree at the 68%-confidence level. The same applies when one considers $\epsilon_\perp$, the scatter perpendicular to the ridge line (see Table 4.9). Both $\epsilon_\bullet$ and $\epsilon_\perp$ decrease when the fit is restricted to elliptical galaxies, but the difference is significant only for $\epsilon_\perp$, not $\epsilon_\bullet$.

When using total luminosity, all $M_\bullet - L_{tot}$ relations agree closely in slope, b_{tot}, irrespective of the method used to obtain L_{tot}. However, the slopes of the improved $M_\bullet - L_{bul}$ relations, $b_{b,min}$ and $(b)_{sph}$, are smaller than b_{tot} at the 1σ-confidence level. This is to be expected: while the high mass end is dominated by elliptical (i.e. pure bulge) galaxies, bulges comprise only a fraction of the total luminosity in the (on average less luminous) lenticular and spiral galaxies. b_{bul} increases when maximum bulge magnitudes or standard decompositions are used, such that $b_{b,max}$ and $b_{b,std}$ are consistent with b_{tot} and $b^{(ell)}$.
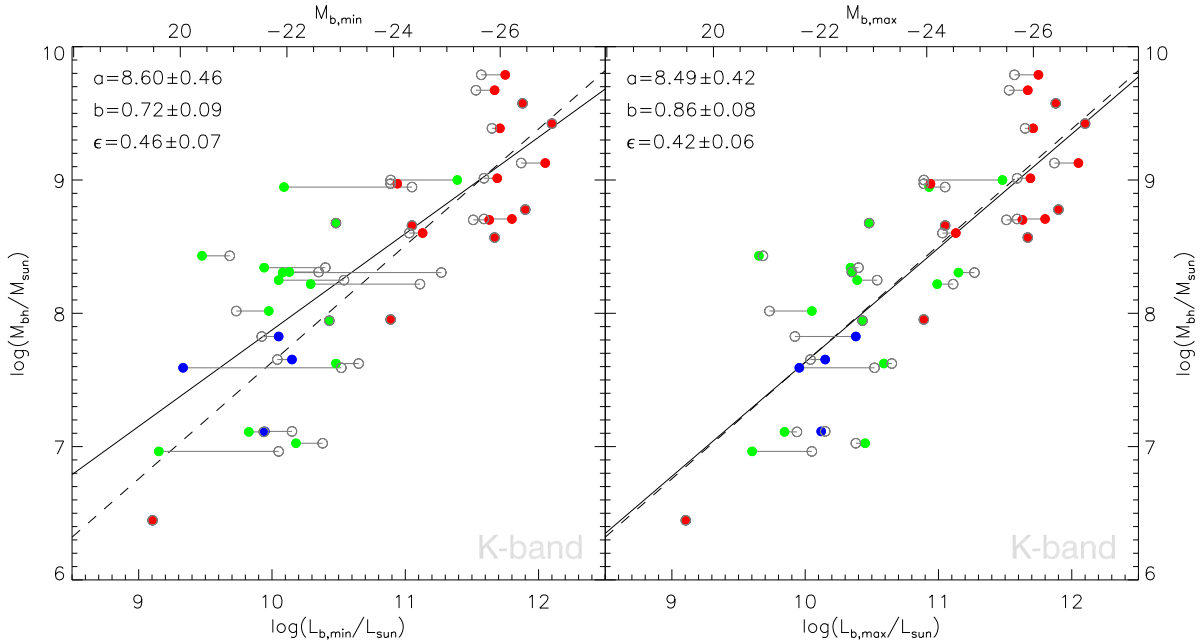
Figure 4.2: Correlations of $M_\bullet$ with improved models' minimal ($L_{b,min}$, left panel) and maximal ($L_{b,max}$, right panel) bulge luminosities. Filled circles, error bars and black solid lines are defined analogous to Figure 4.1. Overplotted in grey are the standard bulge values (open circles) and the dashed line for the corresponding $M_\bullet - L_{b,std}$-relation. Error bars in $M_\bullet$ have been omitted for clarity, but are the same as in Fig. 4.1. Remarkably, the $M_\bullet - L_{b,max}$-relation is practically identical to $M_\bullet - L_{b,std}$. Both panels also illustrate the changes in bulge luminosity as a consequence of applying detailed decompositions. Notably, some $L_{b,min}$ are *larger* than $L_{b,std}$, despite the additional components, and some $L_{b,max}$ *smaller* than $L_{b,std}$ of the same galaxy, despite comprising more than one component of the model. One also sees the effect of cores in elliptical galaxies (red circles), which are masked when obtaining $L_{b,min}$ and $L_{b,max}$.

The fits of the $M_\bullet - L_{tot}$ relation remain virtually unchanged whether all galaxies, or only ellipticals are fitted (except for the mild decrease in ϵ_{tot} as noted above). Consequently, the slope of the $M_\bullet - L_{bul}$ relation, when fitted to the entire sample, is also systematically smaller (at the 1σ-confidence level) than the slope fitted to the sample of ellipticals only, $\epsilon^{(ell)}$. Yet, we caution that $\epsilon^{(ell)}$ is very sensitive to the presence and parameters of NGC221 (M32), the only elliptical with $L \lesssim 10^{11}\,L_\odot$ and $M_\bullet \lesssim 10^8\,M_\odot$ in our sample. Therefore, the evidence for the slope of the $M_\bullet - L_{bul}$ relation being sensitive to the Hubble type of the host is tentative and we do not want to emphasize it.

4.3.2   THE ADOPTED SCALING RELATIONS

Our recommendation is to use $M_\bullet - L_{bul}$ scaling relations based on "improved model" fits to the K-band images. The rationale for introducing galaxy image models that improve on the "standard" bulge(+disk) configuration are described in Chapter 2. In short, they are warranted by considerable and characteristic mismatches between data and standard models, with residuals usually resembling bars, galactic nuclei (AGN or clusters), inner disks and spiral arms. These components are often easily identified visually on the science image. They are known to be morphologically and kinematically distinct from the spheroidal ("hot") stellar component and should therefore be excluded when characterizing the properties of the latter. Such considerations do not apply to elliptical galaxies, although we note that masking the cores in core-Sérsic galaxies (e.g. Ferrarese et al. 2006) improves the luminosity estimate, eliminating the bias induced by the Sérsic profile's mismatch in the central region.

As for which estimate of the bulge luminosity to use, our preference is for L_{sph}, the luminosity of the bulge component plus, when present, an additional spheroidal envelope, for the following reasons. $L_{b,max}$ does not measure the luminosity of the bulge/spheroidal component, but of all components exscept the disk and spiral arms. It therefore marks an upper limit for L_{bul} and was introduced primarily to compare results from standard and improved models. $L_{b,max}$ *would* be the "proper" luminosity only *if* one assumed that the extra components are not separate entities but are instead part of the bulge. By contrast, $L_{b,min}$ is the luminosity of the central component with Sérsic profile ($n > 1$) and higher axis ratio than the disk(s), and therefore corresponds to the commonly adopted photometric definition of "*bulge*". As described in Chapter 2), for five of our galaxies this definition probably does not describe the *spheroidal* ("hot") stellar component entirely. Instead, an "envelope" component is required for suitable image modeling and should be added to $L_{b,min}$ in order to measure the luminosity of the spheroid, L_{sph}. Interpreting the term "bulge" in the sense of "spheroid" rather than the photometric definition above, we adopt the correlation of $M_\bullet$ with L_{sph}, rather than $L_{b,min}$, as the best available characterization of $M_\bullet - L_{bul}$. We note that accounting for the envelope can increase the bulge-to-total ratio from ~ 0.1 to almost ~ 0.9, depending on the galaxy. Even if this affects only 5 galaxies, the characterization of the scaling relation is affected (compare lines 2 and 4, Table 4.4). However, the change is within the parameter uncertainties.

When using total luminosity, we also prefer values derived from improved models, for the same reasons given above, although we note that correlations with total luminosities from standard models and aperture photometry lead to virtually identical correlation parameters. The K-band $M_\bullet - L_{sph}$ and $M_\bullet - L_{t,imp}$-relations are highlighted in Tables 4.2, 4.4 and 4.6, and plotted in Figure 4.3.

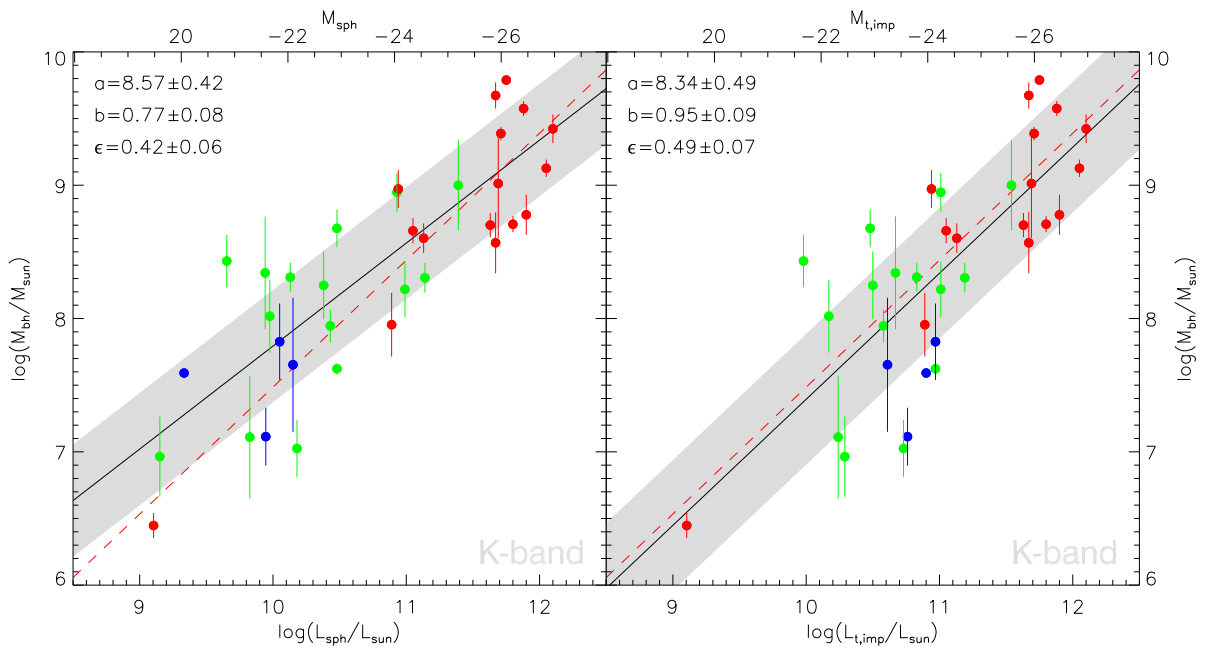**Figure 4.3:** Our adopted correlations of $M_\bullet$ with bulge/spheroid (L_{sph}, left panel) and total ($L_{t,imp}$, right panel) luminosity. Filled coloured circles, error bars and lines are defined analogous to Figure 4.1. The respective intrinsic scatter is indicated by the shaded area, which has a width of $2\epsilon_\bullet$ in the direction of $M_\bullet$. Note the similarity in both relations' width, as well as the similarity between the slopes of $M_\bullet - L_{t,imp}$ and the fit to ellipticals only, $M_\bullet - L_{imp}^{(ell)}$ (red dashed line in both panels).

4.3.3   Comparison with previous studies

In Table 4.5, we compare our results with those from previous studies that investigated the *K*-band $M_\bullet - L_{\text{bul}}$ scaling relation. We also include the relation of Sani et al. (2011) [S11 hereafter] in the 3.6μm-band.

Our zero-point ($a = 8.57 \pm 0.08$) is consistent with the value measured by V12, but is higher than that of MH03 and, in particular, Graham (2007) [G07 hereafter], who re-fitted MH03 data after revising a number of $M_\bullet$ and distance values, and removing five galaxies with respect to the MH03 sample of reliable $M_\bullet$ measurements. Both MH03 and G07 used 2MASS data, which is inferior, both in spatial resolution and depth, to our data or the UKIDSS data used by V12. In Chapter 4, we showed that this typically leads to overestimated bulge luminosities, and speculate that this may explain the lower zero-point resulting from 2MASS data.

Our slope, $b = 0.77 \pm 0.09$, is shallower than found in all previous studies. The difference is above the 1σ-level, and again the smallest difference is found with respect to the V12 estimate. The comparison suggests a general trend towards lower slope with increasing data quality and decomposition complexity. G07 obtains a lower slope than MH03, presumably in part a result of separating[6] the disk from the bulge in three galaxies to which M03 applied a single Sérsic profile. In contrast to MH03 and G07, the resolution and depth of the data allowed S11 and V12 to also model nuclei and bars, and they find a (slightly) lower slope than G07. V12 also accounted for cores, and their result yields $b < 1$ at the 1σ-confidence level. Our slope is shallower still, possibly due to further improved bulge photometry, which typically reduces the luminosity estimate at the lower-mass end (predominantly late Hubble type) and increases it for some Ellipticals.

We note that the choice of fitting method also plays a role, as expected (e.g., Novak et al. 2006): When fitting the *same* data (L_K *and* $M_\bullet$) as used by MH03 (their Table 1) with our likelihood method[7] (lines 2 and 4 of Table 4.5), the resulting slopes are shallower than the relation reported by MH03 (bisector estimator of Akritas & Bershady 1996lines 1 and 3), although they are still significantly steeper than the relations we derived in the present study.

As for the scatter, we again are in agreement with the result V12, deriving a larger ϵ than either MH03 (for their "group 1" sample) or G07, despite using improved data and decompositions. The scatter derived by S11 using 3.6 μm data also agrees more closely with ours, although it is important to keep in mind that both S11 and V12 use samples and sample selection criteria that are different from one another and from our study. S11 exclude pseudobulges identified based on the bulge's location in the fundamental plane and its Sérsic index, which may be highly uncertain

---

[6]by employing other (optical) data

[7]for consistency, we choose not to incorporate uncertainties in *L*, see §4.A.4

and subject to the modeling complexity (see Chapter 2). V12 exclude barred galaxies and an outlier, NGC4342. Irrespective of the suitability of the applied criteria to identify pseudobulges / barred galaxies, and the astrophysical justification to exclude such objects from the analysis, these sample restrictions are expected to decrease the scatter, since by construction they do not apply to elliptical galaxies, and (presumably) only rarely to early-type lenticulars. That is, they tend to bias the sample towards early-type and luminous galaxies, for which numerous studies (including ours) find a slightly decreased scatter. Indeed, V12 find a significantly higher scatter ($0.52^{+0.10}_{-0.06}$ instead of $0.40^{+0.09}_{-0.06}$) when analyzing their full sample of reliable $M_\bullet$ (line 5 in Table 4.5), higher than the scatter of our adopted $M_\bullet - L_{\mathrm{sph}}$ relation ($0.42^{+0.08}_{-0.04}$).

We investigate the effects of the decomposition method on the relation parameters, separately from variance due to the used sample of $M_\bullet$, by fitting relations to the intersection of MH03's full galaxy sample with ours $M_\bullet$ (lines 9-12 in table 4.5). Using the same data as MH03, restriction of the sample leaves the slope unchanged, but increases a and ϵ decreases by an amount comparable to their respective uncertainties (compare line 9 to line 2). We next replace the $M_\bullet$ that MH03 used with our updated values, and find little effect on b and ϵ, but a significantly increased zero-point (line 10). If we retain the $M_\bullet$ used by MH03, but replace the MH03 luminosities with our improved L_{sph} (line 11), the zero point also increases, but not quite as much. Simultaneously, b and ϵ respectively decrease by 0.11 and 0.04 dex, which parallels the change we observed upon replacing standard bulge luminosities ($L_{\mathrm{b,std}}$) with L_{sph} while fitting to our (full) sample. Using both improved L_{sph} and updated $M_\bullet$ (line 12, compared to line 9) combines the above effects (increased a, decreased b, slightly decreased ϵ) and leads to a best-fit relation that is in close agreement with our adopted relation (full sample, line 13). Therefore, the above analysis confirms that improved decompositions are the dominant driver towards a lower slope, and shows that the updated $M_\bullet$ estimates are main (but not sole) cause for the higher zero-point with respect to the $M_\bullet - L_{\mathrm{bul}}$ relation derived by MH03. Meanwhile, the intrinsic scatter appears to be primarily effected by sample selection and decreases only slighly due to improved bulge luminosity estimates.

4.4 DISCUSSION

4.4.1 THE THEORIST'S QUESTION[8]

Our analysis suggests that $M_\bullet$ is equally tightly correlated with L_{bul} as with L_{tot}, as measured by the intrinsic scatter in $M_\bullet$: $\epsilon_{\mathrm{bul}} = 0.42^{+0.08}_{-0.04}$ and $\epsilon_{\mathrm{tot}} = 0.49^{+0.10}_{-0.04}$ (compare lines 4 and 7 of Table 4.4). If the scatter orthogonal to the ridge line of the relation is considered, difference is even smaller

---

[8]we use the apt terminology used by Novak et al. (2006) here and in the next subsection

	ref. (1)	imaging (2)	sample (3)	N (4)	fit (5)	a (6)	Δa (7)	b (8)	Δb (9)	$\epsilon_\bullet$ (10)	$\Delta\epsilon_\bullet$ (+/−) (11)	remarks (12)
(1)	MH03	2MASS K	all	37	AB96	8.20	0.10	1.21	0.13	0.51	–	
(2)	–	2MASS K	all	37	like	8.15	0.10	0.91	0.15	0.53	0.10/0.05	$M_\bullet$, L as in MH03
(3)	MH03	2MASS K	rel	27	AB96	8.32	0.07	1.13	0.12	0.31	–	only secure $M_\bullet$
(4)	–	2MASS K	rel	27	like	8.30	0.08	1.03	0.11	0.33	0.09/0.03	$M_\bullet$, L as in MH03
(5)	G07	2MASS K	rel	22	T02	8.17	0.08	0.93	0.10	0.30	0.03/0.05[*]	5 galaxies removed[†]
(6)	S11	IRAC 3.6μm	res	48	like[‡]	8.19	0.06	0.93	0.10	0.38	0.05	no pseudobulges
(7)	V12	UKIDSS K	all	25	T02	8.38	0.20[§]	0.88	0.06	0.52	0.10/0.06	
(8)	V12	UKIDSS K	res	19	T02	8.71	0.25	0.90	0.08	0.40	0.09/0.06	no N4342,M87,barred[¶]
(9)	–	2MASS K	∩	28	like	8.29	0.10	0.91	0.14	0.45	0.11/0.04	$M_\bullet$, L from MH03[‖]
(10)	–	2MASS K	∩	28	like	8.47	0.10	0.89	0.15	0.48	0.11/0.05	L from MH03[‖]
(11)	–	WIRCam K	∩	28	like	8.39	0.09	0.80	0.11	0.41	0.10/0.04	$M_\bullet$ from MH03[‖]
(12)	–	WIRCam K	∩	28	like	8.60	0.10	0.78	0.11	0.43	0.10/0.04	
(13)	**–**	**WIRCam K**	**all**	**35**	**like**	**8.57**	**0.08**	**0.77**	**0.09**	**0.42**	**0.08/0.04**	

[*]probably upper and lower error bar are confused in Table 4 of G07 (V12 and this work find the upper error on ϵ to be larger than the lower error bar)

[†]with respect to MH03's sample of reliable $M_\bullet$; for details about the removals as well as applied updates of some $M_\bullet$, L_{bul} and distances, see G07

[‡]LINMIX_ERR (Kelly 2007) as stated in S11

[§]the larger error in a is a result of correlation with b, in turn due to V12's choice of magnitude offset (−18 mag instead of the magnitude mean)

[¶]NGC4342 has been removed because it was deemed an outlier of the $M_\bullet - L_{bul}$ relation, M87 because of poor image (sky background) quality, and barred galaxies as identified in V12

[‖]values rescaled to our adopted distances

Table 4.5: Comparison of $M_\bullet - L_{bul}$ relations from previous studies with our results (boldface). Column (1) gives the source of the fit results, where MH03: Marconi & Hunt (2003); G07: Graham (2007); S11: Sani et al. (2011); V12: Vika et al. (2012); and "-": this work. The imaging data used to derive the luminosities are listed in column (2). Column (3) indicates if a subsample was used in acquiring the fit ("all": the full sample of $M_\bullet$ considered in the respective publication; "rel": subsample of reliable $M_\bullet$ estimates as indicated by the authors; "res": sample restricted based on criteria not related to the reliability of $M_\bullet$; "∩ MH03": intersection of our sample of reliable $M_\bullet$ and MH03's full sample), and column (4) the resulting sample size. Column (5) indicates the method used in acquiring the parameter estimates, where the entries are "AB96": BCES algorithm of Akritas & Bershady (1996); "T02": modified FITEXY routine introduced by Tremaine et al. (2002), with errors on $\epsilon_\bullet$ obtained by setting $\chi_\nu^2 = 1 \pm \sqrt{2/N}$; and "like": maximum-likelihood / Bayesian analysis, whereas we set uncertainties $\Delta L = 0$ as discussed in §4.A.4. Columns (6)-(11) present the correlation parameters and 1σ-uncertainties, with values from the literature converted to our convention, $\log M_\bullet = a + b \log(L/10^{11} L_\odot)$, if necessary. Column (12) supplements information on the data set on which the fit was based. If not stated otherwise, $M_\bullet$ and L are the values used by the source given in column (1). The bulge luminosities from this work (last three lines) are our adopted L_{sph}.

($\approx 0.4\sigma$). This result challenges the commonly held view, supported by previous investigations of local BH scaling relations (e.g., Kormendy & Gebhardt 2001; Beifiori et al. 2012). These were albeit performed at optical wavelengths, while ours is the first work to address the issue at NIR wavelengths. It appears therefore plausible that the previously documented larger scatter of the $M_\bullet - L_{tot}$ relation is, at least in part, a consequence of dust obscuration and the presumed higher scatter in optical mass-to-light ratios, especially for disks.

The connection between $M_\bullet$ and total stellar mass, $M_{\star,tot}$ (and implicitly its surrogate, L_{tot}), has been the subject of studies investigating BH scaling relations for active galaxies and their evolution with redshift (e.g. Peng 2007; Kim et al. 2008; Jahnke et al. 2009; Merloni et al. 2010; Bennert et al. 2011; Cisternas et al. 2011). Our result provides a local baseline for these. It further seems to support the idea that BH growth may be linked with the overall potential of the host (as in Ferrarese 2002; Volonteri et al. 2011), traced by its total NIR luminosity (stellar mass). This is also in line with the evidence that, at fixed radiative efficiency, the integrated accretion history of BHs, as traced by active galactic nuclei, parallels the full star formation history of BH host galaxies (e.g., Shankar et al. 2009b). A $M_\bullet - M_{\star,tot}$ relation with scatter similar to that of $M_\bullet - M_{\star,bul}$ is also predicted by the merger-driven models of Jahnke & Macciò (2011). Yet, if repeated sequences of galaxy mergers have characterized the growth of spheroids and disks, and have been strictly accompanied by mergers of their central BHs, the expected relations should become thighter for elliptical (and more massive) galaxies, while we observe only a modest decrease. We emphasize that firm conclusions regarding the relation for elliptical galaxies cannot be made at present, due to the limited size and mass range of the elliptical galaxy sample.

It is of course also not ruled out that in the future, when smaller parameter uncertainties (larger samples, more precise data) are in reach, a difference between ϵ_{bul} and ϵ_{tot} will be established with statistical significance, and that a clearer distinction between further relations specific to galaxy morphological type can be made. Yet, with the current evidence at hand, we suggest that the $M_\bullet - L_{tot}$ relation should be used as an additional constraint in models of BH-galaxy co-evolution.

Our results for the correlation slope and offset may also modify current understanding of the connection between BH and host galaxy. The slope we obtain for (the logarithm of) the $M_\bullet - L_{bul}$ relation excludes a proportionality between $M_\bullet$ and bulge stellar mass, $M_{\star,bul}$, with high confidence. Assuming that the K-band stellar mass-to-light ratio, $M_\star/L_K$, is positively correlated with L_K *on average*, the log-slope of the $M_\bullet - M_{\star,bul}$ relation is even lower than b_{bul}, which is already < 1 with $\gtrsim 99\%$ confidence according to our study. Combining our $M_\bullet - L_{bul}$ relation with, for example, $\log M_\star \propto (1.12 \pm 0.02) \times \log L_K$ (Zhu et al. 2010), a simple estimate yields $\log M_\bullet \propto (0.70 \pm 0.07) \log M_{\star,bul}$. That is, the $M_\bullet/M_{\star,bul}$-ratio *decreases* with host bulge/spheroid mass. This is in agreeemnt with Sani et al. (2011), who found $b_{\star,bul} = 0.79 \pm 0.09$, but in contrast

with the results of Häring & Rix (2004), who measure bulge masses directly from dynamical modeling and find a log-slope significantly greater than unity. Using the same $L_K \rightarrow M_\star$ conversion as above, we find that the $M_\bullet - M_{\star,\text{tot}}$ relation also has a log-slope below unity, albeit with lower significance: $b_{\star,\text{tot}} \approx 0.84 \pm 0.14$. This implies that relative to either the bulge/spheroid or the total mass, BHs grow, or have grown, more efficiently in lower-mass systems.

4.4.2   THE OBSERVER'S QUESTION

Which quantity is a more efficient and reliable $M_\bullet$ indicator? According to the present work, L_{tot} is to be preferred over L_{bul} in this regard. The detailed decompositions and careful case-by-case analysis that we performed in order to separate the bulge light will be all but unfeasible in most contexts of $M_\bullet$ estimation. For programs attempting to measure L_{bul} in an automated way for a large number of galaxies, bulge(+disk) decompositions currently appear to be the best available approximation to galaxy light distributions. We demonstrated that the $\epsilon_\bullet$ expected from measuring L_{bul} by this "standard" method is virtually identical to $\epsilon_\bullet$ of the $M_\bullet - L_{\text{tot}}$ relation. *Even if* more detailed decompositions similar to ours became available for such purposes, the predictive power of the measured L_{bul} would improve only slightly ($\epsilon_\bullet$ decreases from 0.46 to 0.42 in our study). Moreover, the fact that the correlation slope depends on the complexity of the decomposition, and hence on the available data quality, is likely to introduce biases in the results. Yet another argument against the use of $M_\bullet - L_{\text{bul}}$ to estimate SBH masses is the likely dependence of its parameters on the mix of morphological type (ellipticals versus all galaxies). If this trend is confirmed, and as long as the available sample of $M_\bullet$ is not representative of the actual distribution of Hubble types in the universe, Black Hole demography based on the $M_\bullet - L_{\text{bul}}$ relation may suffer from enhanced systematic error.

By contrast, the scaling relation with L_{tot} appears to be independent of Hubble type, is more robust with respect to the employed photometric/decomposition method (see Chapter 2), less dependent on the available image quality (depth, resolution), and may be measured much more efficiently. For example, it can be obtained by model-independent methods such as the curve-of-growth (L_{24}), at least if, as in our study, the background can be estimated reliably and potential interlopers / nearby objects can be masked. Then, parameter-free estimates of total luminosity may even be more accurate than profile fits in some circumstances (bright AGN, embedded disks, strong bars or spiral arms).

Apart from reliability and practical considerations, both our $M_\bullet - L_{\text{tot}}$ and updated $M_\bullet - L_{\text{bul}}$ relations may have consequences on the (local) Black Hole mass function (Shankar et al., in prep.). As reported, for example by Tundo et al. (2007) and Lauer et al. (2007b), currently combining the luminosity function of bulges with $M_\bullet - L_{\text{bul}}$ predicts a significantly larger BH density than

when combining the velocity dispersion function with the $M_\bullet - \sigma_v$ relation, especially at high masses. Both the lower slope $(b)_{bul}$ of our updated relation, and application of $M_\bullet - L_{tot}$ which has a slope comparable to that previously measured for $M_\bullet - L_{bul}$, may reduce the discrepancy in this regime[9].

4.4.3 SYSTEMATIC UNCERTAINTIES AND CAVEATS

As mentioned in §4.3.1 and §4.4.2, the slope of the $M_\bullet - L_{bul}$ relation tends to be overestimated if detailed galaxy decompositions are not available. We stress that this bias does not only pertain to spiral galaxies (late Hubble types). In fact, we detect spiral arms in only 4 of our 35 targets and still find a significantly different slope by using $L_{b,std}$ instead of L_{sph} or $L_{b,min}$. It is difficult to assess wether or to what degree our decompositions included all relevant components, and thus a bias in slope may remain. We also saw that un-masked cores, in concert with fitting single 2D-Sérsic profiles, affect the slope of both relations (with L_{bul} and L_{tot}), while some cores may have remained undetected due to the resolution limit. Yet, unmasked cores have a smaller effect than limited decomposition complexity (cf. the magnitude differences in Chapter 2 and compare, for example, $b_{t,imp}$ with $b_{t,std}$ in Table 4.4). Overall, $(b)_{tot}$ is most likely less affected by systematic error than b_{bul}.

Despite being already the lowest among all published, b_{bul} may be overestimated for yet another reason: the inclusion of envelopes, by setting $L_{bul} = L_{sph}$ instead of $L_{bul} = L_{b,min}$. The rationale for our choice is given in §4.3.2 and Chapter 2, but it may not be appropriate in all galaxies in which we identified an envelope. For example this component may be, or include part of, a "thick" or "hot" disk in some cases, especially when its axis ratio is intermediate between the bulge and disk. Exclusion of the envelope from the adopted bulge luminosity leads to lower values preferably at the low-luminosity portion of the sample; the effect on the slope is comparable to its uncertainty, as documented by the $M_\bullet - L_{b,min}$ relation (line 2 in Table 4.4).

The above considerations also lead us to emphasize that all our bulge measurements rely on the universal application of the Sérsic profile. While it may be a good approximation to the surface brightness in the parts where the bulge light apparently dominates, sometimes a significant fraction of modeled bulge flux resides in the outer parts of this profile (the "wings", especially if n is high), where other components, most importantly the disk, dominate and constraints on the bulge profile are very weak. In other words, a part of the bulge light is mostly extrapolated from the inner (bulge-dominated) regions. If bulges are not well described by a Sérsic profile here, the derived luminosities may be in error, both random and systematic.

---

[9]see also, for example, Gültekin et al. (2009) regarding the strong impact of the intrinsic scatter

The intrinsic scatter of the $M_{\bullet} - L_{\mathrm{bul}}$ relation should, in principle, be lower than value we derive, by the same argument as above regarding the slope: data and decomposition are never "perfect". Yet, considering the 0.04 dex decrease (in the best-fit value) gained by transiting from bulge+disk to improved decompositions based on our high-quality data, further improvement from even better photometry is most likely minimal. For example, if we adopt a coarse estimate of the magnitude error, the corresponding resulting intrinsic scatter decreases by only 0.01 dex (see Appendix 4.A.4). Future parameter changes from sample variance and additional or updated $M_{\bullet}$ will probably exceed those expected from further improved photometry.

All our results depend critically on the systematic accuracy of the available $M_{\bullet}$, including their uncertainties. Systematic uncertainty of $M_{\bullet}$ may originate in unaccounted-for variations of the stellar M/L (see discussion in Gültekin et al. 2009), incomplete orbit library of the dynamical model (Shen & Gebhardt 2010; Schulze & Gebhardt 2011), or unmodeled triaxiality (van den Bosch & de Zeeuw 2010). Neglect or improper modeling of dynamics in circumnuclear gas disks (turbulence, nongravitational forces, asymmetries, inclination) may likewise lead to additional random and systematic errors. $\Delta M_{\bullet}$ will be underestimated if the statistical analysis considers a restricted set of models, resulting in an overestimated intrinsic relation scatter. Currently available measurements of $M_{\bullet}$ differ in modeling technique and statistical treatment. Therefore, a homogeneous modeling of the data, including comprehensive statistical evaluation, would be desirable in all BH mass measurements.

4.4.4 PSEUDOBULGES

Some of the previous studies of the $M_{\bullet} - L_{\mathrm{bul}}$ relation in the near-infrared (Marconi & Hunt 2003; Vika et al. 2012) and mid-infrared (Sani et al. 2011) have found somewhat lower intrinsic scatter than we do. We posit that these differences are mostly a consequence of sample selection, particularly of disregarding outliers and galaxies with pseudobulges (or bars) as identified therein. Pseudobulges by definition do not occur in elliptical galaxies, implying they are found preferentially at the low-mass end of the scaling relations, a range where the correlation is apparently weaker than on average. Excluding the respective galaxies then statistically leads to lower overall scatter, as would removal of low-mass galaxies in general.

In the spirit of our investigation, and due to the very low number of potential "pseudobulge-only" galaxies that we found, we cannot directly compare the mentioned results to ours. Based on our photometry, we find only 4/35 galaxies to not possess a classical bulge, and even here the classification is tentative as the only fulfilled criterion is that their bulge has Sérsic index $n < 2$. We hold that unless pseudobulges can be securely identified in an automated manner from photometry alone, a scaling relation derived from their exclusion is of little use for BH

demographic studies. In the context of BH-galaxy co-evolution models, there still appear to be differing interpretations of the data regarding whether and how pseudobulges follow a separate relation than that defined by "classical" bulges. This is not surprising, considering the range of sample and sub-sample selection as well as data quality and image analysis methods, which we have shown in this work to impact the derived structural parameters of (pseudo-)bulges and hence the identification of pseudobulges to begin with. We also caution that pseudobulges may co-exist with classical bulges (see Nowak et al. 2010 on this), as witnessed during our image analysis: an inner disk component is present in 6 of 18 galaxies with (classical) bulge and large-scale exponential disk. Unless clearly defined and universally measurable pseudobulge criteria are available and applied consistently, and a dichotomy is measured with statistical significance, we therefore discourage fitting subsamples based on pseudobulge distinction.

4.5 SUMMARY AND CONCLUSIONS

We have revisited the $M_\bullet - L_{bul}$ relation using a sample of 35 nearby galaxies of all Hubble types, based on deeper near-IR photometry than previously available, as well as a homogenized database of black hole mass estimates. Using GALFIT3, a careful decomposition was performed for each galaxy, leading to the identification of multiple morphological components (nuclei, bars, small-scale disks and envelopes, in addition to the canonical bulge and large-scale disk) in a significnat fraction of objects.

We find that zero-point and (logarithmic) slope of the $M_\bullet - L_{bul}$-relation differ significantly from those published in Marconi & Hunt (2003) and Graham (2007), but are consistent with the values measured in the recent study by Vika et al. (2012). In particular, we find at the 99% confidence level that BH masses increase more slowly than the K-band bulge luminosity. If we assume that $M_\star/L_K$ is constant or increases with galaxy luminosity, this implies that the correlation between black hole mass and bulge mass, $M_\bullet - M_{\star,bul}$, also has a slope below unity: the most massive galaxies seem to have proportionally lower black hole masses per given stellar (bulge) mass.

We find a maximum-likelihood scatter in the relation of 0.46 dex (in log $M_\bullet$) for a straightforward bulge(+disk) estimate of L_{bul}, decreasing to 0.42 dex if more sophisticated approaches to extract the bulge luminosity are used. This scatter is larger than reported by MH03 (0.3 dex), despite far better photometric data and improved BH estimates adopted in our work. However, our estimate of the scatter is again consistent with the K-band analysis of Vika et al. (2012), as well as with recent results in the optical (Gültekin et al. 2009) and at $3.6\,\mu$m (Sani et al. 2011). Yet, we stress that our results are based on a sample that is unbiased with respect to morphological classification of the host galaxy: our only criterium for inclusion of a galaxy is the availability of a precise measurement of the black hole mass. By contrast, the mentioned studies have often culled the

sample by removing outliers or specific morphological classes (most notably "pseudobulges"), which likely leads to underestimated scatter. Preference for our approach originates, among others, in the envisaged use of the relation for BH demographic studies.

We have also investigated the relation between supermassive black hole masses and *total* galaxy luminosity, $M_\bullet - L_{\rm tot}$, finding that within the uncertainty, $M_\bullet$ appears to be linearly proportional to $L_{\rm tot}$. The scatter of $M_\bullet - L_{\rm tot}$ is consistent with that of our $M_\bullet - L_{\rm bul}$ relation, regardless of the details of the photometric decomposition. This result is at variance with previous studies, and might imply that total, rather than bulge, luminosity (mass) is the fundamental driver in the coevolution of galaxies and Black holes. Notwithstanding, we suggest that the $M_\bullet - L_{\rm tot}$ relation should be included in the boundary conditions of the relevant theoretical investigations.

Our study has shown how difficult a separation of the bulge luminosity is from the total luminosity, even when data with high S/N and spatial resolution are used for quite nearby galaxies. It follows that for galaxies that are more distant and observed with lower signal-to-noise or resolution, $L_{\rm tot}$ is a more reliable proxy for black hole mass than bulge magnitude.

ACKNOWLEDGMENTS

4.A Fitting method

4.A.1 Choice of fit method

We initially fit our scaling relations with the modified FITEXY routine (see Tremaine et al. 2002, T02 hereafter). FITEXY (Numerical Recipies, 2nd edition) is a least-squares minimization algorithm that accounts for Gaussian uncertainties in both coordinates and gives estimates of the uncertainties of the derived linear relation parameters (a, b). We use the implementation available in the IDL Astronomy User's Library[10]. The modification of the routine consists in accounting for intrinsic scatter by adding ϵ in quadrature to the data's y-errors, and finding its "true" value by varying ϵ until $\chi_\nu^2 = 1$.

Broadly following Gültekin et al. (2009) [G09 hereafter], we also fit all relations via the maximum-likelihood method, for the following reasons:

(1) The modified FITEXY algorithm does not provide a confidence interval for ϵ. Although it can be estimated by applying Monte-Carlo resampling, which we also did (bootstrap resampling with $n = 10000$ samples), the bootstrap estimate may be biased (see next point).

(2) For all data sets, the FITEXY bootstrap result for ϵ slightly differs from the fit to the full sample, such that the mean and median of the ϵ_0-distribution are *always* $\sim 5 - 10\%$ smaller. Such behaviour may put in question the data's error bars but also the appropriateness of the model (Hogg et al. 2010). The sample size may also be too small to yield informative bootstrap results, especially with respect to the inferred (average) ϵ.

(3) ϵ is not a parameter of the model underlying modified FITEXY optimization, but chosen a priori to give a particular value of χ^2. We are therefore concerned that this way of accounting for ϵ may bias the results.

We are satisfied to report that the parameter values, as well as the confidence intervals of (a, b), from likelihood-method and FITEXY agree closely (see Table 4.6 for examples), which corroborates the finding of G09. Yet, we prefer and adopt the maximum-likelihood method for our quoted results (Table 4.4), because it

a) assumes a generative model which explicitly aned naturally includes the intrinsic scatter as one of the model parameters to be fitted for,

---

[10]http://idlastro.gsfc.nasa.gov/ftp/pro/math/fitexy.pro

b) easily accomodates for modifications or generalizations, such as non-Gaussian or correlated data uncertainties, and

c) provides complete statistical information in form of the full (3-dimensional) posterior probability distribution, and consequently also straightforward uncertainty estimates of all parameters, including correlation.

4.A.2   MAXIMUM-LIKELIHOOD METHOD

Computation of the likelihood proceeds in a way similar to the method presented in G09, and partially draws from concepts outlined in Bailer-Jones (2012a).

The likelihood function, $\mathcal{L}(\{x\}, \{y\} \,|\, \mathcal{M}_\theta)$, gives the probability of the measured N data points, $\{x\} = \{x_i\}_{i=1}^N$ and $\{y\} = \{y_i\}_{i=1}^N$, under the assumption that the model $\mathcal{M}$ parametrized by θ generated the data. In our case, $(x, y) = \left(\log(L/10^{11}\, L_\odot), \log(M_\bullet /\, M_\odot) \right)$, and $\mathcal{M} = \mathcal{M}_{ab\epsilon}$ is a linear relation between x and y, with offset a and slope b. The third parameter, ϵ, characterizes the intrinsic scatter, which we assume to follow a Gaussian[11] with standard deviation ϵ in the y-direction. Then, using the the notation

$$G_\sigma(x) = \frac{1}{\sigma \sqrt{2\pi}} e^{-x^2/2\sigma^2} \, , \tag{4.2}$$

our model is the probability distribution of y given x (and the model parameters):

$$\mathcal{M}_{ab\epsilon}(y \,|\, x) = G_\epsilon(y - a - bx) \, . \tag{4.3}$$

This characterization of a linear relation with Gaussian intrinsic scatter is not unique: ϵ could as well be assumed to reside in the x-coordinate (luminosity). The resulting fit would differ, as discussed in Novak et al. (2006). Our choice concurs with most recent studies of the $M_\bullet - L_{\mathrm{bul}}$ relation, and corresponds to the physical interpretation that the galaxy property ($x = \log L$) determines the black hole mass (y) via some partially stochastic process. Exploration of the inverse relation, as well as models equivalent to orthogonal least-squares and bisector fits, is beyond the scope of the present study.

Due to measurement uncertainty, which was so far implicit, every datum (x_i, y_i) represents a probability distribution, $P_i(x_i, y_i \,|\, x', y')$, where x' and y' are the (unknown) galaxy properties that resulted in the measurements x_i and y_i . In order to obtain the likelihood ℓ_i of (x_i, y_i) given the model (4.3), we therefore need to integrate over all possible (x', y'):

$$\ell_i = \int \mathcal{M}_{ab\epsilon}(y' \,|\, x')\, P(x')\, P_i(x_i, y_i \,|\, x', y')\, \mathrm{d}x' \mathrm{d}y' \, , \tag{4.4}$$

---

[11]which is an appropriate distribution as shown by G09

where $P(x')$, the probability distribution of true x-values, has been included in order for $\mathcal{M}(y|x) \cdot P(x)$ to be a bivariate distribution in (x, y) (see below). If the individual data points and errors are independent, the likelihood of all data is the product of the individual likelihoods:

$$\mathcal{L} = \mathcal{L}(\{x\}, \{y\} \mid a, b, \epsilon) = \prod_{i=1}^{N} \ell_i . \tag{4.5}$$

Assuming that the measurement uncertainties are described by a 2-dimensional Gaussian,

$$P_i(x_i, y_i \mid x', y') = \frac{1}{2\pi\sigma_{x,i}\sigma_{y,i}\sqrt{1 - \rho_i^2}} \exp\left[-\frac{\tilde{x}_i^2 + \tilde{y}_i^2 - 2\rho_i \tilde{x}_i \tilde{y}_i}{2(1 - \rho_i^2)}\right]$$

$$\text{with} \quad \tilde{x}_i = \frac{x_i - x'}{\sigma_{x,i}} , \quad \tilde{y}_i = \frac{y_i - y'}{\sigma_{y,i}} \quad \text{and} \quad \rho_i = \frac{\sigma_{xy,i}^2}{\sigma_{x,i}\sigma_{y,i}} , \tag{4.6}$$

where $\sigma_{x,i}^2$ and $\sigma_{y,i}^2$ are variances of the measurements x_i and y_i, and $\sigma_{xy,i}^2 = \text{Cov}(x_i, y_i)$ their covariance. Finally, we specify $P(x') \propto \Theta(x' - x_l)\Theta(x_u - x')$ to be constant between some upper and lower limit, x_u and x_l. This choice mimics the implicit assumption usually made in a regression analysis, where any value of x is allowed with equal probability. If the limits extend well beyond the x-uncertainties of the data, integral (4.4) can be approximated as

$$\ell_i \approx c \cdot \int \mathcal{M}_{ab\epsilon}(y' \mid x') P_i(x_i, y_i \mid x', y') \, \mathrm{d}x' \mathrm{d}y' \tag{4.7}$$

and the constant c may be omitted without loss of generality. Inserting (4.6) and (4.3) into (4.7), the integral is a convolution of two Gaussians, which renders another Gaussian as the result:

$$\begin{aligned} \ell_i &= G_{\sigma_i}(y_i - a - bx_i) , \\ \text{where} \quad \sigma_i^2 &= b^2 \sigma_x^2 - 2b\sigma_{xy}^2 + \sigma_y^2 + \epsilon^2 . \end{aligned} \tag{4.8}$$

If additionally one assumes zero uncertainty in the x_i, integrating (4.4) over x' (with $P(x')$ as defined above) is trivial, the approximation (4.7) is not needed, and (4.8) reduces to

$$\sigma_i^2 = \sigma_y^2 + \epsilon^2 . \tag{4.9}$$

This is the likelihood used for our adopted results, and the same as used by G09. We retain (4.7) and (4.8) in order to explore the influence of distance and (apparent) magnitude uncertainties in §4.A.4.

The fit is now performed by maximizing $\mathcal{L}$, or minimizing $-\ln\mathcal{L}$, under variation of the parameters (a, b, ϵ). Since $\mathcal{L}$ and $\ln\mathcal{L}$ are nonlinear in (a, b, ϵ), this requires numeric optimization, which we carry out by means of the Downhill-Simplex-Method (routine AMOEBA from the standard IDL library). The result are the best-fit parameters (a_0, b_0, ϵ_0) given in Tables 4.4, 4.5 and 4.6.

4.A.3   CONFIDENCE INTERVALS

We obtain the parameters' confidence intervals by computing their respective probability distributions, $P_a(a)$, $P_b(b)$ and $P_\epsilon(\epsilon)$. These are each projections of the three-dimensional posterior probability $P(a, b, \epsilon \,|\, \{x\}, \{y\})$ which, in turn, is related to the likelihood $\mathcal{L}$ via Bayes' theorem,

$$P(a, b, \epsilon \,|\, \{x\}, \{y\}) = c \cdot \mathcal{L}(\{x\}, \{y\} \,|\, a, b, \epsilon) \cdot P(a, b, \epsilon) \,, \tag{4.10}$$

where $P(a, b, \epsilon)$ is the prior information and c the normalization constant. The prior is chosen to be a uniform distribution in $(a, b, \ln \epsilon)$. Since the projected likelihood functions are well approximated by a normal (a and b) or log-normal (ϵ) distribution, we elect to limit the support of the prior to the intervals $[a_0 - 4\sigma_a, a_0 + 4\sigma_a]$, $[b_0 - 4\sigma_b, b_0 + 4\sigma_b]$ and $[\epsilon_0 e^{\sigma_\lambda^2 - 4\sigma_\lambda}, \epsilon_0 e^{\sigma_\lambda^2 + 4\sigma_\lambda}]$, where $(\sigma_a, \sigma_b, \sigma_\lambda)$ are the standard deviations of a, b and $\lambda \equiv \ln \epsilon$ as estimated from bootstrapping the best-fit values. Within this parameter range, we therefore expect to include $\approx 99.99\%$ of the (projected) probability in our calculation. We use the Kolmogorov-Smirnov test to quantify the agreement with the assumed distributions, and report the K-S-distances to be of the order of 0.005 (a and b, compared to a Gaussian), and 0.01 (ϵ, compared to a lognormal distribution) for all fitted data sets.

We choose to characterize the parameter uncertainties by their respective central 68.3%-confidence intervals, i.e. the location of the 15.9- and 84.1-precentiles relative to the best-fit value. For a and b with their normal distributions, this is the "1σ"-interval. For the (near-)lognormal distribution that ϵ follows, this type of interval definition is more convenient than other common choices, such as the symmetric or the shortest interval: the parameters $(\lambda_0, \sigma_\lambda)$ of the lognormal distribution,

$$P_\epsilon(\epsilon) = \frac{1}{\sigma_\lambda \sqrt{2\pi}} \frac{1}{\epsilon} \exp\left(-\frac{\ln \epsilon - \lambda_0}{2\sigma_\lambda}\right)$$

may be directly computed from the (asymmetric) interval limits, $[\epsilon_1, \epsilon_2] = [\epsilon_0 - (\Delta\epsilon)_-, \epsilon_0 + (\Delta\epsilon)_+]$, as given in column 7 of Table (4.4), via

$$\lambda_0 = \frac{1}{2} \ln(\epsilon_1 \epsilon_2) \,, \quad \sigma_\lambda = \frac{1}{2} \ln(\frac{\epsilon_2}{\epsilon_1}) \,.$$

Thus, the given limits suffice to completely specify the underlying (log-normal) distribution of ϵ, useful for example in the context of deriving the Black Hole Mass Function.

Notably, the ϵ-coordinate of the 3D-posterior maximum is smaller than that of P_ϵ's maximum (which in turn is smaller than the median and mean). The reason is that ϵ is positively correlated with $|a - a_0|$ and $|b - b_0|$, as it should, considering that ϵ "absorbs" some of the increased degree of model-data mismatch when a and b differ from the optimum.

	luminosity	fit	a_0	Δa	b_0	Δb	$\epsilon_{\bullet,0}$	$\Delta\epsilon_\bullet$	error treatment
	(1)	(2)	(3)	(4)	(5)	(6)	(7)	(8)	(9)
(1)	$L_{\mathbf{sph}}$	**like**	**8.566**	**0.084**	**0.773**	**0.093**	**0.421**	**0.083 / 0.039**	$\mathbf{\Delta M_\bullet}$
(2)	L_{sph}	like+bs	8.567	0.078	0.770	0.097	0.404	0.041	$\Delta M_\bullet$
(3)	L_{sph}	FITEXY	8.566	0.082	0.772	0.089	0.425	–	$\Delta M_\bullet$
(4)	L_{sph}	like	8.540	0.083	0.785	0.093	0.415	0.082 / 0.038	$\Delta M_\bullet$ and Δd
(5)	L_{sph}	like	8.538	0.082	0.790	0.094	0.411	0.083 / 0.039	$\Delta M_\bullet$ and ΔL_{sph}
(6)	$L_{\mathbf{t,imp}}$	**like**	**8.339**	**0.095**	**0.946**	**0.141**	**0.490**	**0.098 / 0.044**	$\mathbf{\Delta M_\bullet}$
(7)	$L_{\mathrm{t,imp}}$	like+bs	8.337	0.094	0.949	0.138	0.473	0.054	$\Delta M_\bullet$
(8)	$L_{\mathrm{t,imp}}$	FITEXY	8.339	0.091	0.946	0.136	0.498	–	$\Delta M_\bullet$
(9)	$L_{\mathrm{t,imp}}$	like	8.341	0.095	0.944	0.141	0.491	0.098 / 0.044	$\Delta M_\bullet$ and Δd
(10)	$L_{\mathrm{t,imp}}$	like	8.341	0.095	0.944	0.141	0.489	0.098 / 0.044	$\Delta M_\bullet$ and $\Delta L_{\mathrm{t,imp}}$

Table 4.6: Comparison of scaling relations as resulting from different fitting methods and error treatment, while always fitting the linear relation (eqn. 4.1) using our adopted $M_\bullet$ throughout. Column (1) indicates the luminosity correlated with $M_\bullet$ (see Table 4.2), and column (2) the fitting method: "like" (likelihood computation, as generally adopted generally throughout our study), "FITEXY" (modified FITEXY routine) and "like+bs" (bootstrap resampling of the maximum-likelihood values). For "like" and "FITEXY", columns (3-8) contain the best-fit parameter values, $(a, b, \epsilon_\bullet)_0$ and the central 68%("1-σ")-confidence interval, $\Delta(a, b, \epsilon_\bullet)$. In case of "like+bs", the best-fit values and intervals are replaced by the mean and standard deviation of the sample of most likely values. The last column informs about the measurement errors accounted for in the fit, where Δd implies that distance uncertainties (see Table 4.1) induce additional correlated uncertainty in both L and $M_\bullet$, and $\Delta L_{\{\cdot\}}$ are based on rough estimates of the magnitude uncertainties: 0.1 mag to all total and elliptical's "bulge" magnitudes, 0.2 mag to bulges from decompositions, and 0.5 mag to NGC1300, NGC3245, NGC3998 and NGC4258. Printed in boldface are our adopted relations. All parameter estimates agree well within the parameter uncertainties. For details about the fitting method, please see appendix 4.A.

4.A.4 TREATMENT OF ERROR IN THE DATA

In order to fit equation (4.1), we assume Gaussian uncertainties in $\tilde{M}_\bullet = \log M_\bullet$ with standard error

$$\sigma_\bullet = \frac{1}{2}\left[\log(M_\bullet - \Delta M_{\bullet,-}) + \log(M_\bullet + \Delta M_{\bullet,+})\right] , \qquad (4.11)$$

where $M_\bullet$ is the best-fit value, and $\Delta M_{\bullet+/-}$ are the limits of the published 1σ-confidence interval, relative to $M_\bullet$. That is, we symmetrize the confidence interval, while the published interval is typically asymmetric in $\log M_\bullet$.

To justify this symmetrization, consider that $\chi^2(M_\bullet)$, from which the uncertainties $\Delta M_{\bullet+/-}$ are typically derived, is generally not symmetric around the location of its minimum. Even if the provided interval is symmetric, it may result from choosing the interval centre as the best-fit

value (e.g., Schulze & Gebhardt 2011). In other words, the probability distribution of $M_\bullet$, as implied by $\chi^2(M_\bullet)$, is neither Gaussian nor symmetric to begin with, and its characterization provided in the literature ($M_\bullet$ and $\Delta M_{\bullet(+/-)}$) is already reduced to 2 (or 3) numbers. Moreover, the $M_\bullet$-confidence interval as derived from $\chi^2(M_\bullet)$ (e.g. using the $\Delta\chi^2 = 1$-countours) generally represent the intended confidence level (e.g. 68%) only approximately, due to non-linearity of the model (see Press et al. 1992). Our symmetrization therefore represents only a small distortion of the *available* information on $M_\bullet$.

In Chapter 2, we concluded that within the adopted method of image decomposition, uncertainties of the derived apparent magnitudes (bulge magnitudes in particular) cannot be assessed in a sound and reproducible manner, and recommend setting them to zero. We show now that even if some educated guess of the uncertainties is made, the effect on the fit results is comparatively small. For example, assuming normally distributed errors, and setting all $\Delta m_{\text{tot}} = 0.1$ mag, which corresponds roughly to the differences between several methods of measuring m_{tot} (see Figure **??** and Table 2.4), the best-fit intrinsic scatter ϵ_0 decreases by ≈ 0.001, that is ≈ 0.02 times the 1σ-uncertainty (compare lines 6 and 10 in Table 4.6). Likewise, a and b are practically unchanged. Uncertainties in bulge magnitudes, Δm_{sph}, should be larger than Δm_{tot}, although not as large as the average difference between $L_{\text{b,std}}$ and L_{sph}. Choosing $\Delta m_{\text{sph}} = 0.2$ mag for most disk galaxies, and $\Delta m_{\text{sph}} = 0.5$ mag for NGC1300, NGC3245, NGC3998 and NGC4258 (stronger residuals or larger uncertainty about the number of components), the parameters change by $\approx 20\%$ of the 1σ-uncertainties (line 5 in Table 4.6). Therefore, omission of the magnitude errors does not negatively impact the accuracy our adopted results.

Finally, we *can* reliably account for uncertainty in the distance measurement: $\sigma_d = 0.4\Delta(m - M)$ (see col. 4 in Table 4.1), which we assume to be normally distributed. On average, our error on the distance modulus is ≈ 0.2 mag, which translates to an uncertainty in $\tilde{M}_\bullet$ and $\tilde{L}$ of ≈ 0.08 dex. This is about half of the typical error in $\tilde{M}_\bullet$. Since both $\tilde{M}_\bullet$ and $\tilde{L}$ are proportional to the distance modulus, σ_d introduces covariance between $\tilde{M}_\bullet$ and $\tilde{L}$. If we set magnitude errors to zero as discussed above, the elements of the data covariance matrix are $\sigma_x^2 = \sigma_d^2$, $\sigma_y^2 = \sigma_\bullet^2 + \sigma_d^2$ and $\sigma_{xy}^2 = \sigma_d^2$ (cf. eqn. 4.6). Then, the likelihood of the i-th measurement (x_i, y_i) (equation 4.8) is a Gaussian with variance

$$\sigma_i^2 = (1 - b)^2 \sigma_{d,i}^2 + \sigma_{\bullet,i}^2 + \epsilon^2 \ .$$

This implies that for our relations, which have a slope $b \approx 1$, the influence of σ_d will be small. For example, assuming $\sigma_{d,i} = \sigma_{\bullet,i}/2$, $\epsilon = 0.4 \approx 2\sigma_{\bullet,i}$ and a slope as low as $b = 0.7$, the contribution of σ_d to the above variance is $\approx 1\%$. The contribution of σ_d would further decrease if magnitude errors were nozero. It vanishes altogether if $b = 1$, since then the errors due to distance then are "parallel to" the relation. In Table 4.6, we present the relation parameters derived from including distance uncertainties (lines 4 and 9): they are very similar to our addopted relations (lines 1 and 6), as expected.

4.B   SIGNIFICANCE OF PARAMETER DIFFERENCES

In tables 4.7-4.9, we present the differences between our parameter estimates for selected $M_\bullet - L_{\{\cdot\}}$ relations as resulting from our WIRCam imaging. In these tables, the row and column headers label the kind of luminosity measurement being correlated with $M_\bullet$, listed in order of ascending parameter mean (which may differ slightly from the best-fit value), as given in brackets below the columns headers. Each pairwise difference is expressed as a fraction of the standard deviation of the respective difference distribution (lower-left portion of each table). In the top-right portion of each table, we supplement the corresponding confidence level (assuming a Gaussian distribution). The relations' $\epsilon_\bullet$ approximately follow a log-normal distribution; hence $\log\epsilon_\bullet$ and their differences are normally distributed and used to determine the standard deviation. $\epsilon_\perp$, the intrinsic scatter orthogonal to the correlation ridge line, is not one of the model parameters but related to them, $\epsilon_\perp = \epsilon_\bullet(1 + b^2)^{-1/2}$. We therefore calculate its mean and standard deviation from bootstrap resampling. In each table, we highlight the comparison between our adopted relations ($M_\bullet - L_{\mathrm{sph}}$ and $M_\bullet - L_{\mathrm{t,imp}}$) in boldface. The tables illustrate our main result: that the correlation of $M_\bullet$ with bulge luminosity is as tight as the correlation with total luminosity at the 68%-confidence level, even when improved decompositions (L_{sph}) are applied instead of bulge/disk decompositions ($L_{\mathrm{b,std}}$).

	$L_{\mathrm{b,min}}$	L_{sph}	$L_{\mathrm{b,std}}$	$L_{\mathrm{t,imp}}$	$L_{\mathrm{imp}}^{(ell)}$
$\langle b\rangle$	(0.723)	(0.773)	(0.875)	(0.946)	(0.952)
$L_{\mathrm{b,min}}$	–	28.6%	67.3%	80.5%	78.3%
L_{sph}	0.366	–	50.0%	**69.4%**	67.4%
$L_{\mathrm{b,std}}$	0.980	0.674	–	29.7%	30.4%
$L_{\mathrm{t,imp}}$	1.295	**1.024**	0.382	–	2.5%
$L_{\mathrm{imp}}^{(ell)}$	1.235	0.983	0.391	0.031	–

Table 4.7: Significances of pairwise differences between correlation slopes (b). For example (printed in boldface), b_{sph} of the $M_\bullet - L_{\mathrm{sph}}$ relation differs from $b_{\mathrm{t,imp}}$ by 1.024 standard deviations, corresponding to the 69.4%-confidence level.

	$L_{\mathrm{imp}}^{(ell)}$	L_{sph}	$L_{\mathrm{b,min}}$	$L_{\mathrm{b,std}}$	$L_{\mathrm{t,imp}}$
$\langle\epsilon_\bullet\rangle$	(0.418)	(0.439)	(0.481)	(0.483)	(0.512)
$L_{\mathrm{imp}}^{(ell)}$	–	16.5%	43.6%	44.9%	60.0%
L_{sph}	0.208	–	35.3%	37.0%	**56.9%**
$L_{\mathrm{b,min}}$	0.577	0.458	–	2.0%	25.6%
$L_{\mathrm{b,std}}$	0.597	0.482	0.025	–	23.7%
$L_{\mathrm{t,imp}}$	0.842	**0.787**	0.326	0.301	–

Table 4.8: As Table 4.7, but for $\epsilon_\bullet$. For example, $\epsilon_{\bullet\mathrm{sph}}$ of the $M_\bullet - L_{\mathrm{sph}}$ relation differs from $\epsilon_{\bullet\mathrm{t,imp}}$ by 0.787σ, i.e. at the 56.9%-confidence level. All $\epsilon_\bullet$ agree at the 60%-confidence level.

	$L_{\mathrm{imp}}^{(ell)}$	L_{sph}	$L_{\mathrm{b,std}}$	$L_{\mathrm{t,imp}}$	$L_{\mathrm{b,min}}$
$\langle\epsilon_\perp\rangle$	(0.264)	(0.320)	(0.335)	(0.344)	(0.357)
$L_{\mathrm{imp}}^{(ell)}$	–	67.8%	74.3%	78.6%	86.1%
L_{sph}	0.990	–	21.8%	**32.9%**	50.3%
$L_{\mathrm{b,std}}$	1.133	0.277	–	11.4%	28.4%
$L_{\mathrm{t,imp}}$	1.241	**0.425**	0.143	–	16.7%
$L_{\mathrm{b,min}}$	1.481	0.679	0.363	0.210	–

Table 4.9: As Table 4.7, but for $\epsilon_\bullet$. For example, $\epsilon_{\perp\mathrm{sph}}$ of the $M_\bullet - L_{\mathrm{sph}}$ relation differs from $\epsilon_{\perp\mathrm{t,imp}}$ by 0.425σ, i.e. at the 32.9%-confidence level.

An advanced treatment of the Intrinsic Scatter:

Variability and Bidirectionality

Abstract

In this chapter, I present an advanced treatment of the *intrinsic scatter* (ϵ) in fitting linear relations. This improved fitting method overcomes two limitations of the commonplace approach that was hitherto adopted in investigations of the BH scaling relations: (1) the assumption that the intrinsic scatter is uniform along the relation, and (2) the assumption that it resides in either the BH mass or the galaxy property, but not both. Motivation to develop the generalization to variable and bidirectional scatter originates not only in the astrophysical relevance of both additional degrees of freedom, but also in mitigating potential biases in the "classical" linear relation parameters, namely the relation offset and slope. I apply the presented method to the correlations of BH mass ($M_\bullet$) with improved bulge and total luminosities (L_{sph} and $L_{\mathrm{t,imp}}$), using the data presented in the previous chapters. The data for the $M_\bullet - L_{\mathrm{sph}}$ relation are found to be consistent with constant intrinsic scatter at the 68%-confidence level, while ϵ of the $M_\bullet - L_{\mathrm{t,imp}}$ relation significantly decreases with increasing luminosity. I conclude by discussing possible extensions and future applications of the principle conceived here.

5.1 Variable intrinsic scatter

The intrinsic ("cosmic") scatter, ϵ, is one of the fundamental parameters that characterize the BH scaling relations. Apart from the relation intercept (a) and slope (b), it is thought to convey information about the processes driving BH-galaxy co-evolution. Cosmological simulations thereof

generally result in BH masses ($M_\bullet$) being correlated with global properties of their host galaxies, and the characterictics of the theoretical correlation depend on the details of the physical processes invoked in the underlying model. Since realistic evolutionary models must comply with the observed correlations, the latter act as a constraint on the former.

Following the discovery of the BH scaling relations with host galaxy bulge luminosity (L_{bul}, Kormendy & Richstone 1995), stellar mass ($M_\star$, Magorrian et al. 1998) and stellar velocity dispersion ($\sigma_\star$, Ferrarese & Merritt 2000; Gebhardt et al. 2000), a non-trivial physical connection between the BH and the host galaxy (bulge) evolution was suggested to be responsible for their emergence (e.g., Kormendy & Gebhardt 2001). Considering the small fraction of galaxy mass that resides in the BH ($\sim 0.15\%$ on average according to Sani et al. 2011), most gas and stellar orbits are gravitationally unaffected by the presence of the BH. Further, if gravity was the only force considered, most of the galaxy's matter could not contibute to BH growth, because the orbits do not bring it close enough to allow for accretion onto the BH. Conseqently, models of galaxy formation were adapted to include the apparently warranted non-gravitational mechanisms that result in BH scaling relations, including their observed intercept and slope (e.g., Silk & Rees 1998; Granato et al. 2004; Hopkins et al. 2006; Croton et al. 2006). More recently, attention has also been given to reproducing the right (i.e., observed) magnitude of correlation scatter (e.g., Jahnke & Macciò 2011; Volonteri et al. 2011; Shankar et al. 2012).

Some of the cited studies also predict a trend of ϵ with host galaxy property: the scatter in $\log M_\bullet$ decreases with increasing bulge and total mass. ϵ should likewise be dependent on galaxy properties that are related to mass (in the present investigation: L_{bul} and L_{tot}). Although generally no quantitative evaluation of this phenomenon is given, it is a generic prediction of simultaneous merging of galaxies and BHs in a hierarchical structure assembly (ΛCDM cosmology, Jahnke & Macciò 2011; Volonteri et al. 2011). It is also obvious in Figure 4 of Croton et al. (2006). Shankar et al. (2012) discuss how the scatter should theoretically increase for galaxies with bulge buildup mainly from secular processes ("pseudobulges") that dominate at the low-mass end, compared to galaxies with merger-driven bulge (spheroid) formation that dominate at the high-mass end of the galaxy mass function. The possibility that the scatter may not be uniform was also briefly discussed in Lauer et al. (2007a).

Therefore, it would be desirable to recover and quantify this possible dependency of ϵ on galaxy property (or equivalently $M_\bullet$) in the *observed* joint sample of $M_\bullet$ and host galaxy properties. This would provide additional prior information on models of BH-galaxy formation, and aid in distinguishing between various evolutionary scenarios. In this section, I propose a method of fitting a linear relation that is capable of modeling such variable intrinsic scatter. It is a simple extension of the method presented in Appendix A of Chapter 4, and likewise based on Bayesian

inference. In the proposed model, the correlation between two quantities x and y is described by

$$y = a + bx + \mathcal{N}\left(0, \epsilon_y^{(\gamma)}(x)\right) , \quad \text{with} \quad \epsilon_y^{(\gamma)}(x) = \epsilon_y e^{\gamma x} , \tag{5.1}$$

where $\mathcal{N}(\mu, \sigma)$ denotes a Gaussian distribution with mean μ and standard deviation σ. The parameter ϵ_y is the intrinsic scatter in the y-coordinate at the zero-point ($x = 0$). The new parameter γ regulates the rate of growth (if $\gamma > 0$) or decline (if $\gamma < 0$) of the variable scatter $\epsilon_y^{(\gamma)}$ with x. $\gamma = 0$ is the special and hitherto applied case of constant ϵ_y (Equation 4.1). The adopted functional form of $\epsilon_y^{(\gamma)}(x)$ appears to be the simplest way of modeling variable intrinsic scatter that is monotonic and well defined for all x, and ensures $\epsilon > 0$ everywhere. Neither a powerlaw nor a polynomial in x fullfill these requirements. In the context of this thesis, $x = \log(L_{\text{bul}}/10^{11}L_\odot)$ or $x = \log(L_{\text{tot}}/10^{11}L_\odot)$, and $y = \log(M_\bullet/M_\odot)$, where the normalization $L_0 = 10^{11}L_\odot$ has been chosen to (approximately) remove correlation between a and b. In this case, i.e. when $x = \log L/L_0$, it follows that $\epsilon_y^{(\gamma)}/\epsilon_y = (L/L_0)^{\gamma/\ln 10}$, which is consistent with $L > 0$. Note that as in Chapter 4, this model stipulates that the intrinsic scatter resides in the y-coordinate, a limitation to which I will return in Section 5.2.

Assuming statistically independent measurements, the likelihood of the data $\mathcal{D} = \{\mathcal{D}_i\}_{i=1}^N$, $\mathcal{D}_i = (x_i, y_i)$ reads

$$\mathcal{L}(\mathcal{D} \,|\, a, b, \epsilon_y, \gamma) = \prod_{i=1}^N \ell_i(\mathcal{D}_i \,|\, a, b, \epsilon_y, \gamma) ,$$

$$\ell_i = \int \mathcal{M}_{ab\epsilon_y\gamma}(y' \,|\, x') \, P(x') P_i(x_i, y_i \,|\, x', y') \, \mathrm{d}x' \mathrm{d}y' \tag{5.2}$$

where $P_i(x_i, y_i \,|\, x', y')$ is the measurement model of datum (x_i, y_i), and

$$\mathcal{M}_{ab\epsilon_y\gamma}(y \,|\, x) = \frac{1}{\epsilon_y e^{\gamma x} \sqrt{2\pi}} \exp\left[-\frac{(y - a - bx)^2}{2\left(\epsilon_y e^{\gamma x}\right)^2} \right] \tag{5.3}$$

the model of the correlation between x and y. As in Chapter 4, I will assume a constant probability $P(x')$ for the x-coordinate in a large interval $[x_l, x_u] \to [-\infty, +\infty]$, mimicking the assumption usually and implicitly made in linear regression. If further the uncertainty of measurement y_i can be described by a Gaussian with standard deviation $\sigma_{y,i}$ for all $i = 1 \dots N$, and no uncertainty is present in the x_i as in case of the luminosities derived in Chapter 2, the likelihood of (x_i, y_i) becomes

$$\ell_i = \frac{1}{\sigma_i \sqrt{2\pi}} \exp\left[\frac{(y_i - a - bx_i)^2}{2\sigma_i^2} \right] \quad \text{with} \quad \sigma_i^2 = \sigma_{y,i}^2 + \epsilon_y^2 e^{2\gamma x_i} . \tag{5.4}$$

Since the (unnormalized) posterior probability distribution (the "posterior", for short),

$$\mathcal{P}(a, b, \epsilon_0, \gamma \,|\, \mathcal{D}) = \mathcal{L}(\mathcal{D} \,|\, a, b, \epsilon_y, \gamma) \cdot \mathcal{P}(a, b, \epsilon_y, \gamma) , \tag{5.5}$$
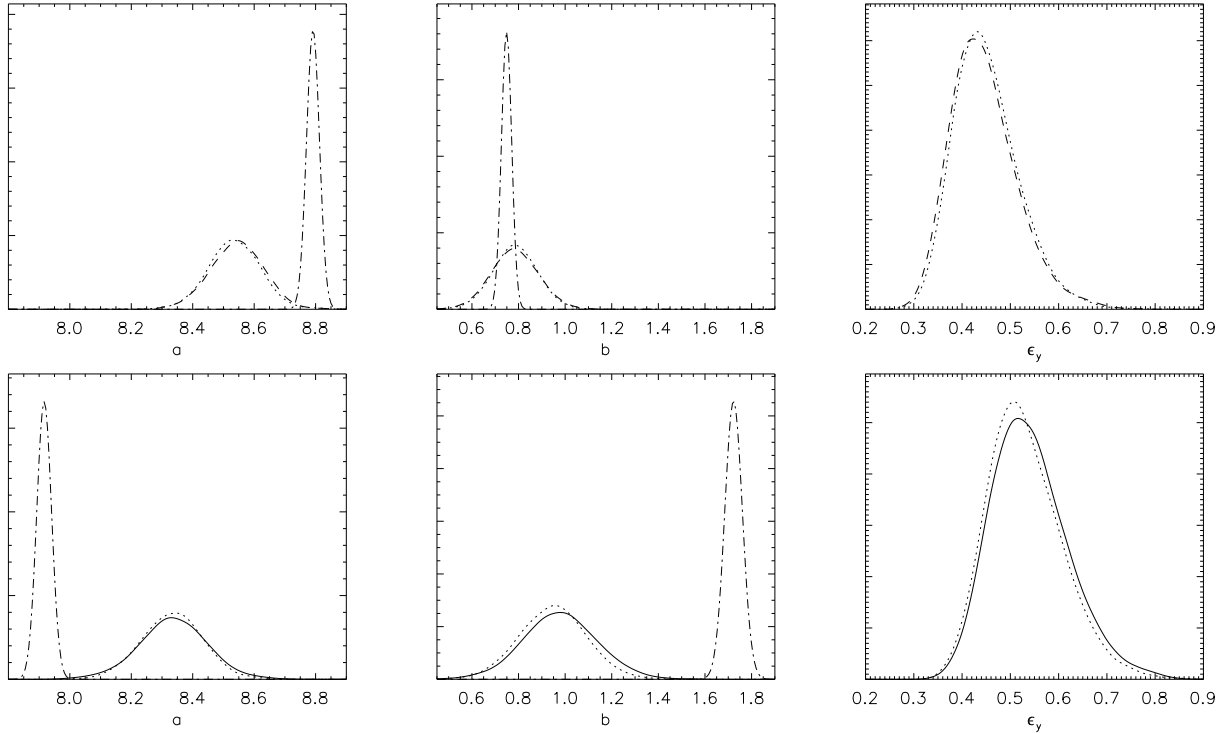
Figure 5.1: Marginalized posterior distributions of a, b and ϵ_y from fitting the $M_\bullet - L_{\text{bul}}$ (upper panels, dashed curves) and $M_\bullet - L_{\text{tot}}$ relation (lower panels, solid curves) using the model (5.1) with variable intrinsic scatter. The scale of y (probability) is arbitrary. For comparison, in all panels the dotted curves show the distributions resulting from models in which the scatter is not a function of luminosity ($\gamma = 0$). The dot-dashed curves result from fitting a model without intrinsic scatter ($\epsilon_y = 0$). The models with and without intrinsic scatter variability render very similar results for (a, b, ϵ_y), but excluding the intrinsic scatter from the model strongly biases the results for a and b.

is now defined over 4 (instead of 3) model parameters, computing it on a (regular) grid becomes impractical. I therefore probe the posterior by means of a Markov-chain Monte Carlo (MCMC) method, specifically choosing the Metropolis-Hastings algorithm (implemented in IDL) to obtain a sample of parameters drawn from the posterior. The prior distribution, $\mathcal{P}(a, b, \epsilon_y, \gamma)$, is chosen to be constant in the interval $a \in [7, 10]$, $b \in [0.4, 4.0]$, $\epsilon_y \in [0, 4]$, $\gamma \in [-1, 1]$, and vanishes elsewhere. The dispersion of the proposal distribution is tuned so that the acceptance rate is ~ 0.5. I let the algorithm draw 80,000 samples, of which the first 40,000 are discarded ("burn-in"). This number of samples was chosen as a minimum to ensuree that there are no apparent insular features or trends in the overall parameter sequence, and that the resulting parameter histograms show no signs of "clustering".

I apply the above model and sampling algorithm to the observed $M_\bullet - L_{\text{bul}}$ and $M_\bullet - L_{\text{tot}}$ relations, using the same improved bulge and total luminosities $L_{\text{bul}} = L_{\text{sph}}$ and $L_{\text{tot}} = L_{\text{t,imp}}$ that were adopted in Chapter 4 to characterize the scaling relations with constant intrinsic scatter. The resulting marginalized posterior probability densities are plotted in Figures 5.1 and 5.2.
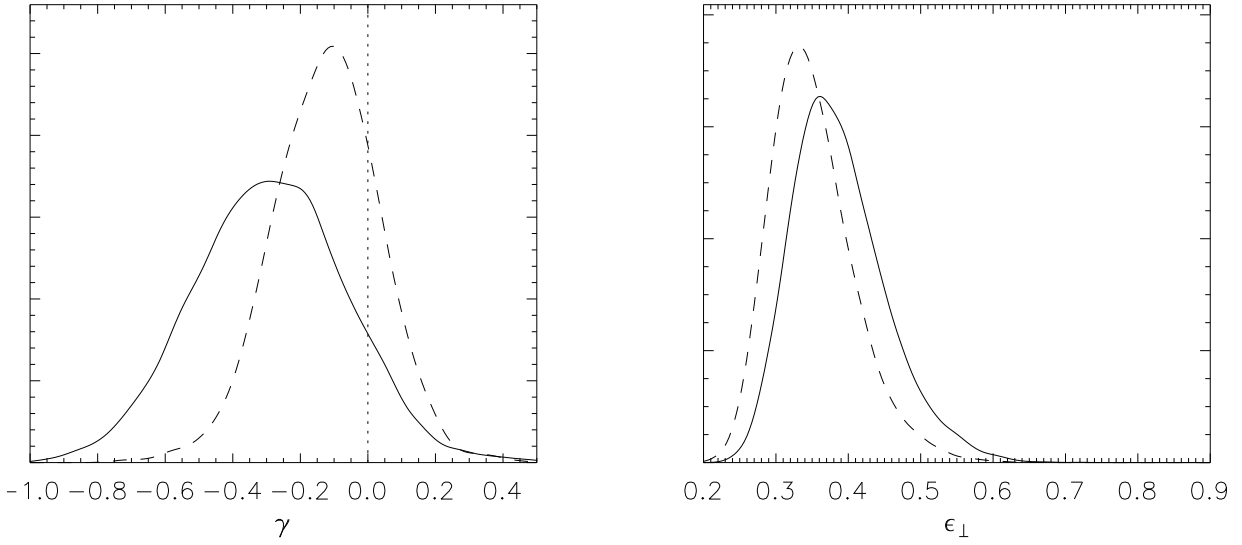
Figure 5.2: Marginalized posterior distributions of the variability scale γ (left panel, $\epsilon_y^{(\gamma)} = \epsilon_y e^{\gamma x}$) and intrinsic scatter orthogonal to the ridge line (right panel, $\epsilon_\perp = \epsilon_y / \sqrt{1 + b^2}$). The scale of y (probability) is arbitrary. Solid curves: results from fitting the $M_\bullet - L_{\mathrm{tot}}$ relation. Dashed curves: fitting $M_\bullet - L_{\mathrm{sph}}$. The left panel conveys the main result of Section 5.1: that the median of γ is < 0 for both relations, implying a decrease of ϵ as a function of $x = \log \left(L/10^{11} L_\odot \right)$, but only for $L = L_{\mathrm{tot}}$ is the difference significant at the 68%-confidence level. The right panel illustrates one of the results of the previous chapter: the intrinsic scatter distributions of both correlations are similar, especially when $\epsilon_\perp$ is considered instead of ϵ_y, due to the larger slope of $M_\bullet - L_{\mathrm{tot}}$ with respect to $M_\bullet - L_{\mathrm{bul}}$.

Each probability density was derived from the respective parameter sample via Gaussian kernel smoothing[1]. In Figure 5.1, $\mathcal{P}(a\,|\,\mathcal{D})$, $\mathcal{P}(b\,|\,\mathcal{D})$ and $\mathcal{P}(\epsilon_y\,|\,\mathcal{D})$ of the $\mathcal{M}_{ab\epsilon_y\gamma}$ model are represented by the thick dashed and solid curves, separately for the $M_\bullet - L_{\mathrm{bul}}$ (upper panels) and $M_\bullet - L_{\mathrm{tot}}$ relation (lower panels). The distributions for γ are plotted in the left panel of Figure 5.2 (solid line: $M_\bullet - L_{\mathrm{bul}}$, dotted line: $M_\bullet - L_{\mathrm{tot}}$). For both relations, much of the cumulative $\mathcal{P}(\gamma)$ resides at $\gamma < 0$. That is, the scatter decreases with $x = \log L$ the majority of the sample. The right panel of the same Figure shows the distribution of the orthogonal intrinsic scatter at the zero-point, $\epsilon_\perp = \epsilon_y / \sqrt{1 + b^2}$, illustrating that the "width" of both relations is very similar.

The median parameter values, and the locations of the 16- and 84-percentiles relative to the median, are listed in line 3 of Tables 5.1 ($M_\bullet - L_{\mathrm{bul}}$) and 5.2 ($M_\bullet - L_{\mathrm{tot}}$). For $M_\bullet - L_{\mathrm{tot}}$, $\gamma = 0$ is not inside the 68%-confidence interval, while the $M_\bullet - L_{\mathrm{bul}}$ relation is consistent with $\gamma = 0$ at the 68%-confidence level. In more general terms, both relations are more likely to have their $\epsilon_y^{(\gamma)}$ decreasing with $\log L$, with slightly greater significance for the $M_\bullet - L_{\mathrm{tot}}$ relation. Yet, there is considerable probability (21% for L_{bul} and 10% for L_{tot}) that ϵ_y does either not depend on L or is even positively correlated with it.

---

[1] kernel dispersion: 20% of the sample variance

	$\mathcal{M}_{\{\cdot\}}$	a	b	ϵ_x	ϵ_y	$\epsilon_\perp$	γ
	(1)	(2)	(3)	(4)	(5)	(6)	(7)
(1)	ab	8.79 ± 0.01	0.75 ± 0.01	–	–	–	–
(2)	$ab\epsilon_y$	8.54 ± 0.08	0.79 ± 0.10	–	$0.44^{+0.07}_{-0.06}$	$0.35^{+0.06}_{-0.05}$	–
(3)	$ab\epsilon_y\gamma$	$8.55^{+0.08}_{-0.09}$	0.78 ± 0.10	–	$0.44^{+0.07}_{-0.06}$	$0.34^{+0.06}_{-0.05}$	$-0.12^{+0.15}_{-0.16}$
(4)	$ab\epsilon_x$	8.54 ± 0.08	0.77 ± 0.10	$0.58^{+0.15}_{-0.09}$	–	$0.35^{+0.07}_{-0.05}$	–
(5)	$ab\epsilon_x\epsilon_y$	8.54 ± 0.08	$0.77^{+0.09}_{-0.10}$	$0.39^{+0.20}_{-0.25}$	$0.32^{+0.13}_{-0.21}$	$0.36^{+0.06}_{-0.05}$	–

Table 5.1: Results from fitting the $M_\bullet - L_{\text{bul}}$ relation, with $y = \log(M_\bullet/M_\odot)$ and $x = \log\left(L_{\text{bul}}/10^{11}L_\odot\right)$ using $L_{\text{bul}} = L_{\text{sph}}$ as adopted in Chapter 4. Given in columns (2-7) are the median parameter values of the samples drawn from the posterior via MCMC, and the location of the 16- and 84-percentiels relative to it. Note that this is slighly different from the convention used in Table 4.4, where the the "central" parameter values correspond to the maximum of the likelihood. $\epsilon_\perp$ in column (6) is not one of the original model parameters, but computed as $\epsilon_\perp^2 = (b^2\epsilon_x^2 + \epsilon_y^2)/(1 + b^2)$. Column (1) indicates the model used in fitting $M_\bullet - L_{\text{bul}}$, by listing the free parameters present in the model. Missing entries indicate that the respective parameter was not included, equivalent to being fixed to zero. For a description of the models, see the text. Rows (1)-(3) give results from the method presented in Section 5.1 (introducing x-dependency of the intrinsic scatter), while rows (4) and (5) are obtained by fitting the model presented in Section 5.2 (dropping the assumpion of the scatter residing in the y-coordinate).

The tables also list results for fitting two special cases of $\mathcal{M}_{ab\epsilon_y\gamma}$. In line 2, $\gamma \equiv 0$ (model $\mathcal{M}_{ab\epsilon_y}$), corresponding to the correlation model used previously in Chapter 4. In line 1, I have additionally fixed $\epsilon_y \equiv 0$ to explore the effect that neglicience of *any* intrinsic scatter in the fitting method has on the resulting linear relation parameters a and b. The results for $\mathcal{M}_{ab\epsilon_y}$ and $\mathcal{M}_{ab}$ are overplotted in Figure 5.1 by the dotted and dot-dashed curves, respectively. Comparing these to the thick dashed and solid curves (model with variable ϵ_y), and lines 1 and 2 to line 3 in the Tables, one can conclude that the potential x-dependency of ϵ_y has no appreciable effect on (a, b, ϵ_y). However, excluding the scatter altogether significantly impacts the distributions of a and b, not only leading to biased median values but also to a significant underestimate of the confidence intervals. It should be noted that the relatively small impact of fixing $\gamma = 0$ may be particular to the data that I have used. For data that show stronger x-dependency of ϵ_y than the current data set, it is well possible that a significant bias in (a, b, ϵ_y) may result from omitting γ. As an aside, the median values and intervals presented in line 2 of both tables confirm the results from Chapter 4, where computation on a grid instead of an MCMC method was used. The small differences in the central values result from quoting the maximum of the likelihood in Table 4.4, while here the median of the marginalized posterior distribution is given, respectively.

	$\mathcal{M}_{\{\cdot\}}$	a	b	ϵ_x	ϵ_y	$\epsilon_\perp$	γ
(1)	ab	7.92 ± 0.01	1.72 ± 0.02	–	–	–	–
(2)	$ab\epsilon_y$	8.33 ± 0.10	0.95 ± 0.14	–	$0.52^{+0.08}_{-0.07}$	$0.38^{+0.07}_{-0.05}$	–
(3)	$ab\epsilon_y\gamma$	8.34 ± 0.11	$0.98^{+0.16}_{-0.15}$	–	$0.53^{+0.09}_{-0.07}$	$0.38^{+0.07}_{-0.05}$	$-0.28^{+0.22}_{-0.23}$
(4)	$ab\epsilon_x$	8.34 ± 0.09	0.93 ± 0.14	$0.56^{+0.14}_{-0.10}$	–	$0.38^{+0.07}_{-0.05}$	–
(5)	$ab\epsilon_x\epsilon_y$	$8.35^{+0.09}_{-0.10}$	$0.92^{+0.14}_{-0.15}$	$0.38^{+0.20}_{-0.26}$	$0.38^{+0.14}_{-0.24}$	$0.39^{+0.07}_{-0.06}$	–

Table 5.2: Results from fitting the $M_\bullet - L_{\text{tot}}$ relation, with $y = \log(M_\bullet/M_\odot)$ and $x = \log\left(L_{\text{tot}}/10^{11}L_\odot\right)$ using $L_{\text{tot}} = L_{\text{t,imp}}$ as adopted in Chapter 4. The layout of the table is as described in the caption of Table 5.1.

5.2 BIDIRECTIONAL INTRINSIC SCATTER

When fitting the BH scaling relations, the intrinsic scatter is usually assumed to reside in the Black Hole mass, $M_\bullet$. This assumption implies that the model, which underlies the "fitting" of the parameters ($a, b, \epsilon = \epsilon_y$) and their *confidence intervals*, considers the galaxy property to determine $M_\bullet$, modulo an uncertainty (stochasticity). This uncertainty is typially taken as described by a Gaussian distribution, and is (like the correlation intercept and slope) characteristic of physical process linking BH and host galaxy. Detailed knowledge of this process is not necessary for the fitting, as it is reduced to two numbers: the mean expected $M_\bullet$ for a given galaxy property (the ridge line of the scaling relation), and the degree of its stochasticity, embodied by the intrinsic scatter (ϵ_y). This approach obviously neglects the possibility that the BH itself may influence the galaxy property, as is usually the case in astrophysical models (simulations) of BH-galaxy co-evolution. This problem has been recognized before, for example in the context of ascertaining the Black Hole Mass Function and correcting for observational bias (Lauer et al. 2007a). Novak et al. (2006) discussed how the relation parameters may change as a result of ascribing the intrinsic scatter to the *x*-coordinate (galaxy property) instead, but presumed that choosing either one or the other is unavoidable within the framework of linear regression. The "solution" (e.g. applied by Graham 2007) consisted in fitting two relations, in which the scatter was assumed to reside alternatively in the BH mass and galaxy property, and afterwards performing some kind of averaging between the best-fit parameters. Such correction for asymmetric dependency hitherto comes, for example, in form of the so-called *bisector fit* (as in the BCES routine developed by Akritas & Bershady (1996), or the *orthogonal least-squares* fit (OLS routine by the same authors). None of these is satisfying, as the underlying statistical model still does assumes unidirectional intrinsic scatter, potentially resulting in biased best-fit parameters. Moreover, in such an approach the assessment of the parameter uncertainties is not well defined.

In order to properly account for the notion that the intrinsic scatter generally resides in *both* BH mass and galaxy property, I define a new model, of which the previous approach is a special

case. The model features two parameters for the intrinsic scatter, one for each coordinate: ϵ_x and ϵ_y. It is based on the concept of a bivariate probability distribution in x ($\log L$) and y ($\log M_\bullet$). As before, let us assume that the probability of encountering a galaxy with property (x, y) is maximized if $y = a + bx$ for some parameters a and b, i.e. for pairs x and y that lie on the relation ridge line. Let us further assume that the ridge line would be the sole possible location of (x, y) in the absence of intrinsic scatter, i.e. if $\epsilon_x = \epsilon_y = 0$. The ridge line defines a bivariate distribution in (x, y), which in case of a linear relation is fully specified by (a, b) and its projection on the x-axis (or equivalently its projection on the y-axis). I will call this intrinsic scatter-free bivariate distribution in (x, y) the *pristine distribution*, $P_{\mathrm{pris}}(x, y \,|\, \theta_{\mathrm{pris}})$ of the correlation model, parametrized by a set of "pristine parameters" θ_{pris}. In case of a linear relation, $\theta_{\mathrm{pris}} = (a, b)$ and

$$P_{\mathrm{pris}}(x, y \,|\, a, b) = P_{\mathrm{pris},x}(x) \cdot \delta(y - a - bx) = \frac{1}{b} P_{\mathrm{pris},y}(y) \cdot \delta(y - a - bx) , \qquad (5.6)$$

where δ is the Dirac delta function, $P_{\mathrm{pris},x}$ and $P_{\mathrm{pris},y}$ are the pristine distribution's projections[2]. Of course, in reality there is generally no pristine distribution of galaxy property and BH mass; it is merely a concept to construct a statistical model of the scaling relation that includes bidirectional intrinsic scatter. Let us assume now that a *real* galaxy finds itself off of the pristine distribution, at some coordinates (x', y'). In this idealized picture, it has originated on some point $(\tilde{x}, \tilde{y})$ described by the pristine distribution, but some process, namely the intrinsic scatter, has changed its coordinates (i.e., its properties or BH mass). If this scattering process is Gaussian, the probability of finding the galaxy at the new coordinates (x', y') is given by

$$P(x', y', \,|\, \tilde{x}, \tilde{y}, \epsilon_x, \epsilon_y) = \frac{1}{\epsilon_x \sqrt{2\pi}} \exp\left[-\frac{(x' - \tilde{x})^2}{2\epsilon_x^2}\right] \cdot \frac{1}{\epsilon_y \sqrt{2\pi}} \exp\left[-\frac{(y' - \tilde{y})^2}{2\epsilon_y^2}\right] , \qquad (5.7)$$

where it was assumed that there is no correlation between the scattering in x-direction and scattering in y-direction[3]. Naturally, ϵ_x and ϵ_y describe the scattering amplitude in both directions, respectively. The "origin" of (x', y') could of course have been anywhere on the pristine distribution. Therefore, the probability of a randomly selected galaxy being located at the *post*-scattering coordinates (x', y') is given by

$$\begin{aligned}
P_{\mathrm{mod}}(x', y' \,|\, \theta_{\mathrm{pris}}, \epsilon_x, \epsilon_y) &= \iint \mathrm{d}\tilde{x}\mathrm{d}\tilde{y} \, P(x', y' \,|\, \tilde{x}, \tilde{y}) \, P_{\mathrm{pris}}(\tilde{x}, \tilde{y}) \\
&= \iint \frac{\mathrm{d}\tilde{x}\mathrm{d}\tilde{y}}{2\pi\epsilon_x\epsilon_y} \exp\left[-\frac{(x' - \tilde{x})^2}{2\epsilon_x^2} - \frac{(y' - \tilde{y})^2}{2\epsilon_y^2}\right] P_{\mathrm{pris}}(\tilde{x}, \tilde{y}) .
\end{aligned} \qquad (5.8)$$

Equation 5.8 is the model for the true galaxy properties. Yet, (x', y') is not what will be observed - the measurement process will generally move our galaxy's properties again, usually in a stochastic way, described by the *measurement model*, $P_{\mathrm{meas},i}(x_i, y_i \,|\, x', y')$. $P_{\mathrm{meas},i}$ is specific to

---

[2] which in general may be parametrized, too

[3] this assumption is not necessary for the principle presented here, but has been invoked for the sake of simplicity

the measurement (x_i, y_i) – therefore the subscript. The true properties (x_i', y_i') are thus known only with finite precision, and need to be marginalized over. This, at last, provides the likelihood ℓ_i of the measured (x_i, y_i):

$$\ell_i(x, y \,|\, \theta_{\text{pris}}, \epsilon_x, \epsilon_y, P_{\text{meas},i}) = \iint dx' dy' \, P_{\text{mod}}(x', y' \,|\, \theta_{\text{pris}}, \epsilon_x, \epsilon_y) \cdot P_{\text{meas},i}(x_i, y_i \,|\, x', y') . \quad (5.9)$$

Notice that still I have not required the pristine distribution to be linear, or made any assumptions about its projected distribution. In order to apply the above scheme to the case of the BH scaling relations, I will use the form (5.6) for the pristine distribution and assume that the probability $P_{\text{pris},x}$ is constant but supported only in some interval $[x_l, x_u]$. Then, (5.8) becomes

$$P_{\text{mod}}(x', y' \,|\, a, b, x_l, x_u, \epsilon_x, \epsilon_y) = \iint \frac{d\tilde{x} d\tilde{y}}{2\pi \epsilon_x \epsilon_y} \left\{ \exp\left[-\frac{(x' - \tilde{x})^2}{2\epsilon_x^2} - \frac{(y' - \tilde{y})^2}{2\epsilon_y^2} \right] \right.$$
$$\left. \times \frac{\Theta(\tilde{x} - x_l)\Theta(x_u - \tilde{x})\delta(\tilde{y} - a - b\tilde{x})}{x_u - x_l} \right\} . \quad (5.10)$$

The integral over $\tilde{y}$ is trivial due to the δ-function, and the remaining integral over $\tilde{x}$ yields

$$P_{\text{mod}}(x', y' \,|\, a, b, x_l, x_u, \epsilon_x, \epsilon_y) = \left[\Phi\left(\frac{\alpha x_u - \beta}{\epsilon_x \epsilon_y \sqrt{\alpha}} \right) - \Phi\left(\frac{\alpha x_l - \beta}{\epsilon_x \epsilon_y \sqrt{\alpha}} \right) \right] \cdot \frac{(x_u - x_l)^{-1}}{\sqrt{2\pi\alpha}} \exp\left[-\frac{(y' - a - bx')^2}{2\alpha} \right]$$

$$(5.11)$$

with $\alpha = b^2 \epsilon_x^2 + \epsilon_y^2$, $\beta = (y' - a)b\epsilon_x^2 + x'\epsilon_y^2$, and $\Phi(x) = (2\pi)^{-1/2} \int_{-\infty}^{x} e^{-x^2/2}$ denoting the cumulative Gaussian distribution. If we now let $x_u \to +\infty$ and $x_l \to -\infty$, that is supporting the pristine distribution over a very large interval, the term in square brackets aproaches unity for any finite (x', y'), the normalization $(x_u - x_l)^{-1}$ can be absorbed into the normalization of the posterior, and the model of a linear relation (a, b) with bidirectional intrinsic scatter (ϵ_x, ϵ_y) becomes

$$\mathcal{M}_{ab\epsilon_x\epsilon_y}(x', y') = \frac{1}{\sqrt{2\pi(b^2\epsilon_x^2 + \epsilon_y^2)}} \exp\left[-\frac{(y' - a - bx')^2}{2(b^2\epsilon_x^2 + \epsilon_y^2)} \right] \quad (5.12)$$

Notice that while the argument of the exponential is symmetric under the exchange $x \leftrightarrow y$, $\epsilon_x \leftrightarrow \epsilon_y$, $a \to -a/b$ and $b \to 1/b$, commensurate with fitting the inverse relation, the pre-factor is not. This is a relic of conditioning the pristine distribution on some fixed interval in x, which causes the probability density in y to depend on b. The above model therefore will generally yield a different result for the inverse relation. The pristine distribution could be symmetrized, for example, by specifying a constant probability density in (x, y) instead of x only. This would imply flexible boundaries in x and y, and additional factor $\sqrt{1 + b^2}$ in the R.H.S of (5.10). A normalization $\sqrt{\frac{1+b^2}{b^2\epsilon_x^2 + \epsilon_y^2}}$ instead of $\sqrt{\frac{1}{b^2\epsilon_x^2 + \epsilon_y^2}}$ indeed makes the approximation (5.12) fully symmetric with respect to inversion of the relation, and is equal to $1/\epsilon_\perp$, the inverse of the orthogonal

intrinsic scatter. As I focus here on the effects of allowing for symmetric (bi-directional) intrinsic scatter, I will adopt (5.12) for the remainder of this chapter.

Model $\mathcal{M}_{ab\epsilon_x\epsilon_y}$ might also be adapted to allow for variable intrinsic scatter, for example in the way propsed in Section 5.1. Then, (5.10) would have to be calculated numerically, since the integration over $\tilde{x}$ would be non-trivial (non-analytic) unless $\epsilon_x \to 0$ as was impicitly the case in Section 5.1. For the sake of simplicity, I therefore limit the present treatment to constant but different intrinsic scatter in ϵ_x and ϵ_y.

Again, $\mathrm{x} = \log\left(L_{\mathrm{bul}}/10^{11}L_\odot\right)$ or $x = \log\left(L_{\mathrm{tot}}/10^{11}L_\odot\right)$ without measurement uncertainties, and the uncertainties in $y = \log\left(M_\bullet/M_\odot\right)$ are Gaussian with individual standard errors $\sigma_{y,i}$. Then, integrating (5.9) with $P_{\mathrm{mod}} = \mathcal{M}_{ab\epsilon_x\epsilon_y}$ (eqn. 5.12) is analytic, resulting in

$$\ell_i(x_i, y_i \,|\, a, b, \epsilon_x, \epsilon_y) = \frac{1}{\sigma_i \sqrt{2\pi}} \exp\left[-\frac{(y_i - a - bx_i)^2}{2\sigma_i^2}\right]$$
$$\text{with} \quad \sigma_i^2 = \sigma_{y,i}^2 + b^2\epsilon_x^2 + \epsilon_y^2 \;. \tag{5.13}$$

The ℓ_i of all data are inserted in $\mathcal{L} = \prod_i \ell_i$ and the posterior calculated according to Bayes' theorem. I will use the same priors for (a, b, ϵ_y) as in Section 5.1, and $\mathcal{P}(\epsilon_x) = \mathcal{P}(\epsilon_y)$. Sampling of the posterior is carried out by the same MCMC algorithm, only now using 10^5 sample points to provide a well mixed Markov chain. The posterior distributions of $(a, b, \epsilon_\perp)$ that result from applying model $\mathcal{M}_{ab\epsilon_x\epsilon_y}$ are plotted in Figure 5.3. $M_\bullet - L_{\mathrm{bul}}$ was fitted in the upper panels (dashed lines), and $M_\bullet - L_{\mathrm{tot}}$ in the lower panels (solid lines). In all panels, the dot-dashed and dotted curves respectively result from alternatively fixing $\epsilon_x \equiv 0$ and $\epsilon_y \equiv 0$, corresponding to models $\mathcal{M}_{ab\epsilon_y}$ and $\mathcal{M}_{ab\epsilon_x}$. Apparently, imposing either restriction on the model does not change a, b or $\epsilon_\perp$ significantly. This is confirmed upon inspection of Tables 5.1 and 5.2, where the median and central 68%-confidence intervals of the parameter posteriors are given. Comparing line 4 to line 2 of Table 5.2 indicates that ϵ_x and ϵ_y are appoximately equal, irrespective of whether the scatter resides in one or both coordinates. In case of the $M_\bullet - L_{\mathrm{bul}}$ relation, ϵ_x is slighly larger than ϵ_y, supposedly because the slope b is significantly < 1.

Plotted in the right panel of Figure 5.3 is the intrinsic scatter orthogonal to the ridge line, $\epsilon_\perp = \sqrt{\frac{b^2\epsilon_x^2 + \epsilon_y^2}{1+b^2}}$. It is interesting though to see how the data seperately constrain ϵ_x and ϵ_y according to model $\mathcal{M}_{ab\epsilon_x\epsilon_y}$. The respective posteriors are displayed in Figure 5.4, along with the sample distribution of the normalized ratio of their difference, $(\epsilon_y - \epsilon_x)/(\epsilon_y + \epsilon_x)$. Not surprisingly, the figures imply that ϵ_x and ϵ_y are not well constrained compared to $\epsilon_\perp$, with a large probability that either of the two is small compared to the other. Yet, the model could determine that for the $M_\bullet - L_{\mathrm{bul}}$ relation, ϵ_x is on average larger than ϵ_y (see also line 5 in Table 5.1). Further, $M_\bullet - L_{\mathrm{bul}}$ and $M_\bullet - L_{\mathrm{tot}}$ differ mostly in ϵ_y, while ϵ_x of both relations is very similar. Finally, Figure 5.5 shows the joint sample of ϵ_x and ϵ_y, demonstrating their expected anticorrelation.
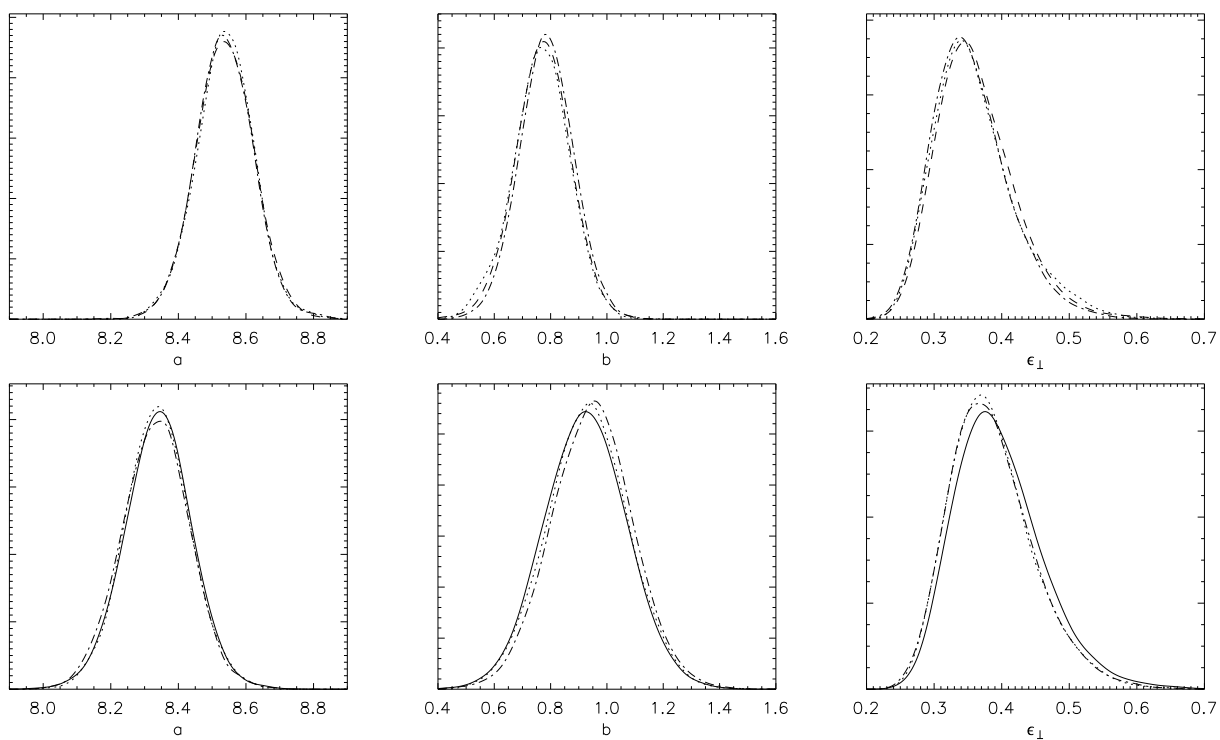
Figure 5.3: Marginalized posterior distributions of a, b and $\epsilon_\perp$ from fitting $M_\bullet - L_{\mathrm{bul}}$ (upper panels) and $M_\bullet - L_{\mathrm{tot}}$ (lower panels). The scale of y (probability) is arbitrary. Dashed and solid curves: using model $\mathcal{M}_{ab\epsilon_x\epsilon_y}$ (eqn 5.12, corresponding to line 5 in Tables 5.1 and 5.2) with intrinsic scatter in both coordinates. The dot-dashed and dotted curves result from fixing $\epsilon_x \equiv 0$ and $\epsilon_y \equiv 0$ respectively, corresponding to models $\mathcal{M}_{ab\epsilon_y}$ and $\mathcal{M}_{ab\epsilon_x}$ (lines 2 and 4 in the same Tables). Apparently, imposing either restriction on the model does not change a, b or $\epsilon_\perp$ significantly.
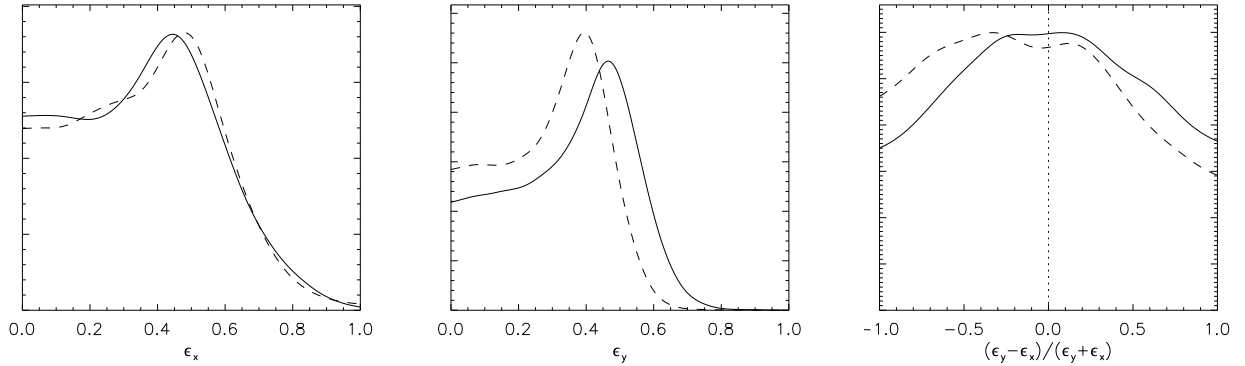
Figure 5.4: Left and middle panel: Marginalized posterior distributions of ϵ_x and ϵ_y resulting from model $\mathcal{M}_{ab\epsilon_x\epsilon_y}$ that allows for intrinsic scatter in both coordinates. The scale of y (probability) is arbitrary. Right panel: the distribution of $(\epsilon_y - \epsilon_x)/(\epsilon_y + \epsilon_x)$, where the abscissa has been defined to equal 1 or -1 in case that all scatter relies in the y- or x-coordinate, and 0 if the scatter is equal in both coordinates. In all panels, the solid curve results from the fit to the $M_\bullet - L_{\mathrm{tot}}$ relation, and the dashed curve from the fit to $M_\bullet - L_{\mathrm{bul}}$. These panels illustrate that both ϵ_x and ϵ_y are not well constrained separately, in contrast to $\epsilon_\perp$ (Figure 5.3). There is considerable probability that either could be very small compared to the other. Despite this, the model is able to determine that ϵ_x and ϵ_y are more likely to be about equal, and that the slighly larger $\epsilon_\perp$ of the $M_\bullet - L_{\mathrm{tot}}$ relation originates in a larger ϵ_y, while ϵ_x of both relations is very similar (cf. the median values listed in the tables).
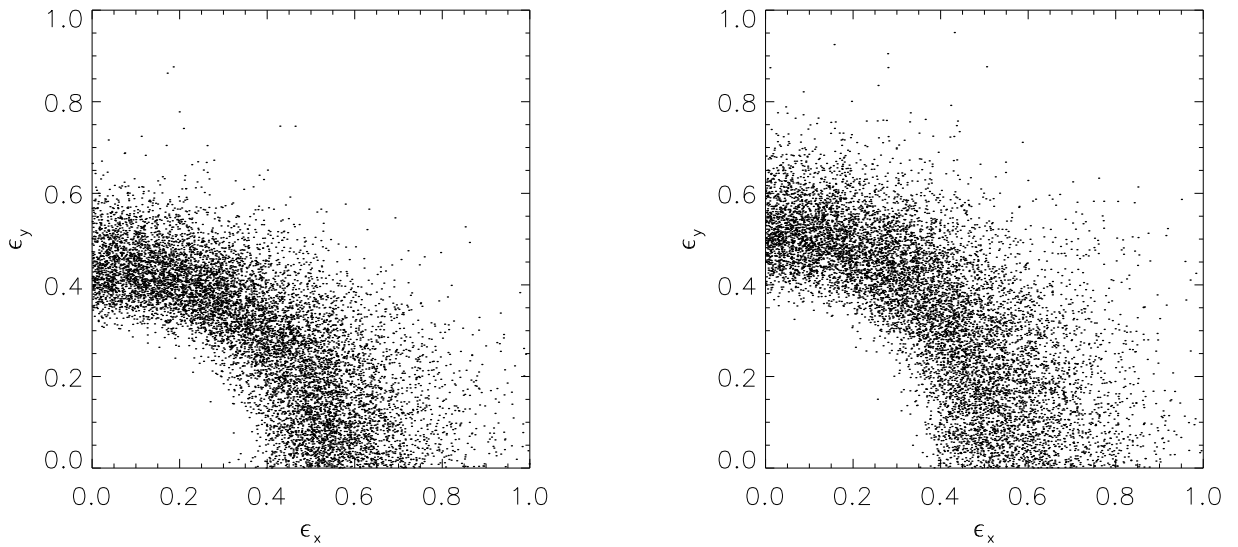
Figure 5.5: Panels showing the joint sample of ϵ_x and ϵ_y. Only 10% of the sample points are actually plotted. Left panel: sample from fit to the $M_\bullet - L_{\mathrm{bul}}$ relation. Right panel: $M_\bullet - L_{\mathrm{tot}}$. As expected, ϵ_x and ϵ_y are anticorrelated.

5.3 DISCUSSION

The commonplace method that is used to fit the BH scaling relations accounts for uniform intrinsic scatter (ϵ) in one coordinate (usually the ordinate, i.e. the BH mass). By developing a new method that allows the intrinsic scatter to vary along the relation, the degree of its variability in the present $M_\bullet - L_{\mathrm{bul}}$ and $M_\bullet - L_{\mathrm{tot}}$ relations could be quantified. If the dependency on $x = \left(\log L / 10^{11} L_\odot \right)$ is parametrized as $\epsilon_y^{(\gamma)}(x) = \epsilon_y \exp(\gamma x)$, the median $\gamma = -0.12$ for the $M_\bullet - L_{\mathrm{bul}}$ relation and $\gamma = -0.28$ for $M_\bullet - L_{\mathrm{tot}}$. This means that the intrinsic scatter of both relations is more likely to decrease with luminosity of the host galaxy instead of being constant, in qualitative agreement with predictions by models of galaxy-BH co-evolution. Yet, for the $M_\bullet - L_{\mathrm{bul}}$ relation, the derived posterior probability distribution of γ is consistent with no dependency ($\gamma = 0$) at the 68%-confidence level. There is still 10%-probability that the intrinsic scatter of the $M_\bullet - L_{\mathrm{tot}}$ relation does not vary or even increases with galaxy luminosity. Therefore, the current data set does not permit a firm conclusion with regard to variability of ϵ. Not surprisingly then, it was found that omission of variability from the model (fixing $\gamma = 0$) does not lead to noticable bias in the other parameters (a, b, ϵ_y). Regardless, it cannot be ruled out that significant bias would occur once the sample size and measurement precision have increased, or if data with stronger scatter variability were fitted. Therefore, the recommendation is to always apply the model developed here in lieu of one which assumes uniform intrinsic scatter.

In a second step, a method was developed that includes intrinsic scatter in both BH mass and galaxy property. The model was again used to fit the BH scaling relations with luminosity. As a result, it was found that the current data do not allow to reliably determine the relative strength of both types of scatter, although the derived posterior distributions slightly prefer a scenario in which the intrinsic scatter in $\log M_\bullet$ and $\log L$ is approximately equal. The results for the other correlation parameters do not appreciably change when assuming the scatter to reside solely in one coordinate. Yet, since this finding may be specific to the data at hand and in order to preclude potential bias, the developed method should be preferred in general, unless bidirectional intrinsic scatter can be excluded a priori on physical grounds.

Independent of the results pertaining to the current $M_\bullet - L_{\mathrm{bul}}$ and $M_\bullet - L_{\mathrm{tot}}$ scaling relations, and despite its limited scope, the above investigation demonstrated the principle and feasibility of extracting astrophysical information contained in the data. It also supports a change of concept with respect to the commonplace fitting methods: Based on Bayesian inference and as already advanced by Kelly (2007) in a more general context, the presented principle interprets the relation between BH mass and galaxy property as a two-dimensional (bivariate) probability distribution, the definition of which is entirely separate from the measurement model. It permits complete characterization and analysis of *all* parameter's posterior distributions, as well as any distributions derived from them. This contrasts with the usually adopted approach of assuming a

unidirectional deterministic dependency between two variables, where the intrinsic scatter is understood as some form of uncertainty in addition to the measurement errors, causing its statistical characterization to be ill-defined. The concept adopted here has the virtue of a straightforward model definition and parameter interpretation. Moreover, it may easily be adapted and generalized, with the only potential practical restriction being the ability to compute the involved integrals in a timely fashion. Naturally, the data may not support such generalized models, or not be able to distinguish between them. Yet, one advantage of Bayesian inference lies in its ability to test exactly that.

Eventually, the significance of different correlation models should be compared by means of their Bayesian evidence, as opposed to merely interpreting the probability distributions of the "new" parameters. Although not performed here, this appears to be one of the most useful goals of future work. Further, the presented method's efficiency and reliabilty in recovering the parameters should be tested by simulated data. Other useful applications and generalizations of the above framework are:

1. The current characterization of the pristine distribtuion is conditioned on either x or y. This asymmetry in the model has nothing to do with assumptions about the instrinsic scatter (e.g., its direction). Applying a pristine distribution that treats both coordinates symmetrically might impact the resulting paremeters significantly and should be pursued.

2. Conversely, by prescribing a (measured) projection of the model distribution on either coordinate, this information can be used to constrain the parameters better and more realistically (see Kelly 2007). A prime example of this is the galaxy luminosity function that could act as a prior on the model's projection on the x-axis (Luminosity). Since the principle presented here models the joint distribution of BH masses and host galaxy luminosity, the Black Hole Mass Function would follow simultaneously. This way, the latter could be characterized reliably, without resorting to an independently derived BH scaling relation which may be based on undesirable, implicit or poorly stated assumptions, in particular with respect to the intrinsic scatter. In this context, allowing for bidirectional and variable intrinsic scatter should prove particularly useful (see discussion in Lauer et al. 2007a).

3. Ideally, the selection function of BH mass measurements would be known and included in the measurement model.

4. The measurement model may be generalized to errors in both coordinates, error correlation (e.g. to account for distance uncertainties), non-Gaussian errors and upper limits - any distribution of the "true" BH mass and galaxy property can be implemented, which includes the measured probability of "no BH". If a BH mass probability is available in form of a representative $M_\bullet$ sample, the likelihood per galaxy could be effectively evaluated by quasi-Monte Carlo integration. The same applies of course to the galaxy property:

for example, a bulge luminosity measurement might be best represented by a sample of values, instead of a single least-squares solution as in case of GALFIT. This sample can be used straightforwardly by the relation model presented here.

5. The connection between x and y may have any functional form, for example non-linear relations, "broken" relations or generally relations where some parts of the data are described by a different relation than other parts, with or without assigning measurements to either sub-relation. The presented scheme would remain the same, only the form of the pristine distribution (5.6) would change. Here in particular, Bayesian evidence would be useful to determine the relevance of different proposed models.

6. Similarly, by assigning a probability of being described by the relation model at all, outliers could be accounted for.

7. The intrinsic scatter need not to be Gaussian. This would allow for scatter with "fatter" tails of the scatter distribution if desired, or for asymmetric intrinsic scatter which can even mimic an upper-envelope relation instead of a ridge-line relation (Batcheldor 2010; Gültekin et al. 2011). As for example done in Gültekin et al. (2009), different functional forms of the scatter could be modeled and their relative significance tested.

8. The scatter intrinsic to both coordinates (ϵ_x, ϵ_y) may be correlated. In case of the BH scaling relations, recovering the correlation coefficient in the distribution that broadens the pristine distribution may convey information about the nature of the physical connection between BH and host galaxy (bulge).

9. Both coordinates' scatter, and the correlation between them, may be modeled by separate variability constants (γ).

10. Any variability of the intrinsic scatter can be modeled – the dependency of the scatter amplitude on either (or both) coordinates is not limited to the suggested simple exponential in x. It may have another functional form, and depend on y instead of x (or both).

11. The principle is fully generalizable to 3 or more variables, for example in the context of fitting the conjectured BH fundamental plane where $M_\bullet$ is fundamentally related to at least two global galaxy properties (see e.g. Marconi & Hunt 2003; Hopkins et al. 2007; Beifiori et al. 2012). Then, the pristine distribution would be supported on a plane (instead of a line). Here in particular, the clean definition of the model and multi-directional treatment of the intrinsic scatter would prove useful to avoid biases and expand the available characterization.

Many of the above generalizations and applications would require numerical integration, where in the present model, analytic evaluation suffices. Finding an integration method that is the best

trade-off between speed and accuracy will be part of the efforts to implement these generalizations. In order to constrain the model parameters with meaningful precision, some of the listed suggestions would likely also require (many) more data points than are currently available for the BH scaling relations. Reduced measurement errors would also increase the information content of the observed sample. Yet and above all, the measurement models (on both $M_\bullet$ and luminosity, especially L_{bul}) should be realistic and unbiased. By the reverse argument, the option of applying a more detailed correlation model is a strong argument for acquisition of such data. Finally, in order to allow an unbiased comparison of theory with the data, the same analysis (fitting method) should be applied to samples produced by astrophysical simulations of BH-galaxy (co-)evolution.

ACKNOWLEDGEMENTS

<div style="text-align: right; font-size: 3em;">*6*</div>

Übermassive Black Hole –

Or exotic initial mass function?[*]

Abstract

We present axisymmetric and triaxial dynamical models of galaxy SDSS J151741.75-004217.6, which, for its moderate luminosity, has an exceptionally high velocity dispersion. The models include a central Black Hole, and when adopting a stellar mass-to-light ratio from spectral fitting and broadband colors, the BH mass ($2 \times 10^{10}\,M_\odot$) is shown to be one of the highest currently known, and comprises as much as $\approx 20\%$ of its host galaxy's stellar mass. At a distance of about 500 Mpc, it is also the most distant known Black Hole with dynamically measured mass. This result is robust under a broad range of assumed dark matter halo masses, but depends on the assumed initial mass function used in estimating the stellar mass. Forcing a Black Hole mass of $< 10^9 M_\odot$, the *i*-band stellar mass-to-light ratio would have to be $> 5 M_\odot/L_\odot$, twice the independently derived value. Consequently, the outcome of this investigation challenges either current SMBH-galaxy co-evolution models, or our understanding of star-formation and stellar physics.

6.1 Introduction

About two decades after being observed for the first time, the BH scaling relations appear well-established. Yet, a few recent measurements of central BH mass ($M_\bullet$) question their universality (Rusli et al. 2011; van den Bosch et al. 2012), placing the respective $M_\bullet$ far off (above) the scal-

---

[*]The analysis presented in this chapter was conducted in collaboration with Remco C. E. van den Bosch

ing relations. In these galaxies, the central BH "weighs in" at a substantial fraction (up to $\sim 10\%$) of their host galaxy's stellar mass ($M_\star$), a factor of ~ 50 higher than expected from the scaling relations ($\approx 0.2\%$). While the expected fraction is only an average value, with an *intrinsic scatter* of $\epsilon \approx 0.4$ dex (standard deviation) around this mean, the mentioned $M_\bullet$ differ from it by ~ 20 standard deviations. Assuming the $M_\bullet - M_\star$ scaling relation is universal and its intrinsic scatter Gaussian, the associated probability of observing such $M_\bullet$ is practically zero[1]. This might imply that they follow a separate BH scaling relation, but at least makes it very likely that they emerge from a different (yet unknown) formation channel than "normal" SMBHs. I will therefore refer to such anomalously high-mass BHs as *Über-massive Black Holes* (ÜMBHs). Our understanding of the processes responsible for formation of ÜMBHs (and their host galaxies) may be advanced by observing further BHs of this kind, and relating their masses to properties of their environment.

Although it is astounding that ÜMBHs exist at all, they are still expected to be rare, and thus difficult to find when probing galaxies for their central BH mass by serendipitous observations. To first order, the local gravitational potential gradient is reflected by the second moment of *tracer* particles' velocity distribution, $\overline{v^2} = \overline{v}^2 + \sigma_v^2$, where $\overline{v}$ is the mean ("streaming") velocity and σ_v the velocity dispersion. If, as in the present investigation, the tracers are stars, one denotes the *stellar velocity dispersion* by $\sigma_\star$. $\overline{v^2}$ and the corresponding models only become sensitive to the presence of the BH within the *sphere-of-influence*. Its radius, $R_{soi} = GM_\bullet/\sigma_\star^2$, is typically $< 1''$ (often $< 0.''1$), even if the BH is "supermassive" ($M_\bullet \gtrsim 10^6 M_\odot$) and the host galaxy relatively nearby ($d \lesssim 50$ Mpc). Therefore, usually $\overline{v}$ and $\sigma_\star$ need to be measured at high spatial resolution in order to determine the central BH's mass (or to detect it at all), making such observations "expensive".

Conversely, the R_{soi} of ÜMBHs can be a sizable fraction of their host's effective radius (R_e). Consequently, ÜMBH *candidates* are indicated by an anomalously high central $\sigma_\star$ of the host galaxy, even if the spatial resolution of the obtained spectrum is insufficient to resolve a "normal" BH's R_{soi}. Note that due to the centering, $\overline{v^2} \approx \sigma_\star^2$ (the average over the aperture). Hence, the measured $\sigma_\star$ traces the central gravitational potential even in the presence of significant (but spatially unresolved) streaming motion. $\sigma_\star$ can be observed at relative ease for a large number of galaxies, and then compared with the value expected from the host luminosity (L) and the Faber-Jackson relation ($L - \sigma_\star$, Faber & Jackson 1976). The ÜMBH candidates are outliers to this relation[2] and may be selected for a more detailed investigation.

Yet, since $\sigma_\star$ reflects the *total* gravitational potential, including the contribution from stellar mass, the latter needs to be accounted for. For example, a steep central stellar density gradient

---

[1] using an asymptotic expansion, $\int_{20}^\infty e^{-x^2/2} \sim 10^{-89}$

[2] more generally, they are outliers to the Fundamental Plane of elliptical galaxies (Dressler et al. 1987; Djorgovski & Davis 1987)

may also cause a high $\sigma_\star$ without need for a (very massive) BH. As $M_\star$ is traced by L (conversion by the *stellar mass-to-light ratio*, $\Upsilon_\star = M_\star/L$), high-resolution imaging of the BH host galaxy is crucial for a successful follow-up analysis, that is to determine the BH mass with confidence.

In practice, dynamical modeling typically assumes $\Upsilon_\star$ to be appoximately constant across the galaxy. This assumption is justified in most early-type galaxies, which our target appears to belong to. Provided sufficient spatial resolution of both the spectral and imaging data, as well as assumptions about the distribution of gas and dark matter (DM), a constant $\Upsilon_\star$ could be determined from the dynamical modeling, and does not need to be supplied externally. In our case, resolution is not sufficient to enable this: $M_\bullet$ and $\Upsilon_\star$ ($M_\star$) are degenerate. Fortunately, spectral and multi-band imaging data are available, and thus $\Upsilon_\star$ can be determined from stellar evolution and population-synthesis (SPS) modeling. We will use this approach to help constrain $M_\bullet$. Alternatively, we make no assumptions about $\Upsilon_\star$, but fix $M_\bullet$ instead, and thereby derive the value of $\Upsilon_\star$ that is required to explain the observations in the absence of an ÜMBH.

6.2 BEFORE DYNAMICAL MODELING

6.2.1 TARGET SELECTION

As discussed in the introduction, candidates for hosting ÜMBHs are galaxies with high central $\sigma_\star$ but low Luminosity (L). Such galaxies also promise to allow measurement of $M_\bullet$ at moderate spatial resolution of the spectrum, provided that the imaging resolves the central surface-brightness profile well. A sample of moderately luminous galaxies with $\sigma_\star > 350$ km/s is listed in Table 2 of Bernardi et al. (2008) [B08 hereafter]. These galaxies have been observed spectroscopically by the Sloan Digital Sky Survey (SDSS), allowing to determine their $\sigma_\star$. Further, high-resolution Hubble Space Telescope (HST) imaging is available for all of them, which aided the authors in identifying them as "singles", that is ruling out a superposition of galaxies to be responsible for the large $\sigma_\star$. From this sample of 23 galaxies, we selected SDSS J151741.75-004217.6 for dynamical modeling. This galaxy has one of the highest $\sigma_\star$ (> 400 km/s), is the second-faintest sample member, and simultaneously the smallest, which makes it the most "extreme" and interesting target. It is the 19th member in B08's compilation; for brevity, we hence name it "B19" during the remainder of this chapter.

The basic properties of B19 are listed in Table 6.1, along with constants used in converting from observed to intrinsic properties. At a redshift of $z = 0.116$, cosmological effects need to be taken into account (luminosity distance, d_L and angular-diameter distance, d_A, as well as k-corrections of the spectra). While distances have been obtained from the NED, using a standard cosmology

quantity	symbol	value	comment/source
cosmology	H_0	$73\,\mathrm{km\,s^{-1}Mpc^{-1}}$	NED
	Ω_M	0.27	NED
	Ω_Λ	0.73	NED
solar absolute magnitude (*i*-band, k-corrected to $z = 0.1$)	$M_{\odot,i}$	4.48	[1]
redshift	z	0.116	SDSS DR6
luminosity distance	d_L	522 Mpc	NED
angular diameter distance	d_A	419 Mpc	NED
i-band apparent magnitude	m_i	16.55	SDSS DR6
galactic foreground extinction (*i*-band)	a_i	0.134	NED
central velocity dispersion	$\sigma_\star$	(360.3 ± 9.4) km/s	Oh et al. (2011)
stellar mass (median ± 95%-confidence)	$M_\star$	$1.13^{+0.65}_{-0.36} \times 10^{11} M_\odot$	MPA-JHU[2]
effective radius	R_e	1.5 kpc	Bernardi et al. (2008)

Table 6.1: Basic properties of our target and constants used in this paper. All values are externally provided as given in the last column.

[1] http://www.ucolick.org/~cnaw/sun.html
[2] Total stellar masses from photometry from the MPA-JHU DR7 release of spectrum measurements, available at http://www.mpa-garching.mpg.de/SDSS/DR7/Data/stellarmass.html .

with $(H_0, \Omega_M, \Omega_\Lambda) = (73\,\mathrm{km\,s^{-1}Mpc^{-1}}, 0.27, 0.73)$, the k-correction is required to estimate the apparent *i*-band magnitude at that redshift. It is implicit in our adopted value of the Sun's absolute magnitude[3], which was derived by redshifting the solar spectrum to $z = 0.1$.

6.2.2 IMAGING AND KINEMATIC DATA

We retrieved the HST/ACS-F775W image of our target galaxy from the Hubble Legacy Archive. This image had been reduced by B08 as part of their original survey to exclude superspoitions from their sample of high-dispersion galaxies, and to derive their detailed photometric properties (Hyde et al. 2008). The F775W filter response is very similar to the SDSS *i*-band; we hence forego a color correction. We require the image's point-spread-function (PSF) for parametrization of the surface brightness profile during dynamical modeling. We reconstruct the PSF image using TinyTim[4], and measure a seeing full-width at half-maximum of $FWHM = 0\farcs065$. The pixel scale of the image is $0\farcs025$, which is sufficient to avoid PSF undersampling.

The ACS image (see Figure 6.1) reveals a smooth light distribution, and the absence of spi-

[3]$M_{\odot,i} = 4.48$, as found in http://www.ucolick.org/ cnaw/sun.html
[4]http://www.stsci.edu/hst/observatory/focus/TinyTim
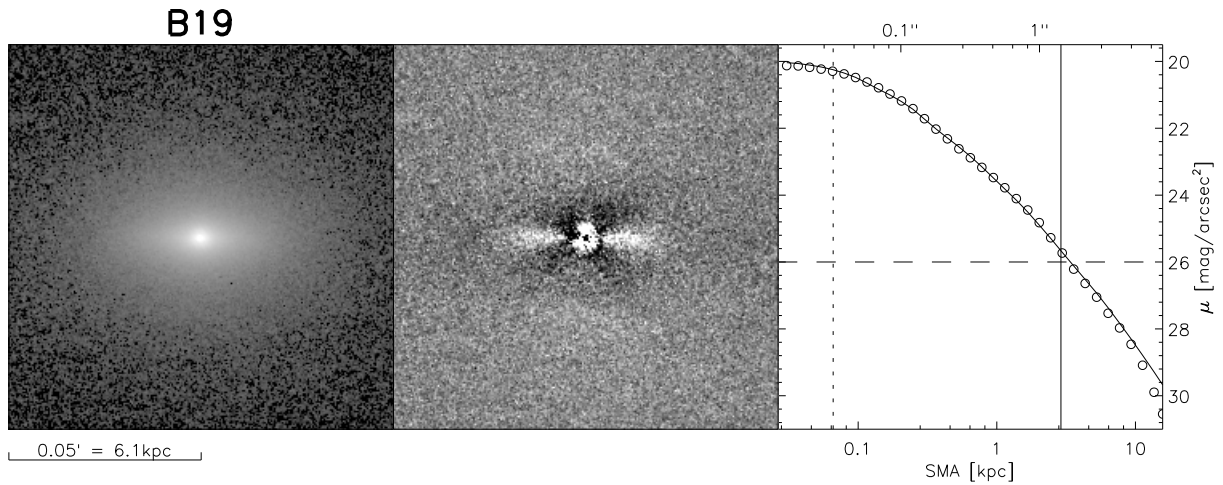
Figure 6.1: The HST/ACS-F77W image of our target (left panel) and the residuals from fitting a 2D-Sérsic profile (middle). The right panel shows the semimajor-axis surface-brightness profiles of the data (open circles) and the Sérsic fit (solid curve), as well as the seeing (dashed vertical line) and the Sérsic effective radius (solid). A weak disk is suggested from the residual image, as well as a central light excess, both of which could not be modeled by a consistent Bulge/Disk (or more) decomposition. Regardless, the agreement between the Sérsic profile and the data is quite good overall.

ral arms, warps, asymmetries or other irregular features. B19 has relatively low average apparent axis ratio ($b/a = 0.61$ according to B08), which is an upper bound for its intrinsic axis ratio. Therefore, B19 probably belongs to the class of early-type "fast rotator" galaxies (Emsellem et al. 2007, 2011, for example). At the same time, it is very small for its luminosity and bears resemblance to the recently discovered compact disk-like systems at redshift $z \approx 2$ (van Dokkum et al. 2008; Bruce et al. 2012).

Our $\sigma_\star$ is based on spectral data from the SDSS DR7. The spectrum was collected with a fiber aperture of $3''$ diameter, under median seeing conditions of $1\rlap{.}''5$ (Joe Hennawi, private communication). Aperture and seeing are a substantial fraction of the effective radius ($0\rlap{.}''74$, corresponding to $1.5\,\mathrm{kpc}$ given in Table 2 of B08 and the angular-diameter distance of $419\,\mathrm{Mpc}$). Thus, $\sigma_\star$ derived from the SLOAN spectrum consitutes an average value over the seeing-convolved aperture, and likely includes substantial contributions from un-resolved rotation. We opt to not use the $\sigma_\star = (412 \pm 27)\,\mathrm{km s}^{-1}$ provided in B08 (SDSS database, aperture-corrected), but the value derived by Oh et al. (2011), $\sigma_\star = (360.3 \pm 9.4)\,\mathrm{km s}^{-1}$, as their analysis includes modeling of emission lines and an advanced quality assessment, amongst others.

6.2.3 PHOTOMETRY AND MULTI-GAUSSIAN EXPANSION

Both our axisymmetric and triaxial dynamical modeling codes require representation of the target's surface brightness by a multi-gaussian expansion (MGE, Emsellem et al. 1994). That is, instead of fitting, for example, a Sérsic profile, or a Sérsic and an exponential as in the common Bulge/Disk-decomposition, all components used have a Gaussian profile (which is a Sérsic profile with index $n = 0.5$). This type of profile is more compact (flat-topped) than "real" galaxies' radial profiles, and therefore multiple Gaussian components are typically needed (typically ~ 10, depending on the galaxy size, structure and the S/N of the data). Using Gaussians as a functional from has the advantage of allowing analytic deprojection of the profile, resulting in representation of the (3D-)luminsity density by (3D-)Gaussians as well. Since Gaussians do not represent a complete orthonormal set of function, the expansion is not unique. As a general rule, one starts from a low number of components, performs the fit each time, and adds components until a satisfactory match with the data is achieved (for exmaple as quantified by the reduced χ^2). One should avoid to produce unecessarily low axis ratio in any of the components, as this restricts the range of viewing angles for which a physically meaningful deprojection is possible. A detailed introduction into MGE of galaxies is given in Cappellari (2002).

Instead of deriving an MGE with the IDL code offered by M. Cappellari[5], we use GALFIT3, which has the advantage of proper pixel weighting using the noise map. B19 shows no signs of isophotal twists, and we fix the orientation of the components to a common value (and centre). For each MGE component, GALFIT3 renders apparent magnitude, m_i, gaussian FWHM$_i$ (in pixels), and flattening q_i. The Gaussian FWHMs need then be converted to angular sizes and the Gaussian dispersions computed, $\sigma_i = \text{FWHM}_i / \sqrt{8 \ln 2}$. The MGE parameters (m_i, σ_i, q_i) are shown in Table 6.3. The global photometry obtained from the MGE is given in Table 6.2. The i-band luminosity was computed via

$$L_i = 10^{(M_\odot - m_i + a_\lambda)/2.5} \cdot \left(\frac{d_L}{\text{Mpc}} \right)^2 \times 10^{10} L_\odot \tag{6.1}$$

using a_λ, $M_{\odot,i}$ and d_L from Table 6.1. Finally, in order to be evaluated by the dynamical models, the MGE component's m_j must be converted to central surface brightness in units of $L_\odot / \text{pc}^2$. For this, we compute the individual Gaussian L_j according to (6.1), use d_A from Table 6.1, and equate

$$\sigma_{\text{pc},j} = \sigma_j \left(\frac{d_{\text{ang}}}{\text{Mpc}} \right) \cdot \text{pc} \quad \Rightarrow \quad I_{0,j} = \frac{L_j}{2\pi q_j \sigma_{\text{pc},j}^2} \tag{6.2}$$

In Table 6.2, as well as in Figure 6.1, we also present the results from fitting B19 with a 2D-Sérsic profile. We find only mild evidence for a disk in the residual image. Interestingly, the Sérsic

---

[5]http://www-astro.physics.ox.ac.uk/ mxc/idl/

MGE model		
apparent magnitude	m_i	16.60
absolute magnitude	M_i	−22.12
luminosity	L	$4.37 \times 10^{10} L_\odot$
2D-Sérsic model		
apparent magnitude	m_i	16.48
absolute magnitude	M_i	−22.24
luminosity	L	$4.89 \times 10^{10} L_\odot$
effective Radius	R_e	$1''4$ (2.9 kpc)
Sérsic index	n	6.9
axis ratio	$q = b/a$	0.52

Table 6.2: Global photometric parameters of B19. Absolute magnitudes include the extinction correction.

m_j	σ_j ['']	q_j
19.81	0.0329	0.491
19.11	0.0957	0.647
19.68	0.378	0.256
19.26	0.220	0.687
18.49	0.660	0.439
18.39	1.28	0.673
17.79	2.95	0.748

Table 6.3: MGE model of our target in the F775W-band, used as input to the dynamical models. m_j are the apparent magnitudes of the j-th Gaussian component, σ_j its dispersion (standard deviation), and q_j its axis ratio.

index is relatively high ($n \approx 7$, whereas $n \sim 4$ would be expected for most elliptical galaxies and higher n for even more luminous central-cluster galaxies), and the effective radius twice the value reported by B08. This may indicate a steeper central profile than the extrapolation of the Sérsic from the outer regions, which could bias the Sérsic to high R_e and n. Indeed, we find mild indication for a central light excess in the residual image, but were not able to adequately account by including a nucleus or additional central Sérsic component. Regardless, the magnitude (as well as the magnitude of the MGE) agree well with the value from the SDSS database (see Table 6.1). The luminosity of the Sérsic model has been computed from the apparent magnitude, m_i, correcting for galactic foreground extinction, a_i.

6.3 AXISYMMETRIC DYNAMICAL MODELS

Our axisymmetric models are based on the axisymmetric Jeans equations (e.g., Binney & Tremaine 2008; van de Ven et al. 2010) in cylindrical coordinates (R, ϕ, z):

$$0 = \frac{\partial \left(R\nu \overline{v_R^2} \right)}{\partial R} + R \frac{\partial \left(\nu \overline{v_R v_z} \right)}{\partial z} - \nu \overline{v_\phi^2} + R\nu \frac{\partial \Phi}{\partial R}$$

$$0 = \frac{\partial \left(R\nu \overline{v_R v_z} \right)}{\partial R} + R \frac{\partial \left(\nu \overline{v_z^2} \right)}{\partial z} + R\nu \frac{\partial \Phi}{\partial z} ,$$

where (v_R, v_ϕ, v_z) are the particle velocities along the coordinate axes, and bars denote the average in the local (small but finite) volume. The Jeans equations relate the second moments of the

local velocity distribution ($\overline{v_R^2}$, $\overline{v_\phi^2}$, $\overline{v_z^2}$ and the "mixed moment" $\overline{v_R v_z}$) to the local tracer particle density (ν) and the local gravitational potential (Φ). Since these consitute two equations for four unknowns once ν (and hence Φ via solving Poisson's equation) is given, the equations cannot be solved unless 2 further assumptions are added. The JAM routine employed in our analysis assumes (1) $\overline{v_r v_z} = 0$, that is, the "velocity ellipsoid" is aligned with the cylindrical coordinate system; and (2) its flattening is constant in the meridional plane, $\overline{v_R^2} = b\overline{v_z^2}$. These assumptions are approximately justified in most axisymmetric systems (Cappellari 2008). $\beta = 1 - 1/b$ is called the *velocity anisotropy*, which by definition is bound between $-\infty$ (no dispersion in the radial direction) and 1 (no dispersion in the tangential plane). The dispersion is "tangentially anisotropic" if $\beta < 0$, "radially anisotropic" if $\beta > 0$, and "isotropic" is $\beta = 0$.

So far, we have considered velocities (their distribution moments) in intrinsic coordinates. However, what is *observed* are their projections on the plane of the sky, encoded in the shapes (broadening) and shifts of spectral features, usually asorption lines in case that stars are the tracer "particle" population. Likewise, instead of the intrinsic $\nu = \nu(\vec{x})$, only the projected density of the tracers can be observed, in form of the *surface brighntess*[6] $I(x', y')$. Thus, ν has to be calculated from I via *deprojection*, which is generally not unique. This is one reason why an MGE is used to characterize $I(x', y')$: the deprojection is unique and analytic, once the viewing angle, i.e. the inclination (i) in case of oblate axisymmetry, is given (Emsellem et al. 1994). Still, the gravitational potential Φ needs to be specified. It can in principle be arbitrary, but is related to the mass density, ρ, via Poisson's equation. One important (usually the dominant) contribution to ρ comes from the stars, $\rho_\star$. Using the (local) *stellar mass-to-light ratio* ($\Upsilon_\star = M_\star/L$), $\rho_\star(\vec{x}) = \Upsilon_\star(\vec{x}) j(\vec{x})$, where the luminosity density j is the result of the MGE deprojection and described by (3D-)Gaussian. If one assumes that *"mass follows light"* per Gaussian component, i.e. that $\Upsilon_\star(\vec{x}) = \Upsilon_\star = $ const., $\rho_\star$ will likewise be described by Gaussians. Other gravitational sources (DM, gas, BH) may be added, as well in form of Gaussian components. It has been shown by Cappellari (2008) that with this MGE parametrization of surface brighntess and (projected) stellar mass density, the observed second moment ($\overline{v_{los}^2}$) of the velocity distribution along the *line-of-sight* (LOSVD) can be calculated in a relatively simple and efficient manner by a single integral.

"JAM", the axisymmetric modeling routine[7] that we employ, makes use of this representation. The computed $\overline{v_{los}^2}$ can be compared to $\overline{v_{los}^2} = v^2 + \sigma_\star^2$ as observed from the spectral lines' mean (v) and dispersion ($\sigma_\star$). The latter are generally measured on several locations ("bins") across the galaxy image. JAM allows to include into the model a central BH, represented by a very small but "dark" Gaussian. It also offers automatic optimization of $\Upsilon_\star$ by minimization of the resulting

---

[6]assuming, as the collisionless Boltzmann equation does, that all stars are identical, the luminosity density is $j(\vec{x}) = L\nu(\vec{x})$, of which $I(x', y')$ is the projection, cf. Binney & Tremaine(2008, §4.1.2)

[7]available at http://www-astro.physics.ox.ac.uk/ mxc/idl/

χ^2 (squared difference of modeled and observed $\overline{v_{los}^2}$, normalized by the latter's measurement uncertainties). We do not make us of this option, but instead calculate $\overline{v_{los}^2}$ on a grid of $(\Upsilon_\star, M_\bullet)$. We choose this approach (1) because it is generally expected (and confirmed by the results) that $M_\bullet$ and $\Upsilon_\star$ are degenerate, and (2) in order to analyze the behaviour of the model in all regions of the parameter space, not only around the locus of the observed $\overline{v_{los}^2}$. Since the SDSS spectrograph fibre, which consitutes the sole available bin in our case, is centred on the target, $\overline{v_{los}^2} = \sigma_\star^2$ and we treat both interchangably in the remainder of this chapter. The integral of $\overline{v_{los}^2}$ over the (circular) fibre aperture is achieved by calculating the model prediction on a regular grid of $0\rlap{.}''15 \times 0\rlap{.}''15$ bins, and the luminosity-weighted sum of those bins which have their centre inside the aperture (after convolving with the $1\rlap{.}''5$ Gaussian seeing).

As mentioned before, our dynamical models require an MGE of the target, as well as the (assumed) viewing angle(s), which cannot be arbitrary for a meaningful deprojection. In the axisymmetric case, the inclination (i) cannot be smaller than allowed by the observed axis ratio, or the MGE component with the smallest axis ratio, q_{min}: $i \geq \cos^{-1} q_{min}$. For the MGE we created, $q_{min} = 0.26 \rightarrow i \geq 75°$. We attempted to establish MGE parametrizations which dispense with a low-q component, but could not achieve a satisfactory fit to the data. this might be surprising as the average axis ratio is about twice as large, ≈ 0.5. On the one hand, and as mentioned in §6.2.3, the residual image suggests the presence of an embedded disk in B19. The low-q component therefore is probably "real" and, at least in an approximate sense, accounts for this (weak) disk component.

We therefore adopt $i = 76°$ as fiducial inclination, as well as a constant $\Upsilon_\star$ throughout the galaxy, i.e. for all Gaussian components except for the BH component. We also use an isotropic velocity distribution ($\beta = 0$) and run JAM on a regular (11^2-grid evenly spaced in the interval $\log M_\bullet \in [6, 11]$ and $\Upsilon_\star \in [1, 9]$. The predicted $\sigma_\star$ are shown in the left panel of Figure 6.2. In order to estimate the effect that changes in i, β and seeing (so far, we have assumed the median seeing during SDSS spectroscopic observations) have, we vary each of these parameters separately and plot the results for $\sigma_\star$ in the right panel of Figure 6.2. Both the choice of inclination (within the allowed range) and seeeing have a negligible impact on the location of $\sigma_\star$ that matches the observed velocity dispersion. Even the influence of β is rather benign, as long as it is varied within reasonable values. As expected, radial anisotropy predicts higher $\sigma_\star$ for a given $(M_\bullet, \Upsilon_\star)$ than tangential anisotropy ($\beta < 0$).

The different assumptions all imply very similar $\sigma_\star$ particularly in the range of $\Upsilon_\star$ inferred by the SPS models. In this range, the $M_\bullet$ needed to match the observed $\sigma_\star$ is also only mildly dependent on the exact value of $\Upsilon_\star$. This allows us to conclude that, within the 95%-confidence intervals of both $\Upsilon_\star$ and $\sigma_\star$, $M_\bullet \in [1.1, 2.3] \times 10^{10} M_\odot$. The shape of the measured $\sigma_\star$-contour in Fig. 6.2 implies that the model behaves differently in two regimes: below $\Upsilon_\star \approx 5$, the BH
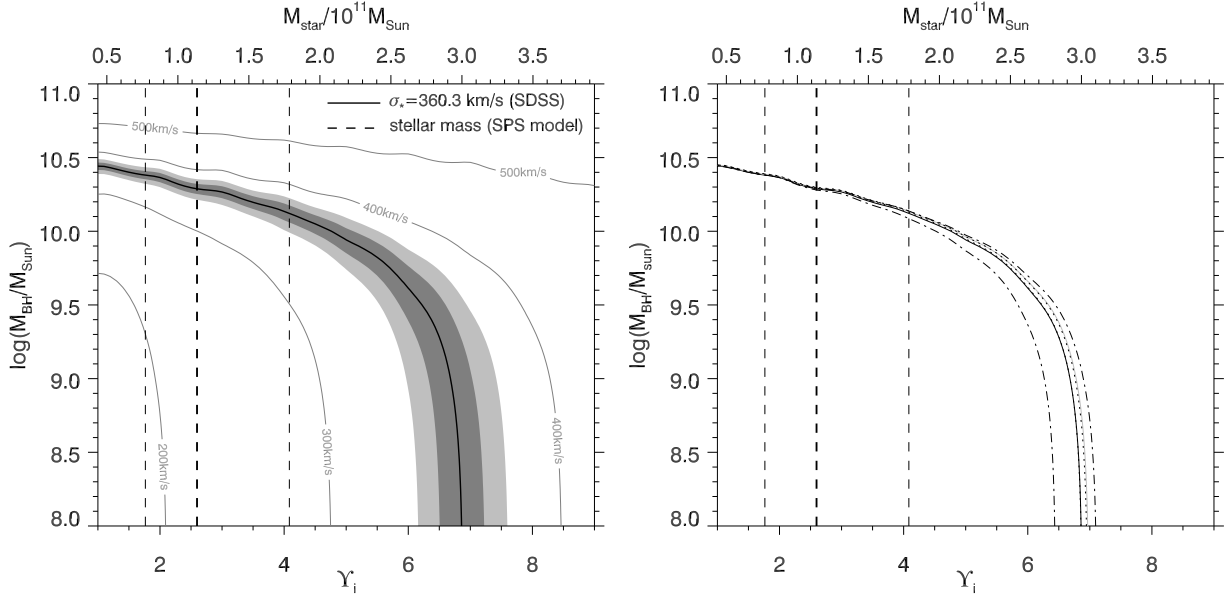
Figure 6.2: $\sigma_\star$-contours in the $(M_\bullet - \Upsilon_\star)$-plane, computed from axisymmetric Jeans models of B19. Left panel: assuming $76°$ inclination, $\beta = 0$ and $1\rlap{.}''5$ spectral seeing. The black solid contour is the locus of the measurement, $\sigma_\star = 360.3\,\mathrm{km s}^{-1}$, and the dark (light) grey regions its $1\sigma(2\sigma)$-confidence regions. Right panel: Loci of the measured $\sigma_\star$ in JAM models with different parameters. The black solid curve is for the same parameters as the left panel. The other curves result from the following changes: $i = 90°$ (grey solid), $\beta = -1.0 \,/\, 0.5$ (upper/lower dot-dashed) and FWHM = 1.0"/2.0" (upper/lower dotted). The dotted overlap with the original parameter curve and that of $i = 90°$, respectively. In both panels, vertical dashed lines denote the median and 95%-confidence region of the stellar mass from SPS modeling (Table 6.1). The top-axis (stellar mass) is $\Upsilon_\star$ multiplied by the MGE-luminosity of B19, $L_i = 4.37 \times 10^{10} L_\odot$.

mass dominates, that is $\sigma_\star$ is mostly only sensitive to changes in $M_\bullet$. Above $\Upsilon_\star \approx 6$, the "optimal" $M_\bullet$ has decreased enough so that $\sigma_\star$ is mostly dependent on $\Upsilon_\star$. This also means that for $M_\bullet \lesssim 10^9 M_\odot$, the model is essentially consistent with the absence of a BH, but this regime is strongly ruled out, as the required mass-to-light ratio of $\approx 7 M_\odot/L_\odot$ is much larger than predicted by the stellar population synthesis model of the SDSS broadband colors ($M_\star/L_i \approx 2.5 M_\odot/L_\odot$, MPA-JHU analysis).

6.4   TRIAXIAL DYNAMICAL MODELS

The previous axisymmetric Jeans models are limited in three ways. First, B19 may not be axisymmetric; it may for example be triaxial and viewed along its major axis, which could make the high $\sigma_\star$ (and surface brightness) more plausible, as already pointed out by Bernardi et al. (2008). It may also be prolate (cigar-shaped) and seen down the minor axis. Second, even if

B19 is oblate, a constant velocity anisotropy (β) per Gaussian component, and a constant "tilt" of the velocity dispersion ellipsoid in the meridional plane are assumed. Although these assumptions may hold approximately for some galaxies, an unusual case like B19 calls for a more general analysis that explores the full range of possible orbital structures and intrinsic shapes, which may explain the high $\sigma_\star$ even in the absence of a putative ÜMBH. Third, the second moments solving the Jeans equations may be unphysical, since the implied phase-space distribution function $f(\vec{x}, \vec{v})$ is not guaranteed to be positive.

Therefore, we use a more general orbit-based technique, the Schwarzschild method (Schwarzschild 1979) to construct realistic dynamical galaxy models with considerable degrees of freedom. The method was first used to fit galaxy models to observed data by Rix et al. (1997), albeit still assuming spherical symmetry. It consists of a given gravitational potential (or equivalently mass density distribution) and calculating (integrating) a large number of different orbits (*the orbit library*), each characterized by energy (E) and angular momentum ($\vec{L}$). The time each orbits spends in a given cell of phase space ($\vec{x}$ and $\vec{v}$) is recorded, and this information projected on the space of observables (surface mass density and line-of-sight velocity distribution, LOSVD). The LOSVD is encoded in the shape and position of the spectral lines by virtue of the Doppler effect (red- and blueshift). Each orbit is then assumed to be populated by a to-be-determined fraction of the total stellar mass. The linear superposition of these orbits (their observables) is then optimized to fit the data by varying the orbital weights. For details about this technique, for example the choice of a suitable grid of orbits see e.g. Rix et al. (1997).

The code we use here is an implementation for triaxial geometry and described in van den Bosch et al. (2008). It employs the MGE parametrization described in §6.2.3 and already used for the axisymmetric models. This means that the mass density is described by a sum of (3D-)Gaussian density profiles with ellipsoidal isodensity surfaces, which can be uniquely and analytically deprojected from the observed surface density (described by the 2D-Gaussian profiles in Table 6.3, and multiplied again by a constant $\Upsilon_\star$), once the *viewing angles* have been assumed. The three viewing angles must be provided pre-modeling, leaving a considerable space of unknowns. Fortunately, the MGE parametrization of the projected density constrains the allowed ranges. Alternatively, and more suitably, the intrinsic shape of the galaxy may be chosen first, from which the viewing angles follow given the projected shape. The intrinsic shape is characterized by $p = b/a$, $q = c/a$ and u, where a, b, and c are the lengths of the major, intermediate and minor axes of the galaxy, and u the scale length compression factor of the system major axis due to projection. In terms of p and q, three basic classes of intrinsic shapes can be distinguished: oblate ($p = 1, q \leq 1$), prolate ($p = q \leq 1$) and triaxial ($q \leq p \leq 1$) systems. Sphericity is a special case of all three with $p = q = 1$.

We choose to explore each of these three principal shapes by one representative model. The oblate case is equivalent to the geometry used by our axisymmetric models (§6.3 and left panel
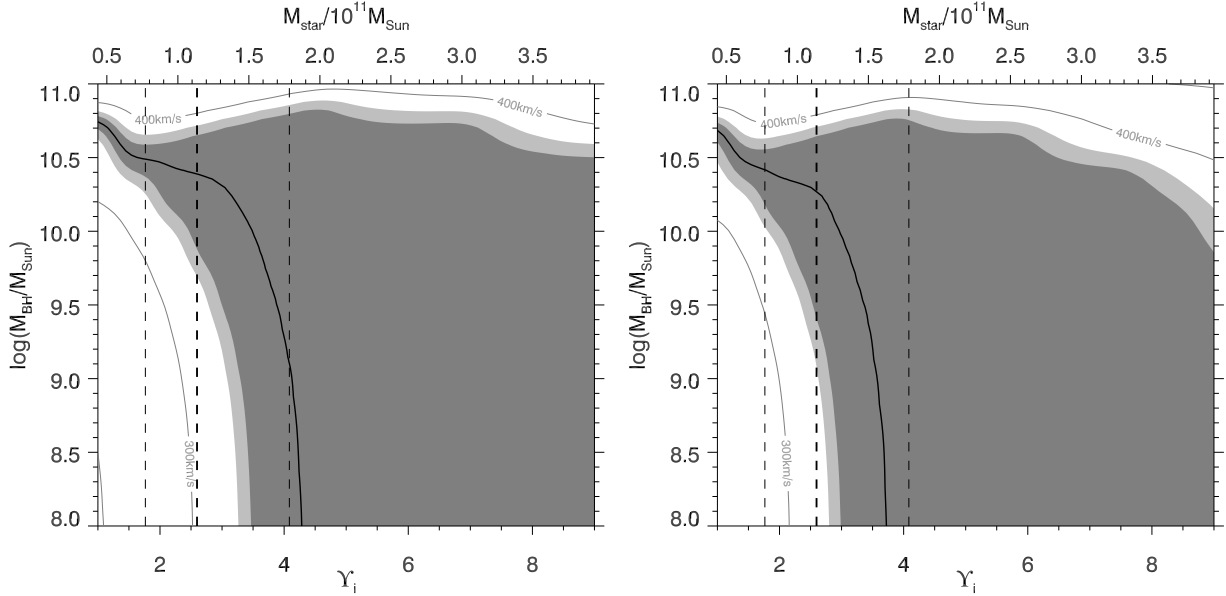
Figure 6.3: Contours of $\sigma_\star$ as a function of $(\Upsilon_\star, M_\bullet)$ as predicted by the Schwarschild models, assuming axisymmetric shape ($i = 76°$). The black solid line is the measurement, and the dark (light) grey areas the $1\sigma(2\sigma)$-confidence region. Vertical dashed lines mark the 2.5%-, 50%- and 97.5-quantiles of the stellar mass estimate from SPS modeling. Left panel: no DM halo. Right panel: DM halo with with NFW profile, $c = 10$ and $M_{200} = 300 M_\star$. The grey areas cover a large parameter space because the Schwarzschild models have great freedom of combining orbits to reproduce the measurement (or a $\sigma_\star$ close to it).

of Figure 6.2) with the fiducial 76° inclination, corresponding to $p = 1$, $q = 0.57$ and $u = 1$. We proceed similarly as before, using the model to predict the $\sigma_\star$ in the spectrograph fibre aperture (after convolution with a $FWHM = 1\overset{''}{.}5$ Gaussian point-spread function). For each assumed mass-to-light ratio $\Upsilon_\star$ and BH mass $M_\bullet$, the orbit library needs to be recomputed in the potential that follows. Further, and in contrast to our axisymmetric modeling, we create a second set of models with an assumed spherical dark matter (DM) halo. The halo is assumed to follow a Navarro-Frenk-White (NFW) profile with concentration index $c_{200} = 10$ (approximate value for a $10^{13} M_\odot$ halo, see e.g. Macciò et al. 2008), and internally represented by an additional set of (spherical) components with Gaussian density profile. Its mass, $M_{200} = M(r = r_{200})$ is chosen to be 300 times the luminous mass. Therefore, the halo is unusually massive for a "normal" galaxy (at $M_\star \approx 10^{11} M_\odot$, $M_{200}/M_\star \approx 100$ according to Moster et al. 2010), chosen to investigate the largest conceivable influence of DM on the dynamics.

The measured $\sigma_\star = (360.3 \pm 9.4)\,\mathrm{km s}^{-1}$ is a boundary condition to the Schwarzschild model, meaning that the code optimizes the orbital weights to produce a $\sigma_\star$ equal, or as close as possible, to the measurement. The results are plotted in Figure 6.3. The black solid line again represents the measured $\sigma_\star = 360.3\,\mathrm{km s}^{-1}$, and the dark (light) shaded areas the $1\sigma(2\sigma)$-confidence region.

From the broad range of $(\Upsilon_\star, M_\bullet)$ over which the measured $\sigma_\star$ is reproduced, in comparison to the axisymmetric Jeans model (Figure 6.2), it can be immediately seen that the Schwarzschild model allows for considerable larger freedom in the system's dynamics. For example, a strong tangential anisotropy of the velocity ellipsoid produces a lower line-of-sight dispersion, even if the enclosed mass (stellar or BH) is large. The general trend remains as in the axisymmetric Jeans models: above $\Upsilon_\star \approx 4$, the BH mass is essentially unconstrained to low values, and below $\Upsilon_\star \approx 3$, $M_\bullet$ is required to be in the range $\approx 10^{10...11} M_\odot$. The domain boundary has moved closer to the estimated $M_\star$, but remains above it – essentially implying an ÜMBH (a more precise statistical characterization of the inferred $M_\bullet$ is given in Section 6.5). The loci of velocity dispersions change only marginally when a DM halo is added.

Although the image of B19 is suggestive of an intrinsically oblate system seen almost edge-on, we must consider the possibility that it is either intrinsically prolate or triaxial if $M_\bullet$ is to be constrained with confidence. For the prolate scenario, we set $p = q = 0.6$ and $u = 1$, commensurate with its apparent axis ratio and a "sideways" viewing direction. The results for $\sigma_\star$ are plotted in the upper panels of Figure **??**, displaying some unusual features, such as $\sigma_\star$ increasing locally if $M_\bullet$ decreases near $(\Upsilon_\star, \log M_\bullet) \approx (6, 10.7)$, and a sharp dependence on $M_\bullet$ in the range $1 < \Upsilon_\star < 6$, $\log M_\bullet \approx 11$. Allowing for a DM halo mediates the former but not the latter behaviour. We suspect this to be indicative of a low overall probability of an intrinsically prolate shape, as the model parameters need to be very finely tuned to reproduce the observations, at least if $\Upsilon_\star < 5$. Clearly, spatially resolved spectral data would be desirable to clear up the situation: for example, detection of rotation around the minor axis would rule out the prolate case.

In the triaxial scenario, the viewing directions are principally along either of semiminor, intermediate or major axis (as well as rotations in the symmetry plane), as far as allowed by the projected shapes of *all* MGE components. In the first two cases, the projected major axis is aligned with the intrinsic major axis, and the intrinsic geometry would be intermediate between the prolate and the oblate case if we see B19 along its intermediate axis. We choose the last case, viewing direction along the intrinsic major axis, as it is in some sense the most "extreme" of the three principal triaxial shapes: B19 is intrinsically longer than what is seen in projection. We choose $p = 0.46$, $q = 0.35$, and the compression factor $u = 0.59$, making B19 quite elongated. As can be seen in Figure **??** (lower panel), our models reproduce the data only in a relatively narrow range, even at large mass-to-light ratios. Yet, the behaviour changes less sharply at some $\Upsilon_\star$ than in the prolate models, and are more reminiscent of the $\sigma_\star$-contour shape predicted by the JAM code. Addition of the DM halo increases $\sigma_\star$, more notably so than for the oblate and prolate models, while the overall model behaviour is unchanged: an anticorrelation of $\Upsilon_\star$ with $M_\bullet$ for constant $\sigma_\star$, as also intuitively expected.

In both prolate and axisymmetric models, an $M_\bullet$ of $\approx 10^{10...11} M_\odot$ is required to explain the data,
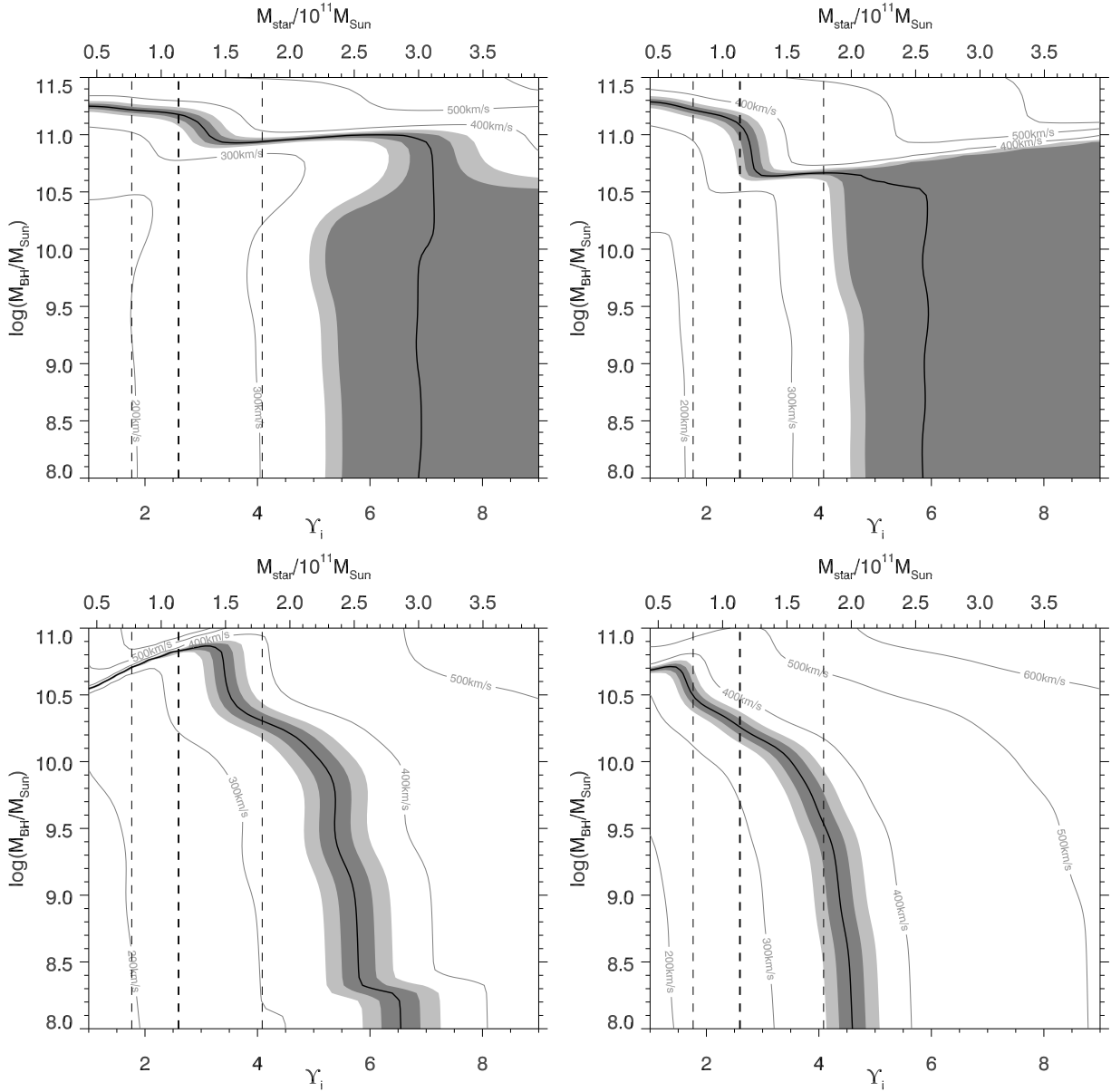
Figure 6.4: Contours of $\sigma_\star$ as a function of $(\Upsilon_\star, M_\bullet)$ as predicted by the Schwarschild models, assuming axisymmetric prolate (upper panels) and triaxial geometry (lower panels). Left panels: models without DM; right panels: including a DM halo. Note that for the plots of the prolate models, the $M_\bullet$-axis has been extended to $\log M_\bullet = 11.5$ (instead of 11.0 as for all other models presented in this Chapter). Description otherwise as in Figure 6.3.

as long as $\Upsilon_\star < 5$.

6.5 INFERRING $M_\bullet$ OR $\Upsilon_\star$

So far, we computed the predicted seeing-convolved and luminosity-weighted velocity dispersion as observed in the SDSS fibre aperture, using first axisymmetric Jeans models, and then more general triaxial Schwarzschild models. In order to determine the probability of $M_\bullet$ or $\Upsilon_\star$, we take an approach akin to Bayesian inference, using the dynamical model-predicted $\sigma_{\star,\text{mod}} = \sigma_\star(\Upsilon_\star, M_\bullet)$ to compute a likelihood:

$$\mathcal{L} = \mathcal{L}(\sigma_\star \,|\, \Upsilon_\star, M_\bullet) = \frac{1}{\Delta(\sigma_\star)\,\sqrt{2\pi}} \exp\left\{ -\frac{(\sigma_\star - \sigma_{\star,\text{mod}})^2}{2[\Delta(\sigma_\star)]^2} \right\} , \tag{6.3}$$

where $\Delta(\sigma_\star)$ is the standard error of the velocity dispersion measurement. Multiplying the likelihood by a prior distribution of $\Upsilon_\star$ and $M_\bullet$ then gives the desired posterior distribution of $(\Upsilon_\star, M_\bullet)$.

We consider first the situation in which the stellar mass-to-light ratio is already known, determined by stellar population-synthesis modeling of the SDSS broadband colors (Table 6.1). The MPA-JHU DR7 release source[8] provides the inferred probability distribution of $\log M_\star$ in form of its $\{2.5, 16, 50, 84, 97.5\}$-percentiles, as well as its mean and mode. The mean, mode and median (50-th percentile) are sufficiently similar, and the intervals sufficiently symmetric, to assume that it approximately follows a Gaussian distribution in $\log M_\star$. The resulting log-normal distribution in $M_\star$ (and $\Upsilon_\star$) is suitable, as $M_\star$ and $\Upsilon_\star$ must be positive. We use the mean, mode, median and interval centres of $P(M_\star)$ to estimate the mean of the Gaussian approximation ($\mu_{\log M_\star} = 11.06$), and the average of the given interval lengths to estimate its standard deviation ($\sigma_{\log M_\star} = 0.08$). Then, $\log \Upsilon_\star = \log M_\star - \log L$ and the prior distribution on $\Upsilon_\star$ is

$$P(\Upsilon_\star) = \frac{1}{\ln 10} \frac{1}{\sigma_{\log \Upsilon_\star}\,\sqrt{2\pi}} \frac{1}{\Upsilon_\star} \exp\left\{ -\frac{\left(\log \Upsilon_\star - \mu_{\log \Upsilon_\star}\right)^2}{2\sigma_{\log \Upsilon_\star}^2} \right\} , \tag{6.4}$$

with $\mu_{\log \Upsilon_\star} = 0.44$ and $\sigma_{\log \Upsilon_\star} = 0.08$. The prior on $M_\bullet$ is assumed to be uniform in $\log M_\bullet \in [8.0, 11.5]$, and zero elsewhere. The posterior in $(\Upsilon_\star, \log M_\bullet)$ is computed and marginalized over $\Upsilon_\star$. The resulting posterior distributions in $\log M_\bullet$, for each of our models (Jeans oblate, Schwarzschild oblate, prolate and triaxial geometry) are plotted in Figure 6.5. There, the dotted curves are the result from including a (very massive) DM halo, while the models without DM halo are represented by a solid curve, respectively. The predicted $M_\bullet$ decreases once the halo

---

[8]http://www.mpa-garching.mpg.de/SDSS/DR7/Data/stellarmass.html

model :	JAM	oblate	oblate+DM	prolate	prolate+DM	triaxial	triaxial+DM
$\log(M_\bullet/L_\odot)$	10.2 ± 0.1	10.2 ± 0.4	10.0 ± 0.6	11.1 ± 0.1	10.9 ± 0.2	10.7 ± 0.2	10.2 ± 0.2
$\Upsilon_\star \, [M_\odot/L_{\odot i}]$	6.8 ± 0.4	6.2 ± 2.3	5.7 ± 2.3	8.0 ± 1.6	7.2 ± 1.8	5.7 ± 0.4	4.4 ± 0.3

Table 6.4: 68%-confidence intervals, given as interval centre and relative location of the limits, for our predictions (posterior distributions) of $\log M_\bullet$ and $\Upsilon_\star$. The former assume the $M_\star$ (and hence $\Upsilon_\star$) provided by the MPA-JHU stellar population synthesis models (see Table 6.1 and eqn. 6.4) as a prior distribution, while the latter use $\log M_\bullet = 8.6 \pm 0.5$ (Gaussian mean±dispersion) from the $M_\bullet - L_{K,\text{tot}}$ relation as a prior on $M_\bullet$.

is assumed, As expected, since part of the observed distribution is caused by the halo potential while the stellar mass is fixed (independent on the halo). The average difference in $M_\bullet$ is on the order of a few $\times 0.1$ dex. Note that Jeans models with DM halo have not been created. All models' $\log M_\bullet$-distributions are fairly narrow (about ± 0.3 around the maximum), except for the oblate geometry, which has a non-negligible "tail" towards low $M_\bullet$, especially if a DM halo is included. For each model, the centre and size of the $\log M_\bullet$ 68%-confidence interval is given in Table 6.4.

It is immediately clear from Figure 6.5 that, as anticipated from the $\sigma_\star$-contours in the $(\Upsilon_\star, \log M_\bullet)$-plane (Fig.s 6.2-**??**), *for all models and geometries*, the largest probability in $\log M_\bullet$ is placed far (about 2 orders of magnitude) above the expectation from the K-band $M_\bullet - L_{\text{tot}}$ scaling relation (left vertical line). Although the BH scaling relation allows for intrinsic scatter of ≈ 0.5 dex, B19's $M_\bullet$ is still about one order of magnitude above the 95%-confidence interval limit of the scaling relation (right vertical line). The expectation from the $M_\bullet - L_{\text{bul}}$ relation is very similar, since B19 has no discernible bulge in the ACS image. If there *was* a bulge, the predicted $M_\bullet(L_{\text{bul}})$ would be smaller, and the variance with our result even greater.

If we do not assume an informative prior on $\Upsilon_\star$, but instead $\log M_\bullet(L_{K,tot} = 8.6 \pm 0.5$ as expected from B19's K-band luminosity and the $M_\bullet - L_{\text{t,imp}}$ relation, we can use our dynamical models to infer $\Upsilon_\star$. Its posterior distributions are plotted in Figure 6.6, and the 68%-confidence intervals are given in Table 6.4. The results hold that $\Upsilon_\star$ must then be $\gtrsim 5$, more than twice of what SPS modling and SED fitting predict, and well outside of the latters 95%-confidence interval. The broadest distribution of $\Upsilon_\star$ is obtained from Schwarschild models of an oblate galaxy geometry, while prolate and triaxial, as well as oblate Jeans models constrain $\Upsilon_\star$ to a relatively narrow range. It seems that the oblate geometry allows for a broader range of orbital structures that are consistent with the data, while prolate and triaxial models need to be relatively "fine-tuned". Similarly, the assumptions implicit in the JAM model restrict the predictions. It should be noted that the results are virtually independent on the assumed $M_\bullet$, as long as it is below $\sim 10^9 M_\odot$.
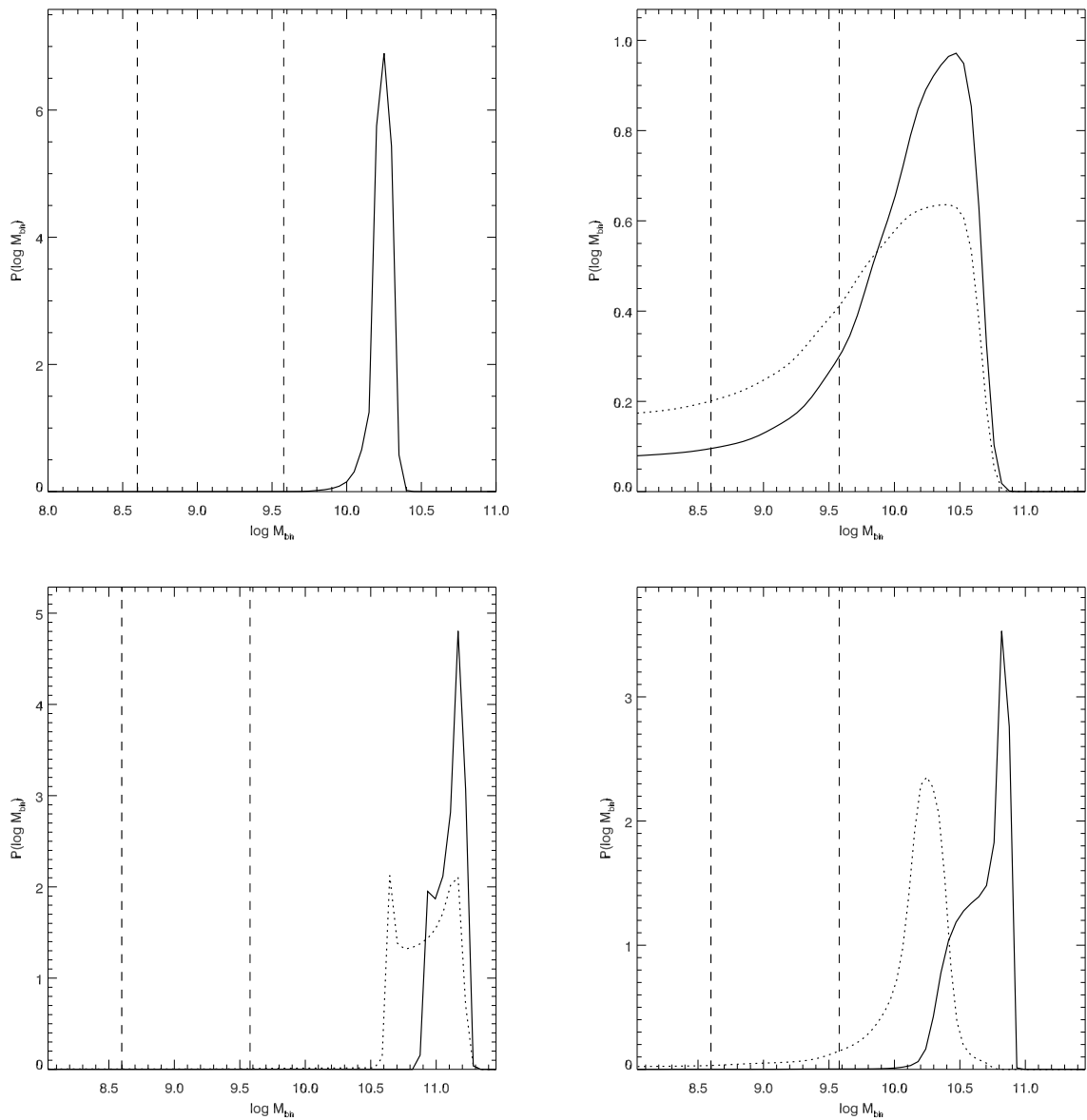
Figure 6.5: Posterior distributions of $\log M_\bullet$, obtained with oblate Jeans modeling (top-left panel) and Schwarzschild modeling (oblate: top-right, prolate: bottom-left, triaxial: bottom-right panel), with (dotted curve) and without (solid curve) a very massive DM Halo ($M_{200} = 300 M_\star$), respectively. SPS modeling was used as a prior on $\Upsilon_\star$ (eqn. 6.4), and a uniform prior on $\log M_\bullet$. The vertical dashed lines denote $\log M_\bullet(L_{K,tot})$ and its upper 2σ-limit as expected from B19's K-band luminosity and the $M_\bullet - L_{t,imp}$ relation derived in chapter 4.
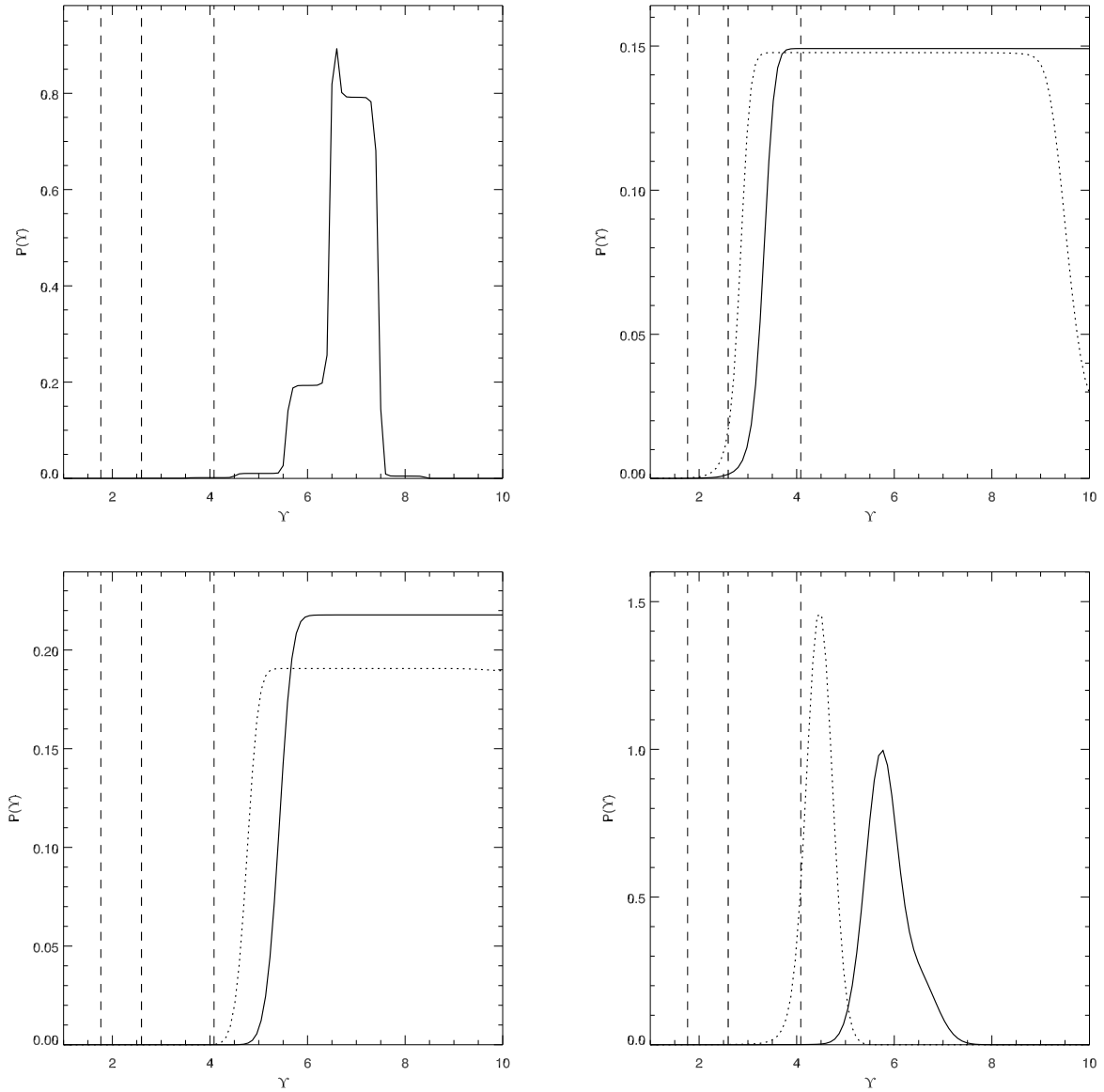
Figure 6.6: Posterior distributions of $\Upsilon_\star = (M/L)$, obtained with oblate Jeans modeling (top-left panel) and Schwarzschild modeling (oblate: top-right, prolate: bottom-left, triaxial: bottom-right panel), with (dotted curve) and without (solid curve) a very massive DM Halo ($M_{200} = 300 M_\star$), respectively. $\log M_\bullet = 8.6 \pm 0.49$ as expected from the K-band $M_\bullet - L_{\text{tot}}$ relation was used as a prior, as well as a uniform prior on $\Upsilon_\star$. The vertical dashed lines denote the [2.5,50,97.5]-percentiles of $P(\Upsilon_\star = M_\star/L_i)$, which is expected from SPS modeling (see Tables 6.1,6.2 and equation 6.4).

6.6 DISCUSSION

Our investigation has shown B19 to host a central Black Hole with $M_\bullet = 1.5 \times 10^{10\pm0.4} M_\odot$ if the stellar dynamics are simulated by triaxial Schwarzschild models and an oblate intrinsic galaxy shape. Addition of a very massive DM halo of $M_{200} = 300 M_\star$ results in $M_\bullet = 1.0 \times 10^{10\pm0.6} M_\odot$. If other intrinsic shapes (prolate / triaxial) are assumed, or a restricted modeling using the solutions of the axisymmetric Jeans equations is performed, the inferred $M_\bullet$ would be even higher, up to $10^{11} M_\odot$, and the 1σ-confidence interval smaller, $\lesssim 0.2$ dex. It should be noted that the result depends on the prior on $M_\bullet$: it was assumed to be uniform in $\log M_\bullet$, implying $P_{\mathrm{pri}}(M_\bullet) \propto M_\bullet^{-1}$. Therefore, a uniform prior in $M_\bullet$ would increase the probability at high $M_\bullet$, although the effect would be significant only for the oblate case where the posterior is relatively broad. Wheras it is perhaps surprising that this result could be obtained with only one observation of the spectrum in a large ($3''$ diameter) aperture under modest seeing conditions ($\approx 1\!''\!.5$), and especially considering B19's distance of ~ 500 Mpc, the data unfortunately do not permit a more precise determination of intrinsic shape and $M_\bullet$.

Regardless, even when the lowest of our $M_\bullet$ estimates is adopted, B19 therefore hosts a BH that is at least ~ 25, and more likely ~ 50, times more massive than expected from the $M_\bullet - L_{\mathrm{bul}}$ and $M_\bullet - L_{\mathrm{tot}}$ relations, considering B19's moderate luminosity of $L = 4.4 \times 10^{10} L_\odot$ (i-band). This implies either that B19 belongs to the high-mass "tail" of the distribution that BH masses and galaxy (or bulge) luminosities follow, or that B19 and its BH followed a different formation process than the "main sequence" galaxies/SMBHs. In other words, B19 and its BH may not belong to the established relations, questioning their universality. Such was already implied by several studies that variously claim pseudobulges, barred galaxies or generally very late-type galaxies to comply with separate scaling relations (with L or $\sigma_\star$) in which $M_\bullet$ is *below* the established relation for (classical) bulges (e.g., Hu 2008; Greene et al. 2010; Graham et al. 2011; Sani et al. 2011). Yet, evidence for this was hitherto rather inconclusive or disputed (Beifiori et al. 2012). On the other hand, recent $M_\bullet$ measurements of Rusli et al. (2011) and van den Bosch et al. (2012) have, like our study, found a $M_\bullet$ that is much *above* the expectation from the scaling relation(s).

If one assumes B19 to belong to the established relation's "wing", this at least also implies with high probability that the shape of the intrinsic scatter is not Gaussian for strong offsets from the relation ridge line, as the implied probabilty of observing such an "übermassive" BH would be far too low to ever be observed. Instead, the distribution wings must be more extended than a Gaussian, which in itself could be an indication of an occasional "extreme" BH-galaxy evolutionary process. In a sense, this hypothesis therefore becomes confluent with non-universality of the scaling relations. More specifically, if simultaneous merging of BH and galaxies in a hierarchical cosmology are primarily responsible to establish an $M_\bullet - L$ (with L tracing $M_\star$) relation at late cosmic times and for massive galaxies (Peng 2007; Jahnke & Macciò 2011), then the observation

we made seems to be almost impossible: all, or almost all, merging partners of B19 must have featured the same unusually high $M_\bullet/M_\star$-ratio, which seems extremely unlikely given the average ratio and the convergence towards the average distribution that (almost) all merging partenrs should have particpiated in. Of course, B19 may not have undergone any major or intermediate mergers; if other processes are neglected, this would imply that what we measure now is still the *BH seed*. Such a high BH seed mass would indeed be sensational. The absence of significant past mergering activity is circumstantially supported by B19's regular isophotes and its small size – which would resemble the presumed evolutionary state of recently detected compact early-type galaxies at high redshift (van Dokkum et al. 2008; Bruce et al. 2012), and by predictions that (especially minor) mergers should increase the observed sizes (Hilz et al. 2012b,a). Therefore, it is thinkable that B19's BH grew by "quiescent", but rich and continuous, accretion of low-angular momentum gas that somehow did not lead to substantial star formation. In this scenario, the mechanisms of allowing the gas to come so close to the centre would be interesting and unusual. On the other hand, possibly B19 did undergo mergers, with the merging parters having "normal" BH-galaxy mass ratios, but then there should have been extremely strong BH feedback that prevented star formation before BH merging and merger-induced gas accretion could increase $M_\bullet$ to the observed value.

The results presented so far relied on assuming the stellar mass for B19, that is the probability distribution thereof, as derived from SED fitting and SPS modeling (the MPA-JHU data release). One may suspect that somehow the population synthesis was compromised by B19's redshift or intervening intergalactic absorption, yet their result is supported by SEAGal/Starlight (SPS modeling of spectra and line indices, see see http://www.starlight.ufsc.br/). Therefore, the only realistic reason for $\Upsilon_\star$ being heavily underestimated by these models, is that its initial mass function (IMF) is unusually bottom-heavy, with a large population of low-mass stars (as stellar $L \propto M^{2.5...4}$ for individual stars). Alternatively, the stellar population might include a substantial fraction of dark stellar remnants. It should be pointed out that our photometry is based on *i*-band imaging, that is at long wavelengths (almost in the near-infrared), where $\Upsilon_\star$ is generally not expected to assume high values.

It has to be kept in mind that only the high-resolution HST/ACS imaging enabled us to obtain the results, by effectivey constraining the stellar mass distribution (for a given intrinsic shape and assuming a spatially invariant $\Upsilon_\star$, i.e "mass follows light"). Unavoidable ambiguity of the intrinsic shape remains. Yet, prolate and triaxial models appear somewhat less likely. This is not because the image would suggest so: the MGE model, which was used to parametrize the projected distribution of surface brightness, clearly permits viewing angles that lead to non-oblate deprojected geometries. Rather, prolate and especially triaxial models require more finely tuned $M_\bullet$ and stellar mass-to-light ratio ($\Upsilon_\star$) to reproduce the obervations. In other words, the oblate model allows for a larger range of orbit "combinations" (orbital weights), if $M_\bullet$ and $\Upsilon_\star$ require

them. This heuristically *suggests* that an oblate shape is more likely.

Resolution of this ambiguity can be reached via at least two avenues. The obvious is to perform spectral observations with higher spatial resolution and larger spatial coverage, including measurement of spatially resolved rotation. For example, a prolate shape would be ruled out if rotation is found to proceed around the projected minor axis (and similarly for oblate shape and rotation around the major axis). The $\sigma_\star$-profile could help breaking the $M_\bullet - \Upsilon_\star$ degeneracy, which so far has required us to adopt an independently determined $M_\star$ for a meaningful $M_\bullet$ measurement, and prevented us to determine both $M_\bullet$ and $\Upsilon_\star$ independently from one another by dynamical modeling alone. Such observations have been propsed for the current observing semester at VLT/FORS, and the observing time granted. Observations are expected to commence in early 2013.

Second, the preferred intrinsic geommetry could be constrained better by Bayesian inference. As the current implementation of the Schwarzschild models automatically optimizes the orbital weights to reproduce the observed dispersion, the models artificially broaden the set of consistent $(\Upsilon_\star, M_\bullet)$ parameters. It can be expected that the models that reproduce the observed $\sigma_\star$ for prolate and triaxial geometry (Figure **??**) have a lower overall probability (evidence) han the oblate models, due to a narrow(er) "peak" in the allowed space of orbital weights. Similarly, even in the oblate case (6.3), models near the edge of the measurement standard errors may be expected to be more unlikely, as they, too, may well require excessive "fine-tuning" of the orbital weights, and possibly "extreme" orbital structures such as strong radial anisotropy. In the future, we plan to characterize the orbital structure from the existing models (i.e. using the best-fit orbital weights), which would possibly not only give insight into the "reasonability" of the orbital structure, but also into the formation of B19. We also plan to extend the current analaysis to several more of the objects with high $\sigma_\star$ (and low L) that were listed in Bernardi et al. (2008). This invesigation should put the assertion of non-universality to a further test, or alternatively demonstrate that some "exotic" IMFs exist in a non-negligible number of galaxies.

ACKNOWLEDGMENTS

7

SUMMARY AND OUTLOOK

The research presented in this thesis was centered on improving and securing the characterization of the local scaling relations linking the masses ($M_\bullet$) of Supermassive Black Holes (BHs) with their host galaxies' bulge and total luminosties (L_{bul} and L_{tot}). Motivation for this came from inconcistencies between previous studies thereof, and from concerns about the reliability of the bulge luminosities on which they were based, which implied, for example, that it could not be decided whether the fundamental correlation of $M_\bullet$ is with L_{tot}, rather than L_{bul}. The uncertainites in the scaling relations' characterization directly translate into uncertainties in secondary BH mass estimators, the demography of BHs, and in constraining current theories of BH-galaxy co-evolution. In order to decrease random and systematic uncertainties of the luminosities that define the scaling relations, we conducted a dedicated imaging survey of 35 galaxies of all Hubble types with directly and securely measured $M_\bullet$. Accuracy of L_{bul} was a concern in particular, since their determination requires disentangling the light of the bulge from that of other morphological components. Therefore, the survey was designed to significantly improve the resolution and signal-to-noise ratio of the data hitherto available for these galaxies. Imaging was performed at near-infrared (NIR) wavelengths, at which dust obscuration is a minimal concern. Special emphasis needed to be placed on the observing strategy and data reduction to ensure accurate removal of the high and variable NIR background that otherwise compromises photometry of extended objects. Owing to the quality of the obtained data and the flexibility offered by of the GALFIT3 fitting code, decomposition of galaxy light and determination of structural bulge parameters could be performed with unprecedented detail.

As a result, it could be determined that the logarithmic slope of the $M_\bullet - L_{bul}$ correlation is lower than previously thought, implying that the average ratio of $M_\bullet$ to bulge luminosity decreases whith increasing L_{bul} (or $M_\bullet$) of the host galaxy. By virtue of the stellar mass-to-light ratio, which is known to increase with bulge luminosity, it immediately follows with high confidence ($\gtrsim 99\%$) that also the ratio of $M_\bullet$ to bulge stellar mass is not constant. At the same time, $M_\bullet$ was

found to be approximately proportional to the *total* luminosity and stellar mass of the host galaxy. Despite the improved data quality and image analysis, the intrinsic scatter (ϵ) of the $M_\bullet - L_{\mathrm{bul}}$ relation did not decrease from previous studies, remaining at $\epsilon \gtrsim 0.42$. Most importantly, it is *not* significantly different from the intrinsic scatter of the $M_\bullet - L_{\mathrm{tot}}$ relation, contrary to commonplace scholary opinion that was based on a few early studies. It could further be determined that the slope of the $M_\bullet - L_{\mathrm{bul}}$ correlation is systematically biased to high values if the decomposition ignores galaxy components other than bulge and disk. In conjunction with the high requirements that measuring L_{bul} places on data quality and analysis, these results imply that the $M_\bullet - L_{\mathrm{tot}}$ relation should be preferred over $M_\bullet - L_{\mathrm{bul}}$ as an indirect $M_\bullet$ estimator. Additionally, they might require a re-evaluation of the currently held view that the formation of $M_\bullet$ and host galaxy *bulge* are intimately connected. Yet, a meaningful exploration of the theoretical consequences was outside of this thesis' scope.

An important theoretical aspect of the BH scaling relations is whether and how their intrinsic scatter changes as a function of the galaxy properties or BH mass. Although such a non-uniform intrinsic scatter is qualitatively predicted by several theoretical studies, quantification of this phenomenon in the observed scaling relations was hitherto not performed. Likewise, the methods that are usually applied to fit the BH scaling relations prescribe that the intrinsic scatter resides in one coordinate only. In this thesis, a method was presented that is capable of determining both the degree of variability in the intrinsic scatter, and allows for its potential bi-directionality. This method was applied to the $M_\bullet - L_{\mathrm{bul}}$ and $M_\bullet - L_{\mathrm{tot}}$ correlations, with the result that the observed intrinsic scatter indeed appears to decrease with host galaxy (bulge) luminosity, but that the current data do not allow conclusions here with high confidence. The intrinsic scatter was found to be probably bi-directional.

In order to further contribute to our understanding of the BH-galaxy connection, this thesis also presented the measurement of a BH mass that apparently does *not* concur with the established scaling relations. The investigation concluded that in this case, $M_\bullet$ is much more massive than expected from its host galaxy's luminosity, as long as reasonable assumptions about the stellar mass-to-light ratio are made. Corroborating a similar finding of a recent publication by van den Bosch et al. (2012), this result therefore questions the universality of the scaling relations and the implied physical processes regulating BH growth and galaxy evolution. The analysis alternatively implies this galaxy may exhibit an anomalously high mass-to-light ratio, which likewise would pose a theoretical challenge.

In this thesis, several methodological aspects of the analysis were explored and developed. As part the NIR-imaging survey, an observing strategy was devised that promotes the accurate removal of the NIR background. A specialized data reduction pipeline facilitating this NIR background removal was developed. It was recognized that the best compromise between random and systematic accuracy could be achieved by analyzing the NIR background *level* separately from

its *structure*. In order to preserve the high quality of the raw images and to prevent degradation of the point-spread function upon co-adding the required 20 ... 100 exposures *per galaxy*, the images needed to be astrometrically re-calibrated. Analysis of the deep final image stacks showed that galaxies, including many early-types, exhibit surprisingly abundant substructure. It was found that the spheroidal stellar component is not always well described by a single Sérsic profile, and that ambiguities in separating the bulge light may persist despite improved data quality. The efforts made to obtain a meaningful, i.e. astronomically interpretable, decomposition indicated that the current photometric definition of bulges in terms of a parametrized surface brightness profile may be sub-optimal. Related to this is the principal uncertainty about the number and profiles of the other components, which could only be reduced here due to the high image quality. Consequentially, meaningful confidence intervals of bulge structural parameters cannot be provided. This study also confirmed that "classical" bulges often co-exist with "inner disks", which may be sometimes be interpreted as "pseudobulges". Considering this and the potential uncertainties in the decomposition, establishing BH scaling relations based on distinguishing galaxies with pseudobulges appears questionable at the moment. As an aside, it was demonstrated that constraints on the (bulge) profile parameters are provided at all radial scales, not only the inner regions of galaxies where the residual amplitudes are typically high. This confirms the findings of Peng et al. (2010), and dispels claims made in Sani et al. (2011).

Following the analysis of this thesis, a number of topics for future work remained or emerged. First, the number of directly measured $M_\bullet$ has approximately doubled since the presented observations of BH host galaxies were proposed. Notably, the share of late-type galaxies in the up-to-date host galaxy sample has increased, for which the detailed photometric analysis performed in this thesis would be particularly useful. Naturally, an increased sample size will probably narrow the confidence intervals of the parameters. Repeating this kind of analysis for the new sample members is also important considering the various sub-relations for galaxies with late-type morpholgy (bars, pseudobulges) that were suggested in the recent literature. The relevance of these sub-relations should be quantified by Bayesian inference. In order to further illuminate the BH-galaxy connection, the simultaneous correlation of $M_\bullet$ with more than one global host galaxy property could also be re-analysed within the Bayesian framework, possibly the method presented in this thesis, that is including variabile and bi-directional intrinsic scatter.

The BH scaling relations and their characerization do not only depend on the size of the sample, but critically also on the accuracy of the data and the given measurement uncertainties. In order to preclude systematic bias, a homogenous analysis of BH masses by non-restrictive models would therefore be desirable. The Schwarschild Method appears to be such a technique for modeling BH masses without unwarranted restrictions. Ideally, the results of the dynamical modeling would be available in form of the full $M_\bullet$ probability distribution (instead of a central value and some confidence interval). Establishing the $M_\bullet$ distribution of a BH measurement should proceed

via Bayesian inference instead of using the χ^2-statistic of the best-fit model. This is particularly true when the data do not strongly constrain the model parameters, as was the case of the BH mass analyzed in the last chapter of this thesis.

Upcoming observational facilities, such as the E-ELT and JWST, may well make it possible to gather sufficient data to robustly constrain BH masses and host galaxy properties for a complete sample of nearby galaxies, thereby removing potential sample selection biases. In conjunction with proper statistical inference as discussed in this thesis, these observations can be expected to yield accurate scaling relations that are fundamental to BH estimators and galaxy co-evolution models, and should make it possible to eventually explain the origin of Supermassive BHs.

ACKNOWLEDGEMENTS

BIBLIOGRAPHY

Akritas, M. G., & Bershady, M. A. 1996, ApJ, 470, 706

Atkinson, J. W., et al. 2005, MNRAS, 359, 504

Bacon, R., Emsellem, E., Combes, F., Copin, Y., Monnet, G., & Martin, P. 2001, A&A, 371, 409

Bailer-Jones, C. A. L. 2012a, A&A, 546, A89

—. 2012b, A&A, 546, A89

Barth, A. J., Sarzi, M., Rix, H.-W., Ho, L. C., Filippenko, A. V., & Sargent, W. L. W. 2001, ApJ, 555, 685

Batcheldor, D. 2010, ApJ, 711, L108

Beifiori, A., Courteau, S., Corsini, E. M., & Zhu, Y. 2012, MNRAS, 419, 2497

Bell, E. F., & de Jong, R. S. 2001, ApJ, 550, 212

Bennert, V. N., Auger, M. W., Treu, T., Woo, J.-H., & Malkan, M. A. 2011, ApJ, 742, 107

Bernardi, M., Hyde, J. B., Fritz, A., Sheth, R. K., Gebhardt, K., & Nichol, R. C. 2008, MNRAS, 391, 1191

Bertin, E. 2006, in Astronomical Society of the Pacific Conference Series, Vol. 351, Astronomical Data Analysis Software and Systems XV, ed. C. Gabriel, C. Arviset, D. Ponz, & S. Enrique, 112

Bertin, E., & Arnouts, S. 1996, A&AS, 117, 393

Bertin, E., Mellier, Y., Radovich, M., Missonnier, G., Didelon, P., & Morin, B. 2002, in Astronomical Society of the Pacific Conference Series, Vol. 281, Astronomical Data Analysis Software and Systems XI, ed. D. A. Bohlender, D. Durand, & T. H. Handley, 228

Binney, J., & Tremaine, S. 2008, Galactic Dynamics: Second Edition (Princeton University Press)

Blakeslee, J. P., et al. 2009, ApJ, 694, 556

Bower, G. A., et al. 1998, ApJ, 492, L111

—. 2001, ApJ, 550, 75

Bruce, V. A., et al. 2012, MNRAS, 427, 1666

Capetti, A., Marconi, A., Macchetto, D., & Axon, D. 2005, A&A, 431, 465

Cappellari, M. 2002, MNRAS, 333, 400

—. 2008, MNRAS, 390, 71

Cappellari, M., Verolme, E. K., van der Marel, R. P., Verdoes Kleijn, G. A., Illingworth, G. D., Franx, M., Carollo, C. M., & de Zeeuw, P. T. 2002, ApJ, 578, 787

Cisternas, M., et al. 2011, ApJ, 741, L11

Cole, S., et al. 2001, MNRAS, 326, 255

Cretton, N., & van den Bosch, F. C. 1999, ApJ, 514, 704

Croton, D. J., et al. 2006, MNRAS, 365, 11

Dalla Bontà, E., Ferrarese, L., Corsini, E. M., Miralda-Escudé, J., Coccato, L., Sarzi, M., Pizzella, A., & Beifiori, A. 2009, ApJ, 690, 537

Davies, R. I., et al. 2006, ApJ, 646, 754

de Francesco, G., Capetti, A., & Marconi, A. 2006, A&A, 460, 439

Devereux, N., Ford, H., Tsvetanov, Z., & Jacoby, G. 2003, AJ, 125, 1226

Djorgovski, S., & Davis, M. 1987, ApJ, 313, 59

Dressler, A., Lynden-Bell, D., Burstein, D., Davies, R. L., Faber, S. M., Terlevich, R., & Wegner, G. 1987, ApJ, 313, 42

Emsellem, E., Dejonghe, H., & Bacon, R. 1999, MNRAS, 303, 495

Emsellem, E., Monnet, G., & Bacon, R. 1994, A&A, 285, 723

Emsellem, E., et al. 2007, MNRAS, 379, 401

—. 2011, MNRAS, 414, 888

Faber, S. M., & Jackson, R. E. 1976, ApJ, 204, 668

Ferrarese, L. 2002, ApJ, 578, 90

Ferrarese, L., & Ford, H. 2005, Space Sci. Rev., 116, 523

Ferrarese, L., & Ford, H. C. 1999, ApJ, 515, 583

Ferrarese, L., Ford, H. C., & Jaffe, W. 1996, ApJ, 470, 444

Ferrarese, L., & Merritt, D. 2000, ApJ, 539, L9

Ferrarese, L., et al. 2006, ApJS, 164, 334

Freedman, W. L., et al. 2001, ApJ, 553, 47

Gebhardt, K., Adams, J., Richstone, D., Lauer, T. R., Faber, S. M., Gültekin, K., Murphy, J., & Tremaine, S. 2011, ApJ, 729, 119

Gebhardt, K., et al. 2000, ApJ, 539, L13

—. 2007, ApJ, 671, 1321

Graham, A. W. 2007, MNRAS, 379, 711

Graham, A. W., Onken, C. A., Athanassoula, E., & Combes, F. 2011, MNRAS, 412, 2211

Granato, G. L., De Zotti, G., Silva, L., Bressan, A., & Danese, L. 2004, ApJ, 600, 580

Greene, J. E., Ho, L. C., & Barth, A. J. 2008, ApJ, 688, 159

Greene, J. E., et al. 2010, ApJ, 721, 26

Greenhill, L. J., Gwinn, C. R., Antonucci, R., & Barvainis, R. 1996, ApJ, 472, L21

Greenhill, L. J., et al. 2003, ApJ, 590, 162

Gültekin, K., Tremaine, S., Loeb, A., & Richstone, D. O. 2011, ApJ, 738, 17

Gültekin, K., et al. 2009, ApJ, 698, 198

Häring, N., & Rix, H.-W. 2004, ApJ, 604, L89

Herrnstein, J. R., Moran, J. M., Greenhill, L. J., & Trotter, A. S. 2005, ApJ, 629, 719

Herrnstein, J. R., et al. 1999, Nature, 400, 539

Hilz, M., Naab, T., & Ostriker, J. P. 2012a, ArXiv e-prints

Hilz, M., Naab, T., Ostriker, J. P., Thomas, J., Burkert, A., & Jesseit, R. 2012b, MNRAS, 425, 3119

Hogg, D. W., Bovy, J., & Lang, D. 2010, ArXiv e-prints

Hopkins, P. F., Hernquist, L., Cox, T. J., Di Matteo, T., Robertson, B., & Springel, V. 2006, ApJS, 163, 1

Hopkins, P. F., Hernquist, L., Cox, T. J., Robertson, B., & Krause, E. 2007, ApJ, 669, 67

Hu, J. 2008, MNRAS, 386, 2242

Hyde, J. B., Bernardi, M., Sheth, R. K., & Nichol, R. C. 2008, MNRAS, 391, 1559

Jahnke, K., & Macciò, A. V. 2011, ApJ, 734, 92

Jahnke, K., et al. 2009, ApJ, 706, L215

Jensen, J. B., Tonry, J. L., Barris, B. J., Thompson, R. I., Liu, M. C., Rieke, M. J., Ajhar, E. A., & Blakeslee, J. P. 2003, ApJ, 583, 712

Kelly, B. C. 2007, ApJ, 665, 1489

Kim, M., Ho, L. C., Peng, C. Y., Barth, A. J., Im, M., Martini, P., & Nelson, C. H. 2008, ApJ, 687, 767

Kormendy, J., Bender, R., & Cornell, M. E. 2011, Nature, 469, 374

Kormendy, J., & Gebhardt, K. 2001, in American Institute of Physics Conference Series, Vol. 586, 20th Texas Symposium on relativistic astrophysics, ed. J. C. Wheeler & H. Martel, 363–381

Kormendy, J., & Richstone, D. 1995, ARA&A, 33, 581

Lauer, T. R., Tremaine, S., Richstone, D., & Faber, S. M. 2007a, ApJ, 670, 249

Lauer, T. R., et al. 2007b, ApJ, 662, 808

Macciò, A. V., Dutton, A. A., & van den Bosch, F. C. 2008, MNRAS, 391, 1940

Maciejewski, W., & Binney, J. 2001, MNRAS, 323, 831

Magorrian, J., et al. 1998, AJ, 115, 2285

Marconi, A., & Hunt, L. K. 2003, ApJ, 589, L21

Marconi, A., Risaliti, G., Gilli, R., Hunt, L. K., Maiolino, R., & Salvati, M. 2004, MNRAS, 351, 169

McClintock, J. E., Shafee, R., Narayan, R., Remillard, R. A., Davis, S. W., & Li, L.-X. 2006, ApJ, 652, 518

McGill, K. L., Woo, J.-H., Treu, T., & Malkan, M. A. 2008, ApJ, 673, 703

McLure, R. J., & Dunlop, J. S. 2004, MNRAS, 352, 1390

Mei, S., et al. 2007, ApJ, 655, 144

Merloni, A., et al. 2010, ApJ, 708, 137

Minchev, I., Famaey, B., Quillen, A. C., Di Matteo, P., Combes, F., Vlajic, M., Erwin, P., & Bland-Hawthorn, J. 2012, ArXiv e-prints

Moster, B. P., Somerville, R. S., Maulbetsch, C., van den Bosch, F. C., Macciò, A. V., Naab, T., & Oser, L. 2010, ApJ, 710, 903

Mould, J. R., et al. 2000, ApJ, 529, 786

Novak, G. S., Faber, S. M., & Dekel, A. 2006, ApJ, 637, 96

Nowak, N., Thomas, J., Erwin, P., Saglia, R. P., Bender, R., & Davies, R. I. 2010, MNRAS, 403, 646

Oh, K., Sarzi, M., Schawinski, K., & Yi, S. K. 2011, ApJS, 195, 13

Onken, C. A., Ferrarese, L., Merritt, D., Peterson, B. M., Pogge, R. W., Vestergaard, M., & Wandel, A. 2004, ApJ, 615, 645

Peng, C. Y. 2007, ApJ, 671, 1098

Peng, C. Y., Ho, L. C., Impey, C. D., & Rix, H.-W. 2010, AJ, 139, 2097

Press, W. H., Teukolsky, S. A., Vetterling, W. T., & Flannery, B. P. 1992, Numerical recipes in FORTRAN. The art of scientific computing

Puget, P., et al. 2004, in Society of Photo-Optical Instrumentation Engineers (SPIE) Conference Series, Vol. 5492, Society of Photo-Optical Instrumentation Engineers (SPIE) Conference Series, ed. A. F. M. Moorwood & M. Iye, 978–987

Rix, H.-W., de Zeeuw, P. T., Cretton, N., van der Marel, R. P., & Carollo, C. M. 1997, ApJ, 488, 702

Rusli, S. P., Thomas, J., Erwin, P., Saglia, R. P., Nowak, N., & Bender, R. 2011, MNRAS, 410, 1223

Sani, E., Marconi, A., Hunt, L. K., & Risaliti, G. 2011, MNRAS, 413, 1479

Sarzi, M., Rix, H.-W., Shields, J. C., Rudnick, G., Ho, L. C., McIntosh, D. H., Filippenko, A. V., & Sargent, W. L. W. 2001, ApJ, 550, 65

Schulze, A., & Gebhardt, K. 2011, ApJ, 729, 21

Schwarzschild, M. 1979, ApJ, 232, 236

Sérsic, J. L. 1963, Boletin de la Asociacion Argentina de Astronomia La Plata Argentina, 6, 41

Shankar, F., Bernardi, M., & Haiman, Z. 2009a, ApJ, 694, 867

Shankar, F., Lapi, A., Salucci, P., De Zotti, G., & Danese, L. 2006, ApJ, 643, 14

Shankar, F., Marulli, F., Mathur, S., Bernardi, M., & Bournaud, F. 2012, A&A, 540, A23

Shankar, F., Salucci, P., Granato, G. L., De Zotti, G., & Danese, L. 2004, MNRAS, 354, 1020

Shankar, F., Weinberg, D. H., & Miralda-Escudé, J. 2009b, ApJ, 690, 20

Shen, J., & Gebhardt, K. 2010, ApJ, 711, 484

Silk, J., & Rees, M. J. 1998, A&A, 331, L1

Tadhunter, C., Marconi, A., Axon, D., Wills, K., Robinson, T. G., & Jackson, N. 2003, MNRAS, 342, 861

Tonry, J. L., Dressler, A., Blakeslee, J. P., Ajhar, E. A., Fletcher, A. B., Luppino, G. A., Metzger, M. R., & Moore, C. B. 2001, ApJ, 546, 681

Tremaine, S., et al. 2002, ApJ, 574, 740

Tundo, E., Bernardi, M., Hyde, J. B., Sheth, R. K., & Pizzella, A. 2007, ApJ, 663, 53

van de Ven, G., Falcón-Barroso, J., McDermid, R. M., Cappellari, M., Miller, B. W., & de Zeeuw, P. T. 2010, ApJ, 719, 1481

van den Bosch, R. C. E., & de Zeeuw, P. T. 2010, MNRAS, 401, 1770

van den Bosch, R. C. E., Gebhardt, K., Gültekin, K., van de Ven, G., van der Wel, A., & Walsh, J. L. 2012, Nature, 491, 729

van den Bosch, R. C. E., van de Ven, G., Verolme, E. K., Cappellari, M., & de Zeeuw, P. T. 2008, MNRAS, 385, 647

van der Marel, R. P., & van den Bosch, F. C. 1998, AJ, 116, 2220

van Dokkum, P. G., et al. 2008, ApJ, 677, L5

Verolme, E. K., et al. 2002, MNRAS, 335, 517

Vika, M., Driver, S. P., Cameron, E., Kelvin, L., & Robotham, A. 2012, MNRAS, 419, 2264

Volonteri, M., Natarajan, P., & Gültekin, K. 2011, ApJ, 737, 50

Zhu, Y.-N., Wu, H., Li, H.-N., & Cao, C. 2010, Research in Astronomy and Astrophysics, 10, 329